NAVAL POSTGRADUATE SCHOOL
Monterey, California

DISSERTATION

THESIS
C6455

DEPENDENCE OF RADAR BACKSCATTER
ON THE
ENERGETICS OF THE AIR-SEA INTERFACE

by

Marie C. Colton

December, 1989

Dissertation Supervisor: Edward B. Thornton

Approved for Public Release; distribution is unlimited

T247188

Security Classification of this page

REPORT DOCUMENTATION PAGE

1a Report Security Classification UNCLASSIFIED
1b Restrictive Markings
2a Security Classification Authority
3 Distribution Availability of Report
Approved for public release; distribution is unlimited.
2b Declassification/Downgrading Schedule
4 Performing Organization Report Number(s)
5 Monitoring Organization Report Number(s)
6a Name of Performing Organization
Naval Postgraduate School
6b Office Symbol *(If Applicable)* 68
7a Name of Monitoring Organization
Naval Postgraduate School
6c Address *(city, state, and ZIP code)*
Monterey, CA 93943-5000
7b Address *(city, state, and ZIP code)*
Monterey, CA 93943-5000
8a Name of Funding/Sponsoring Organization
8b Office Symbol *(If Applicable)*
9 Procurement Instrument Identification Number
8c Address *(city, state, and ZIP code)*
10 Source of Funding Numbers

Program Element Number	Project No	Task No	Work Unit Accession No

11 Title *(Include Security Classification)* DEPENDENCE OF RADAR BACKSCATTER ON THE ENERGETICS OF THE AIR-SEA INTERFACE
12 Personal Author(s) Marie C. Colton
13a Type of Report
Dissertation
13b Time Covered
From To
14 Date of Report *(year, month,day)*
1989, December
15 Page Count
16 Supplementary Notation The views expressed in this paper are those of the author and do not reflect the official policy or position of the Department of Defense or the U.S. Government.
17 Cosati Codes

Field	Group	Subgroup

18 Subject Terms *(continue on reverse if necessary and identify by block number)*
Scatterometry, Air-Sea Interaction, Ocean Wave Dynamics

19 Abstract *(continue on reverse if necessary and identify by block number*

The Normalized Radar Cross-Section (NRCS), the fundamental measurement made by radar scatterometers, was obtained as part of the Water-Air Vertical Exchanges 1987 (WAVES87) experiment. The experiment was designed to evaluate the effects of environmental parameters on the NRCS and was performed from a research tower located in Lake Ontario, on which two microwave scatterometers operating at 14.0 and 5.0GHz were installed for six weeks in the autumn of 1987. The novel aspect of this experiment was that the 14.0GHz radar automatically rotated through 300° in azimuth angle at six different incidence angles to the water surface, accompanied by simultaneous measurements of wind stress and high resolution directional wave spectra. Therefore, the incidence and azimuthal angle behavior of the NRCS was examined as a function of wind speed, friction velocity, wind direction, wave direction and atmospheric stability.

The dependence of the NRCS on wind speed for various incidence angles is similar to previous results. However, the slope exponents of the NRCS vs. 19.5m wind speed curves at intermediate incidence angles are higher than the corresponding open ocean measurements. Scaling the lake neutral wind speed data by the ratio of lake to ocean drag coefficients reduces the slopes of the curves and suggests the drag coefficient has a sea state dependence. The correlation between NRCS and neutral wind speed at 1m is higher (0.91) than between the NRCS and friction velocity (0.73 at 40°). The minima in the sinusoidal modulation of the NRCS as a function of relative wind angle (the angle between the wind and antenna directions) are often shifted (by as much as 45°) such that the minima do not always occur at cross-wind angles. Instead, the angular distance between the NRCS minima in the case of a wind-wave sea appears to approximate the directional spread of the waves about the upwind direction, generally rather less than 180°. The degree of sinusoidal modulation of the NRCS with

20 Distribution/Availability of Abstract
☒ unclassified/unlimited ☐ same as report ☐ DTIC users
21 Abstract Security Classification
Unclassified
22a Name of Responsible Individual
E. B. Thornton
22b Telephone *(Include Area code)*
(408) 646-2847
22c Office Symbol
68Tm

DD FORM 1473, 84 MAR
83 APR edition may be used until exhausted
All other editions are obsolete
security classification of this page
Unclassified

#19.

relative wind angle is highly correlated with significant slope and inverse wave age at 20° incidence angle (0.9 and moderately correlated at 40° (0.75); i.e., increased azimuthal modulation at 20° is associated with a steepe wave field. The dependence of the NRCS on atmospheric stability shows the NRCS to decrease by about 5dB between air-water temperature differences of about -16 to +10°C. This stability effect is removed by parameterization of the NRCS in terms of either the friction velocity or neutral wind speed at 1m, with the neutral wind speed providing the best normalization of the data. The results show that radar scatterometers ar an especially sensitive means by which to study the air-sea interface: the magnitudes of the 5.0GHz and 14.0G NRCS respond nearly instantaneously to changes in the near-surface neutral wind speed, but the directionality of the (Ku-band) NRCS is the result of complicated interrelationships among the influencing environmental variables.

Approved for public release; distribution is unlimited

DEPENDENCE OF RADAR BACKSCATTER ON THE ENERGETICS OF THE AIR-SEA INTERFACE

by

Marie C. Colton
B.S., Florida Institute of Technology, 1978
M.S., Florida Institute of Technology, 1981

Submitted in partial fulfillment of the
requirements for the degree of

DOCTOR OF PHILOSOPHY IN PHYSICAL OCEANOGRAPHY

from the

NAVAL POSTGRADUATE SCHOOL
December, 1989

ABSTRACT

The Normalized Radar Cross-Section (NRCS), the fundamental measurement made by radar scatterometers, was obtained as part of the Water-Air Vertical Exchanges 1987 (WAVES87) experiment. The experiment was designed to evaluate the effects of environmental parameters on the NRCS and was performed from a research tower located in Lake Ontario, on which two microwave scatterometers operating at 14.0 and 5.0GHz were installed for six weeks in the autumn of 1987. The novel aspect of this experiment was that the 14.0GHz radar automatically rotated through 300° in azimuth angle at six different incidence angles to the water surface, accompanied by simultaneous measurements of wind stress and high resolution directional wave spectra. Therefore, the incidence and azimuthal angle behavior of the NRCS was examined as a function of wind speed, friction velocity, wind direction, wave direction and atmospheric stability.

The dependence of the NRCS on wind speed for various incidence angles is similar to previous results. However, the slope exponents of the NRCS vs. 19.5m wind speed curves at intermediate incidence angles are higher than the corresponding open ocean measurements. Scaling the lake neutral wind speed data by the ratio of lake to ocean drag coefficients reduces the slopes of the curves and suggests the drag coefficient has a sea state dependence. The correlation between NRCS and neutral wind speed at 1m is higher (0.91) than between the NRCS and friction velocity (0.73 at 40°). The minima in the sinusoidal modulation of the NRCS as a function of relative wind angle (the angle between the wind and antenna directions) are often shifted (by as much as 45°) such that the minima do not always occur at cross-wind angles. Instead, the angular distance between the NRCS minima in the case of a wind-wave sea appears to approximate the directional spread of the waves about the upwind direction, generally rather less than 180°. The degree of sinusoidal modulation of the NRCS with relative wind angle is highly correlated with significant slope and inverse wave age at 20° incidence angle (0.90) and moderately correlated at 40° (0.75); i.e., increased azimuthal modulation at 20° is associated with a steeper wave field. The dependence of the NRCS on atmospheric stability shows the NRCS to decrease by about 5dB between air-water temperature differences of about -16 to +10°C. This stability effect is removed by parameterization of the NRCS in terms of either the friction velocity or neutral wind speed at 1m, with the neutral wind speed providing the best normalization of the data. The results show that radar scatterometers are an especially sensitive means by which to study the air-sea interface: the magnitudes of the 5.0GHz and 14.0GHz NRCS respond nearly instantaneously to changes in the near-surface neutral wind speed, but the directionality of the (Ku-band) NRCS is the result of complicated interrelationships among the influencing environmental variables.

TABLE OF CONTENTS

I. INTRODUCTION 1

A. REMOTE SENSING OF THE OCEAN 1

B. THE RESEARCH PROBLEM 2

C. NAVAL RELEVANCE: REQUIREMENTS FOR THE WIND VELOCITY AT THE SEA SURFACE 8

D. SUMMARY 10

II. LITERATURE REVIEW 11

A. INTRODUCTION 11

B. HISTORICAL REVIEW OF SCATTEROMETRY 11

C. ELECTROMAGNETIC SCATTERING THEORY 15

D. SPECIFICATION OF THE ROUGH SEA SURFACE 31

E. FUNDAMENTALS OF AIR-SEA INTERACTION THEORY 53

F. SYNOPSIS OF RECENT MODEL FUNCTIONS 66

G. SUMMARY 88

III. THE LAKE ONTARIO WAVES '87 EXPERIMENT 94

A. INTRODUCTION 94

B. THE EXPERIMENTAL SITE 94

C. MEASUREMENTS AND INSTRUMENTATION 101

D. DATA ACQUISITION 115

E. SUMMARY 116

IV. DATA PROCESSING METHODS AND RESULTS 117

A. THE KU-BAND SCATTEROMETER AND ASSOCIATED ENVIRONMENTAL PARAMETERS 117

B. THE C-BAND SCATTEROMETER AND ASSOCIATED ENVIRONMENTAL PARAMETERS 140

C. COMPUTATION OF THE WIND STRESS, HEAT FLUX AND NEUTRAL WIND SPEED 142

D. COMPUTATION OF THE WAVE FIELD PARAMETERS 154
E. SUMMARY 156

V. DISCUSSION AND RESULTS 157
A. INTRODUCTION 157
B. NRCS DEPENDENCE ON WIND SPEED PARAMETERS 157
C. NRCS DEPENDENCE ON WIND DIRECTION 175
D. NRCS DEPENDENCE ON SPECTRAL WAVE PARAMETERS 186
E. DEPENDENCE OF NRCS ON ATMOSPHERIC STRATIFICATION 221
F. NRCS DEPENDENCE ON WATER TEMPERATURE 234
G. SUMMARY 234

VI. SUMMARY AND CONCLUSIONS 236
A. SYNOPSIS OF THE STUDY AND MAJOR RESULTS 236
B. CLOSURE 244

APPENDIX A. DEFINITION OF THE NORMALIZED RADAR CROSS SECTION 246

APPENDIX B. 252

LIST OF REFERENCES 302

INITIAL DISTRIBUTION LIST 315

LIST OF TABLES

TABLE I. PERFORMANCE GOALS FOR SATELLITE MEASUREMENT OF SURFACE WINDS..10
TABLE II. MICROWAVE FREQUENCY BAND DESIGNATIONS..............12
TABLE III. MATRIX OF MODEL FUNCTION CHARACTERISTICS...........92
TABLE IV. SUMMARY OF ENVIRONMENTAL CONDITIONS DURING THE WAVES'87 EXPERIMENT......................................98
TABLE V. CHARACTERISTICS OF THE NRL RADARS..............................104
TABLE VI. COMPARISON OF NRCS VERSUS WIND SPEED SLOPE COEFFICIENTS WITH PREVIOUS STUDIES................................168
TABLE VII. PREDICTED EFFECTS OF SLOPE CHANGES ON NRCS FROM PLANT MODEL (20°, WIND SPEED 6M/S)......................220

LIST OF FIGURES

Figure 1. Environmental Effects on the Normalized Radar Cross-Section 4

Figure 2. Functional Dependence of Normalized Radar Cross-Section on a) Wind Speed for Various Angles of Incidence, θ (Schroeder, et al., 1982); b) Wind Direction (Jones et al., 1977); c) Long Wave Slope (Keller, et al., 1985); d) Atmospheric Stratification (Keller, et al., 1989) 5

Figure 3. Examples of Surface Scattering Patterns 19

Figure 4. Schematic Drawings of the Sea Surface for a) the Kirchoff (Tangent Plane or "Facet") Approximation b) the Bragg-Resonance Model, and c) the Two-Scale Composite Surface Model Where λ_{cm}, k_{cm}: Electromagnetic Wavelength and Wave number; h, Height above Mean Level; l, Correlation Length; L, λ_B: Ocean and Bragg Wavelengths 22

Figure 5. Evidence of First-Order Bragg Scattering (Stewart, 1985 after Wright, 1966) 26

Figure 6. Evidence for First-Order Bragg Scattering and Validity of Two-Scale Model (a) (b) Left, Doppler Spectra from Field Data; (a) (b) Right, Doppler Spectra from Two-Scale Model (adapted from Plant and Keller, 1989) 28

Figure 7. Backscatter Versus Incidence Angle for Three Scattering Regimes (from Stewart, 1985 after Valenzuela, 1978) 30

Figure 8. The Mean JONSWAP Spectrum and Source Functions $\Sigma'(w)$ together with the Computed Nonlinear Energy Transfer Σ'_{nl} (from LeBlond and Mysak, 1978, after Hasselmann, et al., 1973) 40

Figure 9a. The Evolution of Surface Wave Spectra with Fetch, from the JONSWAP Observations. The Fetch Increases with the Number labelling the Spectral Peak (from LeBlond and Mysak, 1978, after Hasselmann, et al., 1973) 41

Figure 9b. Normalized Frequency Spectra Grouped into Classes by U_c/c_p. The Vertical Bars at the Top of the Figure are an Estimate of the 90% Confidence Limits Based on the Standard Error of the Mean (from Donelan et al., 1985) 42

Figure 10. (Left) Delineation of Five Wave Spectral Regions; (Right) Graphical Description of the Frequency Bounds of Region IV (from Shemdin and Hwang, 1988) 46

Figure 11. (Left) Comparison of the Proposed Model with the Donelan and Pierson [1987] model; (Right) Comparison of the Proposed Model with the Pierson and Stacy [1973] model 48

Figure 12. Distribution of the Neutral Drag Coefficient with Wind Speed from the Following Investigations: 1, Large and Pond [1981]; 2, Smith [1980]; 3) Smith and Banke [1975[; 4) Geernaert et al. [1987b]; 5) Geernaert [1986]; 6) Sheppard et al. [1972]; 7) Donelan [1982]; 8) Kondo [1975] (from Geernaert, 1988a) 63

Figure 13. Schematic Diagram of the Internal Boundary Layer (IBL) over a step change of a) surface roughness (from Rao, et al., 1974) and b) temperature (Hsu, 1989). 64

Figure 14a. Comparison of Donelan and Pierson (1987) and Durden and Vesecky (1985) Wavenumber Amplitude Spectra for Upwind Direction and U19.5 = 10m/s 73

Figure 14b. Comparison of Donelan and Pierson (1987) and Durden and Vesecky (1985) Wavenumber Amplitude Spectra for Crosswind Direction and U19.5 = 10m/s 74

Figure 15. Spectral Density Image of Directional Dependence of Durden and Vesecky (Two-Sided) Wavenumber Spectrum 75

Figure 16. (a) Cross-Section vs. Incidence Angle and (b) "Power Law" Wind Speed Exponent as a Function of Incidence Angle from the Durden and Vesecky Model (1985) 78

Figure 17. Wavenumber Spectra from Donelan and Pierson Model (1987) ... 83

Figure 18. Spectral Density Image of Directional Dependence of Donelan and Pierson (One-Sided) Wavenumber Spectrum (from Verma, et al., 1989) 84

Figure 19. Predicted Cross-Sections Against Wind Speed for Different Temperatures (from Donelan and Pierson, 1987) 85

Figure 20a. 25° Incidence Angle. Comparison of Predictions of Plant Model with Ku Band Data Given by Schroeder et al. [1982] and the SASS 1 Model Function. Data Points are those Seasat Cross Sections which Could Be Associated with Good Surface Measurements of Wind. Solid Lines Represent the SASS 1 Model Function, While Dashed Lines Represent Predictions of the Plant Model (from Plant, 1986). 89

Figure 20b. 40° Incidence Angle. Comparison of Predictions of Plant Model with Ku Band Data Given by Schroeder et al. [1982] and the SASS 1 Model Function. Data Points are those Seasat Cross Sections which Could Be Associated with Good Surface Measurements of Wind. Solid Lines Represent the SASS 1 Model Function, While Dashed Lines Represent Predictions of the Plant Model (from Plant, 1986). 90

Figure 21. Map Showing the Location of the Research Tower in Lake Ontario and the Shore-Normal Profile in the Vicinity of the Tower (Donelan et al., 1985) 95

Figure 22. Photograph of the CCIW Tower Configured for WAVES'87..........97

Figure 23. Average Environmental Conditions During WAVES'87 vs. Time (a) Air-Water Temperature, (b) Relative Humidity..............99

Figure 23. (Cont.) (c) Wind Speed and Air-Water Temperature Difference, and (d) Wind Direction. 100

Figure 24. Ku-Band (14 GHz) Radar System Installed on the Boom 103

Figure 25. C-Band (5 GHz) Radar System Mounted on the Tower Railing Facing Southwest 105

Figure 26. Configuration and Half-Power Full Beam-Widths of the Microwave System Antennas. Φy is the Vertical Beamwidth and Φx is the Horizontal Beamwidth 106

Figure 27. Antenna Patterns for C-Band (5GHz) Radar System.......................108

Figure 28. The Bivane Anemometer on the Research Tower Mast (from Tsanis and Donelan, 1987) 112

Figure 29. Analog Record of the First 7.5 Minutes of Data Run 56.................118

Figure 30. Azimuthly Averaged NRCS of First Radar Rotation Plotted against Second Rotation. Upper: 40° v-pol. Lower: 40° h-pol. ..122

Figure 31a. Internal Calibration Voltage of Ku-Band Radar as a Function of Time from Start of Experiment (November 11, 1987) 124

Figure 31b. Internal Calibration Voltage of Ku-Band Radar as a Function of Air Temperature 124

Figure 32. Final 3.5 Minutes of Run 48, Used for Evaluation of the Ku-Band Radar System Noise Level 128

Figure 33. NRCS Versus Azimuth Angle of Radar for all Incidence Angles. Upper: v-pol. Lower: h-pol 130

Figure 34. NRCS Versus Incidence Angle. Upper: v-pol 131

Figure 35. Two-Pass Averaged NRCS as a Function of Radar Azimuth. Dotted Lines Show 95% Confidence Levels Based on Chi-Square Distribution 133

Figure 36a. Histogram of Voltage Measurements from Ku-Band Radar; 20° v-pol 134

Figure 36b. Histogram of Voltage Measurements from Ku-Band Radar; 20° h-pol 134

Figure 37. Averaged and Smoothed NRCS as a Function of the Radar Azimuth Angle 136

Figure 38. Antenna Pattern Correction to Convert Ku-Band 7.0° Beamwidth to 1° Beamwidth 139

Figure 39a. Internal Calibration Voltage of C-Band Radar as a Function of Time from the Start of the Experiment (November 11, 1987) 141

Figure 39b. Internal Calibration Voltage of the C-Band Radar as a Function of Air Temperature... 141

Figure 40. One-Minute C-Band NRCS and Associated Environmental Parameters as a Function of Time from the Start of the Data Run 143

Figure 41a. Shematic Spectrum of Wind Speed Near the Ground Estimated from a Study of Van der Hoven (1957) 147

Figure 41b. Frequency Spectrum of Wind Speed Over Water from Pierson (1983) 148

Figure 42. Normalized Stress Cospectrum after Kaimal et al., (1972). (from Panofsky and Dutton, 1984) 149

Figure 43. Wind and Stability Parameters as a Function of Time: (a) Wind Stress, (b) Drag Coefficient, (c) Wind Speed, (d) Wind and Stress Direction, (e) Bulk Richardson Number and (f) Relative Angle between Wind and Stress Directions 152

Figure 44. Ku-Band Vertical Polarized NRCS versus Friction Velocity for Multiple Incidence Angles. Clockwise from Top Left: Upwind, Downwind, Crosswind near 90°, crosswind near 270° 161

Figure 45. Ku-Band Horizontal Polarized NRCS versus Friction Velocity for Multiple Incidence Angles. Clockwise from Top Left: Upwind, Downwind, Crosswind near 90°, Crosswind near 270° 162

Figure 46. Ku-Band (v-pol) NRCS versus Neutral Wind Speed at 19.5m for Multiple Incidence Angles. Clockwise from Top Left: Upwind, Downwind, Crosswind near 90°, Crosswind near 270° 163

Figure 47. Ku-Band (h-pol) NRCS versus Neutral Wind Speed at 19.5m for Multiple Incidence Angles. Clockwise from Top Left: Upwind, Downwind, Crosswind near 90°, Crosswind near 270° 164

Figure 48. Ku-Band (v-pol) NRCS versus Neutral Wind Speed at 19.5m for Multiple Incidence Angles. 165

Figure 49. Ku-Band (h-pol) NRCS versus Neutral Wind Speed at 19.5m for Multiple Incidence Angles 166

Figure 50. NRCS Versus Neutral Windspeed from Lake Data (as measured), Models and Scaled Lake Data 171

Figure 51. Scaled NRCS Versus Neutral Windspeed for Ku-Band Vertical Polarized Data and Multiple Incidence Angles, Clockwise from Top Left: Upwind, Downwind, Crosswind near 90° and Crosswind near 270° 173

Figure 52. Scaled NRCS Versus Neutral Windspeed for Ku-Band Horizontal Polarized Data and Multiple Incidence Angles, Clockwise from Top Left: Upwind, Downwind, Crosswind near 90° and Crosswind near 270° 174

Figure 53. Three-dimensional Surfaces of Vertical-Polarized NRCS as a Function of Incidence Angles, Friction Velocity and Relative Angle, Chi, (Wind Minus Antenna Angle). Incidence Angle Increases Clockwise from Nadir at Top Left, the Relative Angle is Given in Radians with π Corresponding to the Downwind Look Direction 177

Figure 54. Three-dimensional Surfaces of Horizontal-Polarized NRCS as a Function of Incidence Angle, Friction Velocity and Relative Angle, Chi (Wind Minus Antenna Angle). Incidence Angle Increases Clockwise from Nadir at Top Left 178

Figure 55. Samples of NRCS as a Function of Relative Wind Angle and Fitted Cosine Curves for 20°, v-pol. Windspeed is in Bottom Left Corner of Each Plot 180

Figure 56. Samples of NRCS (v-pol) as a Function of Relative Wind Angle and Fitted Cosine (Plus Sine) Curves 181

Figure 57. Azimuthal Dependence of the NRCS in the Presence of Rain: a) 10°, b) 20°, (Runs 143 to 145) and c) 40° v-pol for Runs 143 to 146. Note attenuation of azimuthal modulation at 40° between runs 143 and 144. 184

Figure 58. Wave Amplitude Spectra from Runs 143, 144, 146 185

Figure 59. One-Minute Block-Averaged C-band NRCS and Environmental Data from Run 87049. Time Associated with Particular Incidence Angles of Ku-band Radar are Annotated on Wind Speed Plot 189

Figure 60. Run 49: a) NRCS Versus Relative Wind Angle for 10°, 20°, 40°, 60° v-pol (Top Row) and h-pol (Bottom Row), b) Directional Spectrum, and c) Polar Plot of Relative Angles Among the Radar, Wind and Waves 190

Figure 61. Azimuthal Modulations of Model Functions (o -- Plant, x -- SASS2, + -- D&P, -.- line SASS1, solid line D&V) and Measurements from Run 49 (*) 192

Figure 62. One-Minute Block Averaged C-band NRCS and Environmental Data From Run 89. Times Associated with Particular Incidence Angles of Ku-band Radar are Annotated on Wind Speed Plot 195

Figure 63. Run 89. NRCS (V-Pol) as a Function of Incidence Angle and Radar Azimuth Angle in Degrees True North. Average Wind Speed for each Incidence Angle is Marked at the End of Each Curve 196

Figure 64. Run 89. NRCS (H-Pol) as a Function of Incidence Angle and Radar Azimuth Angle in Degrees True North 197

Figure 65. Run 89. Directional Spectrum and Polar Plot of Relative Geometry Among Radar, Wind and Wave Angles 198

Figure 66. One-Minute Block-Averaged C-Band NRCS and Environmental Data from Run 79 200

Figure 67. Run 79. NRCS (V-Pol) as a Function of Incidence Angle and Radar Azimuth Angle in Degrees True North. Average Wind Speed for each Incidence Angle is Marked at the End of Each Curve 202

Figure 68. Run 79. NRCS (H-Pol) as a Function of Incidence Angle and Radar Azimuth Angle in Degrees True North 203

Figure 69. Azimuthal Modulation of Ku-band Radar in a Combined Wind/Swell Sea (Run 79) Top: NRCS v. Relative Wind Angle for 10°, 20°, 40° Incidence Angle (v-pol, h-pol); Middle: Perspective Plot of Directional Wave Spectrum; Bottom Right: Polar Plot of Tower, Radar, Wind and Wave Geometry 204

Figure 70. Run 80. Perspective Plot of Directional Spectrum and Polar Plot of Relative Geometry Among Radar, Wind and Wave Angles 207

Figure 71. One-Minute Block-Averaged C-Band NRCS and Environmental Data for Run 75 208

Figure 72. Run 75 NRCS (V-Pol) as a Function of Incidence Angle and Radar Azimuth Angle in Degrees True North. Average Wind Speed for each Incidence Angle is Marked at the End of Each Curve 209

Figure 73. Run 75 NRCS (H-Pol) as a Function of Incidence Angle and Radar Azimuth Angle in Degrees True North. Average Wind Speed for each Incidence Angle is Marked at the End of Each Curve 210

Figure 74. Run 75 Perspective Plot of Directional Spectrum and Polar Plot of Relative Geometry Among Radar, Wind and Wave Angles for 40° and 80° 211

Figure 75. Ratio of A_2 and A_0 Coefficients from Cosine Fits to 20° Ku-Band NRCS (H-Pol) Against Significant Slope. Dashed Line Encircles Anomalous Points as Explained in Text. U: Unstable Atmospheric Stratification; N: Neutral; S: Stable 215

Figure 76 Ratio of A_2 and A_0 Coefficients from Cosine Fits to 20° Ku-Band NRCS (H-Pol) Against Significant Slope.Circled Points were Eliminated from Regression (see text). Line 1: with Bad Points; Line 2: Points Excluded 216

Figure 77. Ratio of A_2 and A_0 Coefficients from Cosine Fits to 20°, H-Pol, Ku-Band NRCS versus Inverse Wave Age. Circled Points Eliminated from Regression as Explained in Text. Line 1 with Points; Line 2: without Points 218

Figure 78. Ratio of A_2 and A_0 Coefficients from Cosine Fits to 40°, H-Pol, Ku-Band NRCS versus Inverse Wave Age 219

Figure 79. Normalized 20°, V-Pol Ku-Band NRCS for Measured Wind Speed of 6.5 to 7.5m/s as a Function of a) Air-Water Temperature Difference, b) Bulk Richardson Number, and c) Stability Parameter 224

Figure 80. Normalized 20°, V-Pol, Ku-Band NRCS for $7.0<U_N(19.5)<8.0$m/s as a Function of a) Air-Water Temperature Difference, b) Bulk Richardson Number and c) Stability Parameter 225

Figure 81. Normalized 20°, V-Pol NRCS for $4.5<U_N(1) < 5.5$ m/s as a Function of a) Air-Water Temperature Difference, b) Bulk Richardson Number and c) Stability Parameter 226

Figure 82. Normalized 20°, V-Pol NRCS for $0.23<u_*< 0.26$m/s as a Function of a) Air-Water Temperature Difference, b) Bulk Richardson Number and c) Stability Parameter 227

Figure 83. Normalized 40°, V-Pol Ku-Band NRCS for Measured Wind Speed of 6.5 to 7.5m/s as a Function of a) Air-Water Temperature Difference, b) Bulk Richardson Number, and c) Stability Parameter 228

Figure 84. Normalized 40°, V-Pol, Ku-Band NRCS for $7.0<U_N(19.5)<8.0$m/s as a Function of a) Air-Water Temperature Difference, b) Bulk Richardson Number and c) Stability Parameter 229

Figure 85. Normalized 40°, V-Pol NRCS for $4.5<U_N(1) < 5.5$ m/s as a Function of a) Air-Water Temperature Difference, b) Bulk Richardson Number and c) Stability Parameter 230

Figure 86. Normalized 40°, V-Pol NRCS for $0.23<u_*< 0.26$m/s as a Function of a) Air-Water Temperature Difference, b) Bulk Richardson Number and c) Stability Parameter 231

ACKNOWLEDGEMENT

The dissertation as a written work has a central theme which is the examination of a scientific hypothesis. What is not written is how the dissertation produces a parallel structure in the student's life in which the dissertation is the central theme with the student's working environment, family, friends and colleagues providing support and guidance. In this respect, the doctoral dissertation is not the work of the individual student.

I have been very fortunate to have parents who always visualize greater things for me, a husband who understands these ambitions and a young daughter who helps me keep everything in the proper perspective. The opportunity to study at the Naval Postgraduate School was initially provided by Prof. Christopher N. K. Mooers (now at Univ. of New Hampshire) and continued by Prof. Curtis A. Collins. I appreciate the efforts and endurance of my committee members: Profs. K. L. Davidson, R. W. Garwood, G. L. Geernaert, G. E. Latta and C. H. Wash. Special thanks are due my major advisor, Prof. E. B. Thornton for his willingness to address a subject which was at first tangential to his primary interests, his ready availability and his skill at knowing how to gently "call a spade, a spade." The technical and moral support of my co-workers and supervisors at the Naval Oceanographic and Atmospheric Research Laboratory is also gratefully acknowledged.

The experiment described herein was planned by Dr. Mark A. Donelan, Dr. William J. Plant (Woods Hole Oceanographic Institution) and Mr. William C. Keller (Naval Research Laboratory), and executed under Dr. Donelan's direction at the Canada Centre for Inland Waters (CCIW), Ontario.

These gentlemen generously gave of their time and considerable expertise during all phases of the dissertation research. The tutelage and hospitality of Dr. Donelan during my extended visits to CCIW are gratefully acknowledged.

There are people who made cameo appearances during the course of the research which influenced the final results in a positive way. At the Jet Propulsion Laboratory, Dr. Michael Freilich suggested additional analyses regarding the processing of the raw scatterometer data and Dr. Scott Dunbar provided me with software to automate some of my procedures. Whenever we crossed paths, Prof. Kristina B. Katsaros (Univ. of Washington) took time to advise me in her special way about the road ahead of me as both a scientist and mother. One day at a conference, Dr. W. Linwood Jones (NASA Headquarters), to whom I had just been introduced, painstakingly rederived my radar calibration equations in an effort to locate a possible error. It is hoped that documentation of this support of students by senior scientists will encourage those who are just beginning their doctoral programs.

I. INTRODUCTION

A. REMOTE SENSING OF THE OCEAN

In the three decades since the launch of the first meteorological satellite, the enormous potential of remote sensing of the Earth's environment has been proved. Products of visible and infrared imagery are routinely used to monitor the evolution of weather systems, oceanic fronts and eddies. Passive infrared and microwave radiometers provide vertical temperature soundings of the atmosphere and information on its moisture content. Active microwave radars serve the dual purpose of measuring sea surface elevation and waves, and inferring sea surface winds over areal expanses, both with accuracies never before realized. To capitalize on these now proven techniques, space agencies have initiated ambitious programs to build and launch environment observing satellites in the early 1990's.

At the heart of these programs are intriguing and unresolved questions, answers to which will provide the basis for next generation instrumentation and delimit the applicability of remotely sensed data. Questions raised are 1) theoretical: How are the spectral emissions/reflections from the earth related to geophysical variables of interest?, 2) technical: How can advances in computer and engineering sciences be incorporated into remote sensing instruments?, and 3) operational: How are the huge volumes of data to be received processed, distributed and analyzed in near real-time? The issue addressed in this study is of the first general type. In particular, the purpose of this study is to evaluate environmental effects on the functional form which relates radar echoes from the sea surface to the sea surface wind vector.

B. THE RESEARCH PROBLEM

1. Statement of the Problem

Radar backscatter at intermediate incidence angles (20 to 70 deg) can be related by a "model function" to the sea surface wind speed and direction due to backscatter which is produced primarily by "Bragg resonant" reflections of the incident radiation from successive crests of short, wind generated capillary-gravity waves (0.2 to 20 cm wavelength). For the signal to be scattered to the radar, these waves must have components traveling along the direction of the antenna line-of-sight. Therefore, the backscattered power displays a strong angular dependence: maxima occur when the antenna is pointed either upwind or downwind, minima occur when the antenna is pointed crosswind. Furthermore, the upwind maximum is usually larger than the downwind maximum; this difference is enhanced for horizontally polarized radiation. The idea, then, behind scatterometer wind vector determination, is that a particular area on the ocean surface viewed from several different directions; i.e., azimuth angles, yields different wind components per azimuth that can be used to determine a single wind vector.

The above information has been incorporated into previous model functions by writing the normalized radar cross-section (NRCS) of the sea as a function of radar incidence angle, radar polarization, and azimuth angle relative to the true wind vector (Jones, et al., 1977; Moore and Fung, 1979; Schroeder, et al., 1982). However, Daley, et al., (1984) identify the deficiencies in this simple type of formulation and list the additional dependencies which may need to be included in the scatterometer model function. Based on recent research, these dependencies are:

(1) cross-section dependence on wave slope and wave direction relative to the wind vector (Keller, et al., 1985, 1989; Li, et al., 1989),

(2) cross-section dependence on air-sea temperature difference, and thus on stability of the marine surface layer (e.g., Keller, et al., 1989),

(3) a lack of self-consistency of the model between vertical and horizontal polarizations (Wentz, 1984; Woiceshyn, et al., 1986),

(4) decreased sensitivity of the model function at low wind speeds (below 7 m/s), (Woiceshyn, et al., 1986),

(5) cross-section dependence on surface contaminants and films (Huhnerfuss, et al., 1983), and

(6) cross-section dependence on viscosity of the water as a function of temperature (Woiceshyn, 1986; Donelan and Pierson, 1987).

For the scatterometer wind velocity to meet the stringent operational requirements of the Navy (±2m/s, ±2.5°) , an updated model function is required.

2. Research Objective

The effects of the various environmental parameters listed above are represented schematically in Figure 1. An increase in wind speed produces an associated increase in the NRCS through amplification of the capillary-gravity waves from which the electromagnetic waves are reflected. Observations show that the wind speed dependence can be represented as a power law (Figure 2a). Referring to Figure 2b, the cross-section varies with wind direction as a result of the anisotropy of the capillary-gravity waves with the relative maxima occurring when the radar beam is directed perpendicular to the wavecrest (upwind/downwind) and the minima occurring when the radar beam is parallel to the wavecrests (crosswind). This behavior is rather successfully modeled as a truncated Fourier cosine series.

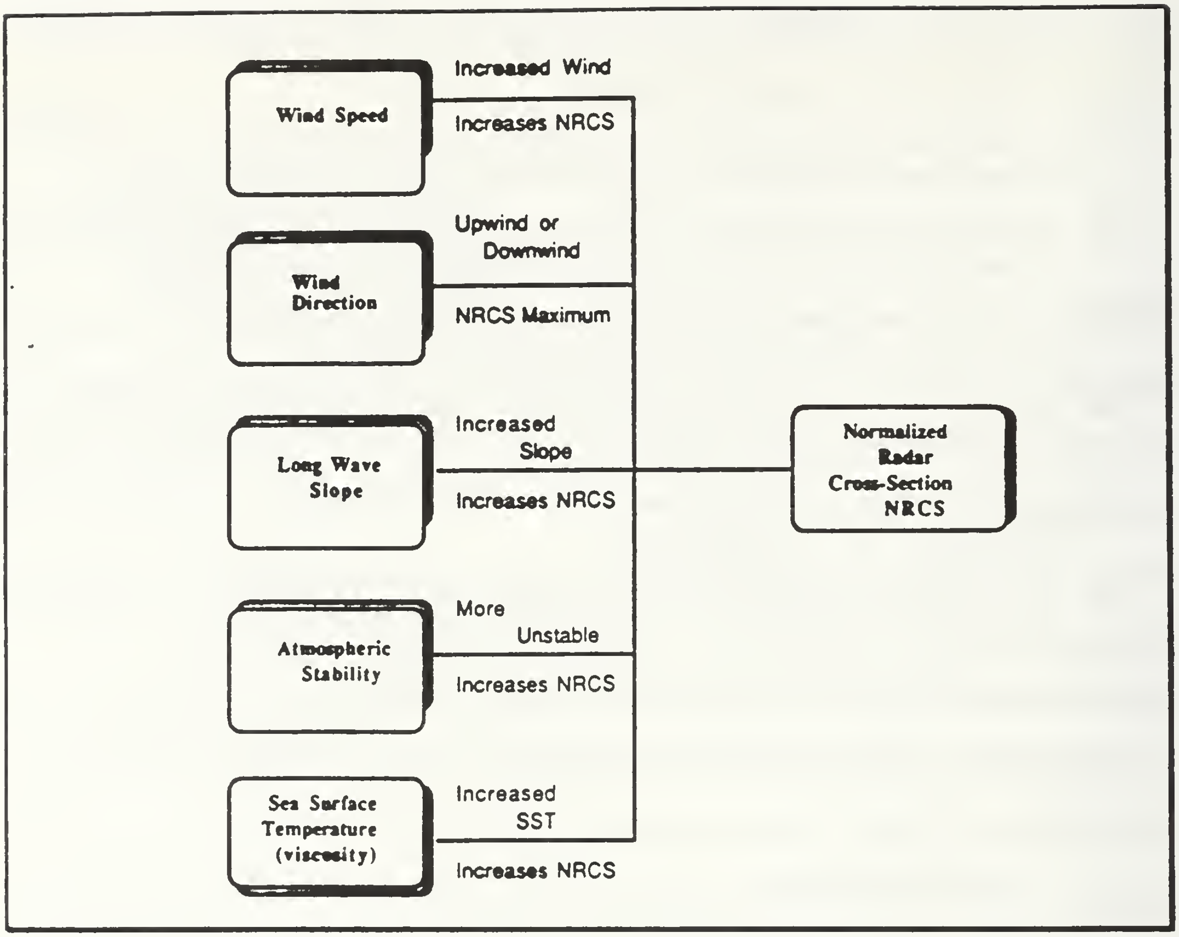

Figure 1. Environmental Effects on the Normalized Radar Cross-Section

If the short waves are tilted towards the radar and modulated in amplitude and frequency by the slope of the longer waves on which they ride, the NRCS will again be increased (Figure 2c). Observational evidence for the long wave influence has been reported by Keller, et al., (1985,1989) who show that the cross-sections increase with wave slope only when the atmosphere is stably stratified. Measurements during neutral and unstable conditions yielded no discernable dependence of the NRCS on long wave slope; it is suspected that the influence of stability is a consequence of the coupling between the surface waves and wind turbulence (see Figure 2d).

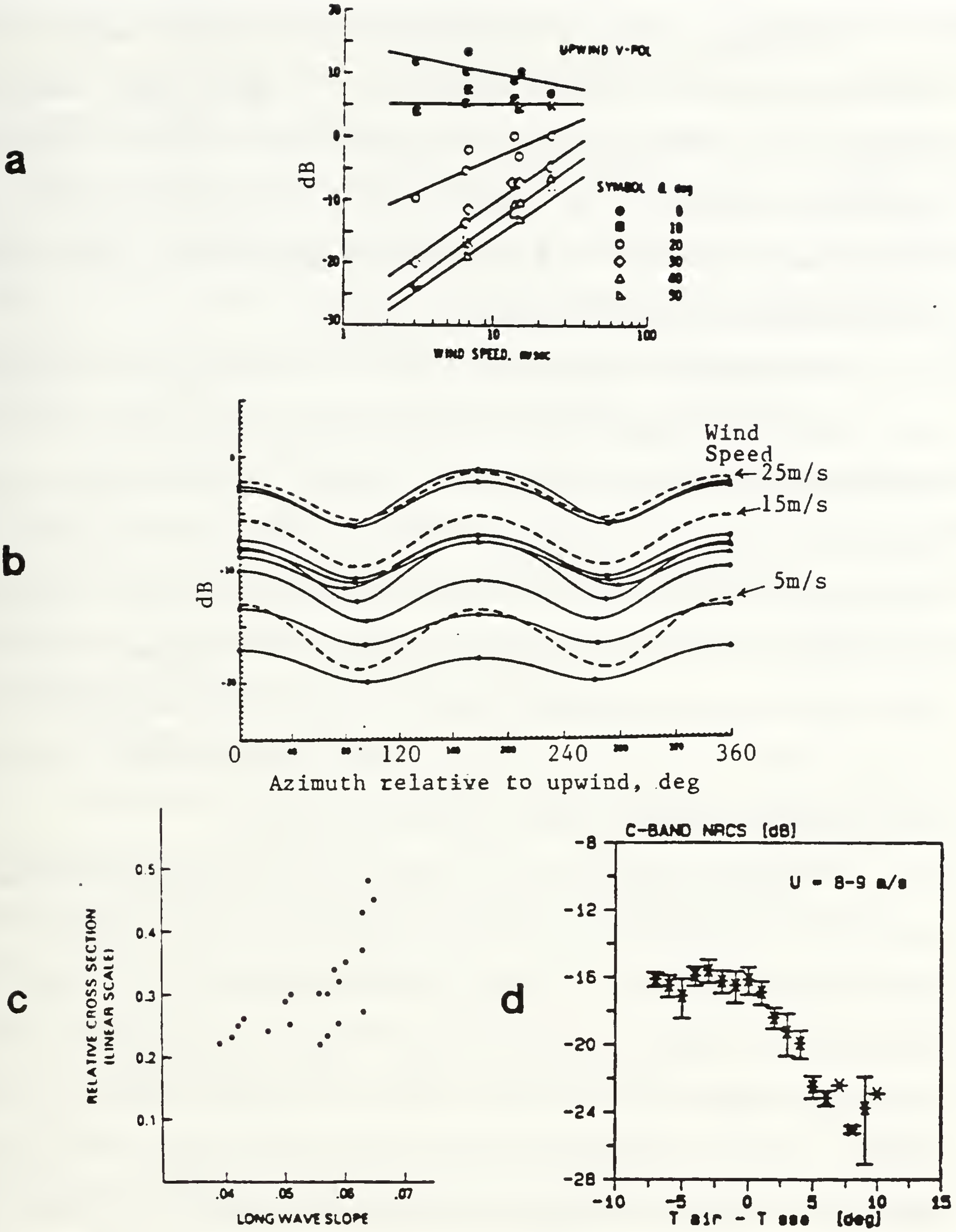

Figure 2. Functional Dependence of Normalized Radar Cross-Section on a) Wind Speed for Various Angles of Incidence, θ (Schroeder, et al., 1982); b) Wind Direction (Jones, et al. 1977); c) Long Wave Slope (Keller, et al., 1985); d) Atmospheric Stratification (Keller, et al., 1989)

Unstable atmospheric stratification, as indicated by a negative air-sea temperature difference (Figure 2d), results in 1) a slightly higher near-surface wind speed, 2) a wind profile which deviates from the neutral stratification, logarithmic form, and 3) an increase in the surface drag coefficient. The NRCS is seen to decrease in response to these changes in the surface layer as the stratification changes from unstable to stable.

The dissipation and growth rates of the capillary-gravity waves have been shown to be proportional to water viscosity (Lamb, 1932) which is an inverse function of water temperature; therefore, this mechanism has been proposed to explain observations which show an increase in the radar backscatter for increasing surface temperature, particularly at low wind speeds (Woiceshyn, et al., 1986; Donelan and Pierson, 1987; Kahma and Donelan, 1988). Keller and Plant (1988) present recent wavetank measurements which do not show a pronounced temperature dependence. Additional observations are needed to reach a definite conclusion.

The physical processes which influence radar backscatter all fall into the realm of describing, modeling and measuring the microphysics of the air/water surface layers. Among other institutions which study these processes, the Canada Centre for Inland Waters has supported air-water interaction experiments since 1976 under its WAVES (Water-Air Vertical Exchange Studies) program (Tsanis and Donelan, 1987). The primary platforms for the CCIW program are laboratory wavetanks and a tower at the western end of Lake Ontario, positioned 1.1km offshore from Hamilton, Ontario. In the autumn of three consecutive years (October-December, 1985-1987), the tower was outfitted with instruments to study wave spectra, wind stress, near-surface wind profiles and water turbulence. The Naval Research Laboratory added two radar scatterometers (14Ghz and 5 Ghz) as elements of the 1986 and 1987 experiments in order to take advantage of the opportunity to obtain collocated radar and environmental measurements. In 1986, both radars were mounted on the tower railing at fixed incidence and azimuth angles. In 1987, the 14Ghz radar was mounted on an antenna rotator and extended on a boom away from the tower. This configuration allowed the radar to be rotated in azimuth at different incidence angle settings.

The *objective of this study* is to examine the effects of the parameters shown in Figure 1 on measured scatterometer returns from an analysis of the WAVES data and to determine if these effects are successfully predicted by currently available model functions. Explanations are offered for the observed and predicted behavior of the radar cross-section.

3. Limitations of the Study

It should be noted that the above list of parameters which affect the cross-section is not complete (Masuko, et al., 1986). In effect, any oceanic phenomenon which has a surface expression may alter the cross-section; e.g., surface slicks caused by collection of surfactants by internal waves or Langmuir circulations (Huhnerfuss, 1983; Hughes and Gower, 1983), surface currents (Phillips, 1981), and the surface adjustment due to topographic interactions in shallow coastal areas (Valenzuela, 1985). Similarly, atmospheric phenomena such as planetary boundary layer rolls and or coastal fronts can be equally important in generating spatially varying surface signatures (Geernaert, 1990).

Due to the location of the study site in Lake Ontario, the atmospheric and oceanic variations described in the above paragraph will not be addressed in this study. The maximum wind speed observed, 15 m/s, is not as great or sustained as would be possible in the open ocean. On Lake Ontario, the longest wave period observed is 8s and "wind rows" aligned with the wind, believed to be due to Langmuir circulations, are the most common form of surface slick. The fetch limits are the geographic bounds of the lake: 1 to 300km. The wind direction is primarily from the west; i.e., the short fetch direction. Finally, the water is fresh versus saline. At the radar frequencies used in the experiment, the dielectric constants of fresh and saltwater are very nearly the same, therefore, the cross-section will not be affected. However, residence time of foam in a breaking wave regime is longer in saline water, which could cause the backscatter observed in the ocean to differ from that on the lake, especially at higher incidence angles and wind speeds (Gucinski, 1986).

C. NAVAL RELEVANCE: REQUIREMENTS FOR THE WIND VELOCITY AT THE SEA SURFACE

Marine wind is the only environmental parameter listed as a requirement in all Naval Warfare areas (Brown and McCandless, 1988). In terms of criticality, only sea-state is more important although the correct specification or prediction of the sea-state has accurate marine winds as a necessary first requirement (Janssen, et al., 1989). Both strategic and tactical naval operations are affected by marine winds.

The surface wind is an important parameter in strategic battle management. For example, the general weather picture (e.g., winds, storms, rain) is essential for decision making, resource management and optimum track ship routing. The systematic observation of ocean areas for effective sea-control and surveillance is hindered by high winds and waves which degrade sonar array performance by increasing ambient noise and reduce radar effectiveness by increasing sea clutter.

All operations at the tactical level can be suspended on account of extreme wind and sea-state conditions. In the traditional sense, these tactical operations or decisions require only a local measure of environmental conditions. However, today's battlegroup size is O(1000 km) which extends the battle horizon to ocean basin scales when the deployment range of modern weaponry is considered. Therefore, next-generation tactical decision aids will have expanded areas of coverage. This concept is already being implemented in the Tactical Environmental Support System (TESS). Shipboard users of this system will use direct readout from overhead satellite passes and conventional data to produce local data products. These products will be supplemented by those produced at central site locations using all available satellite data, model outputs and conventional data.

The pervasive requirement for surface wind coverage at spatial scales of tens to thousands of kilometers argues for global satellite measurements of surface winds. An Operational Requirement (OR) for this capability, which listed the performance goals shown in Table I (Daley, et al., 1984), was issued by the Chief of Naval Operations in 1977. This OR has since been rescinded in order to consolidate requirements for environmental parameters, but the performance goals and requirements are still valid. The

TABLE I. PERFORMANCE GOALS FOR SATELLITE MEASUREMENT OF SURFACE WINDS

NOTE: The double entries indicate the most desirable values on the left and the minimum acceptable thresholds on the right of the slashes.

Surface Wind	Data Receipt Rate Freq	Data Receipt Rate Timeliness	Horizontal Resolution	Measurement Precision	Absolute Accuracy	Range
Speed	3//12 hrs	0.25//3 hrs	10//25 km	5//20 %	2mps//4mps	1-75mps //3-25 mps
Direction	3//12 hrs	0.25//3hrs	10//50km	±5°//10°	±2.5°//10°	0-360°

most recent compilation of OR's shows at least 24 requirements which specify surface wind as an important or critical element.

D. SUMMARY

In this study, radar backscatter as a function of wind speed and direction, long-wave slope, atmospheric stratification and water temperature is examined using data acquired from an instrumented tower in Lake Ontario. A historical review of scatterometry is presented in the next chapter along with background material on wave and air-sea interaction theory which is essential for the interpretation of the results. A review of current model function theory and supporting observations is given in the final section of Chapter II. A description of the experiment and data processing follows in Chapters III and IV. The major results of the study are presented in Chapter V. These findings are summarized and the major conclusions stated in Chapter VI.

II. LITERATURE REVIEW

A. INTRODUCTION

To understand the physics of scatterometry, one must couple electromagnetic, ocean wave and air-sea interaction theories. It is the purpose of this chapter to summarize the aspects of each of these areas which are pertinent to scatterometry. The intent is to make clear how certain environmental parameters can (theoretically) influence the radar measurements and how currently proposed model functions incorporate these parameters. Each of the theory sections (C,D,E) derive, in outline form, the expressions used in the model function section (Section F). A synopsis of the history of scatterometry is presented first in order to provide a larger context in which to set the model function problem.

B. HISTORICAL REVIEW OF SCATTEROMETRY

In his experiment to test Maxwell's electromagnetic theory, Hertz, in 1886 demonstrated that radio waves were reflected from various solid objects. In 1904 Hulsmeyer (Ulaby et al., 1981) applied this result to the tactical problem of ship detection and in the war years to follow, ground-based radars were developed to detect aircraft and ships. These radars operated at meter or decimeter wavelengths, much longer that those of present-day radar scatterometers. To preserve the secrecy of the early radar development program, arbitrary letter designations, which are still in common usage, were assigned to the microwave frequency bands (Table II).

TABLE II. MICROWAVE FREQUENCY BAND DESIGNATIONS

Letter	Frequency Band GHz	Central Wavelength Cm
P	.225 - .390	115
L	.390 - 1.55	20
S	1.55 - 4.20	10
C	4.20 - 5.75	5
X	5.75 - 10.90	3
Ku	10.9 - 18.0	2
K	18. - 26.5	1.35
Ka	26.5 - 36	1.0
Q	36 - 46	.73
V	46 - 56	.58
W	56 - 100	.38

By World War II, airborne radars were used to detect other aircraft and ships-at-sea, and some in the 3 and 10 GHz bands were producing images of the ground. As the instruments were refined, it became clear that radar reflections from ocean waves, which obscured the echoes from the actual targets (sea clutter), would have to be accounted for to improve data interpretation. Thus, the radars were directed at the sea surface itself with the purposes of improving radar performance, developing techniques to study the sea surface, and testing new theories which attempted to explain scatter from the sea (Stewart, 1985).

In one of the first controlled radar measurement experiments, Goldstein (1946) introduced the standard unit of measurement for radar backscatter from the sea, σ°, the (area) normalized radar cross-section (NRCS). Goldstein's results suggested that σ° varied with radar frequency, polarization and incidence angle (Huebner, et al., 1975). From 1959 to 1975, the Naval

Research Laboratory (NRL) continued the efforts to establish the character of the scattering cross-section via an extensive measurements program which used airborne multifrequency radars to examine the dependence of σ° on sea state and wind speed (Guinard, et al., 1971; Daley, 1973). The determination that σ° was in some way proportional to wind speed led to the proposal for a satellite-borne radar, by then known as a scatterometer, to obtain oceanic wind and wave information (Moore and Pierson, 1966). However, at that time, a successful correlation of σ° with wind speed was yet to be established and the technology with which to build a stable, accurate (±2dB absolute) radar was not yet available (Jones et al., 1982).

During the 1970's, the National Aeronautic and Space Administration (NASA) sponsored scatterometer research and development which led to a technically improved aircraft scatterometer (Advance Applications Flight Experiment Radiometer-Scatterometer, AAFE-RADSCAT) and a proof-of-concept spacecraft scatterometer (Skylab, S-193). With the RADSCAT instrument, Jones et al., (1977) demonstrated the azimuthal dependence of σ°; i.e., the cosine-like dependence of σ° with wind direction relative to the antenna. Using the radar data and corresponding *in-situ* data, empirical algorithms ("model functions") were derived to relate the radar backscatter to the ocean surface wind vector. In June 1978, as part of a suite of microwave instruments onboard Seasat, The Seasat-A Satellite Scatterometer (SASS) was launched.

Three months into its planned three year mission Seasat suffered a failure in its power subsystem and communications with the satellite ceased; in November 1978 the mission was officially terminated (Pounder; 1980). Ten years later the scatterometer data from this abbreviated mission are still being analyzed to confirm the instrument as a breakthrough in maritime meteorology and oceanography, but also to reveal the shortcomings in the scatterometer model function (Woiceshyn, et al., 1986).

Follow-on missions to the "proof-of-concept" Seasat were already planned at the time of its failure. NASA had proposed a Seasat-B mission in the summer of 1978. Early in 1979 there was an interagency (NASA, Dept of Defense, Dept of Commerce) proposal for a National Oceanic Satellite System (NOSS, Joint Effort by NASA, NOAA, Navy, 1979 internal report). Both of these systems were to be "high-heritage" and "limited-operational;" i.e., they would carry microwave instruments nearly identical to those on Seasat and no new, high risk (developmental) instruments would be flown. There were some changes proposed for NOSS: the scatterometer was re-designed to have three instead of two antennas, no synthetic aperture radar would be flown and a large-aperture multichannel microwave radiometer was to be developed. NOSS grew beyond its original charter but still survived internal review processes until 1981 when it was cancelled.

Reiterating the need for an improved, all-weather oceanic data base, the Navy proposed N-ROSS (Navy Remote Ocean Sensing System), a supposedly "scaled-down" version of NOSS, in April, 1981 (Honhart, 1984). This satellite was to be the centerpiece of a constellation of ocean observing satellites to be launched in the early 1990's by the US, Europe and Japan. Funding and responsibility for the program was primarily shared by Navy and NASA; NOAA and the Air Force were to provide data acquisition and distribution support. Citing an unacceptable cost growth, the Navy cancelled the program in December, 1986 (Graham, 1987; Matthews; 1987). The replacement launch vehicle for the N-ROSS NASA-Scatterometer (NSCAT) is currently planned to be the Japanese Advanced Earth Observing Satellite (ADEOS), tentatively scheduled for launch in 1995. Therefore, work still continues on the data processing algorithms including the model function.

The European Space Agency will launch a scatterometer on its Earth Resources Satellite-1 in 1990. Looking to the next century, NASA scientists are proposing an alternate design for the Earth Observing Satellite system scatterometers which will use scanning instead of fixed antennas. A scanning system is more difficult to stabilize on orbit, but these antennas are more cost-effective and energy-efficient. Furthermore, they are able to operate as radiometers as well as radars so that it is possible to obtain corresponding passive microwave measurements such as atmospheric moisture parameters. With these changes the scatterometer will become a far more attractive instrument in a programmatic sense (Brown and McCandless, 1988), thereby increasing the chance that the US will have a scatterometer in space sometime during the next decade.

C. ELECTROMAGNETIC SCATTERING THEORY

While scatterometer programs have been proposed and cancelled in the recent past, advances in knowledge of the scattering physics have been steady (Rice, 1951; Barrick, 1968; Wright, 1966, 1968; Valenzuela, 1968, 1978; Fung and Chan, 1969; Keller and Wright, 1975; Brown, 1978; Bahar, 1981; Durden and Vesecky, 1985; Plant, 1986; Holliday, 1986; Donelan and Pierson, 1987). To date, the three most common approaches to scattering problems are physical optics, small perturbation and two-scale composite surface methods[1]. Details of the derivations for these methods can be found in recent publications (Ulaby et al., 1982; Durden, 1986; Plant, 1988). Here, only the assumptions, results and experimental support for these theories are summarized.

1. Fundamentals of Surface Scattering

An expression for the NRCS (see Appendix A) is in terms of the electric field incident on the surface, E_i, and the field scattered from the surface, E_s, for a given incidence angle, θ, azimuth angle, χ, polarization, p, illumination area, A, and range, R:

$$\sigma^{\circ}(\theta,\chi,p) = \frac{4\pi R^2}{A}\frac{\left|E_s(p)\right|^2}{\left|E_i(p)\right|^2} \qquad (1)$$

i.e., the computation of the cross-section requires specification of the scattered field. Fundamentally, this means that the wave equation for E_s is solved using Green's second vector theorem (See Appendix A, Beckmann and Spizzichino, 1987; Ulaby et al., 1982). This theorem states that the field at any point within a source-free domain bounded by a closed surface S can be expressed in terms of the tangential fields on the surface.

For a surface rough in two-dimensions, the "Stratton-Chu" equations result as follows:

$$E_s = K\mathbf{r}_s \wedge \oint\left[-\eta_0 \mathbf{r}_s \wedge (\hat{\mathbf{n}} \wedge \mathbf{H}) + (\hat{\mathbf{n}} \wedge \mathbf{E})\right] e^{ik_{em}\mathbf{r}\cdot\mathbf{r}_s} dS \qquad (2a)$$

---

[1] An alternative method is the generalized "full-wave" approach employed by Bahar (1981) and Brown (1978). Due to its generality, the approach and results are considerably more complicated and less easily interpreted in terms of the ocean wave spectrum. Therefore, this method has not been a widely adopted solution method.

$$H_s = K\mathbf{r}_s \wedge \oint \left[\frac{1}{\eta_0} \mathbf{r}_s \wedge (\hat{\mathbf{n}} \wedge \mathbf{H}) + (\hat{\mathbf{n}} \wedge \mathbf{E}) \right] e^{ik_{em}\mathbf{r}\cdot\mathbf{r}_s} dS \tag{2b}$$

where a time factor of $e^{i\omega t}$ is understood; E, H are the total electric and magnetic fields on the surface, K is the scalar Green's function; R is the range to the surface; $\mathbf{r}_s$ is the unit vector in the scattered direction; η_0 is the intrinsic impedence of the scattering medium, and k_{em} is the electromagnetc (em) wavenumber (Ulaby, et al., 1982). As required by Green's theorem, the scattered field is given in terms of the tangential fields, $\hat{\mathbf{n}} \wedge \mathbf{E}$ and $\hat{\mathbf{n}} \wedge \mathbf{H}$.

These equations simplify to the "Helmholtz Integral" for a surface rough in one dimension from which it is seen that the scattered field at observation point r above the surface requires the field value and its normal derivative at the scattering surface

$$E_s(\mathbf{r}) = \frac{1}{4\pi} \iint_s \left(E \frac{\partial G}{\partial n} - G \frac{\partial E}{\partial n} \right) dS \tag{3}$$

In equation (3) G is the two-dimensional Green's function and the magnetic field H replaces E in the case of vertical polarized incident radiation.

The essence of the scattering problem is the specification of the total field on the scattering surface. If the surface is irregular, then no general solution for the fields exist (Ulaby, et al., 1982) and three solution methods are possible: 1) the field is expanded as a series and the exact boundary conditions are applied (Brown, 1978; Bahar, 1981); 2) the integral equations are solved numerically (Durden, 1986); or 3) approximations of the boundary conditions $\left(E, \frac{\partial E}{\partial n}, \hat{\mathbf{n}} \wedge \mathbf{E} \right)$ are made, allowing closed form solutions to be derived as outlined below. The simplifying assumptions generally include one or more of the following (Beckmann and Spizichinno,1987):

1) (often) the surface is perfectly conducting,
2) the dimensions of the scattering elements are much larger or smaller than the electromagnetic wavelength,
3) the radius of curvature of the scattering elements is much larger than the electromagnetic wavelength,
4) shadowing effects from larger elements are neglected,
5) only the far-field values are computed,
6) multiple scattering is neglected,
7) the density of the irregularities (per unit area or volume) is ignored, and
8) treatment is restricted to a certain model of surface roughness.

These assumptions all relate to the reflection properties of the scattering surface which depend on its electrical properties and roughness. The roughness of a random surface is radar wavelength dependent and is characterized by the rms surface elevation, h, and the surface correlation length, l. The appropriate approximations to use for a particular problem are based on certain limiting values of these two parameters.

To be "smooth," the rms height must satisfy the Fraunhofer condition:

$$h < \frac{\lambda}{32 \sin \theta} \tag{4}$$

where λ is the electromagnetic wavelength and θ is the incidence angle. This condition guarantees that there will be no more than a $\pi/8$ difference in phase between two reflected waves. For wavenumber $k = 2\pi / \lambda$, the limit for a smooth surface is $kh < 0.3$ (Ulaby et al., 1982) and the correlation length, l, is infinite since every point on the surface is correlated with every other point.

Reflections from a smooth surface are "specular" or mirror-like in that the angle of reflection equals the angle of incidence and very little of the radiation is scattered (Figure 3). Therefore, a monostatic (single antenna) radar must transmit at normal incidence to receive backscattered power from a smooth surface.

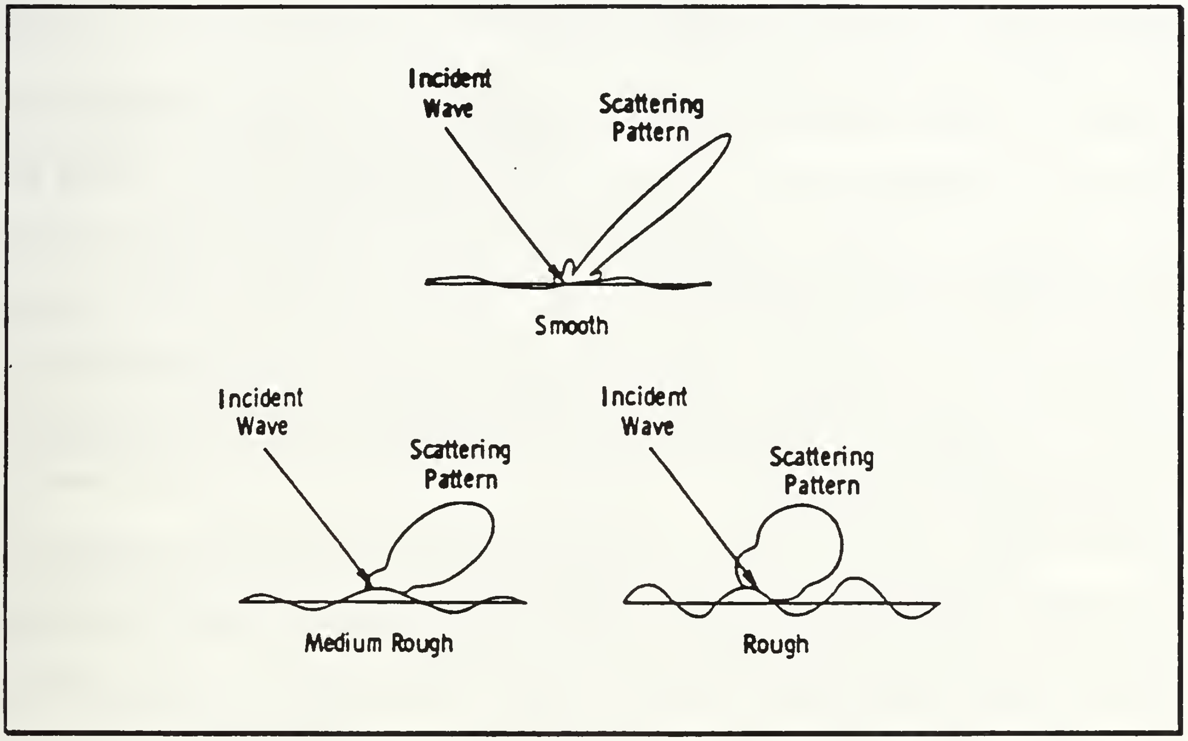

Figure 3. Examples of Surface Scattering Patterns

2. The Physical Optics Approximation

The near normal condition can be met for the sea surface at incidence angles less than about 20° since it is possible to have wave slopes of similar degree to maintain the required normal incidence. In the *physical optics, or Kirchoff approximation,* the roughened sea surface is approximated by small planar "facets," each locally tangent to the sea surface as shown in

Figure 4a. Each facet specularly reflects the incident radiation so that the total surface field is the sum of the incident and reflected fields

$$E = (1 + R)E_i \tag{5a}$$

and

$$\frac{\partial E}{\partial n} = (1 - R)E_i \mathbf{r} \cdot \hat{\mathbf{n}} \tag{5b}$$

where R is the Fresnel reflection coefficient of the tangent plane at a particular point and **r** is the unit vector in the scattered direction. These are the boundary condition approximations for the physical optics method. These approximations are valid when the radius of curvature of the surface elements is much greater than the electromagnetic wavelength and the surface roughness is comparable to or larger than the electromagnetic wavelength (see Figure 4a).

The cross-section is then computed as the sum of the reflected energy from all the facets oriented normal to the radar in the illuminated area using the probability distribution of surface slopes. Assuming an isotropic rough surface and Gaussian distributed surface slopes, Barrick (1968) determined the cross-section to be

$$\sigma^0_{QS} = \frac{|R(0)|^2}{s^2} \sec^4 \theta e^{-\left(\tan^2 \theta / s^2\right)} \tag{6}$$

where R(0) is the Fresnel reflection coefficient at normal incidence and s^2 is the total slope variance of the wave slopes in the x and y directions. If the surface is non-isotropic, then the cross-section in the upwind direction is written

$$\sigma_{QS}^{0} = \frac{|R(0)|^{2}}{2s_{u}s_{c}}\left(\sec^{4}\theta\right)e^{-\left(\tan^{2}\theta/s_{u}^{2}\right)} \tag{7}$$

where s_u and s_c correspond to the slopes in the upwind and crosswind directions (Valenzuela, 1978). The slopes of importance here correspond to ocean wavelengths much longer than the microwavelength (to satisfy the criterion of small radius of curvature). The cross-section in (7) is termed *quasispecular* since it arises from only those parts of the sea surface which are normal to the incident wave vector.

3. The Small Perturbation Approximation

For a slightly rough surface and beyond about 30° incidence angle, comparable wave slopes are not physically realizable so that specular scattering is no longer valid, although scatter is still observed. At these greater angles it has been shown (Wright, 1966) that the response is from a resonance phenomenon between the em waves and the surface height displacements of the surface waves. This phenomenon, known as Bragg-scatter or Bragg-resonance, occurs when the em and ocean wavelengths (λ, L) satisfy the equality:

$$L = \frac{n\lambda}{2\sin\theta} \qquad n = 1,2,\ldots \tag{8}$$

As shown in Figure 4b, when the excess distance from the source to each successive crest is $n\lambda/2$, the round trip phase difference is 360° and the

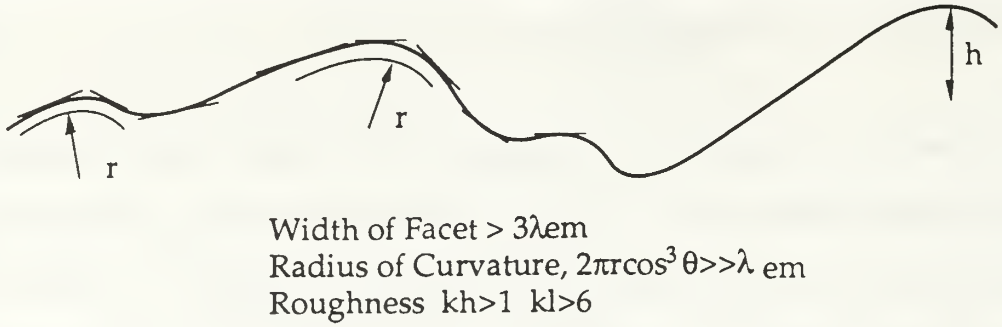

(a) Tangent Plane--the Rough Surface as a Collection of Tangents

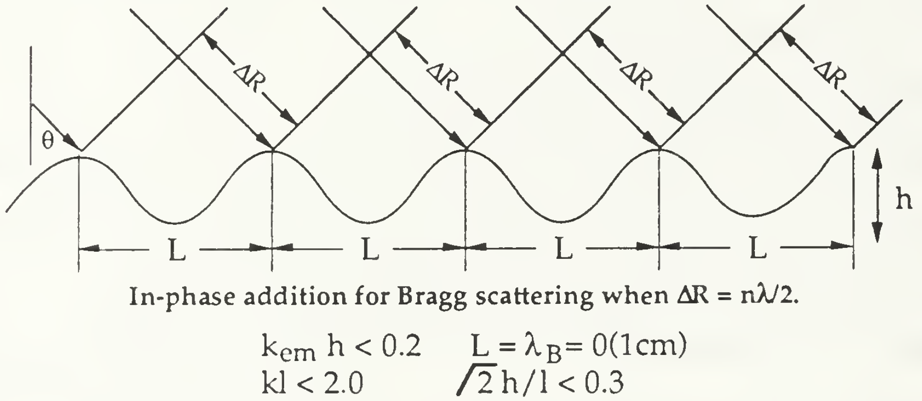

(b) Small Perturbation--Flat Mean Surface and Small Perturbation Imposed

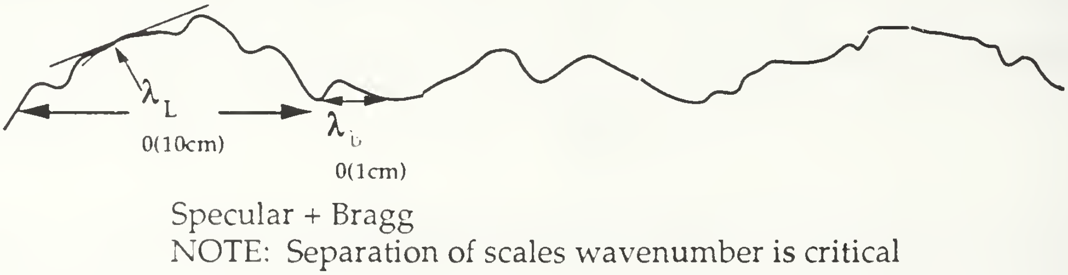

(c) Two-Scale--Small Perturbations Imposed on a Larger Scale Rough Surface

Figure 4. Schematic Drawings of the Sea Surface for a) the Kirchoff (Tangent Plane or "Facet") Approximation, b) the Bragg-Resonance Model, and c) the Two-Scale Composite Surface Model Where λ_{cm}, k_{em}: Electromagnetic Wavelength and Wave number; h, Height above Mean Level; l, Correlation Length; L, λ_B: Ocean and Bragg Wavelengths; λ_L Longer Wave of Two-Scale Surface

reflected signals add in phase. For example, for a radar wavelength of 2.18cm at $\theta = 40°$, the Bragg wavelength is 1.7cm corresponding to an ocean capillary-gravity wave.

For such small waves it would seem that the resonant signal would be swamped by the return from the much larger waves. Average power return from the larger, randomly spaced waves is proportional to the number of the scatterers in an illuminated area. However, in the case of resonance, the average power is proportional to the square of the number of scatterers. Therefore, the resonant effect produces a significant power return, as well as providing a wavelength selective tool for examining the sea surface (Ulaby, et al., 1982).

Assuming that the backscatter is from very short, small amplitude waves, the cross-section is derived using a perturbation approach in which the mean scattering surface is flat and small wave perturbations are superimposed (Figure 4b). "Small" perturbations are defined to have rms surface slopes which are sufficiently gentle ($\sqrt{2}h/l < 0.3$) and surface displacements small compared to the em wavelength ($kh < 0.3$).[2] The total field on the surface is written as the sum of the incident and reflected fields (specular reflection from the flat mean surface) plus a small scattered component from the small amplitude roughness.

---

[2] Chen and Fung (1988) suggest "that a more appropriate description for the range of validity of this model is a two-dimensional space with kh and kl as the axes"; i.e., in addition to small height and slope the horizontal correlation length must also be large compared to the electromagnetic wavenumber.

The rough surface is considered random within a particular L by L area but this random surface repeats itself in distance, L; i.e., is periodic. Flouquet's theorem is then invoked which states that a scattered field from a periodic surface is itself periodic. Therefore, it is appropriate to write the scattered field as a harmonic series expansion:

$$E_s = \sum_{-\infty}^{\infty} B_{mn} E(p+m,n;z) \tag{9}$$

where $E(p+m,n;z) = e^{i\frac{2\pi}{L}(p+m)x} e^{i\frac{2\pi}{L}ny} e^{ik_z z}$, p = 2π / λ sinθ and k_z is the wavenumber component in the z direction. That is, the scattered field is periodic in x and y and propagates upward.

The relationship between the coefficients, B_{mn}, for the different field components is found from Maxwell's divergence equation $\nabla \cdot \mathbf{E} = 0$; .i.e., there are no sources in the region. The boundary condition of perfect conductivity (the tangential fields on the surface are zero) provides the additional two equations needed to solve for the three coefficients. Since it was assumed that kh was small all exponentials involving z are expanded in Taylor's series of kh about $h = 0$ and the coefficients are expanded as increasing powers of the surface elevation. For first-order Bragg scattering only the first terms are retained. The dominant effect of the first order expansion is to give rise to a z-component in the scattered field. Higher order expansions (Valenzuela, 1968) produce cross-polarization effects.

The radar cross-section for resonant scatter from a dielectric (nonconducting) surface is derived to be (Wright, 1968)

$$\sigma^{\circ}(\theta) = 16\pi k^4 \cos^4\theta \left|g_{ij}\right|^2 \Psi(2k\sin\theta, 0) \tag{10}$$

where

$$g_{HH} = \frac{\varepsilon_r - 1}{\left[\cos\theta + (\varepsilon_r - \sin\theta)^{\frac{1}{2}}\right]^2} \tag{11a}$$

$$g_{VV} = \frac{(\varepsilon_r - 1)\left[\varepsilon_r\left(1 + \sin^2\theta\right) - \sin^2\theta\right]}{\left[\varepsilon_r \cos\theta + \left(\varepsilon_r - \sin^2\theta\right)^{\frac{1}{2}}\right]^2} \tag{11b}$$

and $\Psi(k_x, k_y)$ is the two-dimensional ocean wavenumber spectrum. The complex relative permittivity of the ocean, ε_r, is given by $\varepsilon_r = \varepsilon/\varepsilon_0 - i\sigma/\varepsilon_0\omega$, in which the real part represents the capacity of the medium to store electric energy (c.f. a vacuum for which $\varepsilon_0 = 8.85 \times 10^{-12}$Farad/m). The imaginary part represents losses by the medium through the conductivity, σ, at frequency, ω. The subscripts refer to the transmit/receive polarizations of the signal: h-pol/h-pol and v-pol/v-pol. For a perfect conductor,$\sigma = \infty$, $\varepsilon_r = -i\,\infty$, $g_{hh} = 1$ and $g_{vv} = (1 + \sin^2\theta) / \cos^4\theta$. Therefore, resonant scattering of h-pol radiation from a good conductor is more sensitive to incidence angle than is v-pol.

In his classic wavetank experiment, Wright (1966) demonstrated that some of the observed characteristics of backscatter can be explained by this "first-order" Bragg theory. As shown in Figure 5, the measured backscattering and the polarization ratio (σ_{vv}/σ_{hh}) as functions of incidence angle agree rather well with the theoretically computed curves. Wright hypothesized that the differences from the theoretical cross-sections could be due to oversimplifying assumptions regarding the electric fields near the surface when no waves were present.

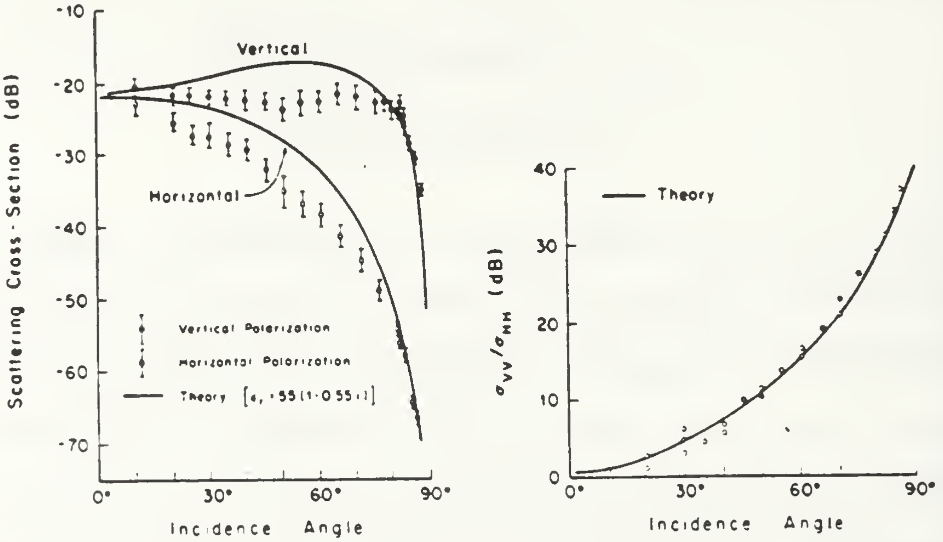

Backscattering cross section as a function of incidence angle for capillary waves on tap water. Left: the scattering section calculated from theory compared with observations. Right: the ratio of vertically to horizontally polarized backscatter, also compared with theory (from Wright, 1966).

Figure 5. Evidence of First-Order Bragg Scattering
(Stewart, 1985 after Wright, 1966)

Further evidence for Bragg-scattering is found via analysis of the Doppler spectrum of the scattered signal. The Doppler spectrum is plotted as the spectral density of radar returns against Doppler frequency shifts "induced in backscattered microwaves due to a surface moving with a line-of-sight velocity toward or away from the radar" (Plant and Keller, 1989). If there are no background currents and Bragg scattering is the appropriate mechanism, then the Doppler spectra will contain peaks at those frequency shifts corresponding to plus and minus the Bragg wave frequency.

Plant and Keller (1989) provide evidence of the Bragg scattering mechanism in field data. Doppler spectra computed from an L-band (16cm) scatterometer positioned at the end of the Coastal Engineering Research Center pier near Duck, North Carolina are shown in Figure 6. As predicted, spectral peaks appear at the Bragg wave frequency of 3.35Hz for the microwave parameters used in this experiment (Figure 6a). The wind direction for this spectrum is 210°, i.e., the offshore direction, and the wind speed is only 4.3m/s; hence, the dominant ocean wavelength will be correspondingly short. On the other hand, the peaks disappear for a spectrum corresponding to the onshore direction (Figure 6b). The longer waves have orbital velocities which contribute to the Doppler shift, thereby broadening the Doppler spectrum. It appears then that the first-order theory is valid until the dominant wind wavelength slightly exceeds the Bragg wavelength (Plant and Wright, 1977). At this point, the $k_{em}h \ll 1$ and the mean surface is no longer flat.

4. The Two-Scale Composite Surface Approximation

These limitations of the pure first-order theory led Wright (1968) and Bass et al., (1968) to propose independently a composite surface (two-scale) theory in which the surface is envisioned to consist of a large scale part which has small curvature and a small-scale part which backscatters according to first-order theory. The sea surface is broken up into an infinite number of slightly rough patches and the net backscattered power is computed as the summation of the power from a single patch distributed over the slopes of the dominant wind waves of the ocean (Figure 4c). The wavenumber spectrum is decomposed into two regions corresponding to the longer tilting waves and the shorter Bragg-scattering waves.

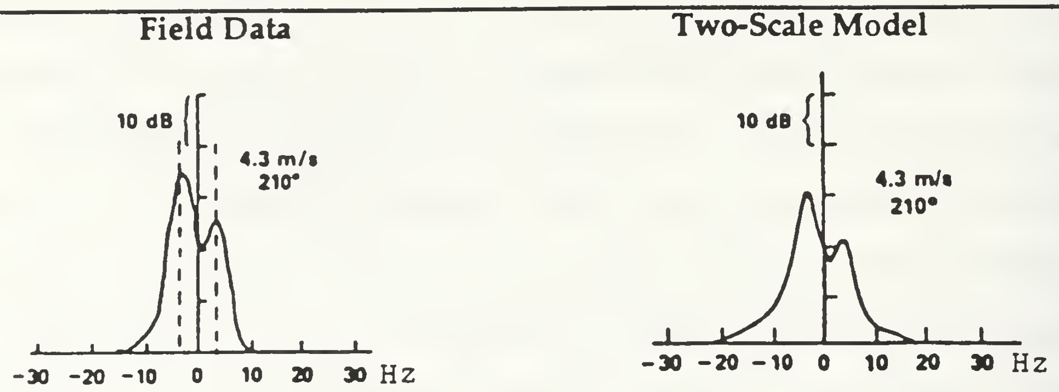

(a) Offshore Wind Direction

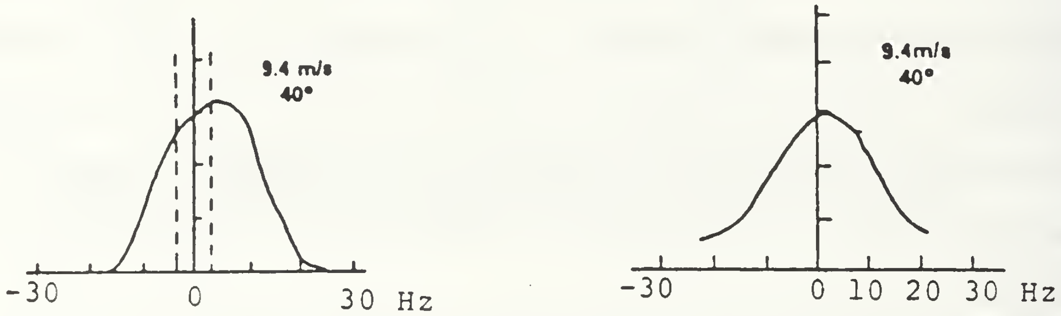

(b) Onshore Wind Direction

Figure 6. Evidence for First-Order Bragg Scattering and Validity of Two-Scale Model (a) (b) Left, Doppler Spectra from Field Data; (a) (b) Right, Doppler Spectra from Two-Scale model
(adapted from Plant and Keller, 1989)

The radar cross-section is the sum of two terms: the quasispecular contribution from the tilted surfaces and the Bragg contribution from the small amplitude waves.

$$\sigma^\circ(\theta) = e^{-4k<h^2>}\sigma^\circ_{QS} + \int \sigma^\circ_{B}(\theta,\gamma,\delta)p(\tan\gamma,\tan\delta)d\tan\gamma d\tan\delta \qquad (12)$$

where

$$\sigma^{\circ}_{B}(\theta,\gamma,\delta) = 16\pi k^{4}\cos^{4}\theta \left| g(\theta,\gamma,\delta) \right| \psi_{s}\left(2k\sin(\theta+\gamma), 2k\cos(\theta+\gamma)\sin\delta\right) \qquad (13)$$

is the Bragg-scatter cross-section for a slightly rough surface tilted by γ in the x-direction and δ in the y-direction.

In (13), ψ_S is the short wavelength portion of the wave spectrum. The quasispecular term in (12) is now reduced by a factor $\exp(-4k^2\langle h^2\rangle)$ due to the small waves which make the specular "facets" less smooth, and the Bragg contribution is altered by the presence of the longer waves which tilt the Bragg waves in and out of the plane of incidence (Valenzuela, 1968). A separation wavenumber must be defined between the two assumed scales for the composite surface to be applied correctly. If such a "spectral gap" exists, then the scales are effectively decorrelated, allowing the linear summation of the two types of backscattered power.

The relationships between backscatter and incidence angle corresponding to the three types of scattering models discussed are illustrated in Figure 7. Composite theory compares well with observed values of σ° for vertical polarization, with an assumed ocean wave spectral form proportional to k^{-4}, but the curves diverge from the observed values for h-pol at higher incidence angles. Assuming higher, somewhat unrealistic, background slopes (10° and 20°) helps to fit the data but the remaining differences imply that other scattering mechanisms may become important for h-pol scattering at grazing angles (Valenzuela, 1978; Donelan and Pierson, 1987). Better agreement (not shown) between observations and theory are found at lower microwave frequencies (.438 Ghz, L-band) than higher frequencies (4.4 Ghz,

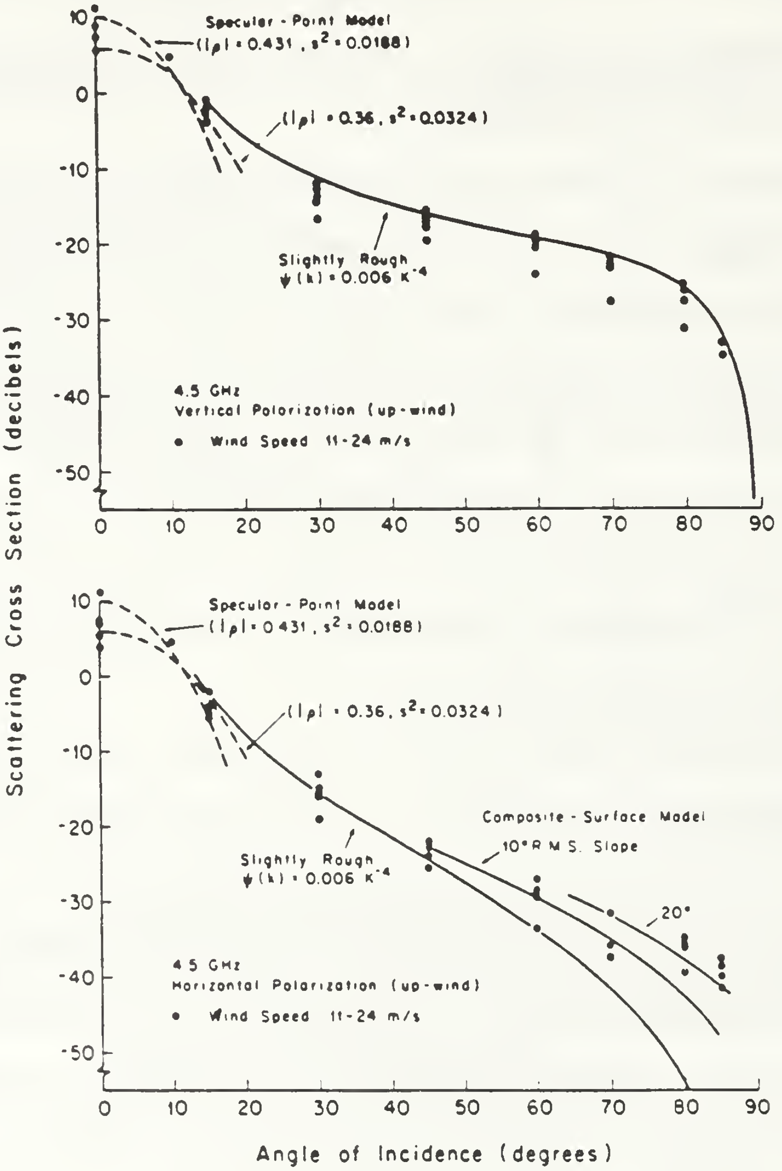

Comparison of measured and theoretical cross sections of the ocean for a radar frequency of 4.5 GHz. Top: vertical polarization. Bottom: horizontal polarization. The variation in the observations is due primarily to variation in wind speed at the sea surface (from Valenzuela, 1978).

Figure 7. Backscatter Versus Incidence Angle for Three Scattering Regimes (from Stewart, 1985 after Valenzuela, 1978)

C-band) (Daley, 1973). Finally, composite surface theory explains the widened spectral peaks observed in the Doppler spectra as being due to the advection of the small-scale structure by the orbital velocity of the longer waves (Figure 6b) (Keller and Wright, 1977).

D. SPECIFICATION OF THE ROUGH SEA SURFACE

The expressions for the radar cross-section in the previous section show that the scattering cross-section is linearly dependent on the two-dimensional ocean wavenumber spectrum. To examine pure Bragg scattering with the first order theory, the spectral density for a small range of wavenumbers near the Bragg wavenumber is required (the high frequency tail of the full spectrum). Two scale composite surface theory also requires the joint probability density function of the upwind and crosswind slopes or, alternatively, the lower frequency gravity wave part of the wavenumber spectrum. Although the correspondence is good between the observed and computed backscatter, the absolute accuracies of the Bragg and two-scale formulations cannot be unambiguously established since a universally acccepted functional form of the two-dimensional wavenumber spectrum has not yet been derived. Thus, present model function research is necessarily semi-empirical and semi-theoretical: wave and radar data are used in a feedback loop with wave theory to derive new forms for the wavenumber spectrum and to determine the physical variables of importance to the development of the ocean waves, thence backscatter. It is at this point that the transition is made from a pure electromagnetic scattering problem to an ocean wave dynamics problem.

1. Ocean Wave Spectra

The ocean surface is an evolving, random rough surface composed of waves which are generally categorized by their generating or restorative forces. The surface waves visible to the observer are most often the result of the driving force of the wind and the restorative forces of surface tension (capillary waves) or gravity (wind generated gravity waves). These waves span wavelengths of millimeters to hundreds of meters (wavenumbers of 1000 to .001 m^{-1}) and have periods of less than O(10s) (intrinsic frequencies of greater than 0.1 s^{-1}). Wave triads or quartets (capillary, gravity waves, respectively) can interact nonlinearly, with the result of an energy transfer among the waves, provided the wavenumbers of the individual waves satisfy certain resonance conditions (Hasselmann, 1962). Energy is removed from the wave system by wavebreaking, the generation of "parasitic" capillaries on the steeper gravity waves, or frictional dissipation at the highest frequencies (Hasselmann, et al., 1973).

All of these competing generation and dissipation mechanisms lead to a random sea surface which is best described by its overall statistics, as formalized by spectral (Fourier) methods; i.e., as a linear superposition of an infinite number of sinusoidal components (Pierson, et al., p.24, 1955). This requirement is satisfied if the components are of small amplitude and slope and can be approximated by a sinusoidal profile. Under these circumstances the Fourier transform of the surface elevation covariance is computed as a function of wavenumber and frequency, with position and time as parameters. This "power spectrum" is the spectral "signature" of the sea surface. Donelan, et al., (1985) point out that the higher-order effects of deviation of the wave profile from a pure sinusoid, nonlinear interactions and viscous dissipation will prohibit the signature from being permanent, but to first order it is an accurate representation of the wave field.

Assuming the wave field is spatially homogeneous and statistically stationary, then the ergodic theory applies: space and time averages from a single time series (realization) are equal to ensemble averages across all possible realizations (Bendat and Piersol, 1986, p. 144). This random ocean surface is then characterized by the covariance, $\rho(\mathbf{r}, t)$, of the surface displacement, ζ, at points separated by a distance $\mathbf{r}(x,y)$ and time, t

$$\rho(\mathrm{r},t) = < \varsigma(\mathrm{x},t_0)\varsigma(\mathrm{x}+\mathrm{r},t_0+t) > \tag{14}$$

where the angle brackets denote an ensemble average. The covariance quantifies the decorrelation scales of the sea surface in space and time. There are then three spectra of varying dimension that can be derived from this covariance (Kinsman, 1965).

The three dimensional (k_x, k_y, ω) wavenumber-frequency spectrum is defined as the Fourier transform of the covariance (Wiener-Kinchin theorem, LeBlond and Mysak, 1978, p. 311)

$$S(\mathbf{k},\omega) = \frac{1}{(2\pi)^3}\int\int\int \rho(\mathrm{r},t)e^{i(\mathbf{k}\cdot\mathrm{x}-\omega t)}d\mathrm{r}dt \tag{15}$$

and inversely,

$$\rho(\mathbf{r},t) = \int\int\int S(\mathbf{k},\omega)e^{i(\mathbf{k}\cdot\mathrm{x}-\omega t)}d\mathbf{k}d\omega \tag{16}$$

At $\mathbf{r}=0$ and $t=0$ equation (15) gives the variance $< \zeta^2 >$ of the surface elevation, or mean-square elevation. The calculation of $S(\mathbf{k},\omega)$ requires simultaneous measurements of surface displacement in time and space, an infrequently performed task which requires an array of wave staffs and intensive data processing (Donelan, et al., 1985).

The two-dimensional wavenumber spectrum required for the NRCS calculation is the integral of the three-dimensional spectrum over all frequencies

$$\Psi(\mathbf{k}) = \int S(\mathbf{k},\omega)d\omega \tag{17}$$

At t=0, the covariance is

$$\rho(\mathbf{r}) = \rho(\mathbf{r},0) = \iint_{-\infty}^{\infty} \Psi(\mathbf{k})e^{-i(k\cdot r-\omega t)}d\mathbf{k} \tag{18}$$

then

$$\Psi(\mathbf{k}) = \frac{1}{(2\pi)^2}\iint_{-\infty}^{\infty} \rho(\mathbf{r})e^{i(\mathbf{k}\cdot\mathbf{r})}d\mathbf{r} \tag{19}$$

This spectrum is also difficult to measure since it requires surface elevation as a function of space, an inherently more difficult *in-situ* measurement to make which involves the use of either stereophotography (Shemdin, et al., 1988), laser optic techniques (Tang and Shemdin, 1983; Keller and Gotwals, 1983) or a spatial array of sensors (Donelan, et al., 1985).

It is much more common to have only a single wave staff acquiring data in time. In this case, a one-dimensional frequency spectrum results which is independent of wavenumber magnitude or direction

$$\Omega(\omega) = \iint_{-\infty}^{\infty} S(k,\omega)d\,\mathbf{k} \tag{20}$$

$$\rho(t) = \rho(0,t) = \iint\limits_{-\infty}^{\infty} \Omega(\omega) e^{-i\omega t} d\omega \qquad (21)$$

and

$$\Omega(\omega) = \frac{1}{2\pi} \int \rho(t) e^{i\omega t} dt \qquad (22)$$

or

$$\Omega(\omega) = \frac{1}{\pi} \int_{0}^{\infty} \rho(t) \cos \omega t dt \qquad (23)$$

since $\Omega(\omega)$ is symmetric about $\omega=0$.

An approximate wavenumber spectrum can be determined from the frequency spectrum using the dispersion relation, $\omega=\omega(k)$. The wavenumber spectrum is often expressed in polar coordinates as the product of a wavenumber magnitude and direction spectrum

$$\Psi(\mathbf{k}) = \Psi(k,\varphi) = S(k)\Phi(\varphi) \qquad (24)$$

where $\mathbf{k} = (k\cos\varphi, k\sin\varphi), k = |\mathbf{k}|$, and φ is the wavenumber bearing (Pierson, 1955). The wavenumber spectrum is obtained from the frequency spectrum using the dispersion relation from which

$$S(k) = \frac{1}{k} \frac{d\omega}{dk} \Omega(\omega) \Big|_{\omega(k)} \qquad (25)$$

(LeBlond and Mysak, 1978). This procedure cannot be used to determine the large wavenumber portion of the spectrum since the intrinsic frequency of the shortest (capillary) waves, ω_0, is Doppler shifted by the orbital velocity of the longer waves on which they ride. The orbital velocity is essentially a slowly varying current of velocity U(x,t) so that the frequency of the short waves is given by

$$\omega(k) = \omega_0(k) + \mathbf{k} \cdot \mathbf{U}(x,t) \tag{26}$$

That is, the relationship between frequency and wavenumber is no longer unique (Atakturk and Katsaros, 1987).

Higher order statistics can be obtained from the wavenumber spectrum. For example, the mean-square slope of the waves is given by the second moment of the wavenumber spectrum (Cox and Munk, 1954)

$$s^2 = \int k^2 \Psi(\mathbf{k}) dk \tag{27}$$

The slope spectrum is often used in the study of the high frequency portion of the wave spectrum since higher wave numbers are weighted more heavily. Cox and Munk (1954) found that the mean-square slope is wind speed dependent. For a clean surface and windspeed at 12.5m in m/s,

$$s^2 = 10^{-3}(3 + 5.12U) \tag{28}$$

and

$$s^2 = 10^{-3}(8 + 1.56U) \tag{29}$$

for a slick-covered surface. In the Cox and Munk study, the slick was artificially generated and composed of diesel fuel and fish oil; the observed slopes may differ with typical concentrations of natural films.

In polar coordinates, with the x-axis pointed upwind, the mean-square slopes in the upwind/downwind and crosswind directions are

$$s_x^2 = \iint_{-\infty}^{\infty} (k\cos\varphi)^2 \Psi(k,\varphi)\,dk\,d\varphi \tag{30}$$

and

$$s_y^2 = \iint_{-\infty}^{\infty} (k\sin\varphi)^2 \Psi(k,\varphi)\,dk\,d\varphi \tag{31}$$

These quantities are of particular interest in the present study since they are required for the computation of the quasispecular and Bragg scattering terms of the two-scale model and for the expressions describing the hydrodynamic modulation of the Bragg waves by the longer waves.

2. The Spectral Transport Equation

The adoption of spectral forms in wave analyses is a statistical means of revealing basic structures in the random wave field. Underlying these statistics are, of course, the physical mechanisms responsible for the waves. The individual wave components generate, propagate and decay at different rates so that the spectral shape changes as the wave field develops. LeBlond and Mysak (1978, p. 322) then pose the question

> ...as to why spectral (and other statistical properties) take the shapes they do at various stages in the life of a wave field. Is it possible to derive predictive (as opposed to purely empirical or phenomemological) theories for the statistical properties of varying wave fields? More specifically, given the statistics of the forcing functions (such as wind, the atmospheric pressure), the boundary and initial conditions and the coefficients of the governing differential equations, each of which will, in general, have a random component, can we compute the solution and its statistics in terms of the statistics of the forcing?

The "radiative transport theory" of the evolution of spectra, which arises in the area of stochastic fluid dynamics (Monin and Yaglom, 1965,1967), provides the mathematical formalism to answer these questions. The application of the theory (Hasselmann, et al., 1973) rests on the assumption that the time and space scales of spectral evolution are much longer than the longest resolvable period and wavelength in a data record. This assumption allows the evolution process to be weakly nonstationary. It is found in the absence of currents that the ocean wavenumber spectral density is conserved along a wavenumber path except for certain exchange processes, denoted by Σ.

$$\frac{d\Psi}{dt} = \Sigma \qquad (32)$$

or,

$$\frac{\partial\Psi}{\partial t} + \frac{d\mathbf{k}}{dt}\cdot\frac{\partial\Psi}{\partial\mathbf{k}} + \mathbf{c}_g.\nabla\Psi = Q_i + Q_{nl} + Q_d \qquad (33)$$

These exchange processes include the energy input by the wind Q_i; Q_{nl}, the redistribution of energy due to nonlinear interactions and the generation of parasitic capillaries on the steeper gravity waves; and Q_d, the dissipation of energy by wave breaking and frictional dissipation,. The group velocity of the waves, $\mathbf{c}_g = d\omega/d\mathbf{k}$, is the velocity at which the wave energy propagates.

A more general expression which allows the waves to be superimposed on a space- and time-dependent mean flow, $U(\underset{\sim}{x},t)$ is in terms of the wave action density,$N(\mathbf{k};x,t)$

$$\frac{dN}{dt} = \Sigma \qquad (34)$$

or,

$$\frac{\partial N}{\partial t}+\frac{d\mathbf{k}}{dt}\cdot\frac{\partial N}{\partial \mathbf{k}}+\left(\mathbf{c}_g+\mathbf{U}\right)\cdot\nabla N=\frac{1}{\omega_0}\left(Q_i+Q_{nl}+Q_d\right) \tag{35}$$

where N = $\Psi(\mathbf{k}) / \omega_0$. The frequency is now defined by equation (26) where ω_0 is the intrinsic frequency of the wave in a coordinate system which is moving with the current, **U**. In the presence of such a current, the wave action is conserved, whereas the spectral density is not.

A visual summary of these equations is given in Figure 8 which shows a typical frequency spectrum and the associated source terms (Hasselmann, et al., 1973). Wind energy is primarily input at and above the frequency of the spectral peak and removed by dissipation at frequencies greater than approximately three times the peak frequency. The nonlinear terms transfer energy from the spectral peak to both higher and lower frequencies, but at the higher frequencies it is cancelled by the dissipative effects. Different stages of the wave spectrum evolution can be evaluated by examining different balances among the terms in the radiative transfer equations (32) and (34). When $d\Psi/dt > 0$, the wave spectrum is in a growth stage, a fully arisen sea is represented by $d\Psi/dt=0$ and the spectrum is in a decaying state when $d\Psi/dt<0$.

3. The Fully Arisen Sea, $d\Psi/dt = 0$

The wave spectrum cannot grow without limit. Instead, for a given constant wind speed, it will reach some maximum state dictated by the length of time the wind blows (duration) and the distance over which the wind blows (fetch). At this point $d\Psi/dt=0$, which implies that the source and dissipation terms are in equilibrium at all frequencies

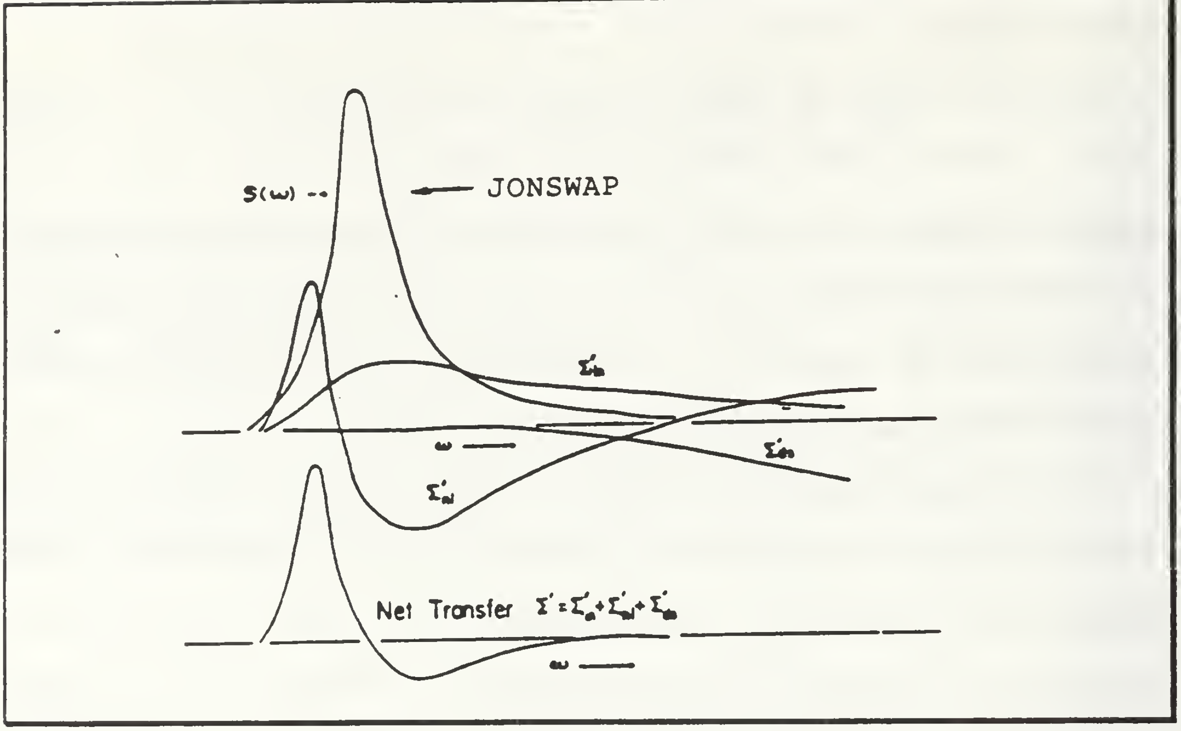

Figure 8. The Mean JONSWAP Spectrum and Source Functions $\Sigma'(\omega)$ together with the Computed Nonlinear Energy Transfer Σ'_{nl} (from LeBlond and Mysak, 1978, after Hasselmann, et al., 1973)

$$Q_i + Q_{nl} + Q_d = 0 \tag{36}$$

At wavenumbers below the wavenumber of the spectral peak, $k < k_p$, the phase speed of the long waves is greater than the wind speed (for a fully developed sea) so that the waves lose some of their energy to the atmosphere only to have it restored by nonlinear transfer of energy from the spectral peak. These long waves are still in a growth stage and can accept more energy without breaking. Near the spectral peak, $k = k_p$, wind input is transferred to higher and lower frequencies by nonlinear interactions. Above the spectral peak but below the wavenumber where viscous effects are predominant, $1.5k_p < k < 3k_p$, (Leykin and Rozenberg, 1984; Donelan, et al., 1985), input from the wind and nonlinear interactions are balanced by dissipation processes, including wave breaking and the formation of "parasitic" capillaries ahead of the steep wave crests of the longer primary waves. Phillips (1958) identified this part of the equilibrium spectrum as the "saturation" range: the spectral density of these wavenumbers is limited by the onset of dissipation processes.

Observed spectra, appropriately normalized, exhibit remarkable similarity with the following characteristics. The wavenumber of the spectral peak decreases with increasing fetch and increasing wind speed and the spectral density increases with increasing fetch and wind speed (Figure 9a)

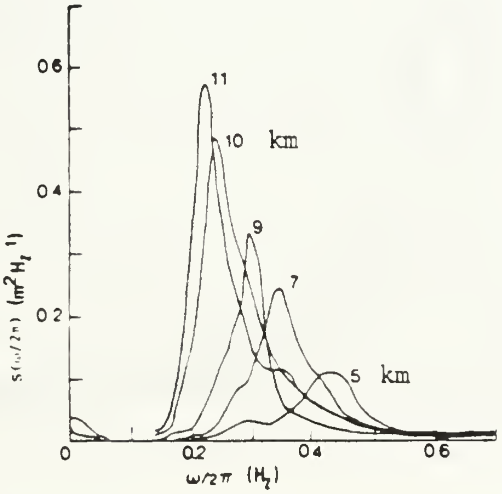

Figure 9a. The Evolution of Surface Wave Spectra with Fetch, from the JONSWAP Observations. The Fetch Increases with the Number labelling the Spectral Peak.
(From LeBlond and Mysak, 1978, after Hasselmann, et al., 1973)

(Kitaigorodskii, 1962; Hasselmann, et al., 1973). There is very little energy below the well-defined spectral peak, while above the peak, the spectral density decreases more slowly (Figure 9b) (Donelan, et al., 1985). Slope spectra (Cox, 1958; Tang and Shemdin, 1983; Shemdin and Hwang, 1988) also display characteristic features. These similarities have led researchers to compute parametric fits to the spectral shape.

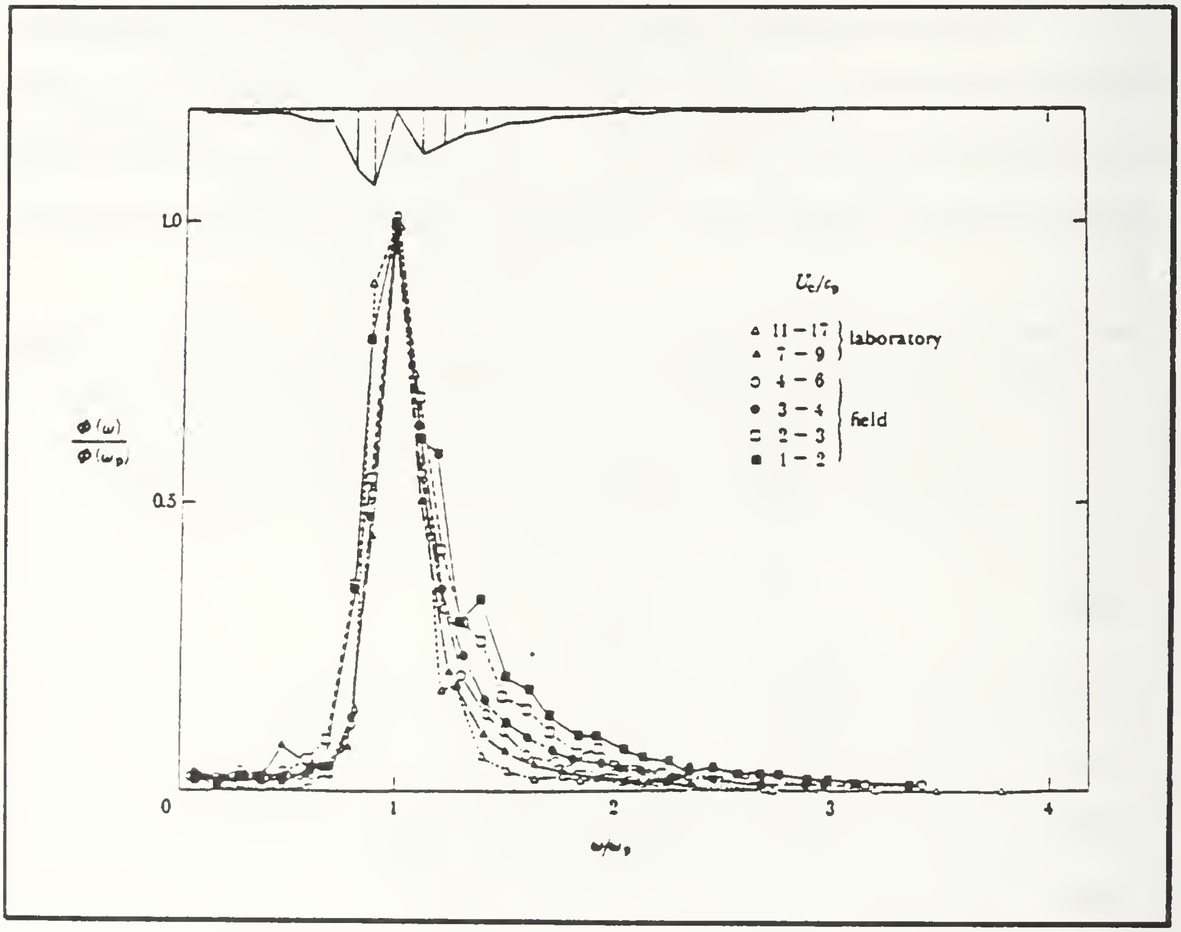

Figure 9b. Normalized Frequency Spectra Grouped into Classes by U_c/c_p. The Vertical Bars at the Top of the Figure are an Estimate of the 90% Confidence Limits Based on the Standard Error of the Mean.
(from Donelan, et al., 1985)

The analytic fitting functions of the earlier models (before 1977) are based on Phillips' concept of a saturation range defined above. Phillips (1958) argued that wavebreaking in the saturation range was a dynamic instability in which the local acceleration of the fluid parcel exceeded the gravitational acceleration, g. Therefore, the spectral density was defined as a function only of frequency (or wavenumber) and gravity. Since the wavenumber spectral density has units of L^4, by dimensional considerations we have

$$S(k) = \beta k^{-4} \tag{37}$$

or, in terms of frequency

$$\Omega(\omega) = \alpha g^2 \omega^{-5} \tag{38}$$

where α and β are universal constants. The spectral slope is either k^{-4} or ω^{-5} and independent of wind speed in the saturation range. Equation (38) is used as the "kernel" of the spectral model proposed by Pierson and Moskowitz (1964) and the Joint North Sea Waves Project (JONSWAP) model proposed by Hasselmann, et al., (1973).

Phillips (1977) modified the form of the saturation range to include the possibility of "microscale" breaking of the short waves (O(10cm)) in the presence of a significant wind drift layer, produced by the tangential component of the wind stress (Banner and Phillips, 1974). Banner and Phillips proposed that the drift current augments the phase speed so that waves whose phase speeds are a small multiple of the surface drift break before reaching their maximum amplitude[3]. The criterion upon which the surface drift is assumed unimportant (after Wu, 1975) is

$$\frac{ku_*^2}{g} << 2 \tag{39}$$

where $u_*^2 = \tau_x / \rho$ is the "friction velocity" of the surface drift layer for an applied wind stress τ_x. The spectral form is then

$$S(k) = k^{-4} f_1\left(\frac{ku_*^2}{g}\right) \tag{40}$$

or,

$$\Omega(\omega) = g^2 \omega^{-5} f_2\left(\frac{\omega u_*}{g}\right) \tag{41}$$

Therefore, in the presence of a wind drift layer, the slopes of the spectrum are k^{-3} or ω^{-4}, assuming f_1 and f_2 are linear.

Phillips (1985) amended his concept of a hard saturation limit, based on observations that the constants, α and β, and the slopes in equations (40) and (41) varied and indicated a wind speed dependence (Leykin and Rozenberg, 1984; Donelan, et al., 1985; Geernaert, et al., 1986). With the additional dependence of wind speed included, the functions in equation (40) and (41) are evaluated as

---

[3] However, Plant and Wright (1977) present empirical results which show the maximum wave height attained by a given wave depends only on its wavelength, i.e., augmented wind drift is not the limiting factor for the growth of the short gravity waves.

$$S(k) = \beta|\cos\varphi|^{\frac{1}{2}} u_* g^{\frac{-1}{2}} k^{\frac{-7}{2}} \tag{42}$$

or,

$$\Omega(\omega) = \alpha u_* g \omega^{-4} \tag{43}$$

Kitaigorodskii (1987) suggests that the equilibrium spectrum changes from the wind speed dependent form ($k^{-3.5}$) to the saturated form (k^{-4}) at about twice the spectral peak. However, scatterometer returns at Bragg wavenumbers above $2k_p$ still display wind sensitivity.

The spectral forms based on the equilibrium range are valid in wavenumber up to the wavenumber where surface tension, T, becomes important $k << \sqrt{\rho g/T}$ (Kinsman, 1965). Beyond this wavenumber and before that where viscous dissipation becomes dominant, the governing variables are the surface tension, gravity, water density, frequency and wavenumber. Radar backscatter is sensitive to wind speed in this wavenumber range so that the spectral form should also display a similar dependence. The waves at the very highest frequencies are damped by molecular viscosity. As stated before, direct observations of frequency spectra in this range are broadened by the Doppler shifts in frequency induced by background currents.

Pierson and Stacy (1973) used field and laboratory data to develop a spectral model which is broken into wavenumber ranges of applicability as specified above. More recently, Shemdin and Hwang (1988) made measurements of the high frequency slope spectra with a laser-optical sensor in order to evaluate the Pierson and Stacy (P&S) model (and others) as well as produce a new empirical model. Their results suggest that there are five spectral regions with frequency bounds as shown in Figure 10. The regions and their associated frequency and slope spectra $(\Phi(\omega), s(\omega))$ are:

1) the inertial range (region I) where

$$\Omega(\omega) = \alpha u.g\omega^{-4} \tag{44a}$$

or in terms of the slope spectrum,

$$s(\omega) = \alpha g^{-1}u. \tag{44b}$$

2) the gravity range (region II) where

$$\Omega(\omega) = \beta g^{2}\omega^{-5} \tag{45a}$$

$$s(\omega) = \beta\omega^{-1} \tag{45b}$$

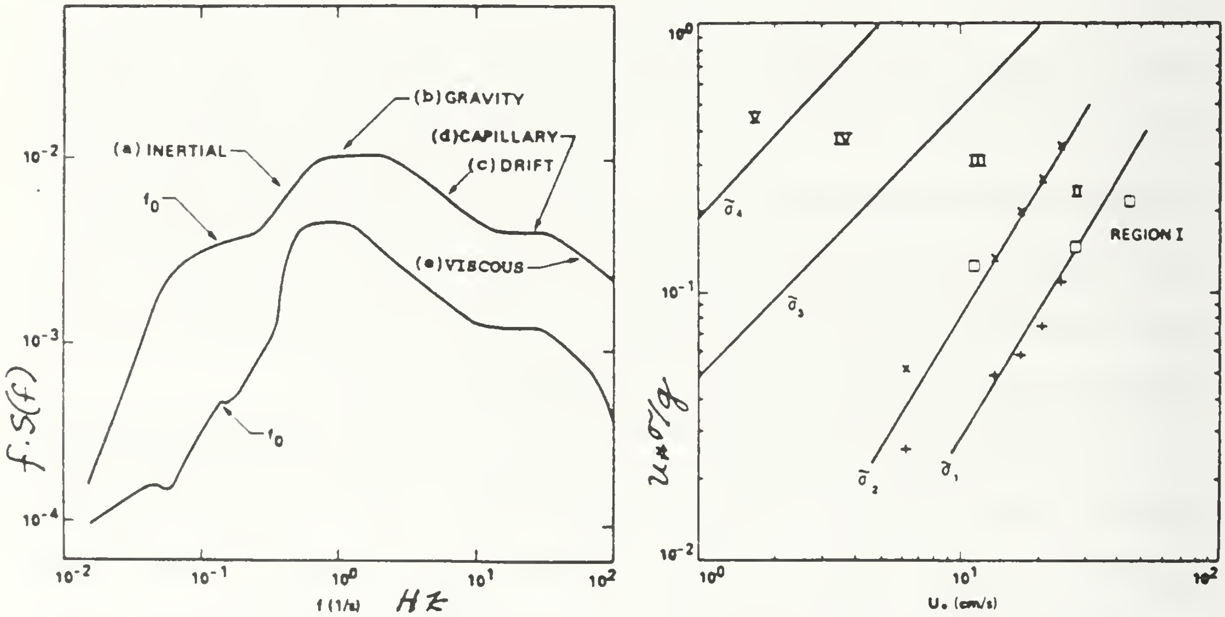

Delineation of Five Wave Spectral Regions (f_0 is the Frequency Corresponding to Peak Energy in the Wave Height Spectrum)

Graphical Description of the Frequency Bounds of Region IV

(from Shemdin and Hwang, 1988)

Figure 10.

3) the surface drift range (region III)

$$\Omega(\omega) = f_1\left(\frac{\omega u.}{g}\right)g^2\omega^{-5} \tag{46a}$$

$$s(\omega) = f_1\left(\frac{\omega u.}{g}\right)\omega^{-1} \tag{46b}$$

4) the capillary range (region IV)

$$\Omega(\omega) = f_2\left(\frac{u.\upsilon}{g}\right)\gamma^{\frac{2}{3}}\omega^{\frac{-7}{3}} \tag{47a}$$

$$s(\omega) = f_2\left(\frac{u.\upsilon}{g}\right)\omega^{-1} \tag{47b}$$

where ν is the kinematic viscosity, γ is the ratio of surface tension to water density, and f_2 is a function defined by Lleonart and Blackmann (1980), and 5) the viscous range (region V) for which a functional form is not yet known.

An alternative method for determining the high frequency portion of the spectrum is to invert the two-scale radar backscatter equation for the functional values of the short wavenumber spectrum (Lawner and Moore, 1984; Chaudrey and Moore, 1984). It is also possible to suggest a model for the spectrum and use the radar measurements to adjust its coefficients (Donelan and Pierson, 1987). This inversion method is predicated on the the existence of an accurate electromagnetic scattering model.

The different spectral forms described above suggest that comparison of radar cross-section model functions reduces to a comparison of wave spectra. The rationale for this statement is shown in Figure 11 which compares the (significantly different) frequency normalized slope spectra for the Pierson and Stacy,(P&S) Shemdin and Hwang (S&H), and Donelan and Pierson models (D&P) (Shemdin and Hwang, 1988). Shemdin attributes the differences between the P&S model and the S&H model to inadequacies in the data set used to generate the P&S model. Differences between the D&P and S&H models in the higher frequency region are attributed to the inversion method used by D&P.

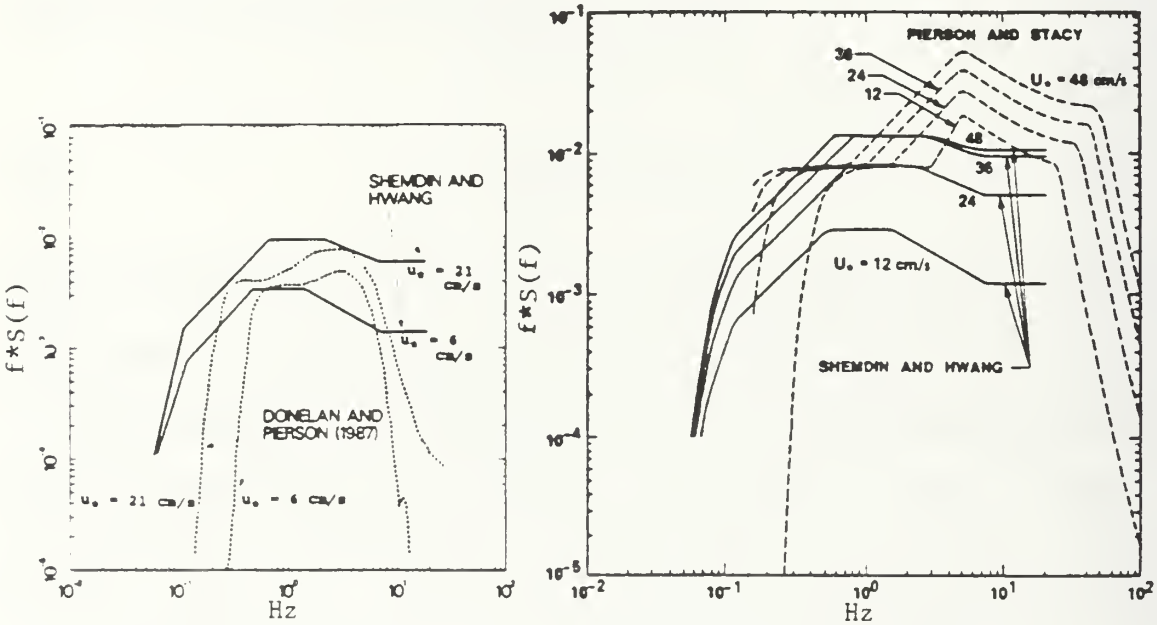

Comparison of the Proposed Model with the Donelan and Pierson Pierson [1987] Model

Comparison of the Proposed Model with the Pierson and Stacey [1973] Model

Figure 11. Slope Spectra Model Intercomparisons from Shemdin and Hwang, 1988.

4. The Source Terms

The examination of the spectral forms in the previous section treated the entire right-hand side of the transport equation only qualitatively as a single entity (see a further discussion in Phillips, 1987). Theoretical treatments of the balance of terms are provided by Kitaigorodskii (1983) and Phillips (1985). Explicit forms of the individual terms are now briefly considered. A review of the literature pertinent to each term is given by Donelan and Hui (1990). Here, only a statement of the functional form for each term is given in order to recognize these quantities in the later discussion of the model functions.

The wind input term is presently thought of as a sum of two terms

$$Q_{I} = \alpha(\mathbf{k}) + \beta(\mathbf{k})\Psi(\mathbf{k}) \tag{48}$$

where $\alpha(\mathbf{k})$ is a linear growth term predicted by Phillips (1957) wave generation theory and $\beta(\mathbf{k})\Psi(\mathbf{k})$ is an exponential growth term due to Miles (1957, 1959). Phillips resonance theory applies only for the initial stage of wave generation when the surface is unperturbed. It is based on the hypothesis that fluctuations in air pressure due to atmospheric turbulence cause waves to be initiated. If the waves so generated move with a phase speed equal to the advective speed of the turbulent eddy, then the waves and pressure fluctuations will be in resonance. The forcing will continue and the results show that the waves will grow linearly in time. Once the waves have developed sufficiently to perturb the air flow above them, then Miles' theory of wave generation by shear flow applies. In this theory, the waves grow exponentially in proportion to the wave energy already present.

Most wave generation studies show that the wave growth is exponential (Plant, 1982) except at very light winds (Kahma and Donelan, 1988). Therefore, attention has been focussed on the specification of the exponential growth rate β(k). Wave tank and field data have been used to detemine the growth rate in terms of friction velocity as (Plant, 1982)

$$\frac{\beta}{\omega} = .04\left(\frac{u_*}{c}\right)^2 \cos\varphi \qquad .08 < \frac{u_*}{c} < 3 \tag{49}$$

or wind speed at 10m (Hsaio and Shemdin, 1983),

$$\frac{\beta}{\omega} = 0.12\frac{\rho_a}{\rho_w}\left[\frac{0.85U(10)\cos\varphi}{c_p} - 1\right]^2 \tag{50}$$

or wind speed at one-half wavelength (Donelan and Hui, 1990)

$$\frac{\beta}{\omega} = (.1 \text{ to } .2)\frac{\rho_a}{\rho_w}\left[\frac{u(\lambda/2)\cos\varphi}{c_p(\lambda)} - 1\right]^2 \tag{51}$$

where c_p is the phase speed of the wave component, ϕ is the relative angle between wind and waves and ρ_a/ρ_w is the air-water density ratio. Using (49), the wind input term is (Plant, 1982; Phillips, 1985)

$$Q_i = 0.04\cos\varphi\omega\left(\frac{u_*}{c_p}\right)^2 N(\mathbf{k}) \tag{52}$$

The nonlinear interaction term, Q_{nl}, in the transport equation (35) represents the redistribution of wave energy among wavenumbers. These interactions occur when several wavenumbers combine to form a new component. Phillips (1960) developed the resonance condition for gravity waves on deep water which occurs at third order (three waves combine to make a fourth)

$$\mathbf{k}_1 + \mathbf{k}_2 = \mathbf{k}_3 + \mathbf{k}_4 \tag{53}$$

In a continuous wave spectrum, an isolated resonant interaction produces a wavenumber which may interact with yet another set of wavenumbers. Therefore, the redistribution of wave energy becomes a conservative property of the entire spectrum; i.e.,

$$\int \frac{dN_4}{dt}(k_4)dk_4 = 0 \tag{54}$$

Hasselmann (1962, 1967) derived the equation for the radiation balance to be

$$\frac{dN_4}{dt} = \iiint G\left[\delta(k_1 + k_2 - k_3 - k_4)\delta(\omega_1 + \omega_2 - \omega_3 - \omega_4)\right]dk_1 dk_2 dk_3 \tag{55}$$

where G is a homogeneous cubic function of N_1, N_2, N_3, N_4 and a homogeneous quadratic function of k_1, k_2, k_3, and k_4. Phillips (1985) then showed through dimensional analysis that the nonlinear term is proportional to the cube of the action density

$$Q_{nl} \propto G^2 N^3(\mathbf{k}) k^4 \omega^{-1} \tag{56}$$

The final term in the transport balance, Q_d, represents dissipation of wave energy, which results from viscous damping, wave breaking, turbulence and dissipation of parasitic capillaries at short gravity wavelengths produced by nonlinear interactions (Donelan and Hui, 1990). The form of the viscous dissipation rate of decay is known from classical wave theory (Lamb, 1932) to be $\beta_v = 4\nu k^2$ where ν is the kinematic water viscosity. The viscosity is an inverse function of temperature; therefore, explicit inclusion of the viscous damping will produce a temperature dependent spectrum. However, viscosity is only important at the highest frequencies when compared to wind forcing because of the quadratic dependence on wavenumber. Theoretical forms for the breaking of waves and generation of parasitic capillaries are not known. Phillips (1985) suggests that it is not necessary to know an explicit form for these processes, rather it is only required that the dissipation term balance the other source terms. Therefore, a dimensional analysis is written for the dissipation rate (Plant, 1986; Donelan and Pierson, 1987). Following Donelan and Pierson (1987)

$$\frac{\beta_d}{\omega} = f_1[\Psi(\mathbf{k}), k, \gamma, g] + \frac{\beta_v}{\omega} \tag{57}$$

That is, the dissipation rate is a function of the wavenumber spectral density, wavenumber, surface tension and gravity, plus viscous dissipation. Then,

$$\frac{\beta_d}{\omega} = f_1\left[k^4\Psi(\mathbf{k}); \frac{\gamma k^2}{g}\right] + \frac{\beta_v}{\omega} \tag{58}$$

Finally, the dissipation term is written

$$Q_d \propto \left\{\omega\left[f_1\left(k^4 N(\mathbf{k})\right); \frac{\gamma k^2}{g}\right] + \beta_v\right\}\Psi \tag{59}$$

With the specification of the source terms, it is then possible to use the transport equation (35) to examine the interdependence of these terms and to model the wavenumber spectrum. The parameterizations of the source terms identify the most plausible environmental variables on which the wave spectrum could depend. These are the wind velocity or wind stress, surface layer stability, wind duration and constancy, fetch, water depth, surface tension, viscosity and water temperature. The selection of slightly different functional forms for these terms will produce correspondingly different radar cross-sections when the resulting spectra are used in radar cross-section models.

E. FUNDAMENTALS OF AIR-SEA INTERACTION THEORY

The previous two sections showed that the ocean wavenumber spectrum was needed for the calculation of the radar cross-section and that this wavenumber spectrum was for the most part, dependent on the wind stress. The wind stress over (relatively flat) land can be directly measured using a drag plate of surface roughness comparable to the ground in which it is installed. No such direct measure of stress is possible over the undulating water surface; therefore, the stress is inferred from quantities which are directly measureable. The purpose of this section is to provide the standard mathematical framework which connects the wind stress to these measured quantities. This summary is a synthesis of similar treatments provided by Byers (1985), Arya (1988), Donelan (1989) and Geernaert (1990).

1. Basic Theory

The atmospheric planetary boundary layer (APBL) consists of the lowest 1000m or so of the atmosphere and is formed as a result of the interactions between the atmosphere and underlying surface on time scales of hours (Arya, 1988). In this layer, the vertical variation of the mean stresses is large compared to the horizontal gradients, therefore, turbulent shear eddies act to transfer heat, momentum and moisture to and from the surface at a rate much faster than simple molecular diffusion (Holton, 1979).

The mean vertical fluxes of momentum, $\overline{u'w'}, \overline{v'w'}$; sensible heat flux, H_S; and latent heat, E_L, in the APBL are given by (using the notation of Geernaert, et al., 1988)

$$\tau = \rho\left\{-\overline{u'w'}\hat{\mathbf{i}} - \overline{v'w'}\hat{\mathbf{j}}\right\} \tag{60}$$

$$H_s = \rho C_P \overline{w'\theta_T'} \tag{61}$$

$$E_L = \rho L_V \overline{w'q'} \tag{62}$$

where τ is the surface stress, ρ_W is the water density, C_P is the specific heat of air at constant pressure, L_v is the latent heat of vaporization, θ_T is the potential temperature, q the specific humidity and $u,v,w,$ are the longitudinal, latitudinal and vertical wind velocity components. Primed quantities represent fluctuations about a mean value where the mean, as denoted by an overbar, is taken over a time long enough for the mean vertical velocity to approach zero. It is assumed that the process is stationary and the ergodic theorem applies. These equations show that the stress can be computed from the covariance of the wind velocity components.

The covariance measurements require a stable platform for accurate measurement of the vertical velocity and fast response sensors. Other methods for determining the wind stress (log-profile, dissipation) are generally neither suitable nor available for use on a standard basis. Therefore, bulk aerodynamic methods are often used to express the stress in terms of more easily obtained parameters; i.e.,

$$\tau_x = \rho C_D \left(U_{10} - U_0\right)^2 \tag{63}$$

$$H_S = \rho C_P C_H U_{10}\left(T_0 - T_{10}\right) \tag{64}$$

$$E_L = \rho L_V C_E U_{10}\left(q_0 - q_{10}\right) \tag{65}$$

where the numeric subscripts indicate the measurement height in meters above the surface. The bulk exchange coefficients are C_D for wind drag (the drag coefficient), C_H for the sensible heat flux (the Stanton number) and C_E for the latent heat flux (the Dalton number). The surface humidity is assumed saturated with respect to the sea surface temperature. All of the coefficients are of magnitude $O(10^{-3})$.

By convention, the wind stress is positive downward and the heat fluxes are positive upward. It is typical to define a "streamwise" coordinate system such that $\overline{v}$ and $\overline{v'w'}$ is assumed to be considerably less than $\overline{u'w'}$, hence the stress is approximated by the x-component of (60) only. This approximation requires that turning of the flow by the Coriolis force can be neglected, which implies that the measurement be made close to the surface where friction has a greater influence.

2. Surface Layer Scaling for Neutral Atmospheric Stratification

The surface layer is defined as the lowest ca. 10% of the APBL in which the Coriolis force can be neglected. Furthermore, in this region the vertical gradients of the atmospheric parameters (u, θ, q) are significantly greater than the corresponding gradients of the fluxes. Therefore, the vertical gradients of the atmospheric parameters are scaled with the (assumed) constant surface fluxes (Businger, 1973). If viscous effects near the surface are ignored and the density stratification is negligible, then a similarity hypothesis is proposed that the velocity gradient depends on height above the surface, the surface stress, and air density; i.e.,

$$\frac{\partial u}{\partial z} = f(z, \tau, \rho) \tag{66}$$

where the surface stress accounts for all other influential parameters such as surface roughness. The only velocity scale which can be made from the above variables is the so-called friction velocity, u_*, where

$$u_* = \sqrt{\frac{\tau}{\rho}} \tag{67}$$

The characteristic length scale has to be z. Therefore, from dimensional analysis

$$\frac{\partial u}{\partial z} = f\left(\frac{u_*}{z}\right) \tag{68}$$

or

$$\frac{\partial u}{\partial z} = \frac{1}{\kappa}\frac{u_*}{z} \tag{69}$$

where κ is the von Karman's constant which is found from experiment to be about 0.4. Integrating equation (69) with respect to z (and now employing the constant flux approximation) yields the logarithmic wind profile, or as known in fluid mechanics literature, the "law of the wall"

$$u(z) = \frac{u_*}{\kappa}\ln\left(\frac{z}{z_0}\right) \tag{70}$$

Actually, it is $\ln\left(\frac{z + z_0}{z_0}\right)$, but z_0 is generally much less than z and (70) is used as an approximation. Here, the integration constant, the *roughness length*, z_0, is a measure of the effective roughness of the surface and is introduced to keep the integral convergent.

A surface is considered aerodynamically smooth if its roughness elements[4] are small enough to allow a viscous sublayer to form near the surface and the elements are completely submerged in this layer. At the top of the viscous sublayer, z is not much larger than z_0, viscosity dominates the stress and

$$z_0 = \frac{0.11u.}{\nu}; \qquad u. < 2(\nu g)^{\frac{1}{3}} \tag{71}$$

where ν is the kinematic viscosity of the air and g is the gravitational constant (Donelan, 1989). The thickness of the viscous sublayer for atmospheric flows is only 1mm; therefore, the ocean surface must be "ultrasmooth" for a viscous sublayer to form. This may occur for very light winds (U < 3m/s).

The typical sea surface is rarely so smooth and for wind speeds greater than about 7.5m/s, the roughness elements interact directly with the turbulent flow. In this case, form drag on the roughness elements accounts for nearly all the stress and the roughness length is proportional to the height of the roughness elements, as well as their areal density, characteristic shapes and dynamic response characteristics (flexibility and mobility) (Arya, 1988; Donelan, 1989). Charnock (1955) proposed that the roughness elements for fully rough flow were the short gravity waves, so that by dimensional analysis

---

[4] "Roughness elements are surface features with sufficient steepness to cause flow separation on their lee faces and hence form drag. The flow may remain attached to quite large features having gentle slopes, but separate from small, abrupt roughnesses," (Donelan, 1989).

$$z_0 \propto \frac{mu_*^2}{g} \tag{72}$$

where m is of the order of 10^{-2}. Cardone (1969) also derived an empirical expression for z_0 purely in terms of u_*,

$$z_0 = \frac{0.684}{u_*} + 4.28\text{x}10^{-5}u_*^2 - 0.443 \tag{73}$$

for u_* in cm/s (See also Garrett, 1977).

Donelan (1989) and Geernaert et al. (1986) reviewed studies which show that Charnock's relation is essentially an asymptotic form for z_0, appropriate only for a fully developed wave field. If the waves are actively growing, then z_0 appears to be more closely related to the wave parameters. Geernaert et al. derive a time dependent form

$$z_0 = 10\exp\left(-\frac{1}{15}u_*^{\frac{-4}{9}}g^{\frac{5}{18}}X^{\frac{1}{6}}t^{\frac{1}{9}}\right) \tag{74}$$

where X is the upwind fetch and t is time and z_0 is in meters. Donelan (1989) suggests that for fully rough flow and wind speed parameter, u_i

$$\frac{z_0}{a} \propto \left(\frac{u_i}{c_p}\right)^b \tag{75}$$

That is, the ratio of roughness length to the rms height of the waves is proportional to the inverse wave age, U/c_p, where c_p is the phase speed. This parameterization makes use of the fact that the longer (faster) waves are less steep. The coefficients, *a* and *b*, differ for differing wind speed parameters; i.e., wind speed at different levels or friction velocity, and field vs laboratory data.

3. The Non-Neutral Surface Layer

The previous section did not consider non-neutral stratification in the surface layer. Monin-Obukhov (1954) proposed a similarity hypothesis which includes buoyancy effects for a non-neutral, surface layer. The hypothesis is that in a horizontally homogeneous, quasistationary, "constant flux" surface layer, the mean flow characteristics depend only on the height above the surface, κz, the friction velocity, u_*, the surface kinematic heat flux, $\overline{w'T'}$, and buoyancy flux, represented here as g/T. The simplifying assumptions are again that the Coriolis force can be ignored, viscous effects are negligible compared to the turbulent fluxes and the influence of surface roughness, boundary layer height and geostrophic winds are completely accounted for by u_*. The result of the dimensional analysis is that the vertical profiles of wind, temperature and humidity are functions of a stability parameter z/L; e.g.,

$$\frac{\partial u}{\partial z} = \frac{u_*}{\kappa z}\varphi\left(\frac{z}{L}\right) \tag{76}$$

where

$$\frac{z}{L} = \frac{-g\kappa z\overline{w'T_V'}}{T_V u_*^3} \tag{77}$$

and L is the Monin-Obukhov length.

The turbulent length scale, L, represents the relative importance of buoyancy to shear effects. It is negative (positive) for unstable (stable) conditions and zero for neutral conditions. The nondimensional bulk

Richardson number has an equivalent interpretation as seen from its definition

$$Ri_B = \frac{gz\Delta T_V}{T_V U^2} \tag{78}$$

where ΔT_V is the difference between the virtual temperatures between two given heights (the air-water temperature difference in the present case). The virtual temperature accounts for a moist atmosphere and is related to the specific humidity by

$$T_V = T(1 + 0.61q) \tag{79}$$

The quantity z/L is a ratio of fluxes, hence it is difficult to measure. When measured directly it is typically "noisy" since the fluxes are second order moments which have large error variances associated with them (see Chapter III, Section C). Therefore, z/L is generally determined from the (first-order) bulk Richardson number and exchange coefficients by

$$z / L = \kappa C_H C_D^{-3/2} Ri_B \tag{80}$$

(see Donelan, 1989; Hsu, 1989).

The universal stability functions in equations (76) for the wind profile were measured over land (Businger, 1971) and found to be

$$\varphi\left(\frac{z}{L}\right) = \begin{cases} (1 - \alpha z / L)^{\frac{-1}{4}} & z/L < 0 \\ (1 + \beta z / L) & z/L > 0 \end{cases} \tag{81}$$

where α and β were 15 and 4.7, respectively for κ=0.37. Panofsky and Dutton (1984) suggest 16 and 5 for these constants (for κ=0.4). Kitaigorodskii and Donelan (1984) propose 17 and 5.4 (for κ=0.4).

The diabatic log profile for the wind is obtained from (81) by integrating from $\zeta_0 = z_0/L$ to $\zeta = z/L$ after the change of coordinates $z = \zeta L$:

$$u(z) = \frac{u_*}{\kappa}\left[\ln\left(\frac{z}{z_0}\right) - \Psi_m\right] \tag{82}$$

where

$$\Psi_m(\varsigma) = \int_{\varsigma_0}^{\varsigma}\left[1 - \varphi_m(\varsigma)\right]\frac{d\varsigma}{\varsigma} \tag{83}$$

Paulson (1970) solved the integral for unstable conditions, $\zeta<0$

$$\Psi_m(\varsigma) = \ln\left[\frac{\left(1+x^2\right)}{2}\frac{\left(1+x\right)^2}{2}\right] - 2\tan^{-1}x + \frac{\pi}{2} \tag{84}$$

where $x = (1-15\zeta)$. For stable conditions $\zeta>0$, and

$$\Psi_m(\varsigma) = -5\varsigma \tag{85}$$

A functional form for the bulk drag coefficient for height z is obtained from the combination of equations (63) and (67)

$$C_D = \frac{u_*^2}{u_z^2} = \kappa^2\left[\ln\left(\frac{z}{z_0}\right) - \Psi_m\right]^2 \tag{86}$$

Here, the surface drift velocity, u_0, was assumed to be negligible[5]. The drag coefficient can then be interpreted physically as a function of measurement height, z, wave state, z_0, and stratification, z/L (Geernaert, et al., 1988a).

---

[5] Geernaert (1986) notes that this omission of the wind drift amounts to only a 2 to 3% error in the wind stress.

Many studies in the recent years have investigated the behavior of the drag coefficient with changes in environmental parameters (see Geernaert, et al., 1988a, for references). The results are usually normalized for stratification and reported in terms of a neutral drag coefficient, C_{DN},

$$C_{DN} = \left[C_D^{-1/2} + \frac{\Psi}{\kappa} \right]^{-2} \tag{87}$$

where (87) is derived by assuming z_o to be constant for a given wind speed.

The drag coefficient has a wind speed dependence since it depends on the roughness length (wave state). Therefore, most investigators plot their measurements against wind speed and parameterize the drag coefficient in terms of the wind speed, although there is a clear dimensional inconsistency.

Some of the more frequently quoted drag coefficient parameterizations are illustrated in Figure 12. The physically based model functions discussed in the next section utilize the Large and Pond drag coefficient (curve 1) which specifies the neutral drag coefficient for the open ocean as

$$C_{DN} = \begin{cases} 0.114 & U < 10m/s \\ 0.001(0.49 + .065U) & U > 10m/s \end{cases} \tag{88}$$

Since Lake Ontario typically has a shorter, steeper wave field, the drag coefficient is comparably higher as shown in the Donelan formulation for Lake Ontario (similar slope as Curve 7, Figure 12):

$$C_{DN} = .001(0.37 + 0.137U) \tag{89}$$

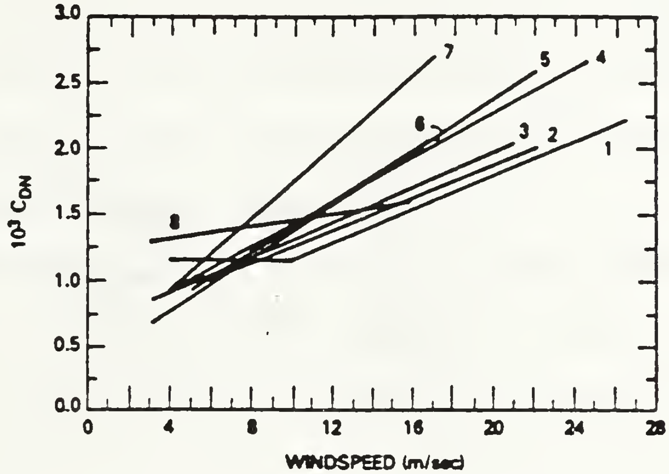

Figure 12. Distribution of the Neutral Drag Coefficient with Wind Speed from the Following Investigations: 1, Large and Pond [1981]; 2, Smith [1980]; 3, Smith and Banke [1975]; 4. Geernaert et al. [1987b]; 5, Geerneart et al. [1986]; 6, Sheppard et al. [1972]; 7, Donelan [1982]; 8, Kondo [1975]. (from Geernaert, et al., 1988a)

Therefore, for a given wind speed the wind stress over the lake will be higher than the same wind speed over the ocean. A proper comparison of the lake cross-section data to the scatterometer model function predictions as a function of wind speed, or stratified on wind speed, then requires that the neutral wind speeds over the lake first be "converted" to an equivalent wind speed over the ocean through an open ocean drag coefficient.

4. The Thermal-Mechanical Internal Boundary Layer

The Monin-Obukhov surface layer scaling described above strictly applies to an equilibrium boundary layer over horizontally homogeneous terrain. However, when such a flow over a uniform terrain encounters a step change in surface conditions such as roughness, an internal boundary layer

(IBL) develops downstream of the discontinuity as illustrated in Figure 13a (Rao, et al., 1974).

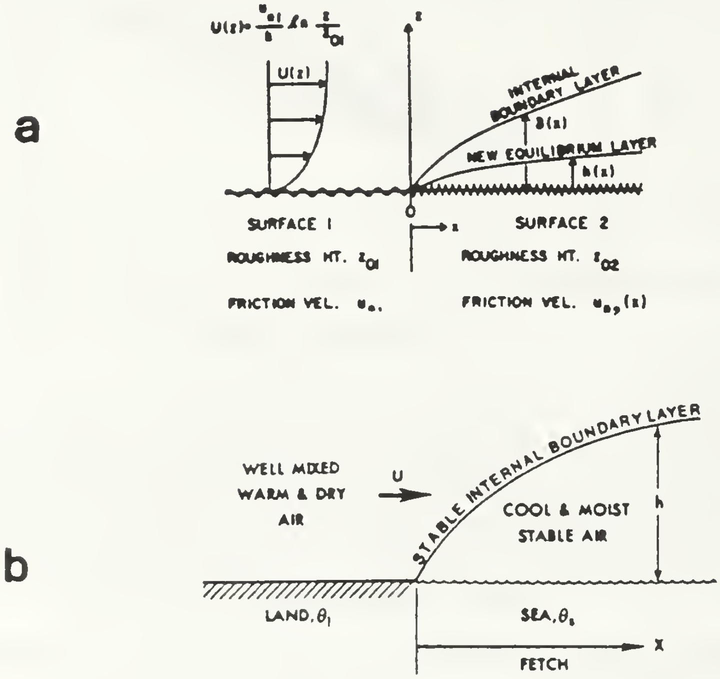

Figure 13. Schematic Diagram of the Internal Boundary Layer (IBL) over a step change of a) surface roughness (from Rao, et al., 1974) and b) temperature (Hsu, 1989).

The research tower used in the present study is located 1.1km from the western shore of Lake Ontario, hence an IBL is formed when the wind blows offshore from the short fetch directions (approximately 180° to 360° True). The continental air masses blowing from these directions flow over the comparatively rough terrain of a midsize industrial city. The associated air temperatures often contrast significantly with the water temperature of the lake since the sources are either warmer air from the Southwest or cold, polar air from the North. Therefore, the IBL formed offshore can be described as both "mechanical," due to a change in surface roughness, and "thermal," due to nonzero land-water temperature differences (Figure 13b). The height of this thermal-mechanical internal boundary layer (TMIBL) increases with distance from shore and its growth rate depends on the degree of contrast between the two regimes.

The existence of an TMIBL is of concern when making wind stress measurements since the air flow above the TMIBL is representative of conditions upstream of the discontinuity, and the air flow within the TMIBL is representative of the downstream conditions. If a true representation of the wind stress over the water surface is the desired quantity, then the measuring device must be far enough from the land/water discontinuity and at a height which is within the TMIBL, in order to not be dominated by the upstream land conditions. Furthermore, the measuring device must be within the new "constant flux" layer (the height above the surface in which the fluxes are within 10% of their surface values) for Monin-Obukhov scaling to apply.

Various parameterizations for the height and growth of the IBL have been derived for a change in surface roughness (Rao, et al., 1974; Claussen, 1987), and a change in temperature (Mulhearn, 1981; Garrett, 1987; Hsu, 1989). For a change in surface roughness from rough-to-smooth, Rao et al. (1974) find that the height-to fetch ratio of the IBL height is about 1/10 and the new equilibrium layer ("constant flux") layer is about 0.5% of the fetch; i.e., in the present case of a 1.1km fetch to the tower (shortest fetch encountered) the IBL is 110m high and the constant flux layer is only 5.5m. In the case of a thermal IBL, Garrett (1987) shows that the growth rate of the layer is slower for stable conditions since the turbulence is buoyantly damped. Hsu (1989) recasts Garrett's results to show that under stable conditions the IBL height is 16 times the offshore fetch (in km); therefore, at the Lake Ontario tower for very stable conditions the IBL height is about 17.6m.

These rough comparisons with the IBL parameterizations have several implications: 1) the anemometer used in the present experiment, which is 11.5m above the surface, is within the internal boundary layer but not necessarily within the "constant flux" layer as defined in Monin-Obukhov scaling. Therefore, the stress measurements may differ by more than 10% of their surface values, and 2) both the atmospheric boundary layer and the wave field are in "growth" stages when the wind blows from the short fetch directions in this experiment. The comparisons made above are for the worst case scenario; i.e., stable flow from the shortest fetch direction. A wide range of wind speed, fetch and stability conditions were encountered during this experiment, and alternative scaling arguments for the computation of the wind stress are not available, therefore, it was assumed that for the most part the anemometer was within the constant flux layer and Monin-Obukhov scaling was employed to facilitate comparison with previous scatterometer studies.

F. SYNOPSIS OF RECENT MODEL FUNCTIONS

The previous sections in this chapter have provided a brief background on electromagnetic scattering, ocean wave and air-sea interaction theory required for the development of a scatterometer model function. The path through these intertwining theories led to the identification of environmental parameters which may affect the radar cross-section. These parameters include: the wind speed (or wind speed parameter), wind direction, long wave field (long with respect to the Bragg wave), atmospheric stratification (as it affects wind speed) and water temperature (as it affects viscosity). Inasmuch as these quantities all relate to the ultimate form of the ocean wavenumber spectrum used in the two-scale scattering model, differences among the "physically based" model functions amount to differences in the specification of the spectrum. The purpose of this section is to outline the forms and predictions of some currently proposed model functions in terms of their treatment of the ocean wavenumber spectrum and their methods for including/excluding the environmental parameters above.

This study is intended to be a demonstration of environmental effects on the cross-section, not a comprehensive test and evaluation of model functions. Therefore, the models are only discussed at a level of detail sufficient to give the reader the justification for comparisons with the field data and the conclusions to be drawn from these comparisons. The attributes of the different models are summarized in Table III at the end of this section.

1. The Seasat Scatterometer SASS1 Model Function (1980)

The genesis of the SASS1 model function is chronicled in Schroeder, et al. (1982). Three candidate model functions produced prior to the Seasat launch were based on statistical fits of cross-section to the neutral wind speed at 19.5m using scatterometer data from aircraft circle flights (Jones, et al., 1977, 1982). After the demise of Seasat, the three model functions went through refinements via a series of workshops in which the predicted wind vectors were tuned to additional *in-situ* data from the Joint Air-Sea Interaction (JASIN) experiment and compared to *in-situ* winds from the Gulf of Alaska

SEASAT experiment, GOASEX (see Brown, et al., 1983 for a description of the *in-situ* data). The models attempted to reproduce the observed increase of the cross-section as some power of the wind speed and the approximately cos2χ dependence of the cross-section on relative wind angle, χ (recall Figure 2b).

The result of these workshops was SASS1, a "power law" model function which relates the NRCS to the neutral wind speed at 19.5m, incidence angle and azimuth angle:

$$\sigma^{\circ}(U,\theta,\chi)_{dB}=10\left[G(U,\theta,\chi)+(U,\theta,\chi)\log_{10}U_{19.5}\right] \tag{90}$$

where the wind speed is in m/s. The G and H coefficients are obtained from lookup tables which tabulate the coefficients as functions of incidence angle (0° to 70° in 2° increments) and azimuth angle (0° to 180° in 10° increments. Two separate tables were produced for vertical and horizontal polarization.

The entries in the tables were a synthesis of the three models and were tuned to eliminate errors between the observed and predicted winds (Wentz, 1984). Of the three models, the Wentz model, which used the aircraft and *in-situ* data to determine the coefficients of a two-scale model was used for table entries between 0° and 12° incidence. Between 24° and 64°, a combination of the three models was used (Schroeder, et al., 1982). Interpolation of the table filled the gap between 12° and 24° and extrapolation extended the table to 70° incidence (Boggs, 1981).

The SASS1 model was used to process the three-months of SEASAT SASS data. Many preliminary studies successfully used the SASS1 wind vectors to demonstrate the utility of scatterometer winds (JGR Special Issue, Feb, 1983), even though problems in the model function were later uncovered, as described below.

2. The Wentz SASS2 Model Function (1984, 1986)

Wentz, et al. (1984) point out systematic errors in the SASS1 derived wind vectors, which are attributed to tuning the scatterometer cross-sections to a very limited *in-situ* data set. As stated in Wentz (1986) the errors are:

1) a positive bias between h-pol and v-pol derived winds,
2) an artificial wind speed gradient across the satellite swath due to incorrect specification of the incidence angle dependence,
3) a positive bias of wind speeds below 6m/s due to the exclusion of low signal-to-noise ratio NRCS values (the logarithmic form of the model function is undefined for zero and negative values of NRCS), and
4) a positive 1m/s bias of the SASS wind speeds.

Wentz (1984) notes that additional physical variables such as the viscosity, wind fetch and duration and long gravity waves which may be important as second order effects, will not significantly alter the power law relationship. As listed in the introduction here, Woicheshyn, et al. (1986) pointed out the above failings in the SASS1 model function. However, they do blame incomplete specification of the physics involved in using the cross-section measurement to predict wind when a power law relationship is used; particularly the neglect of the effects of atmospheric stratification and the water temperature. Wentz (1986) counters that systematic departures from the power law have not been observed and that the errors in the SASS1 algorithm were not due to the form of the power law but rather the original coefficients used in the model.

Based on the observed power law dependence of the cross-section to wind speed and the azimuth dependence with wind direction, Wentz (1984) fits the cross-section data with a truncated Fourier series as follows:

$$\sigma^{\circ} = A_0 + A_1 \cos\chi + A_2 \cos 2\chi \tag{91a}$$

$$A_0 = a_0 U^{\alpha_0} \tag{91b}$$

$$A_1 = \left(a_1 + \alpha_1 \log U\right) A_0 \tag{91c}$$

$$A_2 = \left(a_2 + \alpha_2 \log U\right) A_0 \tag{91d}$$

where α_n is the power law coefficient. The coefficients a_n and α_n are dependent on the polarization and incidence angle. Instead of fitting the coefficients to any particular data set, the coefficients were computed by assuming some statistics about the global wind field: the wind speed as deduced from the SASS measurements are assumed to have a Rayleigh distribution, and a uniform distribution of wind direction[6]. The assumptions are validated by comparing wind speeds computed from the SASS1 model and the aircraft data used to produce the SASS1 model. The comparisons show better agreement between the SASS2 predictions and the aircraft data than similar comparisons with the SASS1 predictions. There is still a systematic 0.5m/s bias between the h-pol and v-pol wind speeds which becomes greater with increasing incidence angle.

---

[6] The assumption of a uniform distribution of wind directions seems intuitively less defensible since the global winds have a definite latitudinal dependence. However, Wentz states that the predictions of the model function are not particularly sensitive to the actual distribution used; therefore, the uniform distribution is employed for the sake of simplicity.

3. The Durden and Vesecky Model (1985, 1986)

The SASS1 and SASS2 model functions accept the two-scale scattering theory as the physical basis for the observed cross-sections but the theory is not explicitly used to calculate the cross-sections. Furthermore, they are em frequency specific. In the Durden and Vesecky model (D&V) model, patterned after the Fung and Lee (1982) model, the radar cross-section is computed using the two-scale theory, as described in Section C of this chapter. The separation wavenumber is chosen such that both the curvature of the large-scale surface and the mean-square height of the surface are small in order to minimize the rms error in the two-scale model, as defined by Durden (1986). The use of the two-scale model requires a form of the ocean wavenumber spectrum, the definition of the separation wavenumber, long wave slopes and a probability distribution function of the slopes, and an atmospheric surface layer theory which connects the wind stress to the wind speed. The D&V model also requires water temperature and salinity for the computation of the dielectric constant in the polarization constants (equations (12), Section C).

The wavenumber spectrum is split at the wavenumber, $K_c = g/U_{19.5}^2$, into a low wavenumber portion and a high wavenumber portion

$$\Psi(k,\varphi) = \frac{0.004}{2\pi} k^{-4} \begin{cases} e^{-0.74\left(\frac{K_c}{k}\right)^2}\left[1 + c\left(1 + e^{-sk^2}\right)\cos 2\varphi\right] & k < 2m^{-1} \\ \left(\frac{bku_{\cdot}^2}{g_{\cdot}}\right)^{a\log_{r}\left(\frac{k}{K_l}\right)}\left[1 + c\left(1 - e^{-sk^2}\cos 2\varphi\right)\right] & k > 2m^{-1} \end{cases} \qquad (92)$$

where $$g_* = g + \frac{T}{\rho_w} k^2 \tag{93}$$

is a modified gravitational parameter which includes surface tension, T, at high wavenumbers. The low wavenumber portion is the Pierson-Moskowitz similarity spectrum (1964) which has a k^{-4} wavenumber dependence. Durden and Vesecky (1985) extend the Pierson-Moskowitz spectrum to include the effect of the wind drift layer on microscale breaking at the higher wavenumbers by making the wavenumber spectrum a function of u_*^2/g as in equation (39) of Section D. The functional dependence is assumed to be a power law in which the exponent is a function of wavenumber.

$$S(k) = Bk^{-4}\left(bk\frac{u_*^2}{g_*}\right)^{r(k)} \tag{94}$$

The exponent is modeled as a logarithm of the wavenumber, $r(k) = \log(k/K_t)$, based on observations that the cross-section power law with wind stress varies with the radar frequency (Jones and Schroeder, 1978; Fung and Lee, 1982). The separation wavenumber, K_t, is the wavenumber at which $\frac{ku_*^2}{g} << 1$ is no longer valid; here K_t is taken as 2. The wavenumber magnitude spectrum is illustrated in Figure 14 for $U_{19.5}$ = 10m/s and upwind(ϕ=0) and crosswind (ϕ=90) conditions (Verma, et al., 1989).

The directional dependence of the spectrum is the cos2φ term enclosed in square brackets of equation (92) and is displayed in Figure 15. The multiplicative exponential factor in equation (92) was introduced by Fung and

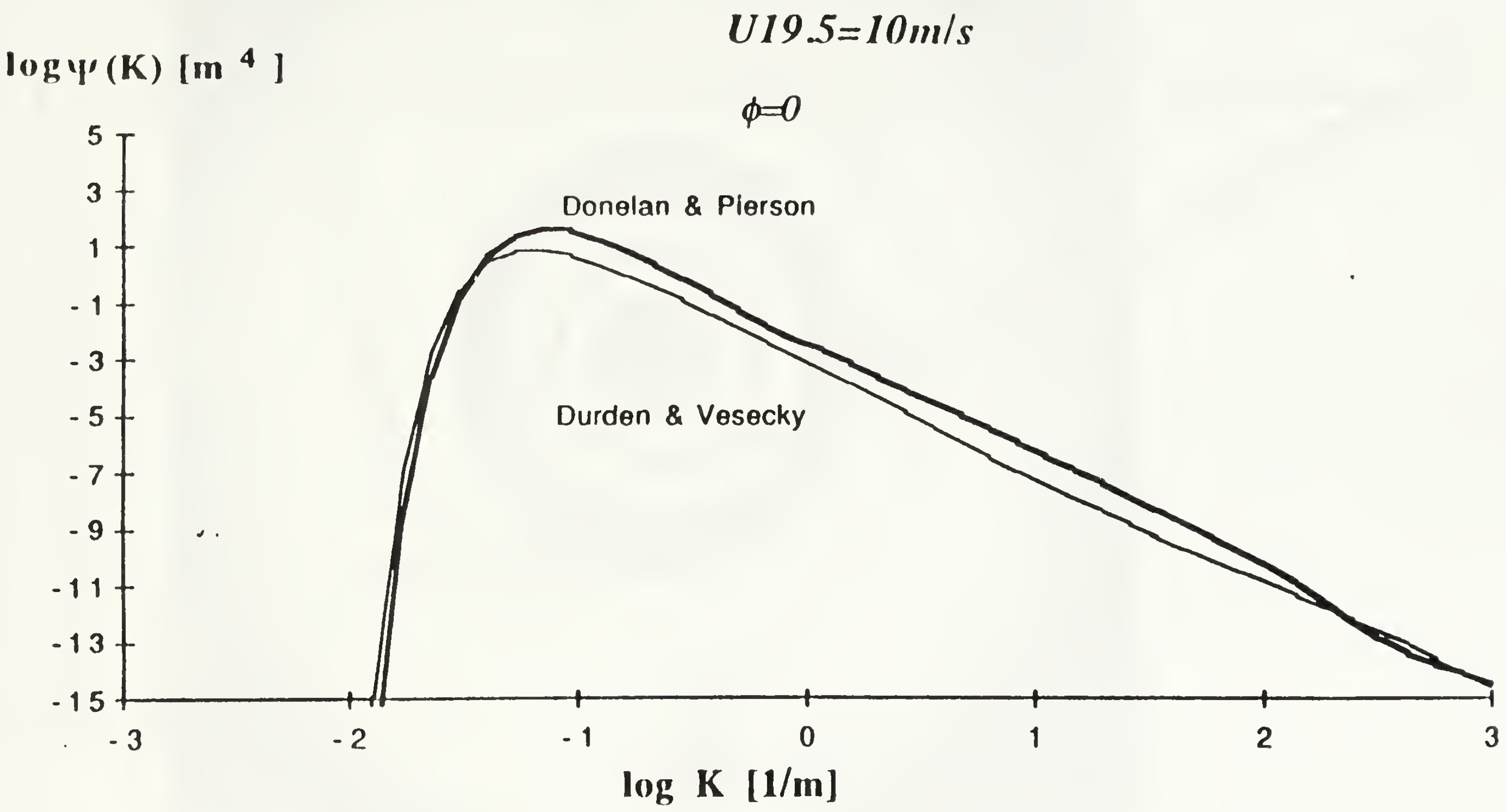

Figure 14a. Comparison of Donelan and Pierson (1987) and Durden and Vesecky (1985) Wavenumber Amplitude Spectra for Upwind Direction and U19.5 = 10m/s.

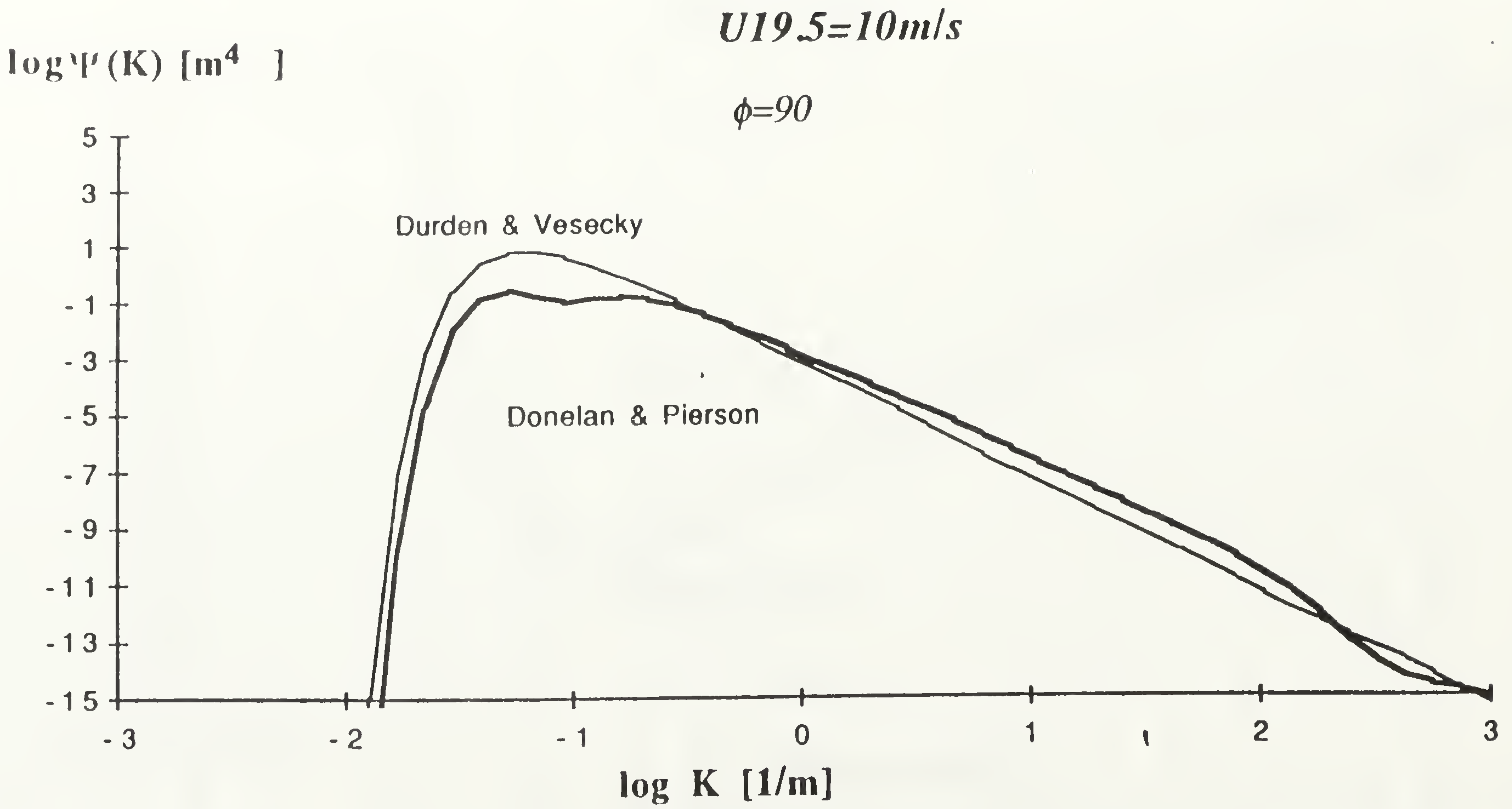

Figure 14b. Comparison of Donelan and Pierson (1987) and Durden and Vesecky (1985) Wavenumber Amplitude Spectra for Crosswind Direction and U19.5 = 10m/s.

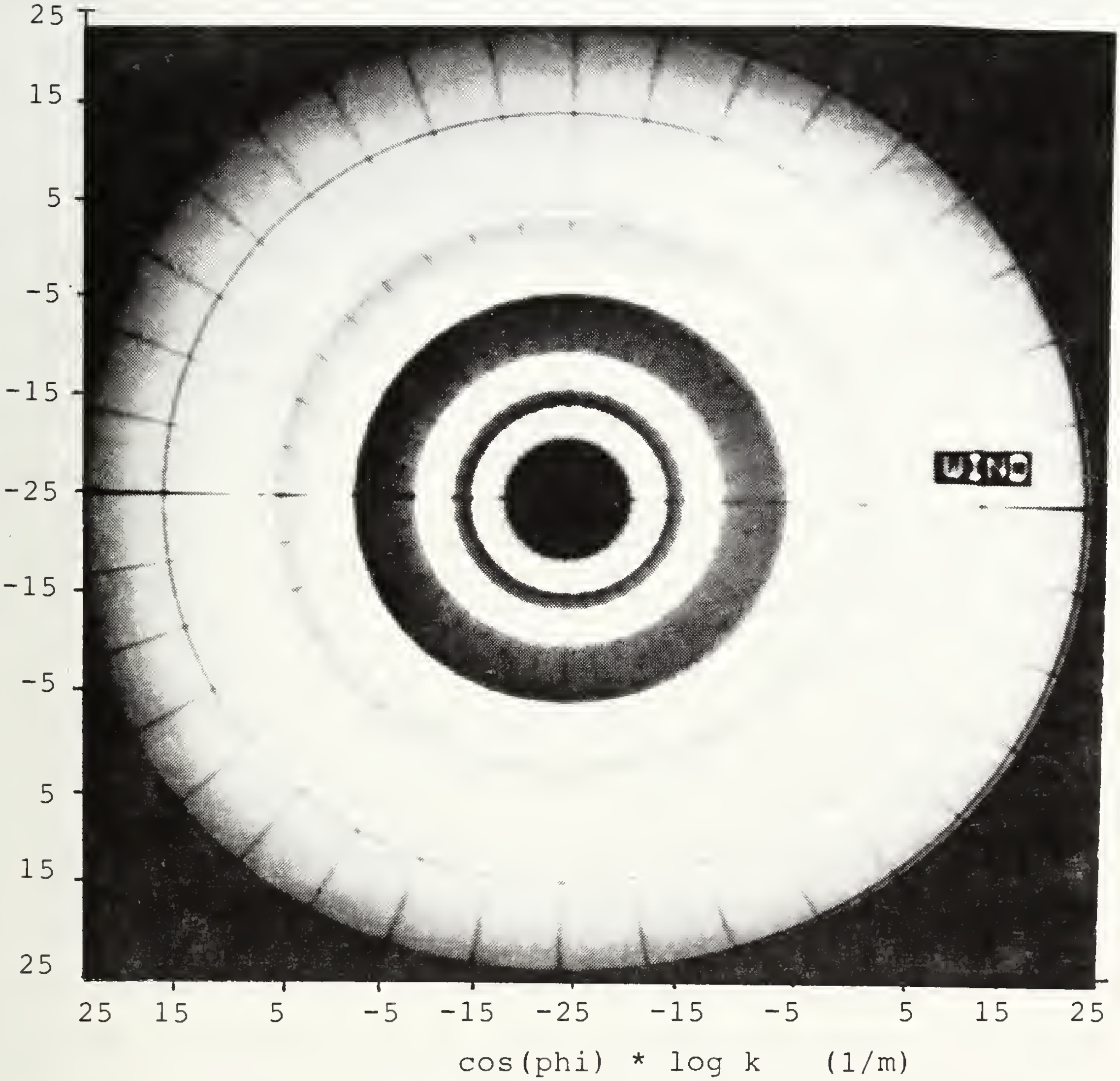

Figure 15. Spectral Density Image of Directional Dependence of Durden and Vesecky (Two-Sided) Wavenumber Spectrum for Wind Speed = 10m/s, phi = Wind Direction and k = wavenumber.

Lee (1982) to model the observed increase in cross-section azimuthal modulation with radar frequency; the coefficient c must be determined from measured quantities. Here, c is determined by forcing the cross-wind to upwind slope ratio to be equal to the Cox and Munk (1954) value for a clean sea surface. The azimuthal modulation of the cross-section produced by this directional spectrum is symmetric in the up and downwind direction, with minima exactly at the crosswind directions.Hydrodynamic modulation of the small-scale waves by the large-scale waves is accounted for by introducing a modulation parameter, *m*,

$$\Psi_s(k) = (1 + m s_u)\Psi(k) \qquad k > K_d \tag{95}$$

where s_u is the large-scale slope in the upwind direction (Jones, et al., 1978) and $\psi_s(k)$ is the high wavenumber portion of the wavenumber spectrum ($k>2$). The parameter, *m*, can be adjusted to "calibrate" the model to a particular data set; i.e., hydrodynamic modulation produces the upwind/downwind asymmetry in the azimuthal modulation and shifts the minima downwind from the crosswind directions (Li, et al., 1989).

The wind stress is related to the wind speed at 19.5m by the surface layer model of Large and Pond (1981) where the neutral drag coefficient at 10m defined by Large and Pond is first converted to a value at 19.5m. The corresponding wind stress is computed from equation (82) with the air-sea temperature difference used to compute the stability correction function, Ψ. The wind stress is then converted to a neutral wind speed at 19.5m by assuming z_0 has the functional dependence as derived by Cardone (1969) (73).[7] Fung and Lee (1982) point out that this equation is valid for $U_{19.5} > 3.5 m/s$. The D&V model produces erroneous results for wind speeds below this value.

Predictions of the cross-section with this model are reproduced in Figure 16a from Durden and Vesecky (1985). For a frequency of 13.9GHz and wind speed equal to 15m/s, the h-pol and v-pol calculated values are within 3dB of the observations obtained from Guinard (1971). However, the polarization ratio $\sigma_{VV} / \sigma_{HH}$ is larger than observed. The predicted upwind wind speed "power law" exponents are compared to the observations in Figure 16b. The predicted exponents for both polarizations show reasonable agreement with the observations with the greatest discrepancy at 20°.

4. The Donelan and Pierson model function (1987)

The Donelan and Pierson (D&P) (1987) model function also uses the quasispecular two-scale scattering theory as its basis; therefore, the same quantities as specified for the D&V model are required here. Some differences from the D&V model should be noted about the computation of ε, the dielectric constant, and R(0) the Fresnel reflection coefficient at normal incidence. The dielectric constant in the D&V model is computed directly, here it is assigned for a particular frequency, temperature and salinity from standard tables (Saxton and Lane, 1952). The polarization constants are then

---

[7] This expression for z_0 uses a different form for C_{DN} versus windspeed than that of Large and Pond. This discrepancy can be reconciled by recomputing the numeric constants in (73) using the data of Large and Pond.

A

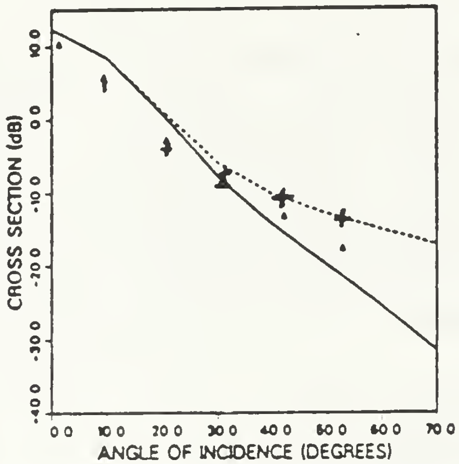

Variation of the normalized radar cross section (NRCS) with angle of incidence at 13.9 GHz and 15 m/s. (——) Calculated HH polarization. (---) Calculated VV polarization. Values were calculated at 10° increments. The Δ's are observed values for HH polarization, and the +'s are observed values for VV polarization [26].

B

K_u-BAND UPWIND WIND-SPEED EXPONENTS

Source	Angle of Incidence					
	0°	10°	20°	30°	40°	50°
Calculated HH pol.	-.69	0.15	1.40	1.61	1.69	1.74
Observed HH pol.[26]	-.36	0	1.00	1.65	1.98	1.93
Calculated VV pol.	-.69	0.14	1.38	1.53	1.57	1.60
Observed VV pol.[26]	-.46	0	1.05	1.68	1.77	1.96

Figure 16 (a) Cross-Section vs. Incidence Angle and (b) "Power Law" Wind Speed Exponent as a Function of Incidence Angle from the Durden and Vesecky Model (1985)

computed at one degree incidence angle increments using the standard dielectric constant to build a lookup table which is then interpolated for particular conditions. The Fresnel coefficient at normal incidence is multiplied in the D&P model by 0.65, as suggested by Valenzuela (1978), while in the D&V model it maintains its full value.

The full wavenumber spectrum in the D&P model is constructed by "patching" together two independently derived spectra for the low and high wavenumbers, separated at a wavenumber k_Γ. The low wavenumber end of the spectrum (for wavenumbers less than ten times the spectral peak) is proportional to the mean wind speed at 10m and was derived from an empirical analysis of wave data (Donelan, et al., 1985)

$$\Psi(k,\varphi) = \frac{1.62x10^{-3}\overline{U}(10)}{k^{3.5}g^{0.5}}\exp\left(-\frac{g^{2}}{k^{2}\left(1.2\overline{U}(10)\right)^{4}}\right)\left\{1.7^{F(\overline{U}(10),k)}h\left(\frac{k}{k_{p}}\right)\sec h^{2}\left[h\left(\frac{k}{k_{p}}\right)\varphi-\overline{\varphi}\right]\right\} \tag{96}$$

where $$F(\overline{U}(10),k) = \exp\left[-1.22\left(\frac{1.2\overline{U}(10)k^{0.5}}{g^{0.5}}-1\right)^{2}\right]$$

The peak of the spectrum, k_p for fully developed seas is given by

$$k_{p} = \frac{g}{1.2\overline{U}(10)^{2}} \tag{98}$$

The mean-square long wave slope is found by integrating this part of the spectrum using (27). Donelan and Pierson (1987) note that they were unable to reconcile the slopes determined from this spectrum to the Cox and Munk slope values; therefore, for internal consistency they used their integrated values.

The high wavenumber spectrum (at the Bragg wavelengths) is based upon a proposed balance between the energy input to the short waves by the wind to that dissipated through wave breaking and viscosity. The growth rate (wind input) is modeled by

$$\frac{\beta}{\omega} = 0.194\frac{\rho_{a}}{\rho_{w}}\left[\frac{\overline{U}\left(\frac{\pi}{k}\right)}{c_{p}\left(\frac{\pi}{k}\right)}-1\right]^{2} \tag{99}$$

where $U(\pi/k)$ is the mean wind speed just above the waves at a height of one-half the Bragg wavelength and $c_p(\pi/k)$ is the phase speed of the short waves. The normal stress is claimed to be more important in the amplification of the capillary waves (Kinsman, 1965) and is represented in (100) by the wind speed to phase speed ratio in the wind input term. The dissipation term is determined by the dimensional analysis outlined in Section D. The balance between wind input and dissipation then yields the high wavenumber spectrum:

$$\Psi_s(k) = k^{-4}\left[\frac{0.194}{\alpha}\frac{\rho_a}{\rho_w}\left(\frac{\overline{U}\left(\frac{\pi}{k}\right)}{c_p\left(\frac{\pi}{k}\right)}-1\right)^2 - \frac{4\nu k}{\alpha c_p(k)}\right]^{\frac{1}{n}} \tag{100}$$

where $\alpha=f_1(Tk^2/\rho_w g)$ and $n=f_2(Tk^2/\rho_w g)$. These coefficients are used to match the two pieces of the spectrum together and they are obtained from gravity wave spectra and radar data. The model spectra, computed for water temperatures of 0° and 30°, and various wind speeds are shown in Figure 17.

The directional dependence of the spectrum (Figure 18) is modeled as

$$\Phi(\varphi) = \mathrm{sec}h^2\left[h_1(\varphi - \overline{\varphi})\right] \tag{101}$$

where φ is the radar look direction, $\overline{\varphi}$ is the peak direction of the downwind traveling waves and h_1 is an empirically derived value that controls the spreading of the waves about the peak direction. The value of h_1 decreases for increasing wind speed; i.e., the waves spread out more about the wind direction. Also, h_1 keeps the two-dimensional spectrum from going to zero at $|\varphi - \overline{\varphi}| = \pi/2$.

The short waves are modulated by the longer waves by writing the modulation as a function of the downwind slope of the tilting waves, s_d, after Reece (1978):

$$\Psi_s(k) = \begin{cases} (1 - ms_d)\Psi(k) & |ms_d| \le \frac{1}{2} \\ (1 - 0.5sgn(ms_d))\Psi(k) & |ms_d| > \frac{1}{2} \end{cases} \tag{102}$$

where m is determined empirically. The modulation will cause an upwind/downwind asymmetry in the computed cross-section values. Here, D&P set m=1 to fit the model output to observed upwind/crosswind differences in the NRCS.

The remaining quantity to be specified is the wind speed parameter at height π/k, $U(\pi/k)$, where the value of π/k or $\lambda/2$ is O(2cm). Citing theoretical and empirical work, D&P maintain that the logarithmic profile of the mean wind extends to this small height above the surface and that at these heights atmospheric stratification effects will be negligible since the air-sea temperature difference approaches zero[8]. Therefore, the law of the wall is applied to obtain

---

[8] However, calculating $\overline{U}\left(\frac{\pi}{k}\right)$ from U(10) should still require stability correction if $(T_0 - T_{10})$ is nonzero, while $\left(T_0 - T_{\frac{\pi}{k}}\right)$ approaches zero.

$$\overline{U}\left(\frac{\pi}{k}\right)=\overline{U}(10)\left[1+\frac{(C_{DN})^{\frac{1}{2}}}{\kappa}\left(\ln\left(\frac{\pi}{10}\right)-\ln k\right)\right] \qquad (103)$$

where the neutral drag coefficient can be either of the empirical expressions as found by Large and Pond for the open ocean (88) or Donelan, for the lake, (89).

The radar cross-sections predicted using the D&P model increase with wind speed and are strongly influenced by water temperature at low wind speeds due to viscous dissipation of the short waves. In fact, a threshold wind speed dependence upon incidence angle and water temperature occurs at each wavenumber when dissipation balances input and the bracketed term in equation (100) equals zero. Below this threshold the viscosity inhibits the generation of the corresponding Bragg wave, the spectrum ceases to exist, and no backscatter is produced (see abrupt drop of the spectra in the lower part of Figure 17; see <2m/s Figure 19). Just above the threshold and up to approximately 10m/s for Ku band (Figure 19), the cross-sections over warmer water are several dB higher than over cooler water. Beyond 10m/s the influence of water temperature is not as apparent except for high incidence angles. At very high wind speeds (>30m/s) the cross-sections level off and "rollover," displaying a negative correlation with increasing wind speed. The authors propose that the decay is due to the decrease of $U\left(\frac{\pi}{k}\right)$ as U_{10} increases because of the increase in C_{DN} with U_{10}.

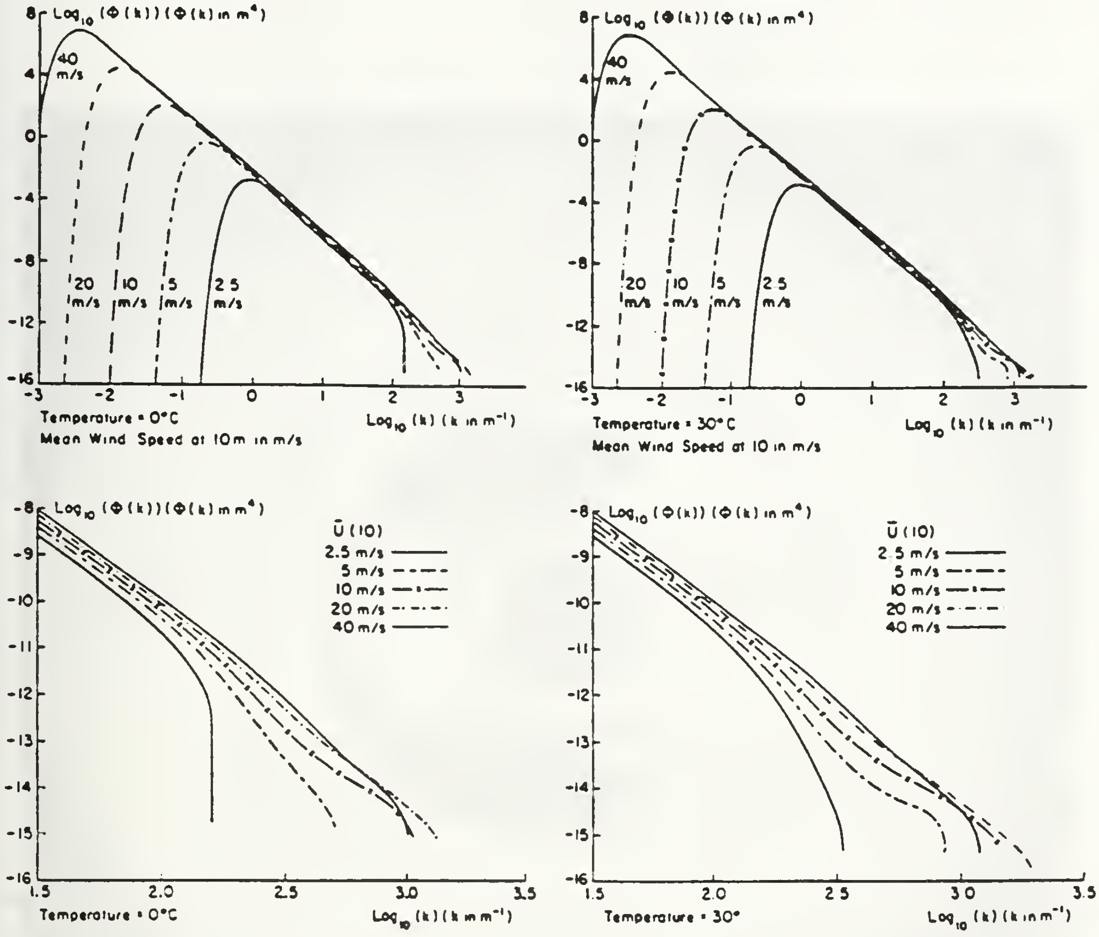

Sections through the wave number spectrum, $\Phi(k)$ in m^4 versus k per meter at upwind for mean wind speeds at 10 m of 2.5, 5, 10, 20, and 40 m s^{-1}. (top left) Full spectrum for 0°C water temperature. (Top right) Full spectrum for 30°C water temperature. (Bottom left) Details of spectrum of 0°C for $\log_{10} k$ greater than 1.5. (bottom right) Details of spectrum for 30°C for $\log_{10} k$ greater than 1.5.

Figure 17. Wavenumber Spectra from Donelan and Pierson Model (1987).

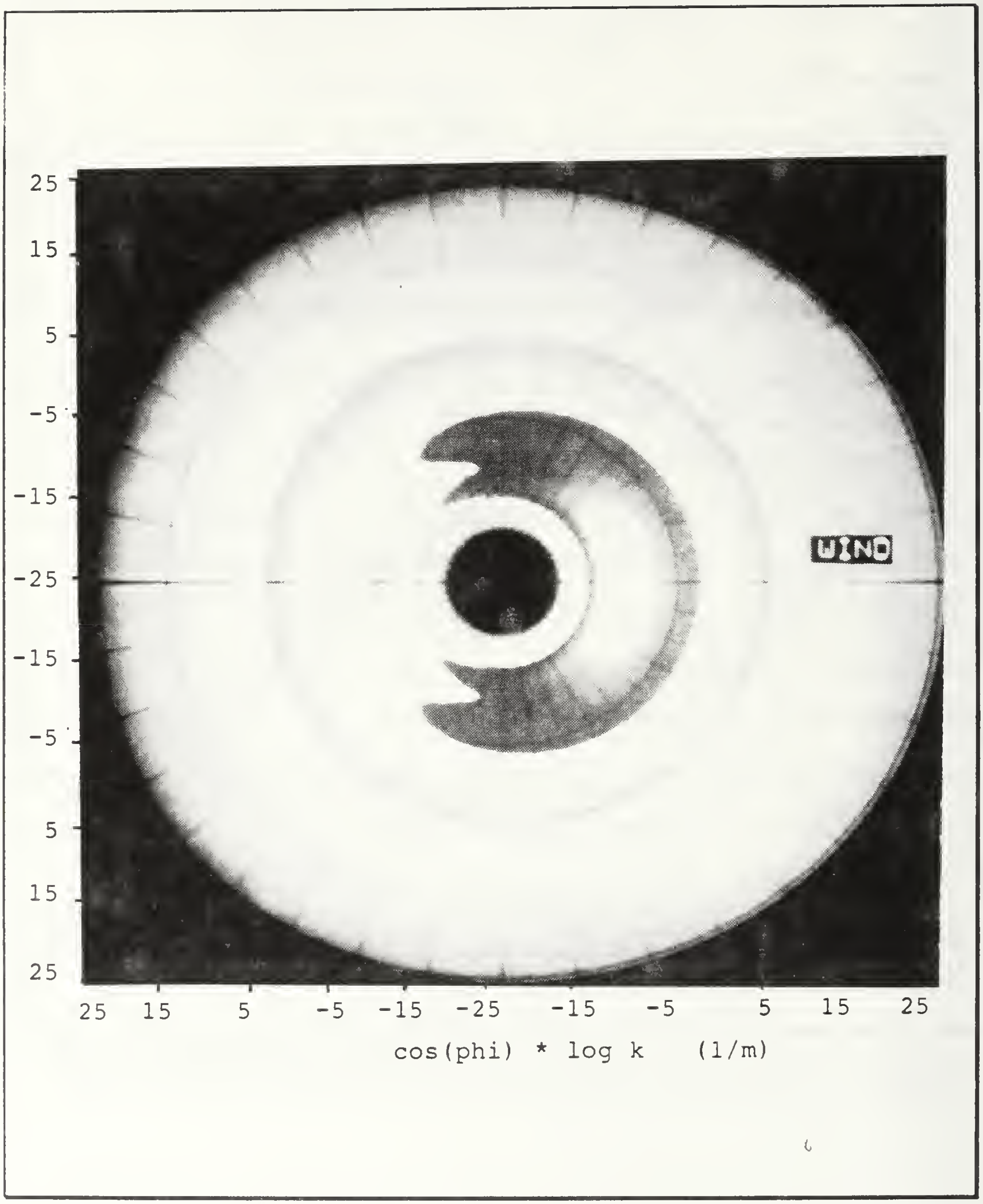

Figure 18. Spectral Density Image of Directional Dependence of Donelan and Pierson (One-Sided) Wavenumber Spectrum (from Verma, et al., 1989) for Wind Speed = 10m/s, phi = Wind Direction, and k = Wavenumber.

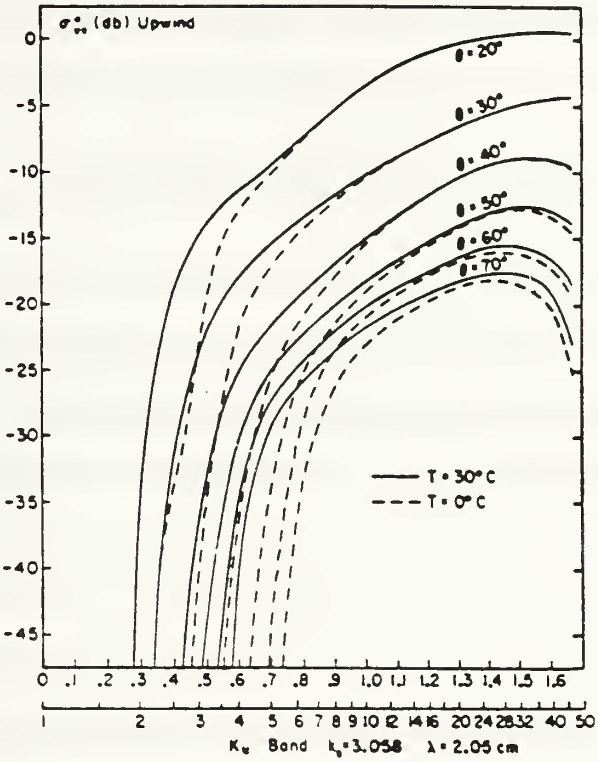

Vertically polarized backscatter for the two-scale model for K_u band at upwind with $\log_{10} \bar{U}(19.5)$ in meters per second on the abscissa and $\sigma_{VV}{}^{0}$ in decibels on the ordinate. The solid curves are for a water temperature of 30°C and the dashed curves are for a water temperature of 0°C. θ is the incidence angle. The auxiliary scale is the wind speed at 19.5 m in meters per second.

Figure 19. Predicted Cross-Sections Against Wind Speed for Different Temperatures (from Donelan and Pierson, 1987).

5. The Plant Model (1986)

Plant (1986) noted that the existing model functions did not include an explicit accounting of the nonlinear interactions between the short Bragg waves and the longer dominant waves. To examine the possible dependence of σ° on the long-wave, short-wave interactions, Plant (1986) applies the principle of conservation of wave action to develop a spectral model for the short, wind generated waves. Defining short wave action as $N(\mathbf{k},\mathbf{x},t) = \rho c(\mathbf{k})\psi(\mathbf{k},\mathbf{x},t)$ for the short wavenumber **k**, the governing equation is

$$\frac{\partial N}{\partial t} + \left(\mathbf{c}_g \cdot \mathbf{U}\right) \cdot \frac{\partial N}{\partial x} - \frac{\partial}{\partial x}(\mathbf{k} \cdot \mathbf{U}) \cdot \frac{\partial N}{\partial \mathbf{k}} = \beta N + D \tag{104}$$

where $\mathbf{c}_g$ is the group velocity, **U** the horizontal current due to the orbital velocity of longer waves and D is a decay term which includes dissipation, short wave-wave interactions and wind-wave interactions. The form of D is found by dimensional analysis to be a function of $k^4\Psi(\mathbf{k})$ as in equation (59), Section D.

The long wave modulation of the short waves is then modeled by writing the wave action as N = <N>(1+M) where <N> is the average action density and M is a term representing the modulation transfer function (MTF) of the long wave-short wave interactions. Equation (104) is ensemble averaged to yield an equation for the average action balance among long wave-short wave interactions, wind input and dissipation. Expanding <N> in a power series of s^2, the mean square long wave slope, solving for the zeroeth and first order, and substituting the spectral definition for N yields the following form for the short wavenumber spectrum:

$$\Psi(\mathrm{k}) = Ak^{-4}\left[\frac{\beta}{\omega} + \frac{m_i}{\omega}\Omega s^2(1 + \gamma_0 + \gamma_1)\cos(\theta_s - \theta_L)\right] \tag{105}$$

where k, K are the short (long) wavenumbers; ω, Ω are the short (long) wave frequencies; m_i is the imaginary part of the modulation transfer function; s^2 is the long wave slope; θ_S, θ_L are the short and long wave directions and $\gamma_0 = f(k, K, N_0)$ and $\gamma_1 = f(k, K, m_i)$.

To evaluate $\Psi(\mathbf{k})$ further requires a form for the wave growth β, chosen here to be (Plant, 1982)

$$\beta = \begin{cases} 0.04\dfrac{u_*^2}{c_p}\omega\cos(\theta_s - \theta_{wind}) & ; \quad |\theta_s - \theta_{wind}| < \dfrac{\pi}{2} \\ 0 & ; \quad elsewhere \end{cases} \tag{106}$$

The wavenumber spectrum is functionally dependent on friction velocity, long wave slope and the angular variation of the short wave growth. The azimuth variation of the cross-section arises primarily from this cosine dependence in the growth term with a smaller contribution from the modulation term.

Plant (1986) assumes neutral conditions and uses the neutral drag coefficient of Large and Pond (1981) to determine u_* from equation (86) using a range of assumed wind speeds at 10m. The mean square slope of the long waves in equation (105) is estimated from the Cox and Munk (1954) values for a slick-covered surface, equation (29). The difference in wind speed between 12.5m and 10m is ignored[9].

The spectrum is used in the composite surface expression for σ° to yield cross-sections with incidence angle, azimuth angle, polarization and wind speed dependences. For the purposes of this preliminary model, Plant considers only the pure Bragg scattering regime; therefore, the model applies only at incidence angles between 20° and 60° incidence angles. The predictions of Plant's model compare most favorably with SASS1, SASS2 and aircraft data at incidence angles between 30° and 50°. The predicted h-pol values are typically low and the crosswind values fall well below the data at 25° incidence angle and at low wind speeds (Figure 20a). The cross-section was found to increase with long wave slope but not as much as observed (Keller, et al., 1985). Plant concludes that the most important variables to be understood for further progress to be made in scatterometry algorithms are short-wave growth rates and the surface wind stress. Since these are derived quantities, the fundamental variables implicated in this statement are viscosity, atmospheric stability and long wave slopes (Geernaert, et al., 1986).

---

[9] The slope equation published in Plant (1986) and that used in the model program are inconsistent. Since the code uses the Cox and Munk values (equation 29) and the diagrams in the paper are produced from the code, it is assumed here and verified by Plant (pers. comm.) that (29) was the correct equation.

G. SUMMARY

The theoretical understanding of the physical basis for scatterometry requires working knowledge in the interrelated theories of electromagnetic scattering, ocean wave dynamics and air-sea interactions. The scattering of electromagnetic radiation from evolving, random surfaces leads directly to the most poorly understood, but currently, most actively researched problems in ocean wave dynamics: wave generation by the wind, nonlinear interactions, wavebreaking and long wave-short wave modulations. The presence of the moving waves affects the air flow above them and also precludes direct measure of the stress on the surface. Therefore, the connection of the winds to the waves is accomplished indirectly in air-sea

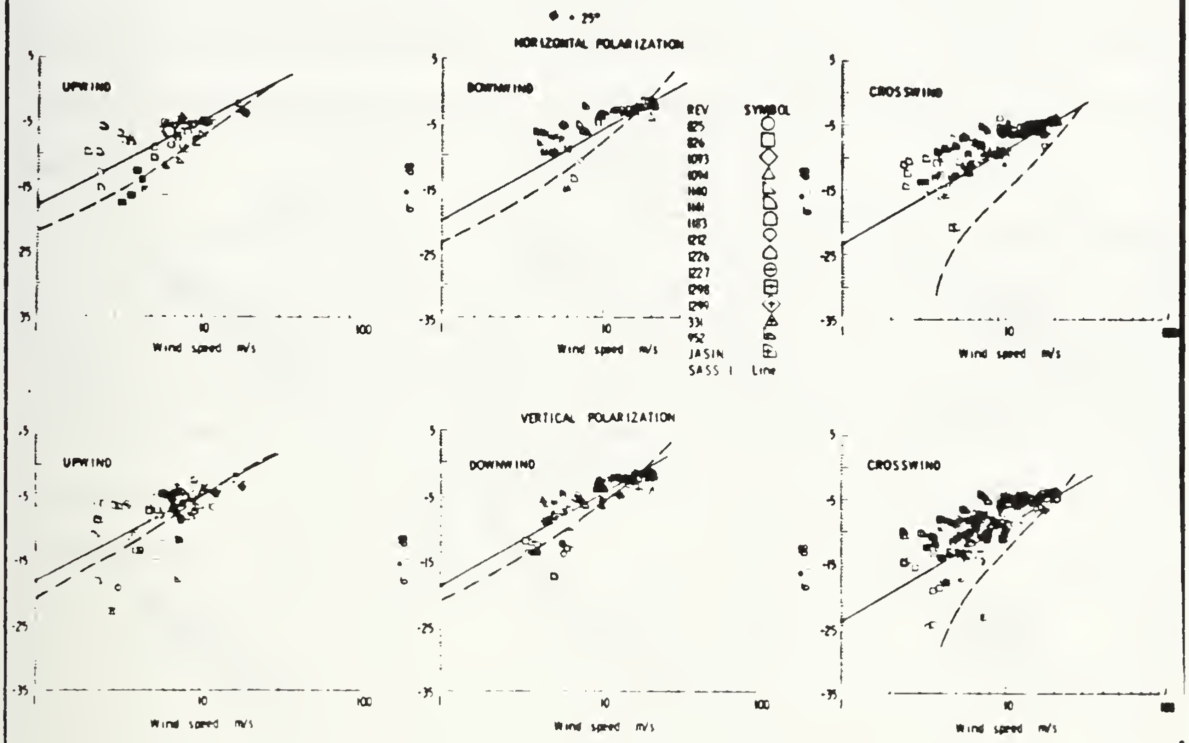

Figure 20a. 25° Incidence Angle. Comparison of Predictions of Plant Model with K_u Band Data Given by Schroeder et al. [1982] and the SASS 1 Model Function. Data Points are those Seasat Cross Sections which Could Be Associated with Good Surface Measurements of Wind. Solid Lines Represent the SASS 1 Model Function, While Dashed Lines Represent Predictions of the Plant Model (from Plant, 1986).

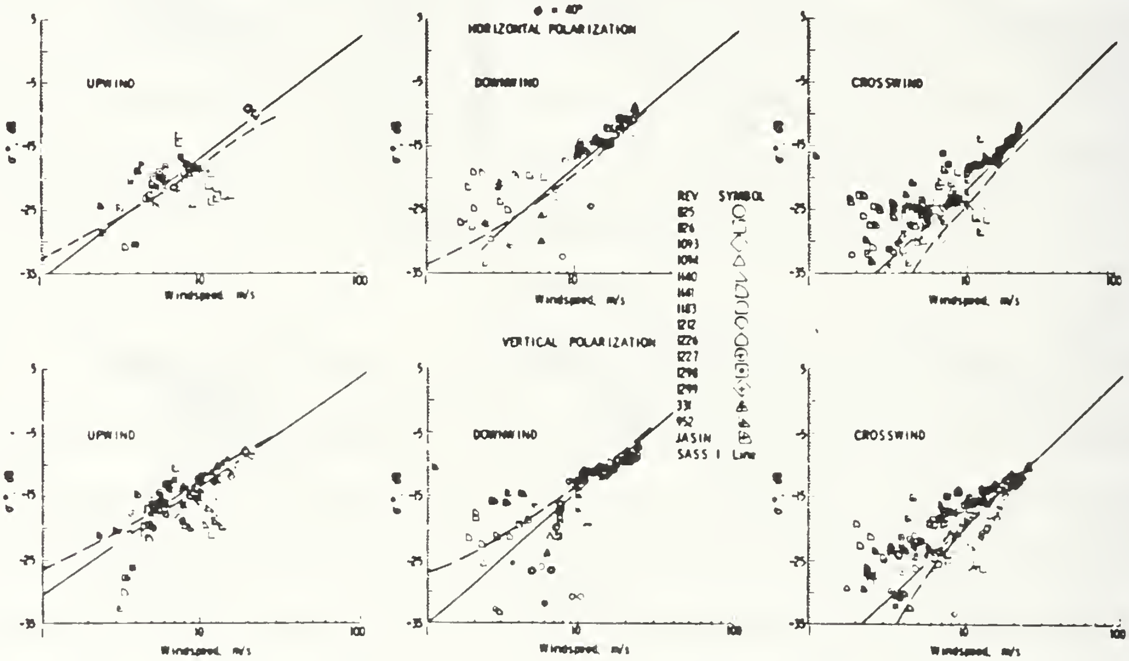

Figure 20b. 40° Incidence Angle. Comparison of Predictions of Plant Model with K_u Band Data Given by Schroeder et al. [1982] and the SASS 1 Model Function. Data Points are those Seasat Cross Sections which Could Be Associated with Good Surface Measurements of Wind. Solid Lines Represent the SASS 1 Model Function, While Dashed Lines Represent Predictions of the Plant Model (from Plant, 1986).

interaction theory by the parameterization of the surface roughness in terms of a drag coefficient or roughness length. These quantities are themselves functions of the wave state, wind speed and atmospheric stratification. Since the wind stress is of central importance to ocean circulation studies, wave dynamics and remote sensing an entire body of literature which documents attempts to define appropriate parameterizations has sprung up in the past decade.

The authors of the model functions described in this chapter attempt to consolidate into a scatterometer model function current information regarding the intertwining theories. In the process, certain environmental parameters are identified which may affect the radar cross-section. It now remains to be seen if the proposed dependencies are supported by observations.

TABLE III. MATRIX OF MODEL FUNCTION CHARACTERISTICS

MODEL (Author)	SCATTERING THEORY	INTRINSIC RADAR PARAMETER	WAVE THEORY	SURFACE LAYER MODEL	COMMENTS
SASS1 SASS Team (1980)	"Power law"/cosine statistical fit of aircraft scatterometer and in-situ measurements (RADSCAT, JASIN GOASEX)	0°-70° Incidence Ku-band Only Symmetric in azimuth; minima at 90°, 270°	None	Kondo (1975) model enters implicitly in the conversion of in-situ windspeed to $U_N(19.5)$ See Boggs (1981)	See problems noted in text, p.3
SASS2 Wentz, et al. (1984, 1986)	"Power law"/cosine statistical fit to SEASAT data	0°-70° incidence Ku-band only Symmetrical in azimuth	None	Assumes global wind speed has a Rayleigh distribution, wind direction is uniformly distributed	
Durden & Vesecky (1986)	Quasispecular Two-Scale Model Scattered Fields computed numerically	0°-70° incidence All frequency Symmetric in azimuth Requires T_{SEA}, Salinity for dielectric constant	$\psi(k)=S(k)\Phi(\varphi)$ $S(k)$: Pierson-Moskowitz spectrum low wavenumbers; stress dependence at high wavenumbers $\Phi(\varphi)$: $\cos 2\varphi$ dependence, effective only near Bragg wavenumber Linear modulation of high wavenumbers using Cox & Munk (1954) clean sfc slopes	Large & Pond drag coefficient Cardone z_0 corrects for stability $\varphi(z/L)$ needs T_{AIR}, T_{SEA}	Produces erroneous results for U<3.5 mps due to Z_o. Extension of basic wave model by Fung & Lee (1982)

TABLE III. MATRIX OF MODEL FUNCTION CHARACTERISTICS (CONT.)

Plant (1986)	Two-Scale Bragg-scattering domain only	20°-60° Incidence All frequency Symmetric in azimuth Constant dielectric constant = 81	$\psi(k)$ derived from balance of terms in wave action equation; magnitude and directional dependence arises from cosine form of wave growth parameterization. Uses Cox & Munk (1954) slick covered slope equation to estimate long-wave slope	Neutral Conditions, Large & Pond drag coefficient	Predicts σ° has a long wave slope dependence
Donelan & Pierson (1987)	Quasispecular Two-Scale	0°-70 Incidence All frequency Symmetric in Azimuth Look up table for dielectric constant, requires T_{SEA}, Salinity.	$\psi(k)=S(k)\Phi(\varphi)$ S(k): Donelan (1985) spectrum for low wavenumbers; balance of wind input with wave breaking and viscous dissipation at high wavenumbers $\Phi(\varphi)$: Sech^2 (wind-wave angle) Linear modulation of high wavenumbers using slopes determined from integration of empirical/theoretical spectrum	Neutral conditions Large and Pond or Donelan drag coefficient uses Neutral wind at $\frac{1}{2}$ Bragg wavelength	Predicts water temperature, wind speed, dependent threshold wind speed for σ°.

III. THE LAKE ONTARIO WAVES '87 EXPERIMENT

A. INTRODUCTION

The hypothesis of this study is that the radar cross-section varies with the wind vector and other environmental parameters; in particular, atmospheric stratification, long wave slope and water temperature. Experiments were conducted in 1986 and 1987 from an instrumented, moored tower in Lake Ontario in order to obtain the data necessary to test the hypothesis above. The fundamental measurements included wind speed and direction, air-water temperatures, relative humidity, radar cross-section and wave spectra. The purpose of this chapter is to describe the experiment and instruments by which these measurements were obtained.

B. THE EXPERIMENTAL SITE

The data analyzed in this study were acquired between 11 November and 12 December 1987 from an instrumented, bottom-mounted tower at the western end of Lake Ontario, near Hamilton, Ontario (Figure 21).[1] The tower, constructed by the Canada Centre for Inland Waters, has been in nearly continual use since 1976 for wave and air-water interaction research.

As described by Donelan et al. (1985, p. 515), the tower is positioned 1.1 km offshore at a location with the following characteristics :

---

[1] Selected data from the WAVES 86 experiment are also used in some of the analyses which require a longer averaging interval or to augment the range of environmental conditions.

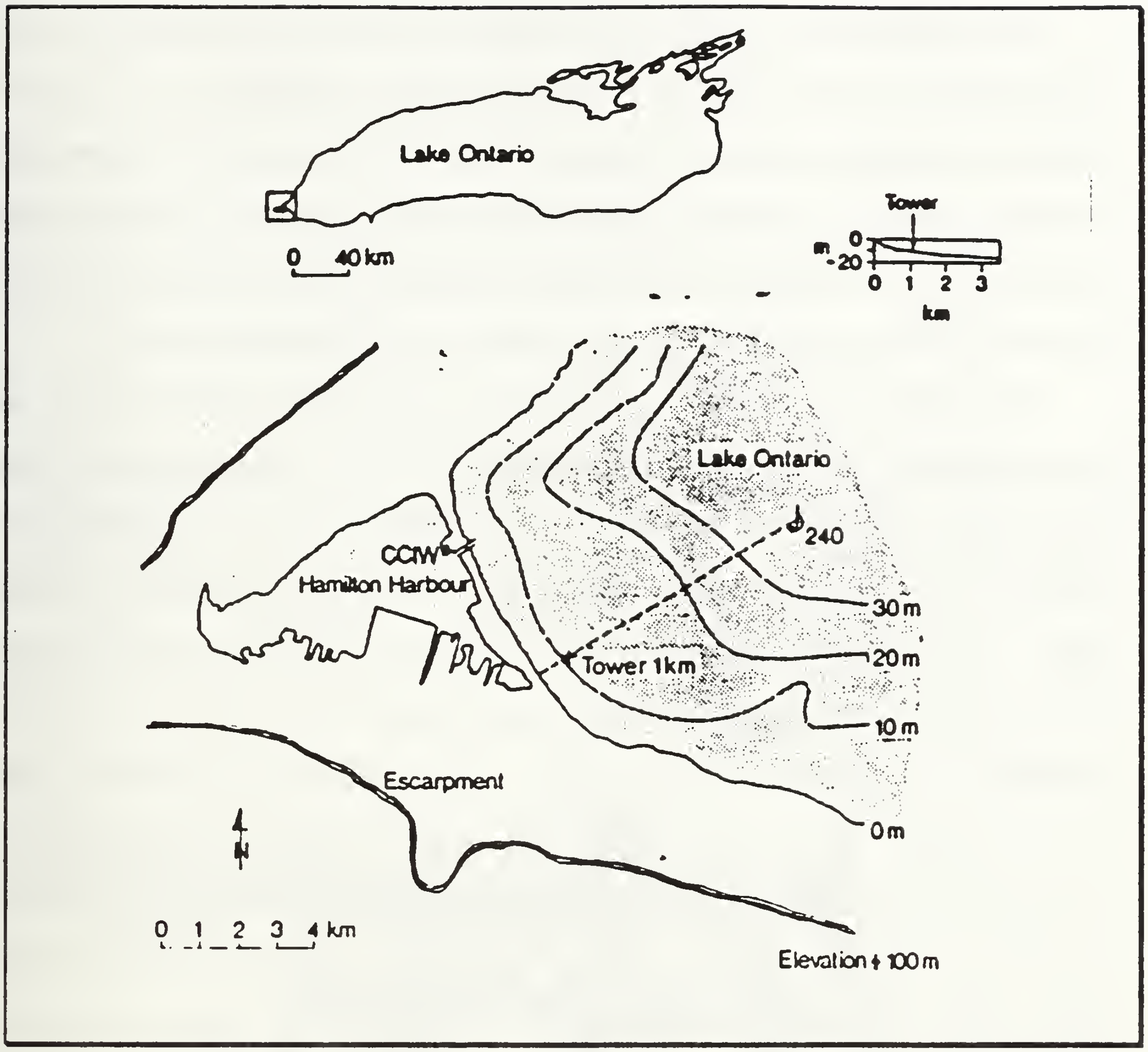

Figure 21. Map Showing the Location of the Research Tower in Lake Ontario and the Shore-Normal Profile in the Vicinity of the Tower (Donelan, et al., 1985)

> ...the bottom slopes relatively rapidly (about 11 m/km) from the shore to the location of the tower at 12 m depth; whereas at and beyond the tower, the bottom slope is gentle (1.5 m / km). In addition, the shoreline is very straight and the bottom contours are parallel for 3 km in both directions. The annual variation in water level is less than 0.5 m; tides, seiches and wind set-up change the water level by, at most 0.1 m; there are no significant tidal or seiche currents, and other less organized currents are typically less than 10 cm/s.

The structure is of a bilevel design (Figure 22) with an upper deck (100 m^2) constructed of open grating to minimize flow distortion, and a lower walkway four meters above the water surface. At the center of the upper deck is a mast on which the meteorological sensors are mounted; at the foot of the mast is the data acquisition system (DAS) housing. Power to the tower (6 KW at 600 V) is supplied from an onshore source via an underwater cable.

During the WAVES 87 experiment environmental conditions at the tower exhibited the ranges summarized in Table IV. Comparison of these values with climatology shows that the environmental conditions were typical of late autumn in Lake Ontario (Great Lakes Climatological Atlas, 1986). To give an overall perspective to the experiment, the average values of air and water temperatures, air/water temperature difference, relative humidity, wind speed and wind direction for each run are plotted as time series in Figure 23. An unusually warm weather period which occurred during the week of 11 November 1987 (Days 5-10, Figure 23a) greatly expanded the range of air-water temperature differences beyond the climatological norm. The air - water temperature difference was mostly negative during the next two weeks of the experiment and the final week had several days of relatively warm air temperatures. The relative humidity was quite variable, ranging from 40 to 100%; precipitation is noted for those days which show a constant 90% value (see Figure 23b, Day 14). Only moderate wind speeds less than 15m/s were measured in the part of the data set currently available to

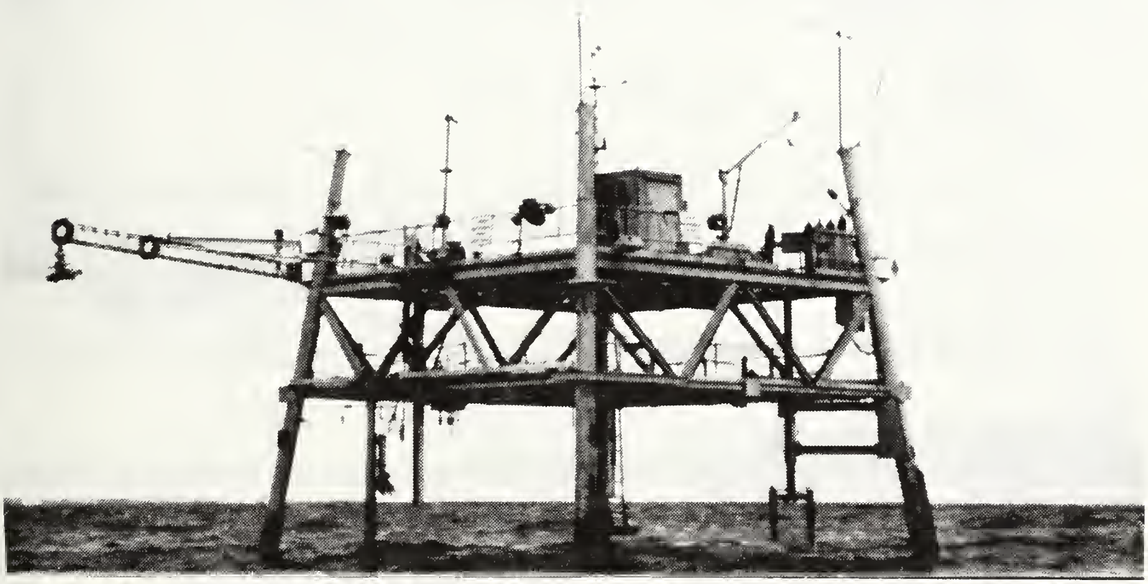

Figure 22. Photograph of the CCIW Tower Configured for WAVES'87.

TABLE IV. SUMMARY OF ENVIRONMENTAL CONDITIONS DURING THE WAVES'87 EXPERIMENT

Air Temperature	-10 to 17° C
Water temperature	3.8 to 7.0° C
Air-water temperature difference	-13.8 to 9.6° C
Relative humidity	40 to 100%
Wind speed	< 15 m/s
Wind direction	all directions except 90-180°
Significant Wave Height	< 3 m

Wind speed	< 5 m/s	5 - 7.5 m/s	>7.5 m/s
No. of data runs	39	40	47

Fetch	Short	Long
No. of data runs	100	26

(as determined from wind direction: long fetch cases occur when the wind direction is between 57 and 83 deg T)

Stability	Unstable	Neutral	Stable
	$\Delta T-0.5$	$\lvert \Delta T \rvert<0.5$	$\Delta T>0.5$
No. of data runs	56	8	62

(here, an indication of stability is given by the air-water temperature difference)

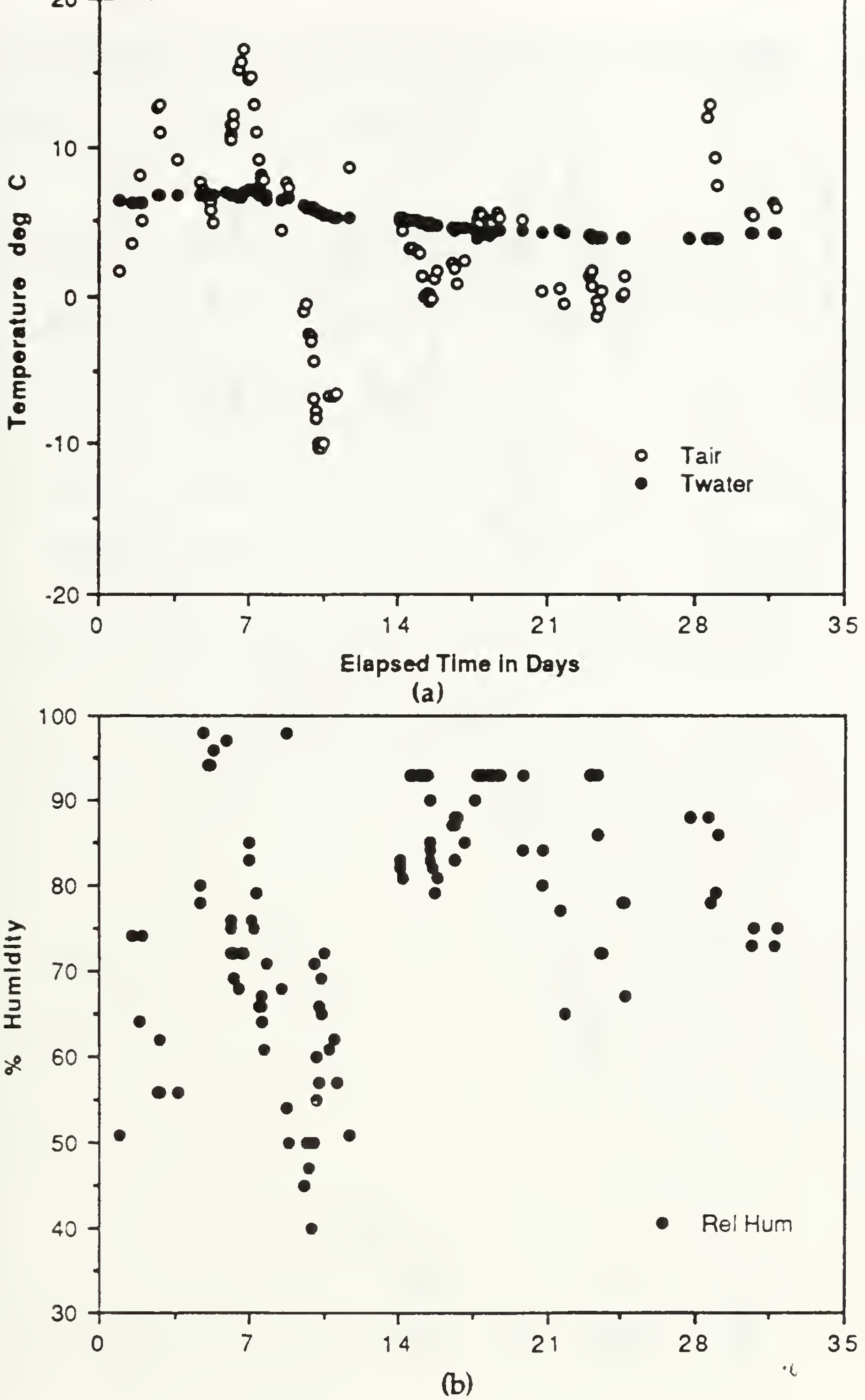

Figure 23. Average Environmental Conditions During WAVES 87 vs. Time (a) Air-Water Temperature, (b) Relative Humidity

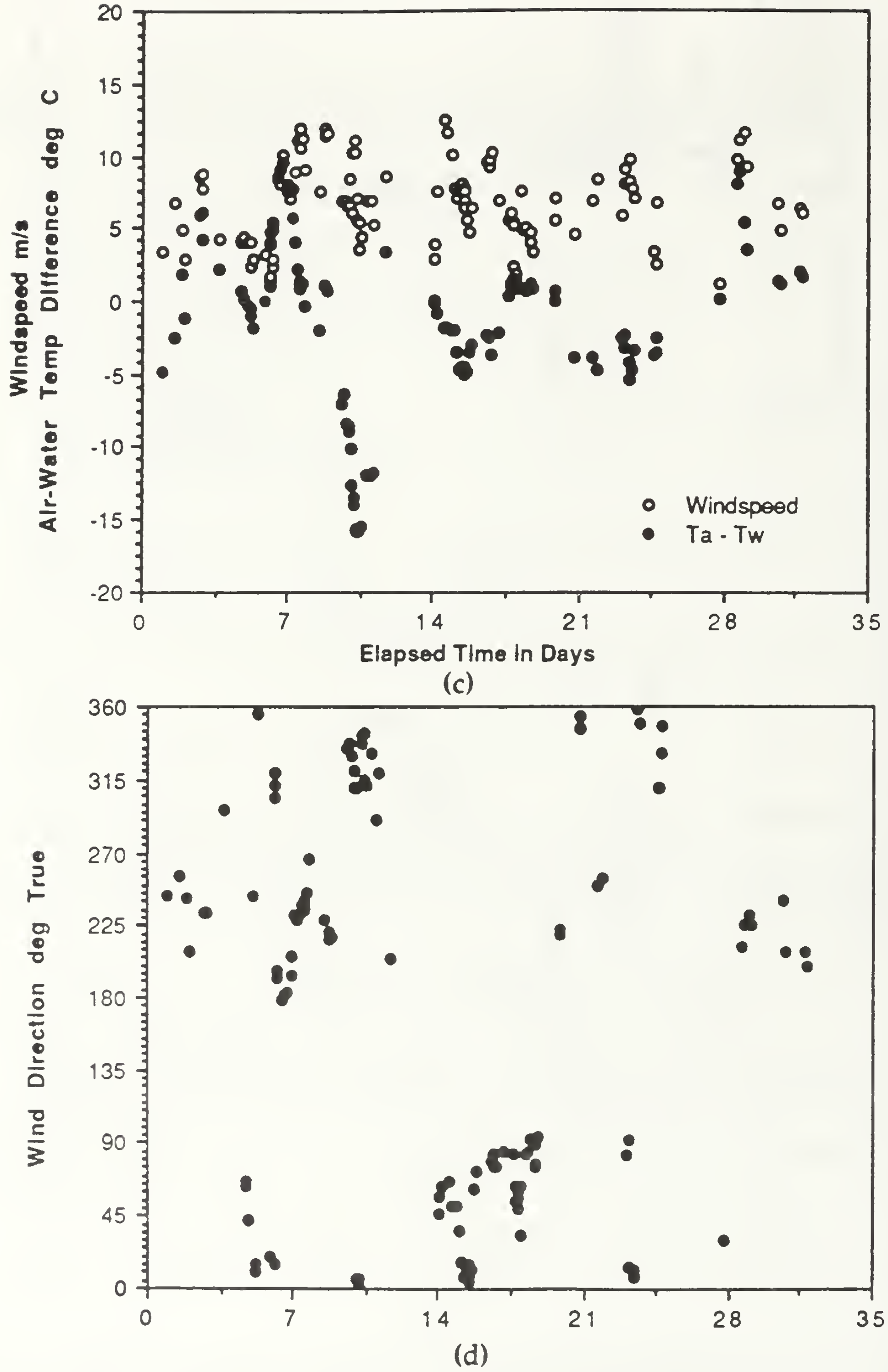

Figure 23. (Cont.) (c) Wind Speed and Air-Water Temperature Difference, and (d) Wind Direction.

the author (Figure 23c)[2]. A feature to note is that there were no winds from the southeast quadrant of the compass (90° to 180°).

C. MEASUREMENTS AND INSTRUMENTATION

1. Normalized Radar Cross-Section from the Microwave Scatterometers

The intrinsic and operating characteristics of the NRL scatterometers are described in Table V. There were two dual-pol, continuous wave, coherent microwave radars used in the experiment, one operating at 14 GHz frequency (Ku-band) and the other at 5 GHz (C-band). The received signal is beat down by a local oscillator to a 60 MHz intermediate frequency (IF) offset. This signal is then run into an IF amplifying circuit which passes the full bandwidth and beats down the signal to zero audio frequency (baseband). The final filter on the system passes frequencies between 3 dB power points at 1 Hz and 1.7 Khz. The filter removes dc antenna feedthrough at the low frequencies and noise at the high frequency end while allowing passage of the full Doppler bandwidth in-between the half-power points. Because there was a limit of 48 data communication channels available to telemeter data from the tower, only the amplitude modulated signal from the scatterometers was retained. This signal is proportional to the fields received by the antennas averaged over 0.6 msec due to the filtering. Thus, upon calibration and squaring, the signal provides the radar cross-sections as desired, but it does not allow discrimination of the Bragg scatterers as can be obtained through analysis of Doppler frequency shifts in the frequency modulated signal.

---

[2] A storm event occurred during the last week of the experiment for which the wind speeds exceeded 15m/s; however, the radar data from these last few runs have not yet been processed.

The Ku-band scatterometer was mounted on an antenna rotator and then extended on a boom 7.6 m from the tower and 7.6m above the water surface (Figure 24). The rotator varies the azimuth angle of the radar in a windshield wiper fashion, omitting those angles at which the beam intersects the tower. One 300 degree sweep is made every ten minutes by stepping five degrees in azimuth approximately every ten seconds. The incidence angle of the radar was also varied in the sequence summarized in Table V in order to cover the entire range of reflection angles from specular to grazing. The C-band radar was mounted on the tower railing 8.2m above the water surface at 45° incidence angle and 250° T (from true North) (Figure 25)[3].

The two microwave systems are illustrated schematically in Figure 26. The Ku-band radar consisted of a dual-pol, 15 cm circular horn transmitter and two rectangular horn receiving antennas, one for each polarization. The longer wavelength C-band antenna requires a larger antenna, hence this system was composed of a 61 cm dual-pol parabolic reflector, and two rectangular horn receiving antennas[4]. A 0.8 cm lucite septum was inserted at

---

[3] The original intent was to have the 5GHz radar on the rotator alongside the 14GHz radar. Due to weight limitations on the rotator, the ideal arrangement of two rotating scatterometers was abandoned and the 5GHz radar was fixed on the railing.

[4] The rectangular horns were used as receivers instead of a second parabolic dish in order to reduce the physical size of the system and to eliminate cross-talk between the antennas. This was an important consideration for the tower-based radars since they were not continuously monitored throughout the experiment.

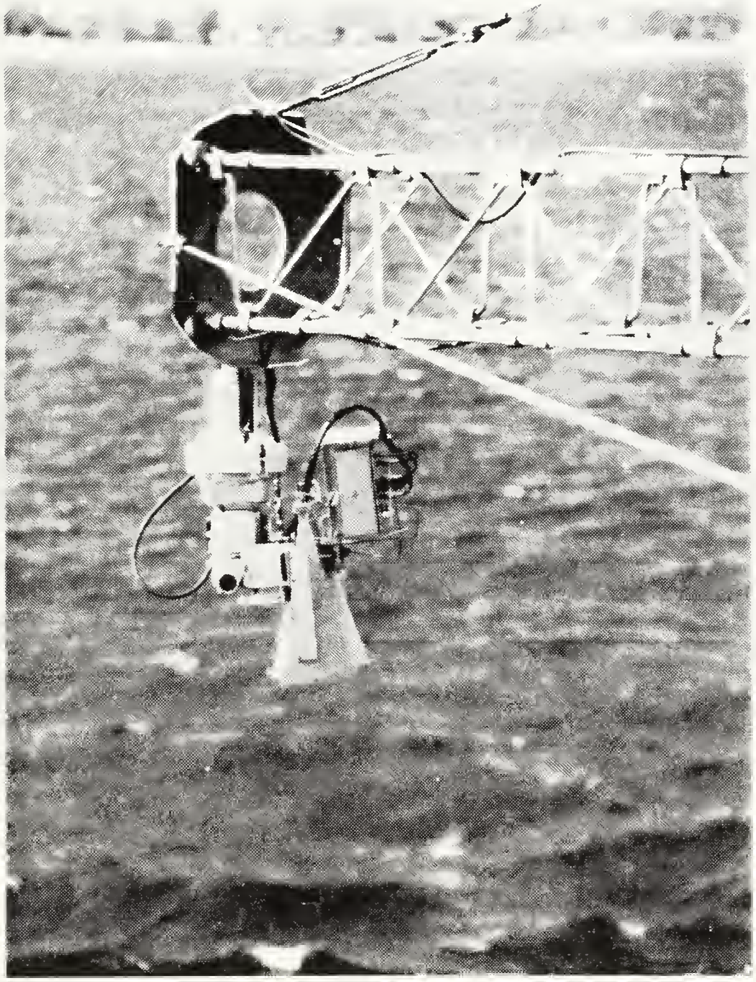

Figure 24. Ku-Band (14 GHz) Radar System Installed on the Boom

TABLE V. CHARACTERISTICS OF THE NRL RADARS

FREQ GHz	MEASURED VARIABLE	WAVE LENGTH	BRAGG WAVE 20 40 60 80	H or VPOL	DYNAMIC RANGE
Ku-band (14.0)	NRCS	2.14	3.1 1.6 1.2 1.1 all cm	dual	72 dB
C-band (5.0)	NRCS	6.00	4.2 cm at 45 deg	dual	72 dB

AZIMUTH ANGLE VARIATION

Ku-band scatterometer sweeps through approx 300 deg every ten minutes, from 95 through 0 to 30 deg T.

C-band scatterometer is fixed at 250 deg T.

INCIDENCE ANGLE VARIATIONS

	Recording Period	Angle	Comment
Ku-band radar	5 minutes	0	Specular reflections
	10 minutes	10	"Calibration" angle no wind speed dependence
	20 minutes	20	Spec/diffuse (soft) boundary
	"	40	Diffuse (Bragg) scatter
	"	60	Diff/grazing (soft) boundary
	"	80	Grazing angle reflections (system noise evaluation)
	95 min continuous run		
C-band radar	Fixed on tower railing at 45°.		

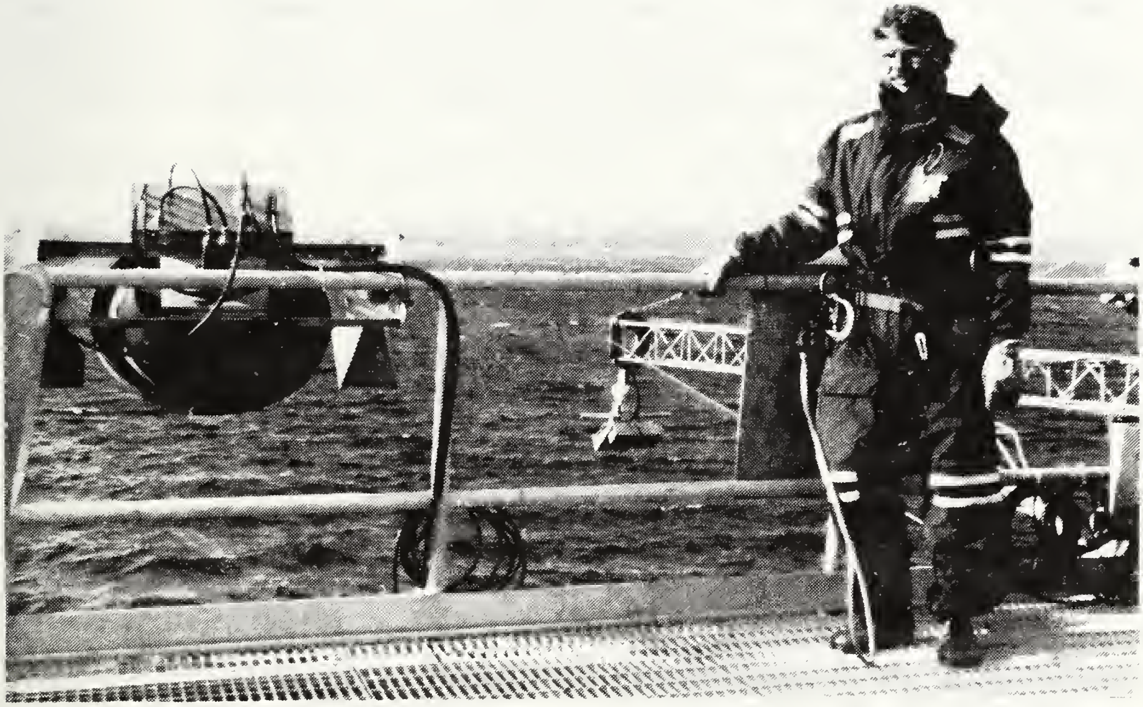

Figure 25. C-Band (5 GHz) Radar System Mounted on the Tower Railing Facing Southwest

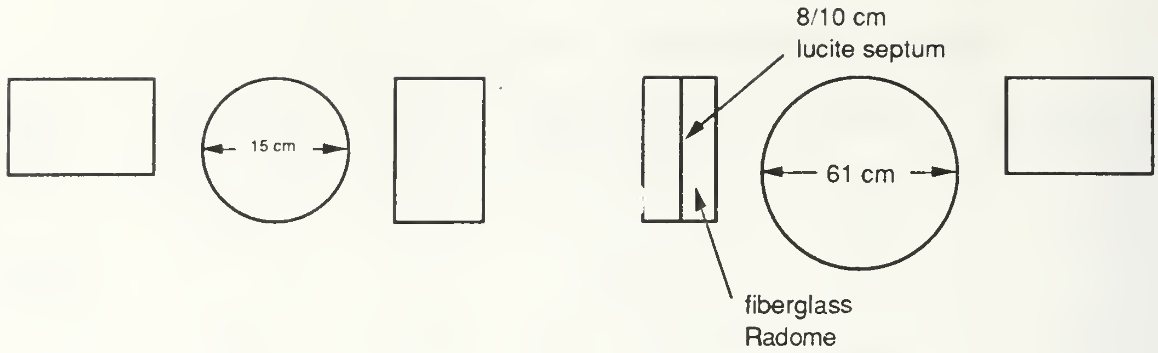

Coordinates: 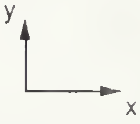

	VPOL Receiver Rectangular Horn		Dual-Pol Transmitter Circular Horn		HPOL Receiver Rectangular Horn
Φ_y	12.6°		9.1°		
Φ_{y2}		7.3°			
Φ_x	10.6°		7.7°		
Φ_{x2}		6.2°			
Φ_y			7.7°		10.6°
Φ_{y2}				6.2°	
Φ_x			9.1°		12.6°
Φ_{x2}				7.3°	

14.0 GHZ Ku-Band System

Coordinates: 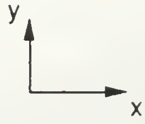

	HPOL Receiver Rectangular Horn		Dual-Pol Transmitter Parabolic Reflector		VPOL Receiver Rectangular Horn
Φ_y	21°		7.3°		
Φ_{y2}		6.6°			
Φ_x	21°		6.6°		
Φ_{x2}		5.3°			
Φ_y			5.5°		21°
Φ_{y2}				5.0°	
Φ_x			7.5°		21°
Φ_{x2}				7.0°	

5.0 GHz C-Band System

Figure 26. Configuration and Half-Power Full Beam-Widths of the Microwave System Antennas. Φ_y is the Vertical Beamwidth and Φ_x is the Horizontal Beamwidth

the midpoint of the h-pol receiving antenna to match its antenna pattern to that of the v-pol receiving antenna.

The mainbeam and first sidelobes of the C-band transmitting antenna and the h-pol receiving antenna are shown in Figure 27. The half power beamwidth (HPBW) of the transmitting antenna (width of beam 3 dB below peak) is 5.5° while the receiving antenna has a considerably wider beamwidth of 21°. The wider pattern is used in conjunction with the narrow transmitting pattern since it allows for some alignment error when attempting to focus the individual beams on the same illumination area.

The first sidelobes of the transmitting antenna are about 15 dB below the peak and 9° off the main beam direction. The receiving antenna sidelobes are approximately 19 dB below the main peak and 56° off the mainbeam. These two patterns are combined into a (h-pol) two-way pattern using the principle of multiplication of antenna patterns to yield the solid line shown in the figure. Here it is seen that the disadvantage of the wider receiving pattern is that it does not suppress the sidelobes as much as would a narrow main beam with sidelobes matched in position to those of the transmitting antenna. In the two-way pattern the HPBW is 5.5° and the first sidelobes are 9° off and approximately 17 dB below the main lobe. This implies that the radar cross-section must vary by 17 dB in only 9° in order for the sidelobes to significantly contaminate the total cross-section measurement. The v-pol two-way pattern is the same as the h-pol pattern since the two receiving antennas have the same one-way pattern. A similar analysis of the Ku-band system gives a vertical by horizontal HPBW of 7.3° by 6.2° for the mainlobe, and first sidelobes 26 dB below and 9° off the main peak.

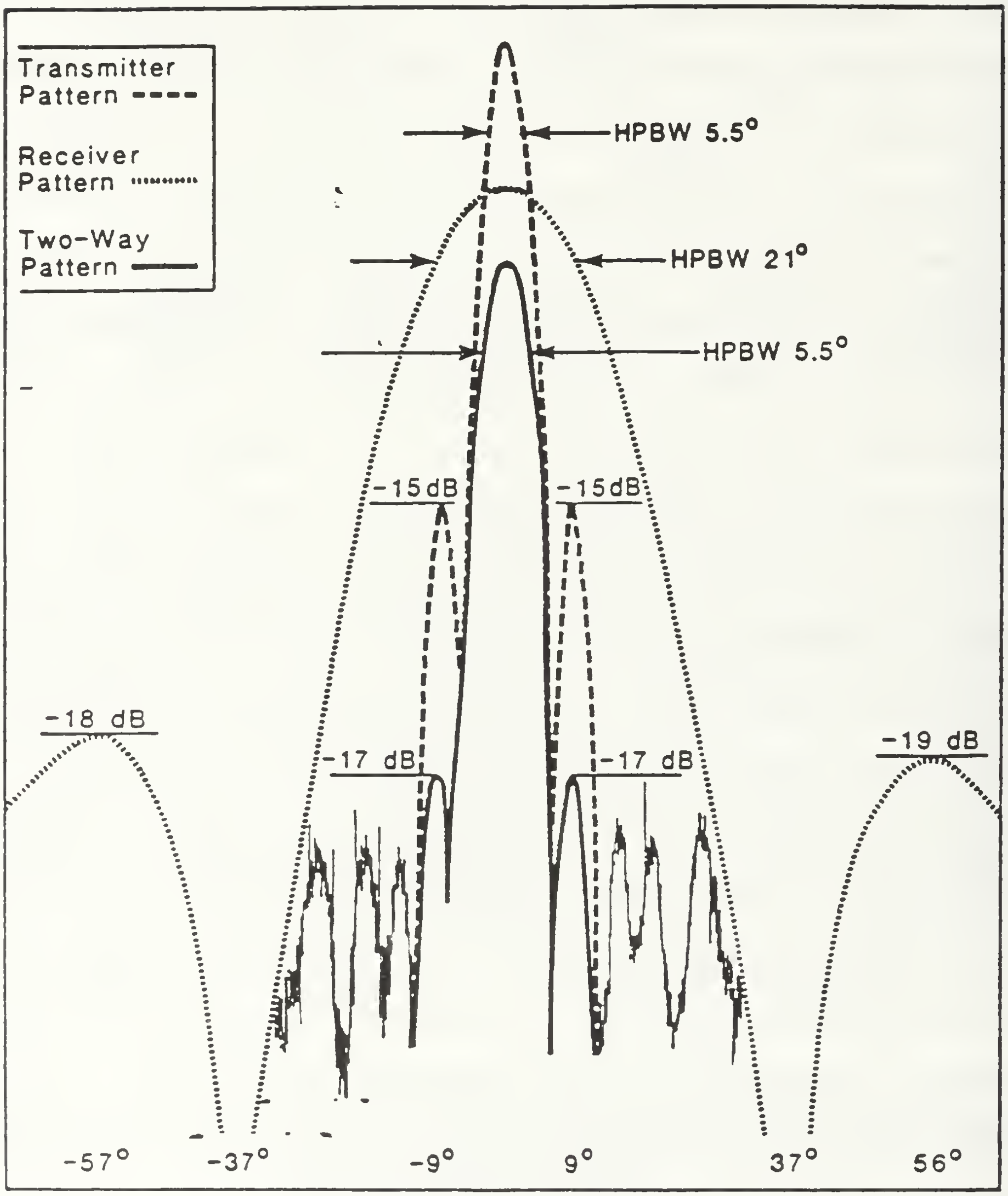

Figure 27. Antenna Patterns for C-Band (5GHz) Radar System

The elliptical surface area, A, illuminated by the radars is calculated from the two-way antenna beamwidths as

$$A = \frac{a^2 \Phi_{y2} \Phi_{x2}}{\cos^3 \theta} = \left(\frac{R \Phi_{y2}}{\cos \theta} \right) (R \Phi_{x2}) = l_y l_x \tag{107}$$

where a is the antenna height, Φ_{y2}, Φ_{x2}, are the vertical and horizontal two-way beamwidths at half power, and θ is the incidence angle (Plant, 1990). Since the one-way beamwidths at half power for the transmitting and receiving antennas are unequal, the two-way beamwidth is calculated as the sum of the inverses of the individual one-way beamwidths (Silver, 1949)

$$\Phi_{x2}^{-2} = \Phi_{x1R}^{-2} + \Phi_{x1T}^{-2} \tag{108}$$

where Φ_{x1R} and Φ_{x1T} are the one-way horizontal receiving and transmitting beamwidths of the receiving and transmitting antennas. A similar expression is used to compute the vertical two-way beamwidth, Φ_{y2}. Using the values given in Figure 25 for the one-way beamwidths and given that a is equal to 7.6m, the illumination areas (l_x by l_y) for the different incidence angle settings of the Ku-band radar are .82 by .97m^2 (at 0° incidence angle), .84 by 1.0m^2 (10°), .88 by 1.1m^2 (20°), 1.1 by 1.6m^2 (40°), 1.7 by 3.9m^2 (60°), 4.8 by 32.2m^2 (80°). The C-band area of illumination is about .75 by 1.3m^2 for θ and a equal to 45° and 8.2m.

It is important that the illuminated area be in the far-field of the transmitting antenna. That is, far enough away from the source that the components of the total field due to the source itself can be neglected and the spherical wavefronts of the impinging radiation are essentially planar, thereby allowing uniform illumination of the area. For a single antenna, the limiting distance which defines the far-field to within a $\pi/8$ error in phase is determined from

$$R_{FF} = \frac{2D^2}{\lambda} \tag{109}$$

where D is the largest linear dimension of the antenna and λ is the electromagnetic wavelength. The one-way beamwidth Φ_1 can be approximated by λ/D; therefore, by substitution,

$$R_{FF} = \frac{2\lambda}{\Phi_1^2} \tag{110}$$

In the present case of separate transmitting and receiving antennas, the two-way beamwidth must be used. From equation (110), with equal receiving patterns $\Phi_2^2 = \frac{1}{2}\Phi_1^2$, and

$$R_{FF} = \frac{\lambda}{\Phi_2^2} \tag{111}$$

Finally, with unequal vertical and horizontal beamwidths, the far-field distance is

$$R_{FF} = \frac{\lambda}{\Phi_{x2}\Phi_{y2}} \tag{112}$$

In the case of the Ku-band system, the far-field distance is 1.5m for λ equal to 2.14cm. The range of the Ku-band radar varied from 7.6m at nadir to 44m at 80° incidence; therefore, all measurements were made in the far-field. Similarly for the C-band antenna and λ equal to 6cm, the far-field distance is 5.6m and all measurements were made in the far-field.

2. Wind Speed and Direction from the Bivane Anemometer

A Gill-type bivane anemometer, mounted on the tower mast at 11.5 m (Figure 28), was used to measure total wind speed and simultaneous azimuth and elevation angles of the wind (R.M. Young Co., 1974). The wind speed sensor is a four blade polystyrene propellor which drives a tachometer generator mounted in the counterweight section of the vane assembly, whose output is a d.c. voltage directly proportional to wind speed. The wind speed range measureable with this propellor is from a threshold speed of about 0.2m/s to a maximum of 31m/s. The propellor was designed to provide approximately one revolution for each foot of wind for all wind speeds. In fact, this criterion is met for all wind speeds above 1.2m/s, which means that between the threshold speed of 0.2m/s and 1.2m/s, the propellor is "spinning up" and the wind speeds are not reliable.

The fin portion of the vane assembly is also molded of polystyrene. With the passage of a wind gust (threshold speed 0.2m/s), the light vane moves horizontally and vertically to maintain equilibrium of wind pressure on the vertical and horizontal vane surfaces. Changes in azimuth are transmitted through the main vertical shaft to the shaft of a linear conductive plastic potentiometer by a set of gears with a one-to-one ratio. Changes in elevation angle are transmitted by a pulley to a small bead chain passing down the hollow vertical shaft to a pulley mounted on the elevation potentiometer. A counterweight on the lower pulley eliminates backlash in the system. Elevation angles of $\pm 50^\circ$ are measureable. With a constant voltage applied to the elements of the potentiometers, the voltage outputs are directly proportional to the position of the vane.

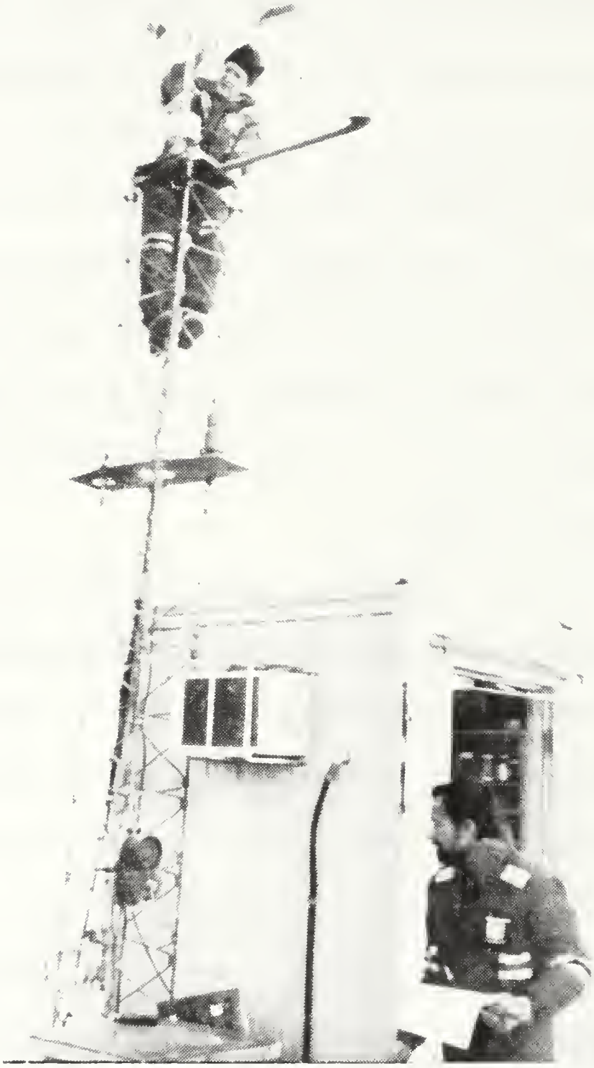

Figure 28. The Bivane Anemometer on the Research Tower Mast 11.5m above the Water Surface

The azimuth potentiometer has a 5% open section which equals 7° to 9° rotation ("dead angle"). Therefore, the full scale calibration of the azimuth signal is only 352° instead of the full 360°. In the field, the "dead angle" is aligned with true South. When the wind is from the South, the voltage will oscillate between the minimum and maximum values (0V, 160°; 5V,152°). The average value (2.5V,about 156°) will have a correspondingly large standard deviation which can be monitored and corrected for in data processing.

For optimum performance, the propellor and vane assemblies have carefully matched dynamic response characteristics. The distance constant of the propellor (the wind passage for 63% recovery for a step change in speed) is 1.0m. The delay distance of the vane (the wind passage for 50% recovery from a step change in direction) is 1.0m and its damped natural wavelength (distance in which directional oscillations are reduced by 1/e) is 5.8m.

3. Wave Spectra from a Six-Element Wave Staff Array

The six wave staffs deployed in this experiment were arranged at the apices and center of a pentagon. The distance between the center staff and the outer wave staffs is 0.25m. The azimuthal resolution of this symmetrical array depends on processing parameters, here taken to be 5°; the range of wave periods resolved is 0.6 to 8.0s.

Following Der (1976), the sensors are capacitance transduction devices which produce output voltage signals proportional to surface elevation. The sensors in WAVES87 were comprised of 6m teflon-sheathed wire probes of 4.8mm outer diameter and associated signal conditioning electronics. Assuming uniformity in the cross-sectional area of the teflon sheath, in its surface and its chemical composition; then the capacitance of the proble will be linearly related to the length submerged. The major source of error is stray capacitance-to-ground which is maximized when the probe is fully exposed; i.e, is most nearly like a vertical antenna perpendicular to a ground plane. Wetting errors due to water films and algae adhering to the teflon surface, account for most of the hysteresis exhibited by these sensors. According to Tsanis and Donelan (1988), the wave staffs had a very stable linear calibration during the WAVES87 experimental period and were cleaned almost weekly from any impurities and algae that had accumulated on them.

4. Air Temperature and Relative Humidity from the Fast Response Sensors

The air temperature thermistor at 11.5m had a time constant of 0.2s and was shielded to minimize direct solar warming. The relative humidity sensor was mounted beneath a plate at the top of the mast on which the base of the anemometer rests. The sensing element is a thin film capacitor composed of an upper and lower electrode with an organic polymer dielectric about one micron thick (WeatherMeasure Corp., 1975). Water vapor is absorbed into the polymer after the vapors pass through the upper metal electrode thereby changing its capacitance. Comparison of the capacitor output to a reference signal provides a DC voltage proportional to humidity. Since the upper electrode must be as transparent to water vapor as possible, the thin electrode results in quick response to changes in humidity. The response time of the fast response sensor element is less than one second at

68F to 90% of the final relative humidity value. The accuracy of the sensor is better than ±3%.

5. Surface Water Temperature from an *in-situ* Thermometer

The water surface temperature sensor is contained in a modified "bucket" which is fixed just beneath the water surface against one of the tower legs. The bucket has an annular space between its lid and body and a small hole in its base. As a wave washes over the bucket it is periodically filled and then slowly drained through the hole. In this way, the sensor is always wet and measures a temperature corresponding to the upper 10 cm of water (Tsanis and Donelan, 1987).

6. Ancillary Measurements

Synoptic charts of surface pressure, temperature and wind velocity were obtained from Fleet Numerical Oceanography Center on a daily basis from 9 October to 11 December to provide a larger context for the local weather at the experimental site and to facilitate selection of test cases based on similar weather conditions.

Aside from the radars, information regarding the instruments installed on the tower was obtained primarily from Tsanis and Donelan, 1987. Calibration of the sensors was performed in the laboratory before and after field exposure.

D. DATA ACQUISITION

Two alternate modes of data acquisition were employed. In the high frequency (continuous) mode, all sensors were sampled and recorded at 20 Hz for 95 minutes and in the low frequency (averaging) mode, samples were made at 20Hz and averaged every ten minutes. The continuous mode was used mostly during regular work hours only, since this mode required an attendant. When significant weather events occurred, watches were posted and the high frequency mode continued through the night.

The 20 Hz, 48 channel data were digitized on the tower and transmitted to a trailer onshore where they were automatically received by an IBM-AT microcomputer. They were then stored on the IBM's 30 MB hard disk and plotted in analog form on chart recorders for real-time monitoring. Each 95 minute run required 7 Mb so that the hard disk is full after four runs. At this point the data were copied onto 40 MB magnetic tape, the hard disk erased and the logging sequence reinitiated by the operator.

The ten minute averaged data followed the same procedure as above except that they were written directly to floppy disks.

E. SUMMARY

The WAVES87 experiment was performed from a tower in Lake Ontario during October to December, 1987. One aspect of the experiment was to investigate environmental effects on the NRCS measured by radar scatterometers. In support of this investigation, the tower was outfitted with a suite of instruments which provided the meteorological and limnological parameters thought to influence the NRCS. This chapter described the experimental site and the weather conditions which prevailed during the experiment. The intrinsic and operating characteristics of the radars, bivane anemometer, temperature and humidity sensors, and wave staffs were discussed with the intent of identifying the limitations of each of these devices.

IV. DATA PROCESSING METHODS AND RESULTS

The 14 data channels pertinent to this study were copied from the raw data magnetic tapes to backup tapes at CCIW and subsequently were written to the NPS IBM3033 mainframe computer for processing. At this stage, the data consisted of voltages to be converted to geophysical units via the laboratory calibration equations. Next, the raw environmental data needed averaging in time intervals which were sensible for a particular geophysical parameter and the resulting averages assigned a time tag for subsequent collocation of multiple parameters. Since the rotating Ku-band radar moved in azimuth every ten seconds, while the C-band radar was fixed in one position, different averaging schemes were applied to the individual radars and their associated environmental parameters.

A. THE KU-BAND SCATTEROMETER AND ASSOCIATED ENVIRONMENTAL PARAMETERS

An example of the voltage outputs of the Ku-band radar channels is shown in analog form in Figure 29, which illustrates the first 7.5 minutes of Run 87056 separated into three 2.5 minute segments of elevation (incidence angle) (EL), azimuth (AZ), Ku-band horizontal polarization (KuH) and Ku-band vertical polariztion (KuV) voltages. For approximately 40s of the first minute the radar samples the calibration circuit while at its "home" position of 60° (incidence) and 250° T North (azimuth). In the next 50s, the radar completes its movement to the initial starting point of 0° incidence and 95° T azimuth. The calibration circuit is switched for the Ku-hpol and Ku-vpol channels and typical random signals are observed.

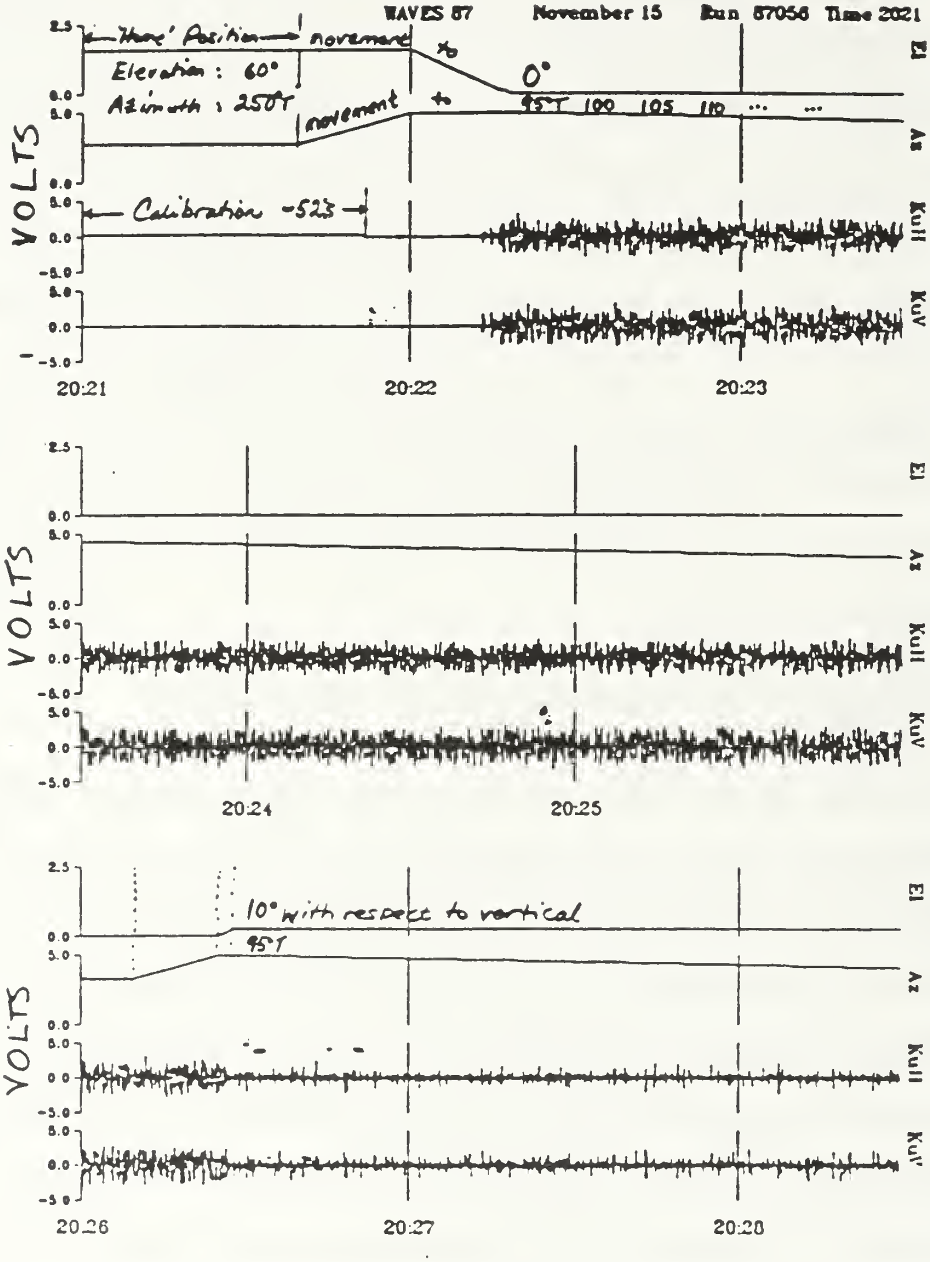

Figure 29. Analog Record of the First 7.5 Minutes of Data Run 56

The azimuth signal is seen to decrease in small increments, until about four minutes have elapsed. At this time, the incidence angle is increased to 10° and the radar is rotated back to 95° T. This procedure is repeated for the remaining incidence angles (recall Table V) except that the radar does not return to 95° T each time but simply steps backward from the end of the previous azimuth sweep.

1. Incidence and Azimuth Angle Position

The incidence and azimuth angle positions of the Ku-band radar were calibrated before and after the experiment using the most precisely known physical positions of the radar as anchor points. That is, elevation was measured with respect to true vertical as visualized with a Sperry digital level, as observed on the antenna rotator azimuth/elevation meter and as measured by the rotator output voltage. The azimuth angle was calibrated with respect to the known tower orientation of 250° T and the points ± 90° of 250° T. With this calibration method, it is believed that the incidence angle is absolutely determined to within 1° and the azimuth angle is absolutely determined to within 5°.

The radar incidence and azimuth angles are determined by the voltage levels recorded on the appropriate data channels. The voltage values at each elevation setting are known, virtually constant and measured for no less than four minutes. Therefore, the radar incidence angle movements in the analog data record are easily discriminated as changes from the known values (within a small tolerance). Spikes in the incidence angle voltage measurements, which are misinterpreted as elevation movements, are compensated for by requiring that the apparent movement span at least five consecutive data points.

The azimuth angle determination proved much more difficult. Tolerance checks based on explicit voltage values are not possible for the azimuth angle movements for which the voltage increment between azimuth steps is only 71mV and the measurement period is less than ten seconds. To discriminate between adjacent steps, a five point running mean of the azimuth voltage is computed. A step change is considered to have occurred when the difference between two consecutive averages exceeds 7mV. All of Ku-hpol and Ku-vpol voltage values up to the step change are binned together and their statistics (mean, variance, skewness and kurtosis) are computed in preparation for the cross-section computations.

The azimuth direction was computed during the preliminary data processing stage using the average azimuth voltage and the calibration equation as measured in the field. However, small amounts of noise in the voltage measurement occasionally caused the wrong direction to be produced by the calibration equation (usually the direction was shifted backwards by one five degree bin and the data in the previous bin overwritten). The error induced by this bin shifting was cumulative: the position at the end of a ten minute azimuth sweep was as much as 15° from the true value. Visual examination of the analog plots revealed other anomalies: the total number of five degree bins per azimuth sweep was 59 instead of 60, bin durations were occasionally shorter or longer than the ideal 10s length, voltage spikes in the bin produced anomalous movements, and there was no clear separation between the first and second pass at some incidence angles. For these reasons, a less automatic but more reliable, procedure was adopted for assigning the correct azimuth direction.

In this procedure, a counter equal to the correct bin number is initialized at the start of each azimuth sweep. The counter is then incremented (decremented) at each azimuth step of a forward (backward) sweep. In this way each real azimuth step is assigned a unique direction. Comparison of the bin numbers chosen this way to those computed by the actual calibration equation reveal no difference until a "noisy" average voltage measurement occurs. Only at this time does the calibration equation compute the wrong backwards shifted value, while the counter correctly moves to the next step.

The occasions on which the forward sweep goes beyond the fifty-ninth bin, i.e., the lowest voltage is .47xx instead of .5xxx, are accounted for by setting the initial value of the bin counter one unit higher than normal on the backward sweep. Voltage spikes are accounted for by requiring a bin to consist of a certain minimum number of points (usually 100 of the possible 180). Bins which are truly shorter or longer than the normal 10s are still correctly differentiated by changes in the running mean values. Finally, separation of the two sweeps is accomplished when necessary by splitting the second sweep from the first according to a time duration limit of 608s for the first sweep. The absence of a systematic bias between the forward and backward sweeps was established by plotting the azimuthally averaged cross-sections from the first and second passes against each other for several data runs (Figure 30).

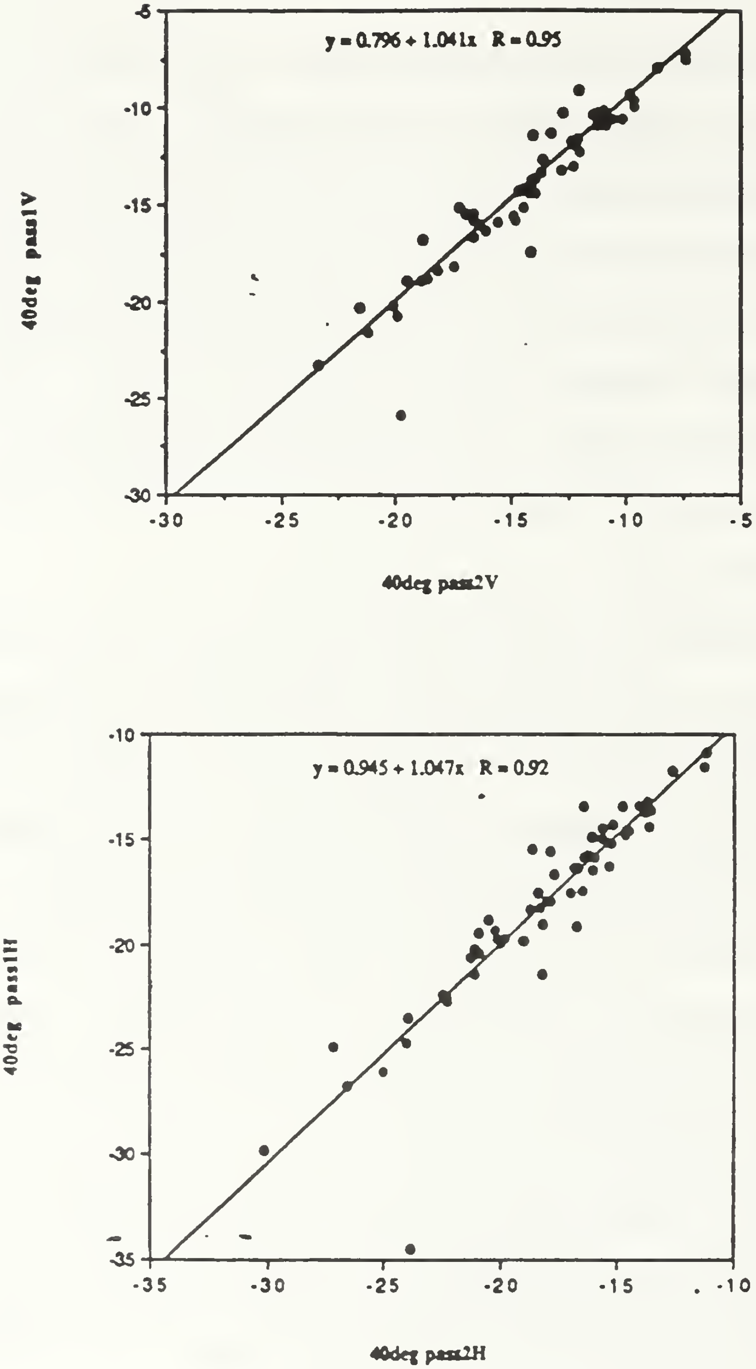

Figure 30. Azimuthly Averaged NRCS of First Radar Rotation Plotted against Second Rotation. Upper: 40° v-pol. Lower: 40° h-pol.

To summarize the Ku-band radar position processing, the full length analog plots of azimuth and incidence angle voltages are visually examined to identify anomalous movements or potential problems. These problems always fall into the above mentioned categories, hence standard corrections are written into the data processing software. The corrections are applied by setting the appropriate flags in the data statements of the processing program.

1. Internal Calibration

Errors in the cross-section values due to performance characteristics of the radar components are eliminated through internal calibration of the radar at the beginning of each full 95 minute data run. A portion of the transmitted signal is sampled after its passage through the internal components of the radar system (amplifier, mixers, and oscillator). The measured calibration voltage is recorded on the Ku-hpol channel. In Figure 29, the calibration period is 51.6S (nominal: 50s) and the calibration voltage is 0.299 volts (nominal: 0.30 volts). Over the course of the experiment, the calibration voltage increases at a rate of approximately 2mV/day (Figure 31a) but it shows no dependence on air temperature (Figure 31b) as would be expected if the efficiency of these internal components were affected by air temperature.

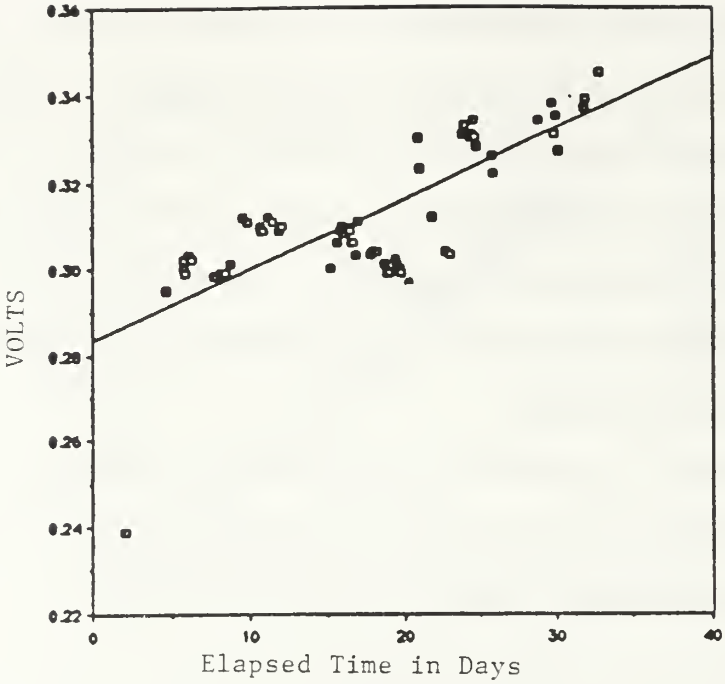

Figure 31a. Internal Calibration Voltage of Ku-Band Radar as a Function of Time from Start of Experiment (November 11, 1987)

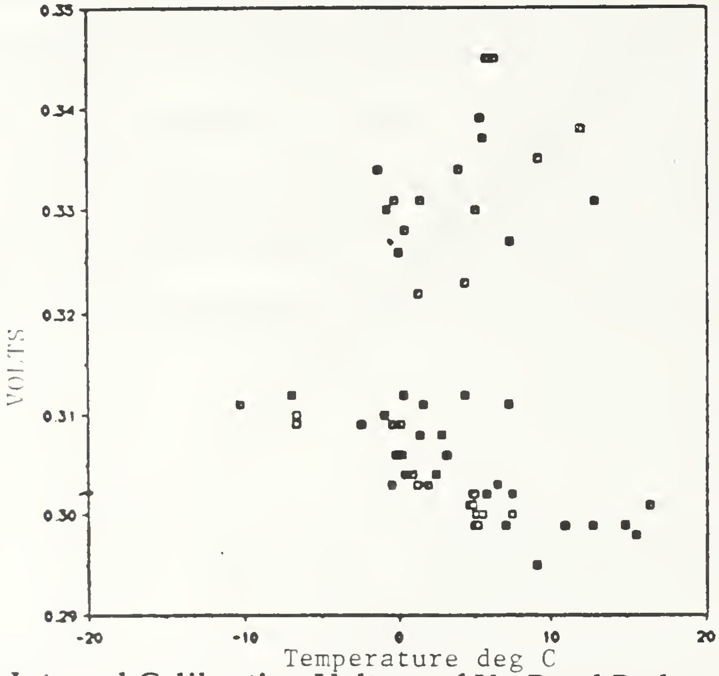

Figure 31b. Internal Calibration Voltage of Ku-Band Radar as a Function of Air Temperature

Drift of the calibration voltage is compensated for by using the actual measured calibration voltage in the NRCS computation except for the runs which do not begin at the radar home position. For these incomplete runs, the laboratory calibration voltage of 0.30 volts was used.[1]

3. External Calibration

The radar system was calibrated at NRL before and after the experiment using two metallic spheres of known radar cross-section to establish the absolute calibration of the measured cross-section. The spheres were suspended from strings and oscillated to discriminate the radar return from background reflections by the Doppler shift of the returns from the moving spheres. A 1 KHz filter was used to eliminate returns from nonmoving objects (noise).

The radar equation which expresses the power received at the antenna in terms of the antenna properties and the target cross-section is written as

$$\rho = \frac{P_R}{P_T} = \frac{\lambda^2 G \sigma}{(4\pi)^3 R^4} \tag{113}$$

where ρ is the ratio of the power received (P_r), to the power transmitted (P_t), λ is the microwavelength, G is the antenna gain, R is the range to the target and σ is the target cross-section. The cross-sections measured in the field are absolutely calibrated by forming the ratio of ρ_s of the sea-surface to ρ_c for the calibration sphere and deducing a calibration constant. Since the antenna parameters are identical for each ρ, the ratio becomes

---

[1] The preferred value would have been either the value from the next closest data run or the regressed value derived from the time series of the calibration voltage. Since the data were not processed in sequence and since the calibration voltages were required at the start of the data processing, the laboratory value was adopted as the default.

$$\frac{\rho_s}{\rho_c} = \frac{\sigma_s}{R_s^4} \frac{R_c^4}{\sigma_c} \tag{114}$$

so that the sea-surface cross-section is

$$\sigma_s = \frac{\rho_s}{\rho_c} \left(\frac{\sigma_c R_s^4}{R_c^4} \right) \tag{115}$$

The area-normalized radar cross-section is then

$$\sigma^\circ = \frac{\sigma_s}{A} \frac{\sigma_c}{\rho_c R_c^4} \frac{R_s^4}{A} \rho_s \tag{116}$$

With the illuminated area A defined as in equation (107), and R = a/cosθ, then

$$\sigma^\circ = \frac{\sigma_s a^2}{\rho_c R_c^4 \Phi_x \Phi_y} \frac{1}{\cos\theta} \rho_s \tag{117}$$

$$\text{or } \sigma^\circ = C_O \, \rho_s$$

where $C_O = c'/\cos\theta \, \rho_s$ accounts for the system and calibration constants and incidence angle. This constant was found to be 2.31 / cosθ for the Ku-band radar.

4. System Noise Evaluation

A continuous wave radar, such as those used in this experiment, is always transmitting a signal. Hence, system noise defined as the voltage measured by the radar in the absence of any target, is estimated by minimizing the return signal. Typically, this means pointing the antenna into free space away from any potentially reflecting targets. In this experiment, when under very low wind conditions, the 80° incidence angle was considered equivalent to looking into free space. These data were used to compute an "equivalent noise variance," N, which was then subtracted from the signal variance in the computation of the absolute cross-section.

The basis for the equivalent noise variance is that if the computed cross-section is actually representative of the system noise only, then P_R is a constant and

$$\rho_s = \frac{<\sigma^{o}>}{C_0} \tag{119}$$

should be nearly equal for the 60° and 80° incidence angles, where the average on the cross-section, denoted by angle brackets, is over all azimuth angles. In this noise case, the cross-sections are constant with azimuth and their magnitudes increase with incidence angle by virtue of the radar equation. From equation (117), the ratio of the average cross-section at 80° to that at 60° is

$$\frac{<\sigma^{\circ}_{80}>}{<\sigma^{\circ}_{60}>} = \frac{c'(\cos 80)^{-1}}{c'(\cos 60)^{-1}}\frac{\rho_s}{\rho_s} = 2.87 \tag{120}$$

In log space the ratio is a positive difference of 10log(2.87) or 4.5 dB between the 80° and 60° average cross-sections.

Figure 32 illustrates the last 7.5 minutes of Run 87048 from which a noise computation is made. At this stage, the radar is at 80° incidence and about

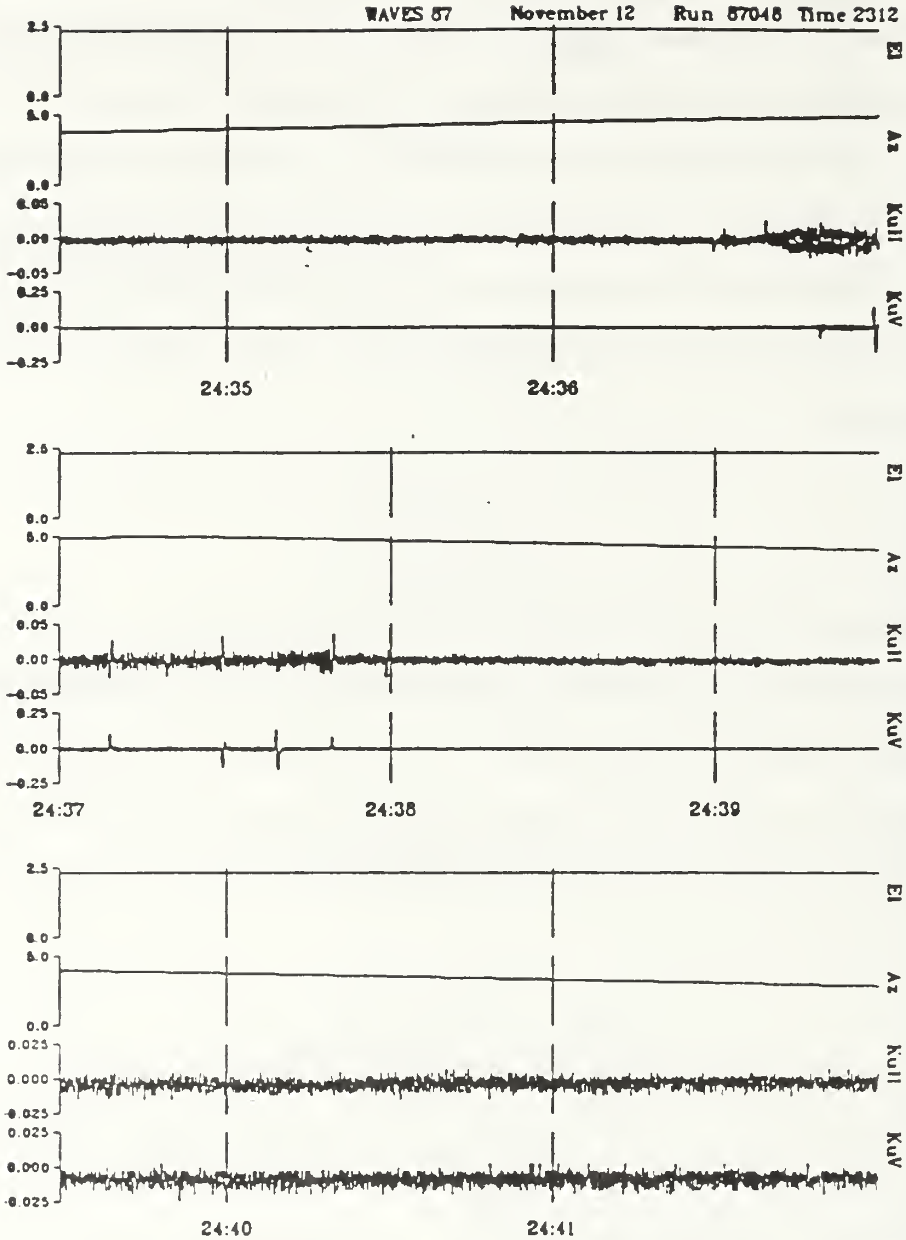

Figure 32. Final 3.5 Minutes of Run 48, Used for Evaluation of the Ku-Band Radar System Noise Level

two minutes into the second azimuth sweep. Return from the tower legs is observed as large sinusoidal fluctuations between times 24:36 and 24:38. Because of these erroneous returns, the five azimuth bins at the extreme ends of the sweep at 60° and 80° are eliminated from further analysis. Beyond 24:38 the returns are clearly down to the digitization level of the instrument. The average wind speed for this run was 2.6 m/s.

Using these data and the internal calibration voltage, the NRCS was computed and plotted as a function of azimuth (Figure 33) and incidence angle (Figure 34). As explained above, the h-pol NRCS at 80° is in fact a relatively constant value greater in magnitude than that at 60°. From equation (4), the noise variance, N, was computed to be 1.6E-04 volts-squared. Other similarly low wind speed runs were used to arrive at an average noise value of 1.5E-04 volts-squared. This value is then used to compute the lower limit of NRCS values for each incidence angle from

$$\sigma^{\circ}_{min} = \frac{2.31}{\cos\theta}(1.5E-04) \tag{121}$$

which yields σ°_{min} of -34.6 dB (0°), -34.5 dB (10°), -34.3 dB (20°), -33.4 (40°), -31.5 dB (60°) and -26.9 dB (80°). In subsequent analyses, NRCS values lower than these for a particular incidence angle are eliminated from consideration.

5. Normalized Radar Cross-Section (NRCS)

In this experiment, the radar return voltage was measured by a linear detector. Therefore, the return power is computed from the mean-square ac voltage variance, $\overline{V_{ac}^2}$, or the voltage variance, σ_v^2, since

$$P \propto \overline{V_{ac}^2} = \sigma_v^2 \tag{122}$$

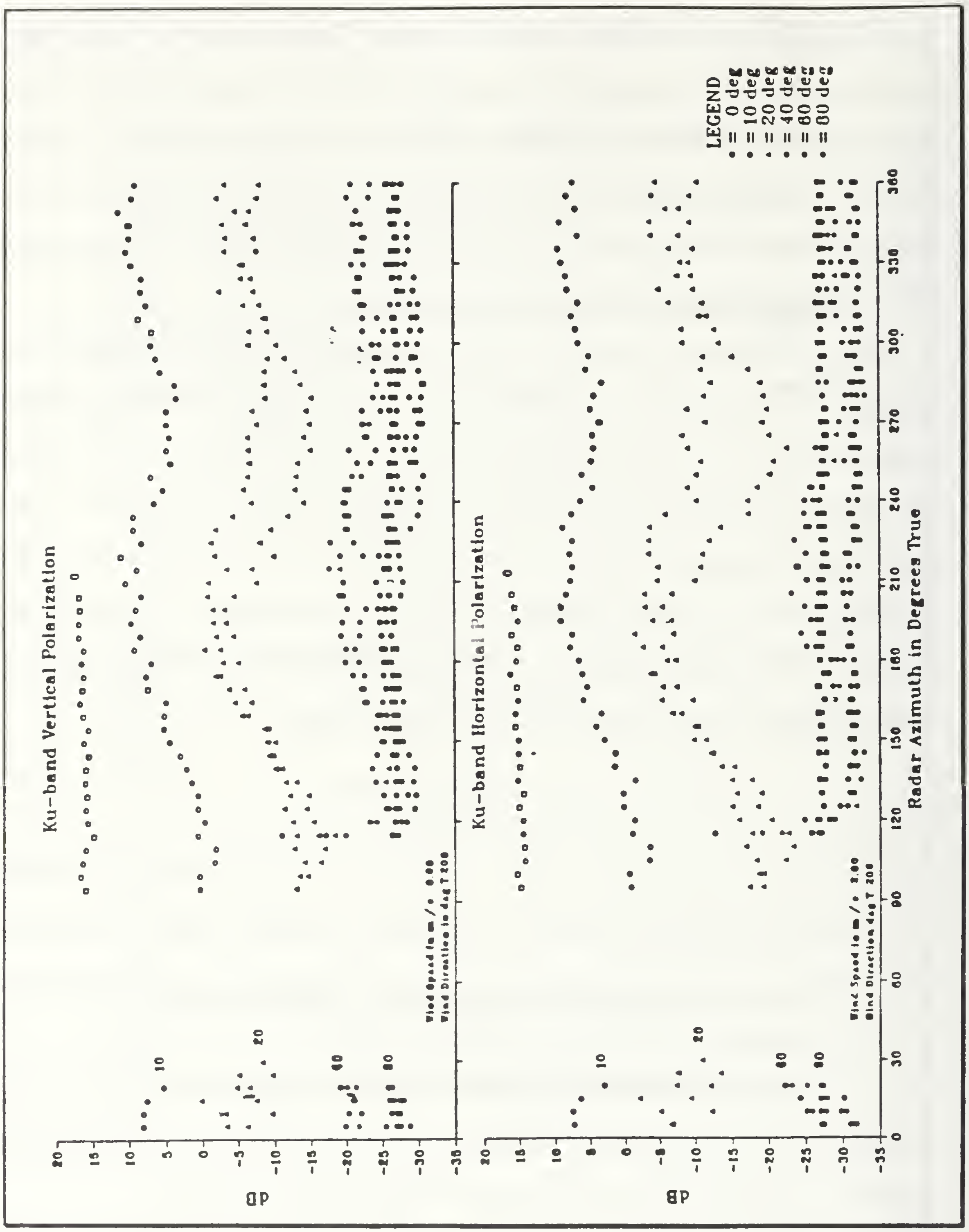

Figure 33. NRCS-Versus Azimuth Angle of Radar for all Incidence Angles. Data Run 48, November 18, 2312 GMT. Upper: v-pol. Lower: h-pol

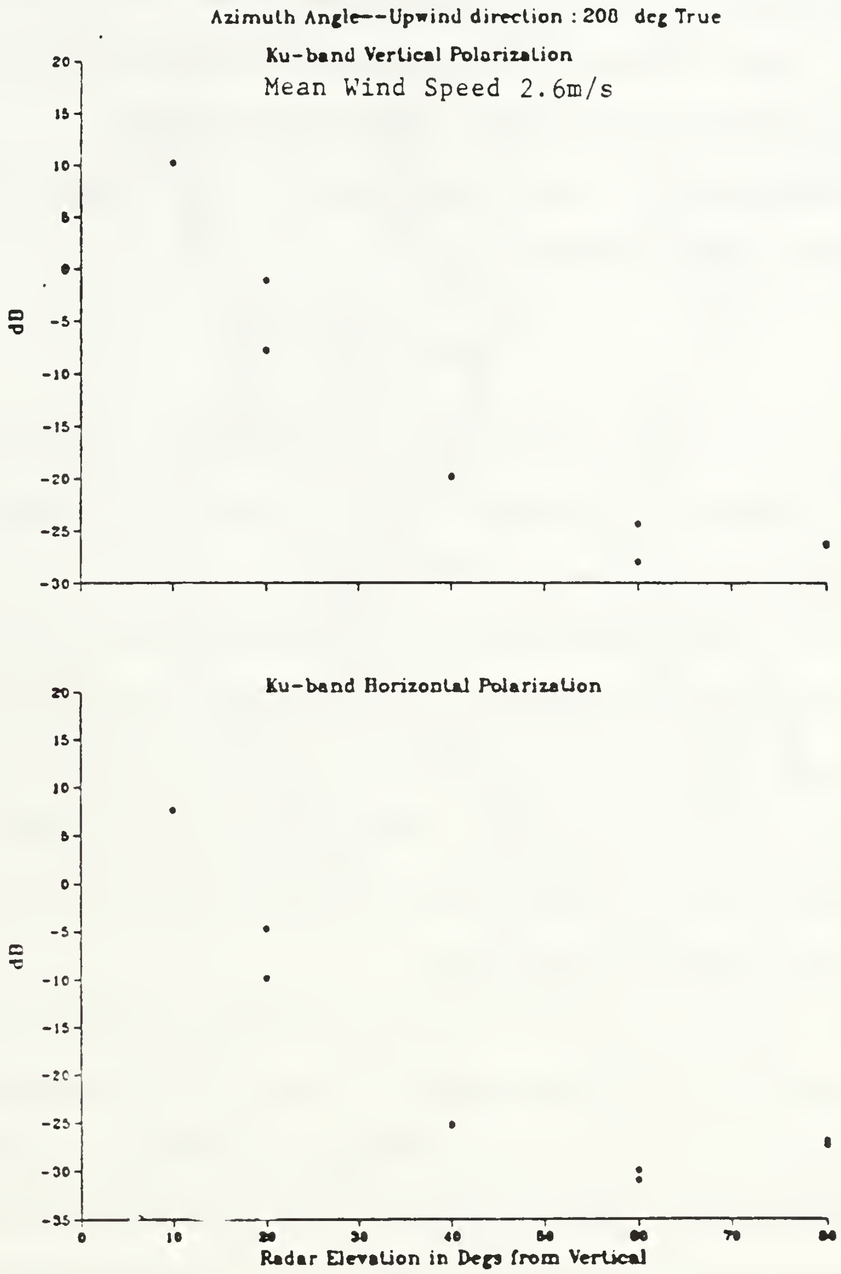

Figure 34. NRCS Versus Incidence Angle. Data Run 48, November 18, 2312 GMT. Upper: v-pol; Lower: h-pol

Here, only the mean-square ac component of the return voltage, V_{ac}, is considered since the voltages are Doppler shifted due to the moving water surface. The dc component due to microwave leakage between the antennae is removed from the returns with a 1Hz high pass filter

The NRCS is then computed from the voltage values in each azimuth bin using the formula

$$\sigma_\ell^\circ = C_0\left(\frac{\sigma_v^2}{V_{cal}^2} - N\right) \tag{123}$$

where σ_ℓ° is the area-normalized (nondimensional) cross-section intensity (not dB), σ_v^2 is the voltage variance, V_{cal}^2 is the calibration voltage squared, N is the noise value, and C_0 is the calibration factor.

The cross-sections were then plotted as a function of radar azimuth angle. Although the azimuthally averaged values from the first and second passes were comparable (recall Figure 30), the individual pass values at a particular azimuth bin often exhibited significant scatter (Figure 33). Therefore, the two-pass values were averaged to reduce the scatter and reveal more of the azimuthal dependence.

The error bars on Figure 35 are at the 95% confidence level and are estimates of the random measurement error for each average assuming that the voltage variances, from which the cross-sections are determined, are chi-square distributed. This assumption is valid provided that the measured voltages are normally distributed. Figure 36a and 36b illustrate histograms of all voltages at incidence angle 20° and both polarizations, from which it is

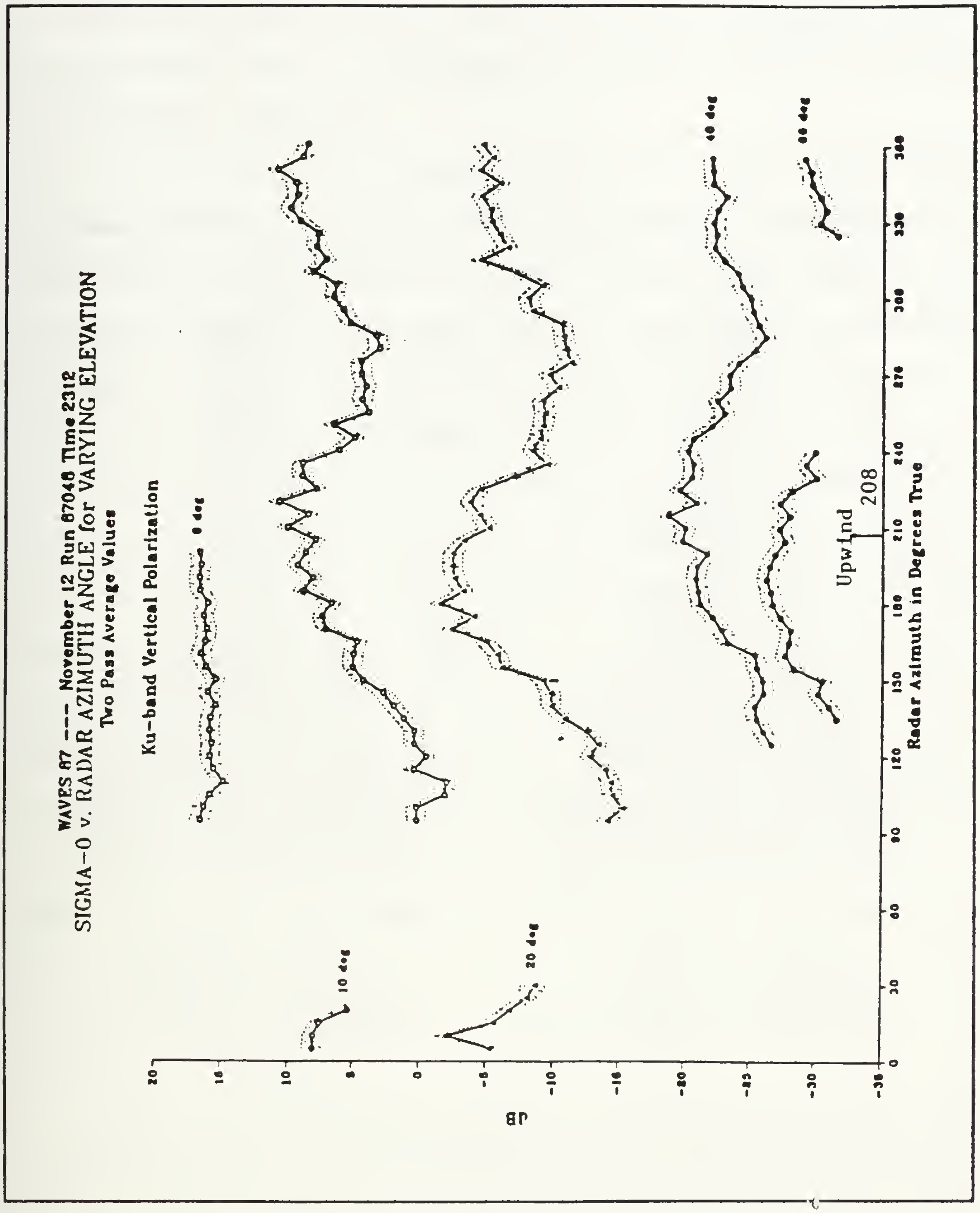

Figure 35. Two-Pass Averaged NRCS as a Function of Radar Azimuth. Dotted Lines Show 95% Confidence Levels Based on Chi-Square Distribution

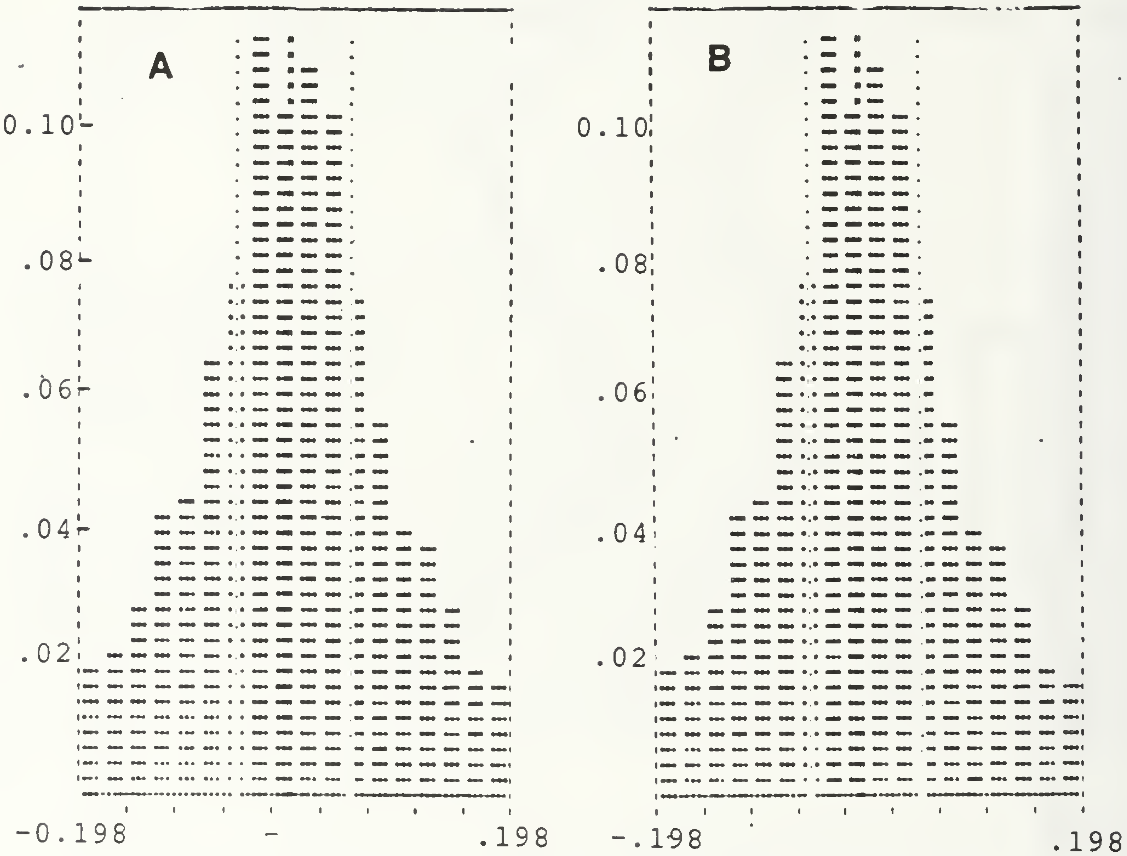

Mean -4.88E-03
Variance 8.35E-03
Skewness 4.15E-02
Kurtosis -6.58E-01 (+3)

Mean -3.39E-03
Variance 6.98E-03
Skewness 4.18E-02
Kurtosis -3.01E-01 (+3)

Figure 36. Histograms Showing Gaussian Distribution of Voltage Measurements from Ku-Band Radar. (left) 20° v-pol, (right) 20° h-pol.

seen that the voltages are in fact very nearly Gaussian as required. Because each averaged value has 360 degrees of freedom, the error bars are correspondingly small (±1dB).[2]

The final step in the processing of the cross-sections was to smooth the averaged values across three azimuth bins using a 1:2:1 weighted average filter (Figure 37). In the analysis figures to follow, the cross-section values will be identified when necessary as individual pass, two-pass averaged or smoothed values according to their level of processing as described above.

6. Field Calibration using the Nadir and 10 Degree Incidence Data

After smoothing the cross-sections and plotting them with respect to azimuth, it was noticed that the nadir incidence angle v-pol and h-pol values were offset from each other. Specular scattering theory predicts no difference between v-pol and h-pol at nadir; therefore, this bias was taken to be a calibration error between the two polarizations. On average, the bias was about +1.5dB (v-pol larger than h-pol). Since it was not known which polarization was in error, the correction procedure was to subtract

---

[2] Under most circumstances, the first and second pass values are close enough that their individual error bars would overlap, implying that they come from the same population. However, there are occasions when the pass by pass values are sufficiently separated to suggest that the cross-sections are from different populations. These data runs should be examined on a point by point basis and correlated with (possible) short term changes in the wind field.

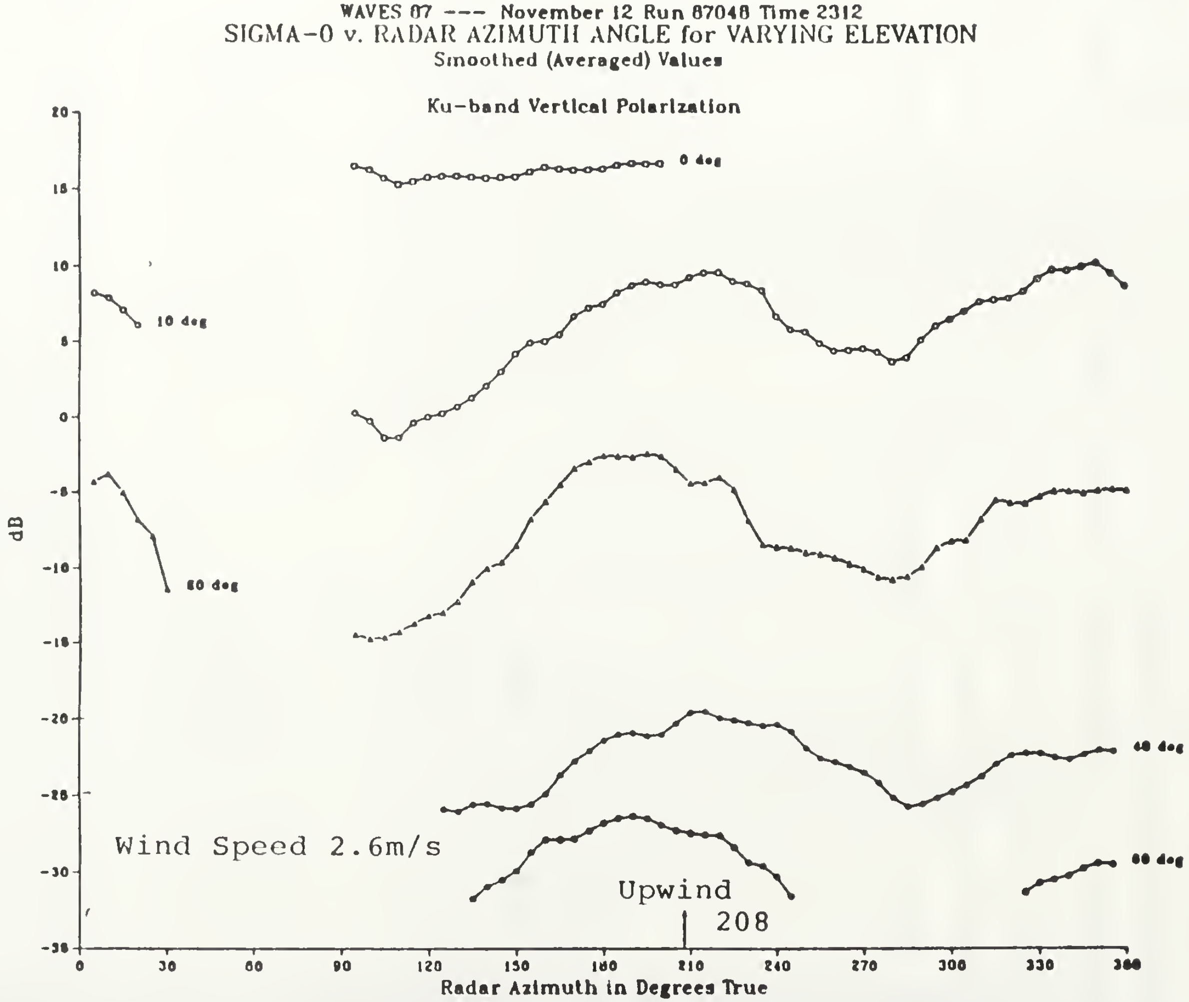

Figure 37. Averaged and Smoothed NRCS as a Function of the Radar Azimuth Angle

half of the bias from the v-pol and add half to the h-pol cross-section values. This method produces identical cross-section values for the two polarizations at nadir.

The NRCS is negatively correlated with wind speed at nadir and positively correlated at progressively higher incidence angles (recall Figure 2). The 10° incidence angle is the "transition" angle between the two regions and as such, displays virtually no dependence on windspeed and minimal dependence on wind direction. Therefore, this angle is used as an external "field" calibration point. This calibration point may be more representative of the true calibration since the radar is designed to detect Doppler shifts in the radar returns induced by the movement of the ocean surface. This situation is only simulated in the laboratory procedure through the use of an oscillating or rotating sphere.

Initial comparisons of the measured NRCS with the model function predictions as a function of incidence angle showed a positive 2 to 3 dB bias between the measured and predicted values at all incidence angles. Before attributing erroneous physical meaning to these biases, a further antenna pattern correction was applied to the NRCS data using the 10° incidence angle data.

It was presupposed that the tower radar cross-sections at 10° may be higher than the corresponding predictions from the model functions which were tuned to airplane or satellite scatterometers, since the tower radar antenna has a beamwidth of nearly 7° as compared to 1° or less for the higher altitude scatterometers. That is, while the tower radar has a *boresight* direction of 10°, the average power may be coming from an angle less than this, thus producing higher cross-section values.

To estimate the offset which would arise from the wider beamwidth, SASS1 and SASS2 predictions at 10° (averaged over all azimuth and windspeeds between 3 and 11m/s) were "smeared" over a 7° beamwidth by assuming a Gaussian antenna pattern for the tower radar. The SASS1 and SASS2 model functions were chosen for this calibration since they are purely statistical fits of data from RADSCAT (1.5° beamwidth) and SEASAT SASS (0.5 ° beamwidth).

The half-power points of the Gaussian curve are mapped to the radar antenna half power points (of known incidence angles), Figure 38. The standard coordinates of the Gaussian curve are then obtained as +/-0.67 or 1.34 standard deviations; i.e., about 5° per standard deviation. The averaged cross-section intensity values of either the SASS1 or SASS2 model over 5° to 15° are then weighted by the Gaussian ordinates to obtain the average value at 10° for a 6.7° beamwidth.

For SASS1, the averaged value was 7.73dB or 0.73dB higher than that obtained from the 1.5° HPBW of the aircraft RADSCAT. Similarly, the averaged value was 7.44dB for the SASS2 model was about 1.1dB higher. Therefore, about 1dB of the bias in the tower radar data can be attributed to the wider antenna beamwidth.

6. Environmental Parameters

Since the air/water temperatures, relative humidity, surface elevation, wind speed and wind direction are generally nearly constant

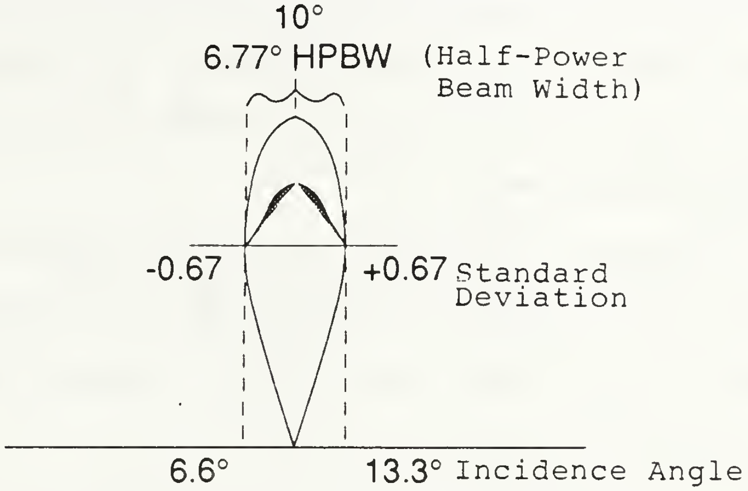

Antenna Pattern and Half-Power Points of Gaussian Curve Superimposed

One standard deviation of Gaussian Curve Maps to 5°:

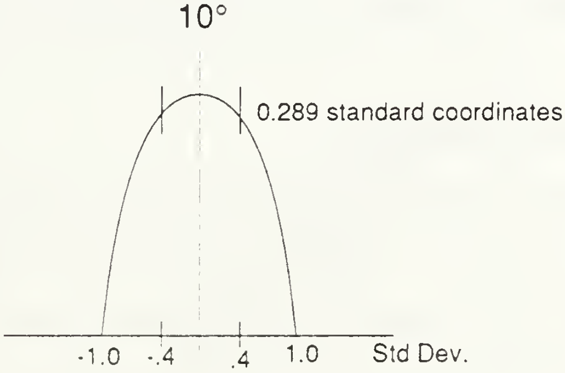

Therefore,

$$\text{Average Value over Beam} = \frac{\Sigma\omega_i \, \sigma^\circ_i}{\Sigma\omega_i}$$

Where σ°_i values come from SASS2

Figure 38. Antenna Pattern Correction to Convert Ku-Band 7.0° Beamwidth to 1° Beamwidth

during a 95 minute run, one minute running means, evaluated every 10s are computed for these quantities. The first mean is calculated from the first full minute of data after the radar reaches its initial starting position. A centered time tag of 30s is associated with the mean, hence neither the first two radar bins (10s, 20s) nor the last two bins (5690s, 5700s) will have associated environmental parameters.

It should be noted that the one minute running mean value of wind direction is used to compute the relative angle between the antenna and wind directions for each azimuth bin. The wind speed values are handled in several different ways as shall be described in Section C of this chapter.

B. THE C-BAND SCATTEROMETER AND ASSOCIATED ENVIRONMENTAL PARAMETERS

The data processing for the C-band radar is much simpler since it is fixed in one position throughout the experiment at 45° incidence and 250° T. azimuth.

1. Internal Calibration

As with the Ku-band radar, the C-band radar has an internal calibration cycle at the beginning of each 95 minute data run which is recorded on the hpol channel. The calibration period is also 50s (nominal) but the calibration voltage is -1.3V (nominal). Contrary to the Ku-band radar, the C-band calibration voltage shows no particular drift with time (Figure 39a) but there is clearly a dependence on air temperature (Figure 39b)[3]. The actual measured value of the calibration voltage is used to compute the NRCS.

---

[3] In retrospect, a multiple regression of the calibration voltage on time and air temperature should have been performed for both the Ku- and C-band radar calibration voltages.

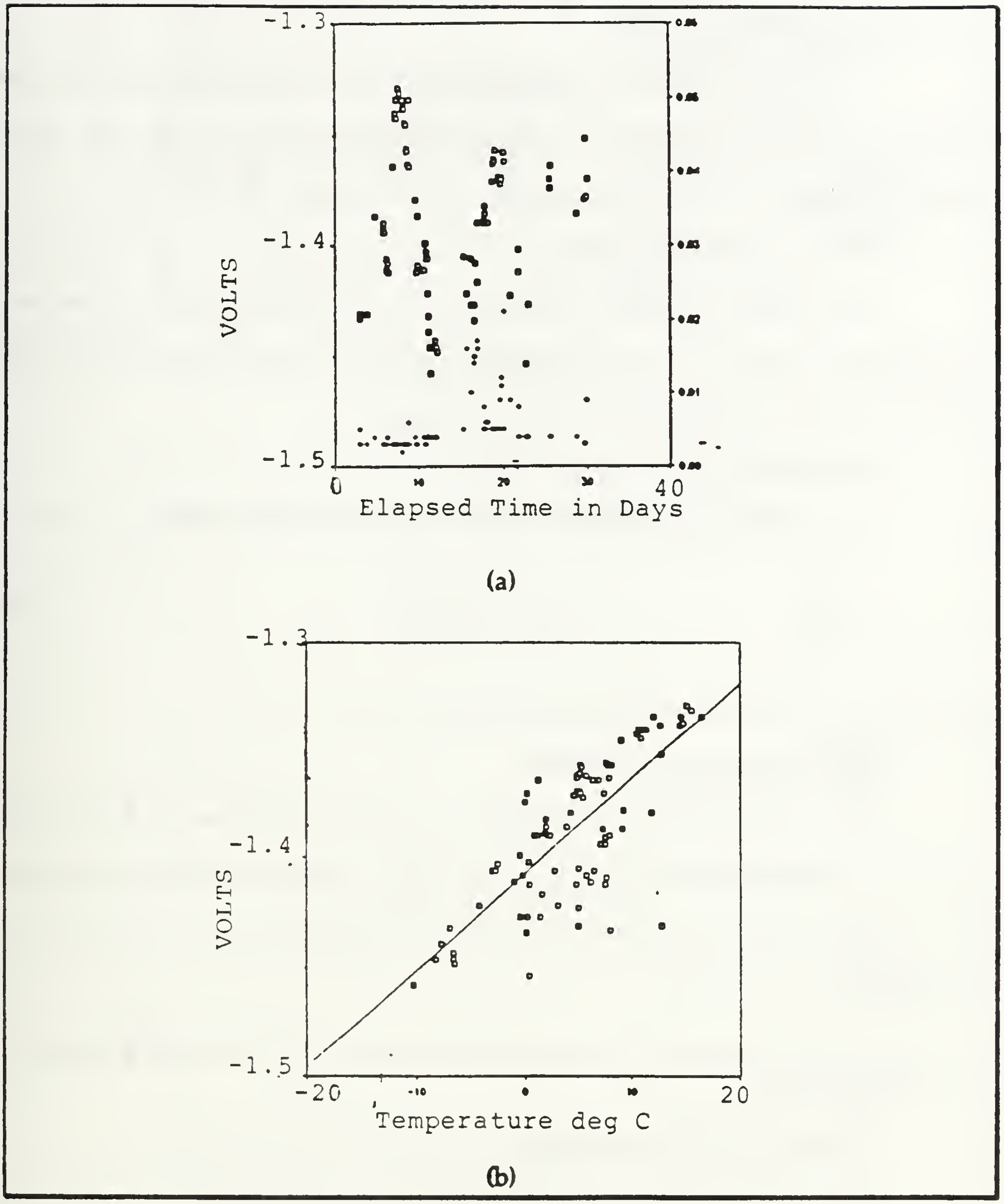

(a)

(b)

Figure 39. Internal Calibration Voltage of C-Band Radar as a Function of a) Time from the Start of the Experiment (November 11, 1987) and b) Air Temperature.

2. External Calibration

The C-band radar was calibrated at NRL before and after the run using two metallic spheres of known cross-section in the same fashion as the Ku-band radar. The calibration constant C_0 at θ equal to 45° is 11.09.

3. System Noise Evaluation

No estimates of the system noise were made since the radar was permanently aimed at 45° to the surface and the values of the returns were well above the system noise.

4. Normalized Radar Cross-Section

The NRCS is computed in one-minute data blocks using the formula

$$\sigma_\ell = 11.09\left(\frac{\sigma_v^2}{V_{cal}^2}\right) \tag{124}$$

where σ_V is the voltage variance within the data block.

5. Environmental Parameters

The environmental parameters are also computed in one-minute blocks to align in time with the C-band NRCS values. Judging from Figure 40, it is clear that the radar measures nearly instantaneous changes in the wind speed.

C. COMPUTATION OF THE WIND STRESS, HEAT FLUX AND NEUTRAL WIND SPEED

1. Justification of the Method

The observation that the radar is representative of short-term changes in wind speed again confirms the basic premise of scatterometry: microwave radars operating at centimeter wavelengths are sensitive to wind

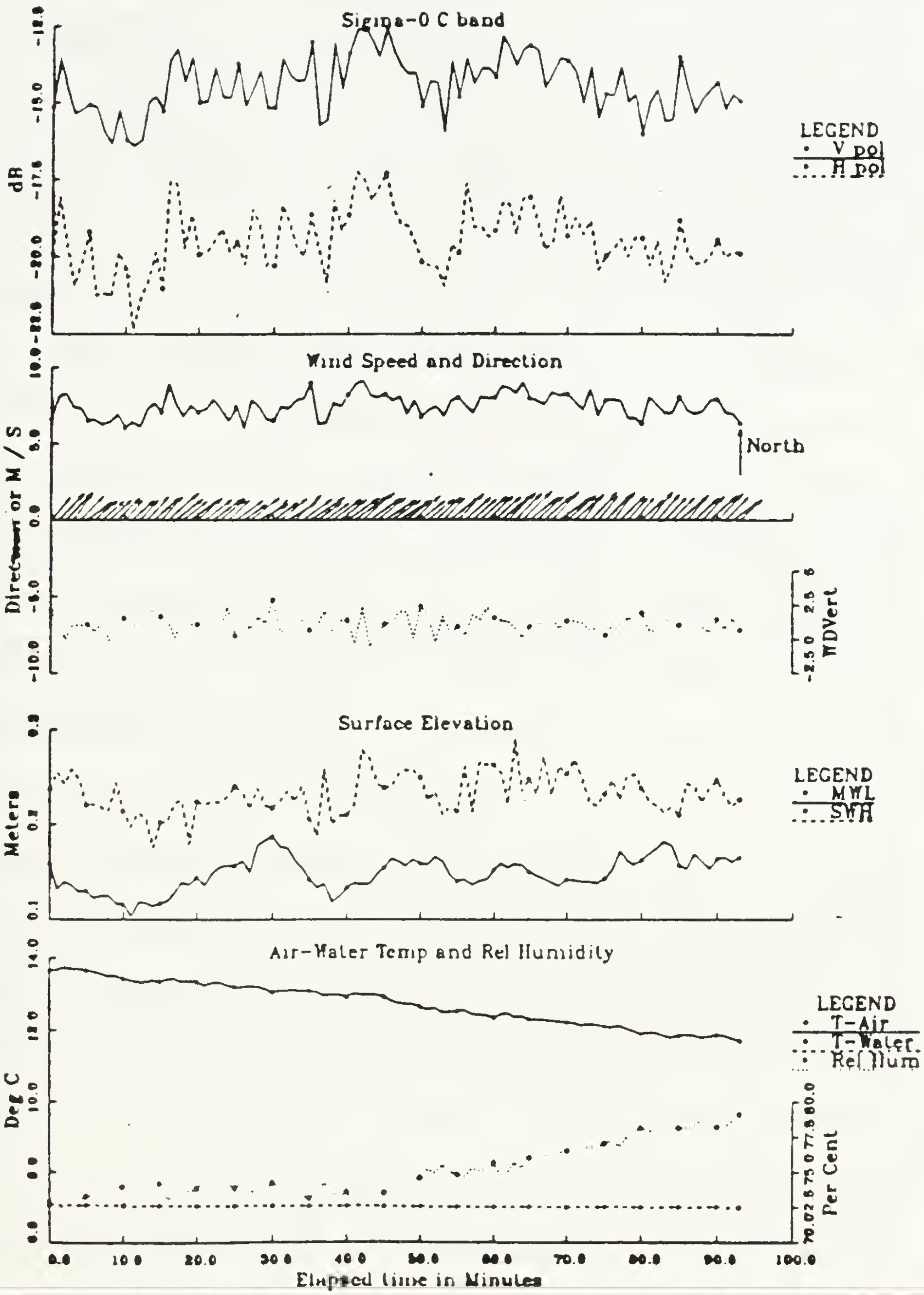

Figure 40. One-Minute C-Band NRCS and Associated Environmental Parameters as a Function of Time from the Start of Data Run 80, November 18, 0501 GMT.

generated capillary waves which have growth and decay time scales of the order of seconds. This implies that the proper development of a physically-based radar model function must consider the local (microscale) problem of momentum transfer to waves which are small compared to the longest gravity waves present in the larger, spatially-averaged (macroscale) wave field. Since the momentum transfer from the wind to waves is quantified by the friction velocity, u_*, in the growth rates of the short waves, the wind stress should be evaluated at time intervals comparable to the time-scale of these waves in microscale studies, i.e., O(seconds).

On the other hand, the macroscale wave field exerts a drag on the wind which modulates the wind stress. The stress is supported by a range of wavenumbers whereas the radar is wavenumber selective (within a small band about the Bragg wavenumber). Therefore, a different time scale is needed to quantify sea-state effects on the wind stress. With the assumption of horizontal homogeneity in the surface wave field and ignoring the microscale, the typical approach to this problem has been to determine an overall roughness scale, z_0, or drag coefficient, which parameterizes the wave drag on the wind (recall Chapter II, Section E) Wave state and stratification have time and space scales much larger than the microscale, therefore the drag coefficient has inherently longer time scales O(minutes) and larger spatial scales, (O(100m)).

The separation of the microscale effects from the macroscale is accomplished by writing

$$u_*^2\Big|_{O(\sec)} = C_D\Big|_{O(\min)}(U_z - U_O)^2\Big|_{O(\sec)} \tag{125}$$

In this expression, the observed rapid changes in the cross-section with wind speed are accounted for by using a short time scale wind speed to compute the wind stress. The modulation of the stress over longer time scales is accounted for by computing a longer term drag coefficient. The procedure is to compute u_* and the mean wind, <u>, from the wind components over the long time scale and then to form the ratio of u_*^2 to $<u>^2$ for the long-term drag coefficient. This drag coefficient is used in (125) with the short term wind speed average to compute a short term stress.

There are several ways to measure (compute) wind stress, to date the most reliable and accurate is the eddy covariance technique as used here (Geernaert, et al., 1988a; Fairall, et al., 1988). In this method, the instantaneous wind speed is considered to consist of a mean U_i, and fluctuating component, u_i'

$$u_i = U_i + u_i' \tag{126}$$

where u_i is the wind component in the i-th direction. The engineering requirements to be satisfied in the eddy correlation method are the necessity for reliable fast response wind, temperature and humidity sensors and a stable platform so that no artificial vertical motions are introduced; i.e., $\overline{w}$ must approach zero.

The stress is then estimated directly by forming the covariance between the fluctuating horizontal and vertical components of the wind and applying Reynold's rules of averaging[4]. The stress component in the x-direction is then

$$\overline{u'w'} = \overline{(u-U)(w-W)} \tag{127}$$

and, in the y-direction,

$$\overline{v'w'} = \overline{(v-V)(w-W)} \tag{128}$$

where the overbar denotes an average. The stress vector is then

$$\boldsymbol{\tau} = \rho\left(-\overline{u'w'}\hat{\mathrm{i}} - \overline{v'w'}\hat{\mathrm{j}}\right) \tag{129}$$

with magnitude

$$|\tau / \rho| = \left[\left(\overline{u'w'}\right)^2 + \left(\overline{v'w'}\right)^2\right]^{\frac{1}{2}} \tag{130}$$

and direction, α, relative to the wind direction, given by

$$\alpha = \tan^{-1}\left(\frac{\overline{v'w'}}{\overline{u'w'}}\right) \tag{131}$$

The velocity components are subjected to a coordinate transformation such that the $\overline{-u'w'}$ component is aligned with the (20 min mean) wind (along the shaft of the bivane) and $\overline{-v'w'}$ is to the right of the wind direction.

Turbulence theory provides the guidance for the separation of the time scales required in (125). It has been noted that a "spectral gap" occurs at periods of about one hour between the low frequency wind speed maximum ("synoptic peak") and the high frequency wind speed maximum ("turbulent peak"), Figure 41a (Lumley and Panofsky, 1964). From the figure it appears that if the averaging interval is between 0.4 and 4 hours then the longer period wind speed contributions will be separated from the higher frequency fluctuations, with the (apparently) best partition occurring between 0.7 and 1.0hr (42 to 60min). The figure is for overland data, a similar spectral gap occurs over water as obtained from Lake Ontario data, Figure 41b. (Pierson, 1983).

---

[4] For a stationary process, all the fluctuating quantities average to zero, the correlation between the fluctuations and the average quantities must vanish, and the averaging process applied to an average must reproduce the same average (Panofsky and Dutton, p. 88, 1984).

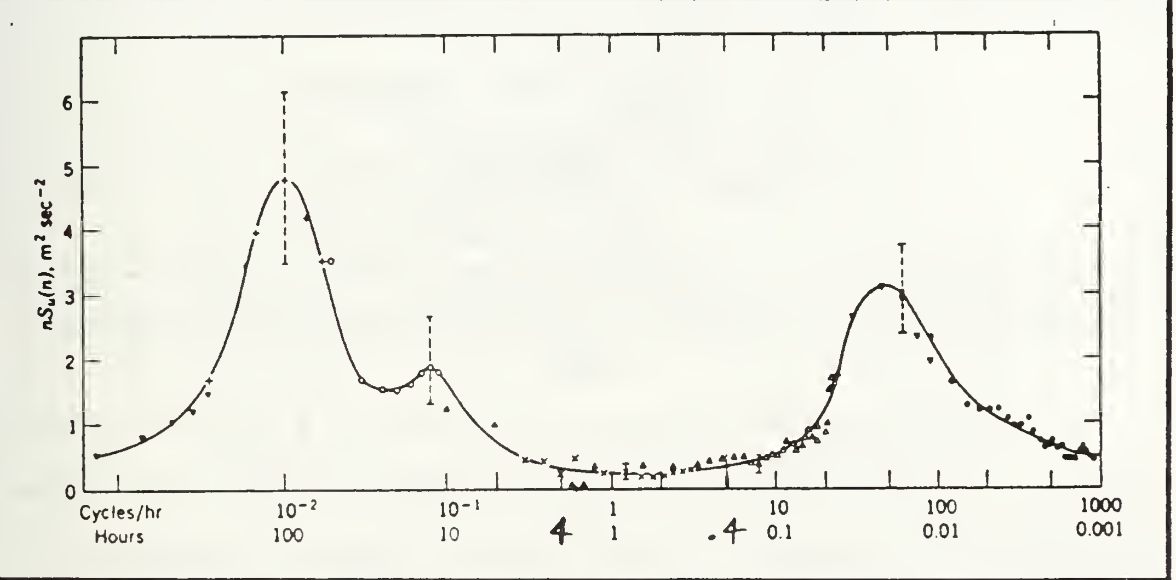

Figure 41a. Schematic Spectrum of Wind Speed Near the Ground Estimated from a Study of Van der Hoven (1957) (from Lumley and Panofsky, 1964)

The u-w cospectrum as computed with standard spectral methods can also be used to determine the appropriate averaging interval. As shown in Figure 42, most of the turbulent energy is contributed at frequencies between .001 Hz (17min) and 10 Hz. Therefore, averaging intervals at least

17min long are required for adequate representation of the fluctuating components. Longer averaging times will include energy from the synoptic scale features.

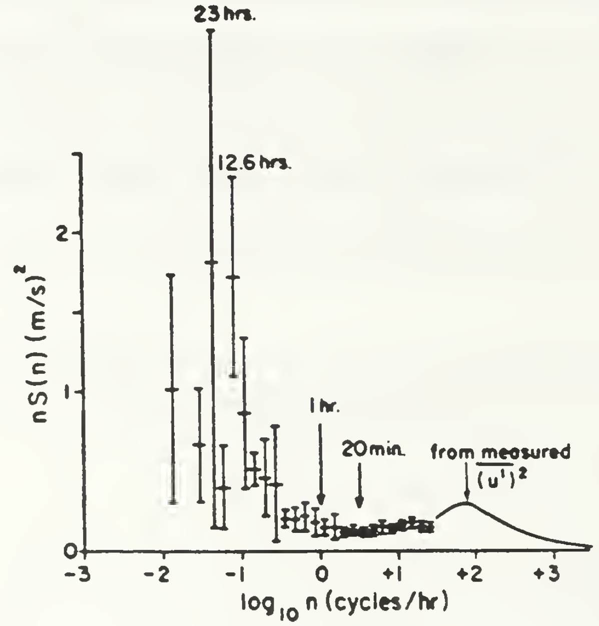

Figure 41b. Frequency Spectrum of Wind Speed Over Water from Pierson (1983)

The entire planetary boundary layer (PBL) has a characteristic time scale associated with the rotation and advection times of the largest eddies contained within the layer. The near-neutral PBL height in mid-latitude, h_{pl}, can be modelled by

$$h_{pl} = \frac{c\,U_*}{f} \qquad (132)$$

where c is an empirical constant of about 0.3 and f is the Coriolis parameter of order $10^{-4}\ s^{-1}$ (Tennekes, 1973). The largest eddies in the layer will be of height equal to h_{pl} and rotate at $\pi h_{pl}/U$, where U is the PBL mean wind speed, assuming the eddy is circular. Then

$$T = \frac{\pi h_{pl}}{U} \qquad (133)$$

or

$$T = \frac{.3\pi}{f}\sqrt{C_D} \qquad (134)$$

which is about 5min for C_D equal to 10^{-3}. Therefore, to measure these larger scale fluctuations requires time records of at least 10min to sample at the Nyquist frequency.

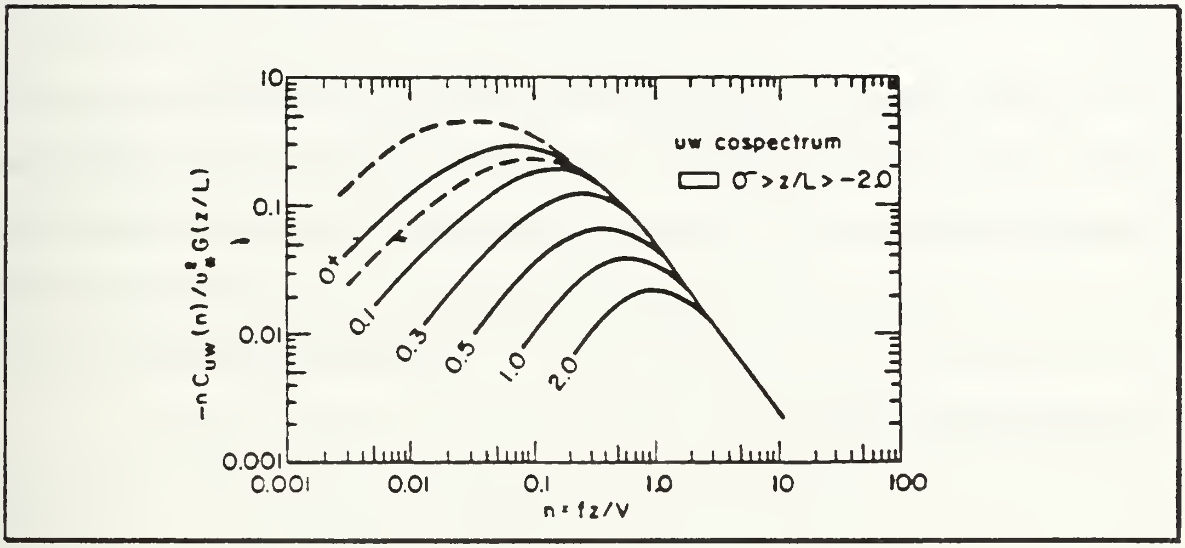

Figure 42. Normalized Stress Cospectrum for Varying Stability after Kaimal et al., (1972) (from Panofsky and Dutton, 1984)

The above considerations are summarized as follows: the turbulent covariance is adequately measured with a sampling interval of about 20min, which is twice the Nyquist frequency of the largest eddies in the boundary layer, and also still within the spectral gap between the synoptic and turbulent peaks in the wind speed spectrum. The fact that 20 minutes is at the upper limit of the spectral gap means the stress values will be slightly underestimated. Nevertheless, in this study a 20min averaging period was selected for the computation of the wind stress.

The wind speed averaging interval (microscale) was chosen at first for convenience to be 10s to correspond to the Ku-band radar azimuthal movements. However, this short time interval introduced significant variance in the computed short term stresses so that one minute running mean wind speeds, centered on the radar measurements, were subsequently used. The selection of a one-minute average was based on a calculation that showed the one-minute means to reduce the variance in the wind speed by 50%.

The choice of averaging interval for the wind stress determines the accuracy of the computed stress. Wyngaard (1973) recast Lumley and Panofsky's (1964) results to give an expression for the averaging time, $T_{u'w'}$, needed for a specified accuracy in the covariance. For neutral conditions at a measurement height, z, wind speed, u, and specified accuracy, ε, the averaging time is given by

$$T_{u'w'} = \frac{20z}{\varepsilon^2 U} \tag{135}$$

For lower wind speeds, the averaging time is longer unless compensated for by reducing the measurement height. Conversely, for a given wind speed, the averaging interval is longer at higher measurement heights. With $T_{u'w'}$ = 20min, z=11.5m, and U=7.5mps, the average accuracy of any particular covariance computed in the present study is ±16%. Under very unstable conditions, the numerator in (135) increases to 100z, therefore, the accuracy is reduced to ±35% of the true value.

With the acceptance of these accuracies comes the question of how exactly to calculate the averages. The averaging scheme must produce continuous averages which are differentiable to any order required by the equations of motion and they must satisfy Reynold's rules of averaging. Here it was decided to use a moving 20min average evaluated every 10s in order to maintain continuity of the drag coefficient between independent 20min records and to allow correlation of the computed drag coefficient with a particular 1min (microscale) wind speed. This averaging method allows each Ku-band azimuth bin to be assigned a unique stress value.

As Panofsky and Dutton (1984) point out, running averages are continuous but they do not satisfy Reynold's postulates exactly. They maintain that the defect is not serious as long as the averaging period is chosen in correspondence with the spectral gap.

3. Results of the Method

Using the 20min u_* and wind speed values, a 20min drag coefficient is computed and corresponding one-minute stresses (Figure 43a-c) , as well as a 20 min running mean bulk Richardson number (Figure 43e).

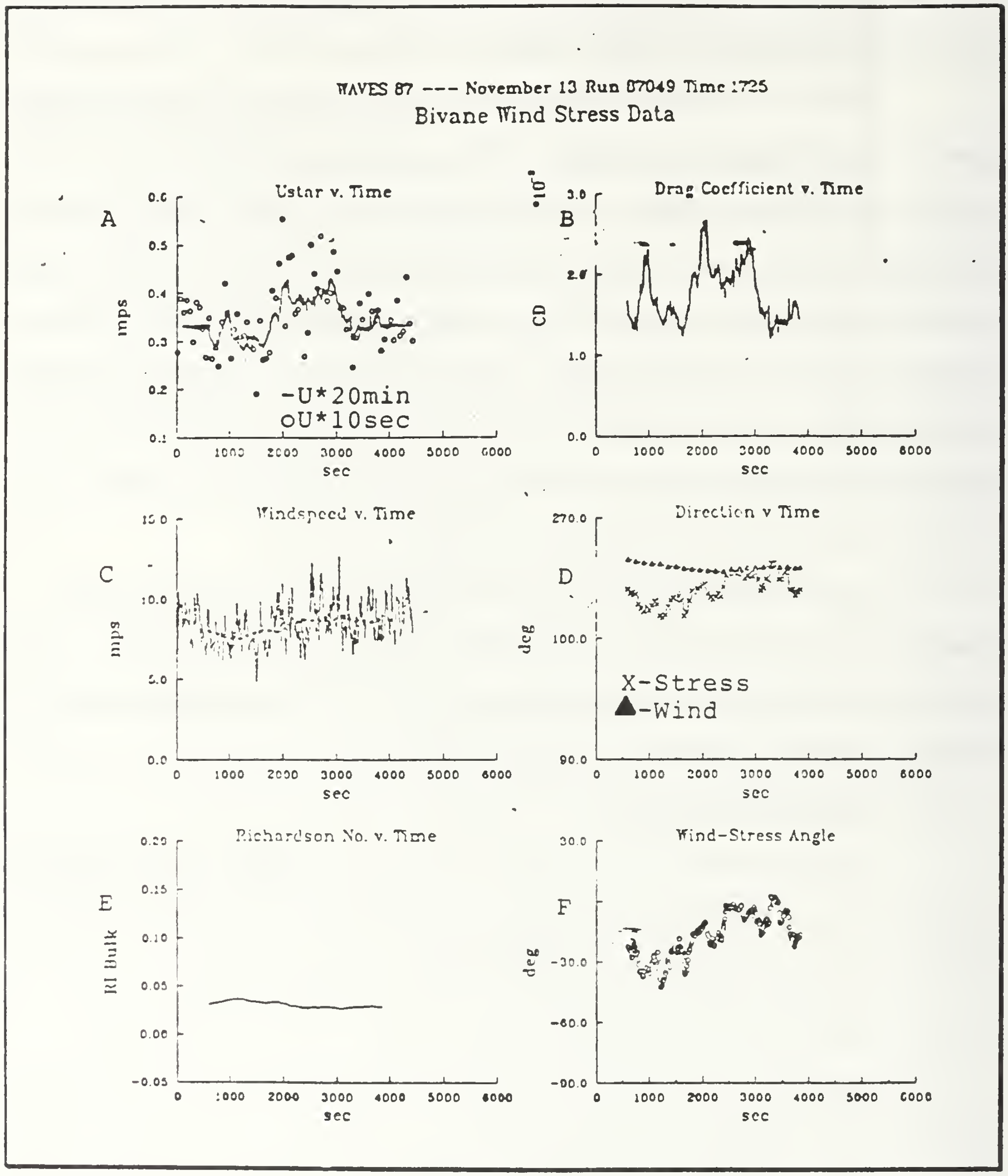

Figure 43. Wind and Stability Parameters as a Function of Time: (a) Wind Stress, (b) Drag Coefficient, (c) Wind Speed, (d) Wind and Stress Direction, (e) Bulk Richardson Number and (f) Relative Angle between Wind and Stress Directions

Variations in the azimuthal dependence of the NRCS may be due to relative differences between the wind direction and wind stress vector. Therefore, the wind vector and wind stress vector directions were computed and plotted (Figure 43d,f). In the example shown, the drag coefficient has a mean value of about .0018, no trend, but significant temporal variations, which span a range of values from .0012 to .0026. The twenty minute drag coefficient follows the variation of the stress as normalized by the mean wind speed. Similarly, the one-minute stress has the overall character of the longer-term 20 minute drag coefficient, but it also incorporates the effect of the short time scale variations in the wind speed.

The atmospheric stratification was stable for this data run as indicated by the positive value of the Richardson number. Under stable conditions, Geernaert (1989) found that the stress vector is often directed to the left of the wind vector as is shown in Figure 43f.

4. Conversion to a Neutral Wind Speed

The wind speed predictions of the existing scatterometer model functions are in terms of a neutral wind speed at 19.5m. Therefore, comparison of the results of this experiment to model predictions requires that the measured wind speeds be converted to their corresponding neutral values.

The procedure is to first convert the measured 20 minute drag coefficient to its neutral value using the integrated stability profile, equation (87). Then, the one-minute neutral wind speed at the measurement height is given by

$$u_N(11.5) = C_{D_N}^{-\frac{1}{2}} u_* \tag{136}$$

with the one-minute friction velocity, u_*. At any other level, z,

$$u_N(z) = u_N(11.5)\left[1 + \frac{\sqrt{C_{DN}}}{\kappa}\ln\left(\frac{z}{11.5}\right)\right] \tag{137}$$

The stability parameter, z/L, is required for the integrated stability function (83) and in this study it was obtained from equation (80) using the empirical relationship between z/L and Ri_B established by Donelan (1974):

$$\frac{z}{L} = \begin{cases} 7.4Ri_B & Ri_B < 0 \\ 6.0Ri_B & Ri_B > 0 \end{cases} \tag{138}$$

for $-0.05 \leq Ri_B \leq 0.02$ and wind speeds $4 < U(10) < 17$m/s. Here, the twenty minute running mean value of the bulk Richardson number was used in (138).

D. COMPUTATION OF THE WAVE FIELD PARAMETERS

1. One-Dimensional Wave Spectra

One-dimensional wave spectra were computed using measurements from the wave staff at the center of the pentagonal array. The laboratory calibration equations converted the wave staff output voltage to surface elevation and fast Fourier transforms were used to evaluate the spectra (Bendat and Piersol, (1986)). Since the data runs varied in length from fifteen to ninety-five minutes, the 20Hz data were blocked in 51.2s records (1024 points) to ensure sufficient degrees of freedom for the computation of a reasonable spectrum for even the shortest runs.

First order descriptive quantities obtained from the one-dimensional spectra were the frequency (period) of the spectral peak, f_p, and peak wavelength, L_p. The wavelength was computed from the linear wave dispersion relation, using the peak frequency and the numerical method of Wu and Thornton (1986); i.e., for a given wave period, T, the wave length is

$$L_p = \frac{g}{2\pi} T^2 \tanh \frac{2\pi d}{L_p} \tag{139}$$

where d is the water depth. The significant wave height was computed from the standard deviation of the surface elevation, σ

$$H_{\frac{1}{3}} = 4\sigma \tag{140}$$

Second order quantities computed were the significant slope

$$\S = \frac{\sigma}{L_p} \tag{141}$$

peak phase speed

$$c_p = f_p L_p \tag{142}$$

and wave age

$$W = \frac{c_p}{U} \tag{143}$$

for wind speed, U. These quantities are descriptive of the degree of wave development: longer waves have smaller slopes and faster propagation speeds.

2. Two-dimensional (Directional) Wave Spectra

A limited number of directional spectra were computed using the full array of wave staffs and the maximum likelihood processing method outlined in Tsanis and Donelan (1988). The one-dimensional spectra were frequently noted to be bimodal at low wind speeds (containing low and high frequency peaks), and under these circumstances the radar cross-section exhibited anomalous azimuthal behavior. Therefore, the purpose of these directional spectra was to confirm that the long wave (low frequency peak) was traveling down the long axis of the lake and the short wave (high frequency peak) was more or less in the wind direction. The hypothesis was that if the swell was propagating at a moderate angle to the wind it may modulate the short wind waves and Bragg waves, hence the azimuthal dependence of the radar backscatter.

E. SUMMARY

This section has described the data processing methods used to convert the WAVES87 raw data into useable geophysical and radiometric quantities. The final data set consists of the Ku-band (10s) and C-band (1min) NRCS temporally collocated with wind speed, air and water temperatures, significant wave height, bulk Richardson number, stability parameter, neutral wind at several heights, wind stress, and measured and neutral drag coefficients. Each data run also has associated with it a one-dimensional wave spectrum from which peak frequency, wavelength, significant slope, phase speed and wave age are computed. A set of twelve directional spectra, representative of a range of wave conditions, was obtained for the initial examination of long wave effects on the radar cross-section.

V. DISCUSSION AND RESULTS

A. INTRODUCTION

Methods by which the raw data were processed to obtain the radar cross-sections and collocated geophysical parameters of interest were described in the previous chapter. Random and systematic errors of each variable must be kept in mind as the following analyses and interpretations are performed. An additional source of variability is that the correlations between the radar measurements and the geophysical variables involve different temporal and spatial averaging schemes. In spite of these caveats, clear dependencies of the radar cross-section on environmental parameters will be demonstrated.

The organization of this chapter follows the schematic diagram of Figure 1. The behavior of the NRCS with wind speed will be discussed first, followed in turn by discussions of the observed effects of wind direction, long waves, atmospheric stratification and water temperature.

B. NRCS DEPENDENCE ON WIND SPEED PARAMETERS

As noted in the discussions of the scatterometer model functions, there is some controversy regarding the appropriate wind speed parameter to relate to the NRCS (i.e.; traditionally the wind speed, neutral wind speed or wind stress). Ideally, the most appropriate wind parameter should reduce the number of dependent variables; in particular, eliminate the stratification dependence and reduce the wave dependence. The possibilities are then to use what is known as the neutral wind at some level (equation 137) or to use directly the wind stress at the surface. As a measurement convenience, existing model functions predict neutral wind speed at 19.5m although it is quite certain that this rather artificial quantity is not responsible for the generation and growth of the capillary waves to which the NRCS is sensitive. On the other hand, the (neutral) wind speed very near the sea surface is included dynamically in some expressions for the short wave growth rate, which hold that it is the ratio between the wind speed and phase speed of the waves which amplifies the waves.

The difficulty with the choice of the neutral wind at any level is that its determination is based on a particular surface or boundary layer model: i.e., z_0 or drag coefficient. Air-sea interaction specialists have yet to identify an open ocean standard which normalizes the drag coefficient for wave state in addition to measurement height, wind speed, and stability. Even with a satisfactory standard, it is not necessarily possible to extend the assumed logarithmic profile directly to the surface since the waves influence the wind field above them up to about one wave height (Snyder, et al., 1981). Therefore, correlation of the wind just above the surface with radar backscatter is hindered by the difficulty of measuring the near surface wind.

The alternate parameter of choice is then the friction velocity or wind stress, which by virtue of its definition, is stability independent. However, verification of a wind stress algorithm for the scatterometer has the same verification problem of the drag coefficient/neutral wind verification problem mentioned above. While the use of wind stress should hypothetically eliminate a second order dependence on stability, the influence of wave state on the resulting model function based on friction velocity may increase. Note that the stress represents the slope spectrum of all surface waves while Bragg scattering is due to waves within a small range of wavenumbers; i.e., wave modulation of the stress spectrum will differ from the degree of Bragg wave modulation by longer waves. At some point a major effort to measure the wind stress at sea will have to be conducted in order to establish the open ocean drag coefficient to which all other measurements can be scaled.

In the present study, the wind stress was measured using a bivane anemometer and processed as described in the previous chapter. The friction velocity values were used to determine the drag coefficient and then the neutral wind. All of the neutral winds were based on stability corrections which used the bulk Richardson number to estimate z/L as in (80). Friction velocity values less then 0.12m/s were omitted from the plots and data interpretations (wind speed too low for bivane), as were points for which the relative humidity was above 90% (probable rain) and two runs which were of questionable value (one of short duration and one contaminated by specular returns from what appears to be a solid object). The NRCS values were all reduced by 1.0dB in the following plots to account for the wider beamwidth of the tower radar to allow comparison with the satellite based model functions.

The data were stratified by upwind, downwind, crosswind near 90° and crosswind near 270° relative wind angles with an allowance of ±5° about each prescribed direction. The vertically and horizontally polarized "smoothed" radar cross-sections were then plotted as a function of the measured friction velocity (Figures 44, 45) and the neutral wind at 19.5m (Figures 46 and 47 for comparison with the model functions) and the neutral wind at 1m (Figures

48 and 49). The 1m neutral wind level was employed instead of one-half Bragg wavelength in order to be more realistic about the application of the logarithmic wind profile in the presence of the waves.

The figures show the dependence of the cross-section on the wind parameters for each of the incidence angle settings of the Ku-band radar. There is still considerable scatter in the data; however, the scatter of the data points and the slopes of the lines at each angle are consistent with previous results. At nadir there is a small negative dependence on wind speed or stress, reflective of the increased scatter of the incident radiation as the surface becomes roughened by the wind waves[1]. The ten degree incidence angle is nearly wind speed independent although the best fit least squares line does generally assign either a small positive or negative slope value. The slopes of the lines increase with incidence angles up to 60° (the downwind slopes being the exception). At 60° the h-pol data begin to show sensitivity to incidence angle by becoming more scattered. The 80° data still display some dependence with wind speed in the upwind direction for the vertical polarized data; the horizontal polarized cross-sections at 80° generally fall below the noise level of the radar.

---

[1] This data set could be used to examine the wind speed algorithm used in altimetry, especially as regards the significant wave height contribution to the measured cross-section. It should be noted here, however, that the data editing criteria used in the present analysis no doubt "overedit" at nadir where the cross-sections are more a function of the long waves than the vagaries of the wind stress. In addition, since the backscatter is isotropic in direction, all of the data points should be used irrespective of wind direction instead of being stratified by relative wind angle.

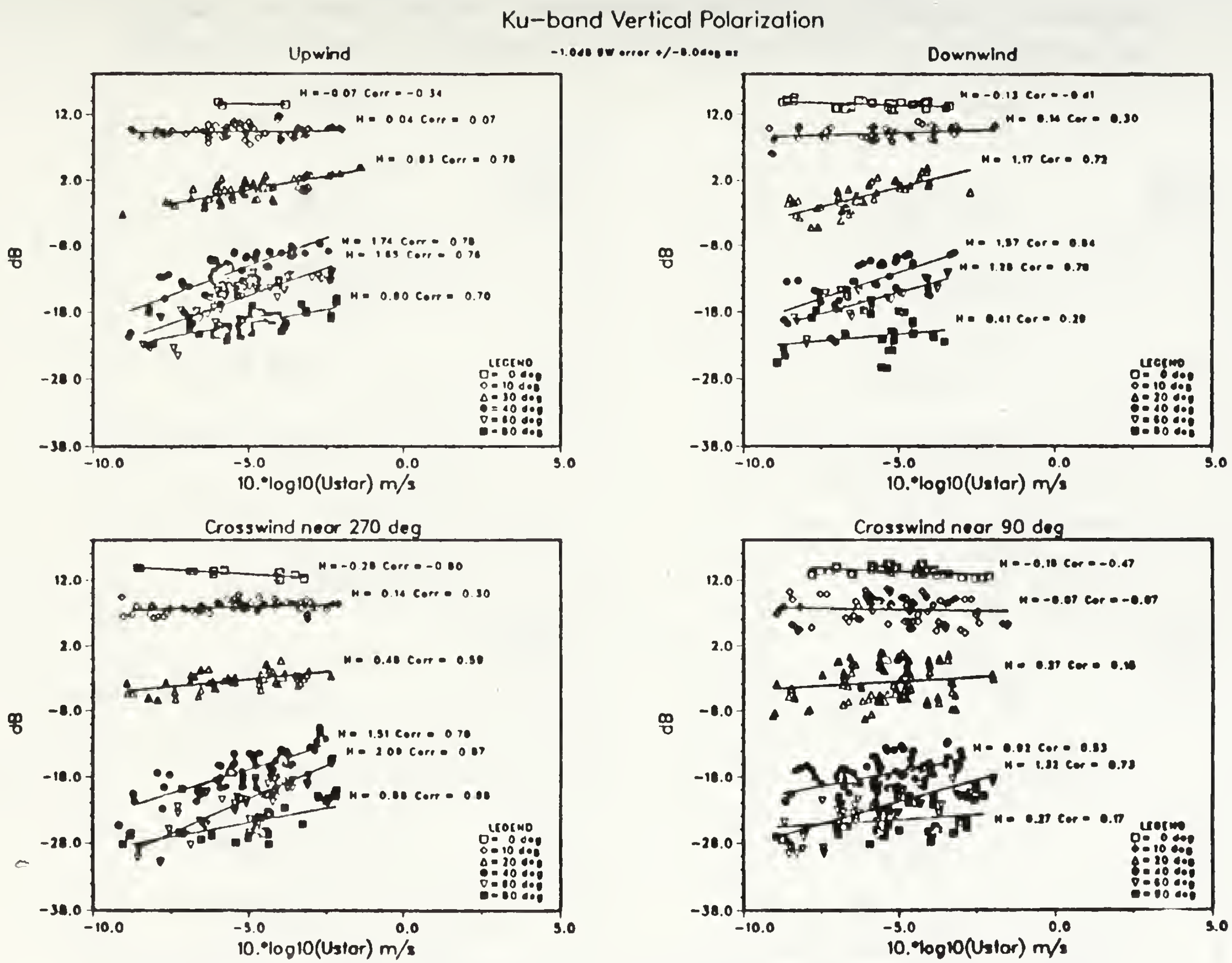

Figure 44. Ku-band Vertical Polarized NRCS versus Friction Velocity for Multiple Incidence Angles. Clockwise from Top Left: Upwind, Downwind, Crosswind near 90°, Crosswind Near 270°

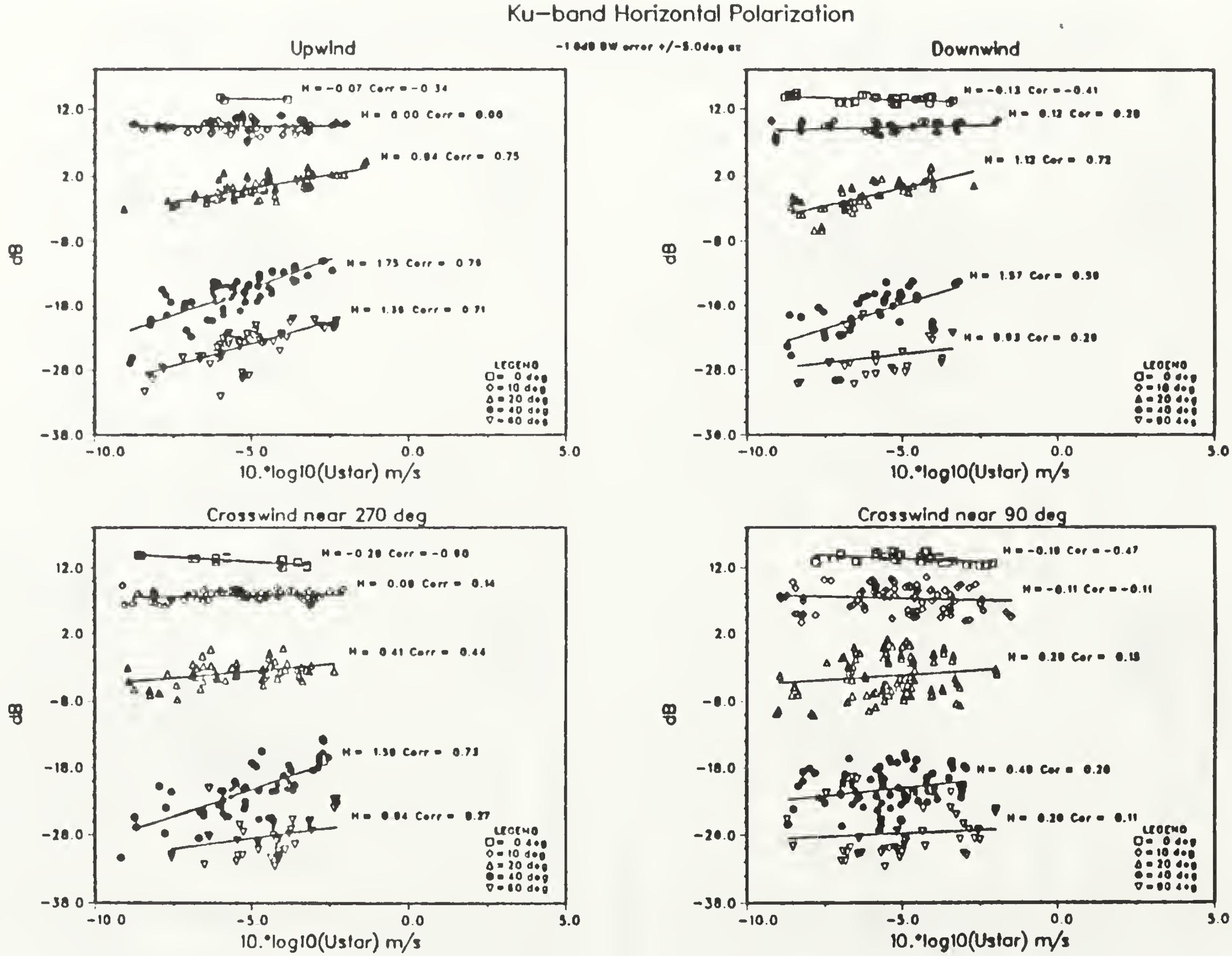

Figure 45. Ku-band Horizontal Polarized NRCS versus Friction Velocity for Multiple Incidence Angles. Clockwise from Top Left: Upwind, Downwind, Crosswind near 90°, Crosswind Near 270°

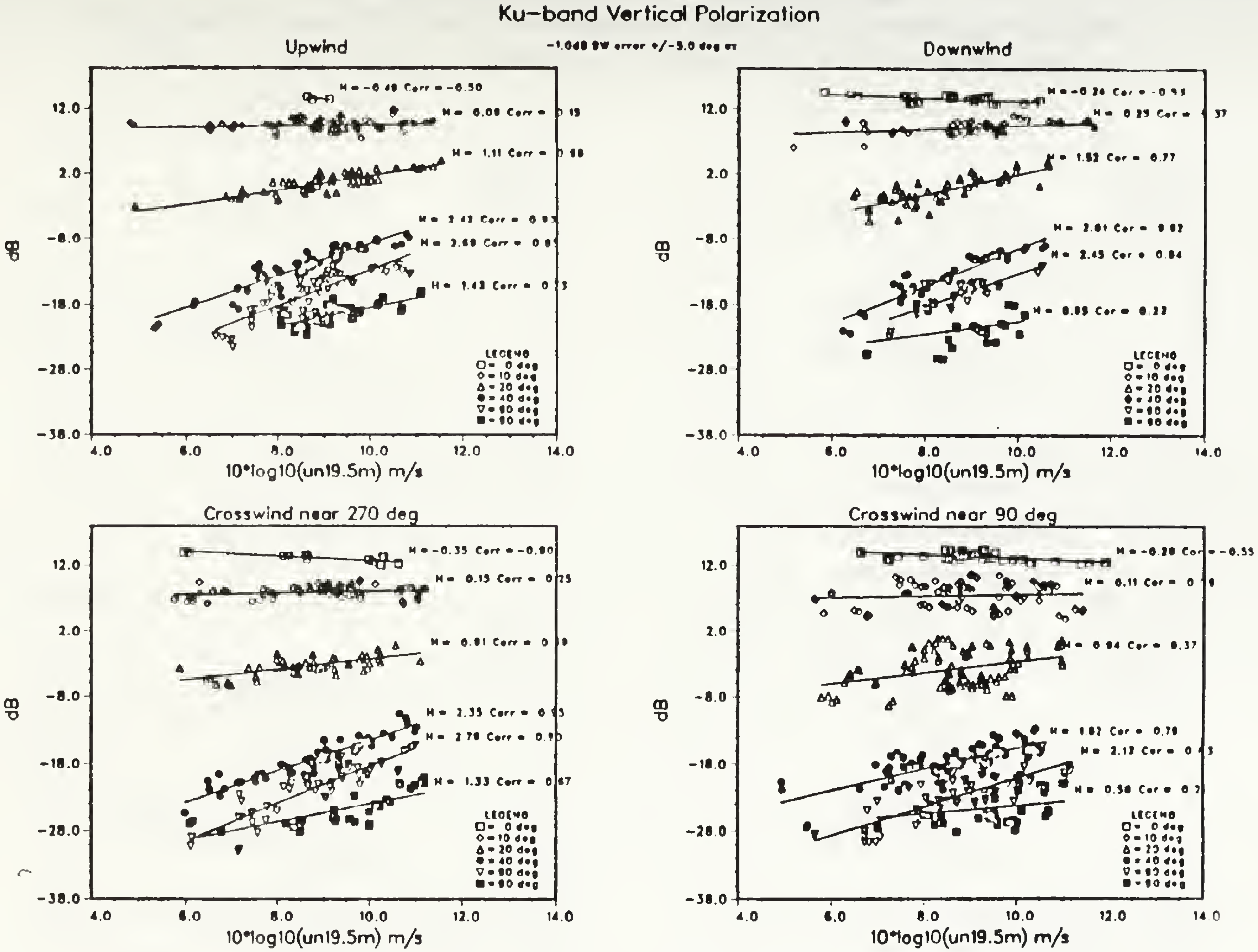

Figure 46. Ku-band NRCS (v-pol) Versus Neutral Wind Speed at 19.5m for Multiple Incidence Angles. Clockwise from Top Left: Upwind, Downwind, Crosswind Near 90°, Crosswind Near 270°

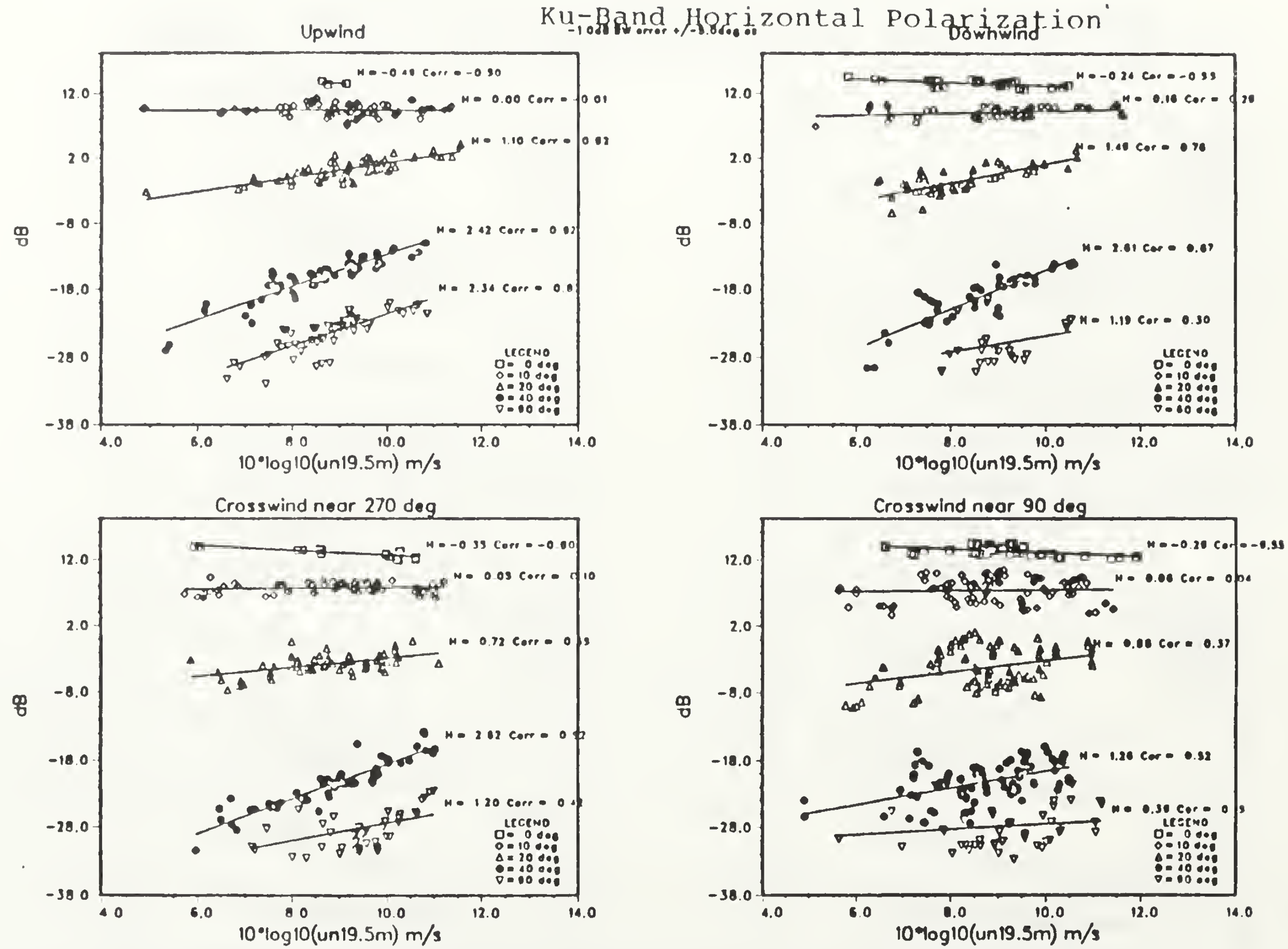

Figure 47. Ku-band NRCS (h-pol) Versus Neutral Wind Speed at 19.5m for Multiple Incidence Angles. Clockwise from Top Left: Upwind, Downwind, Crosswind Near 90°, Crosswind Near 270°

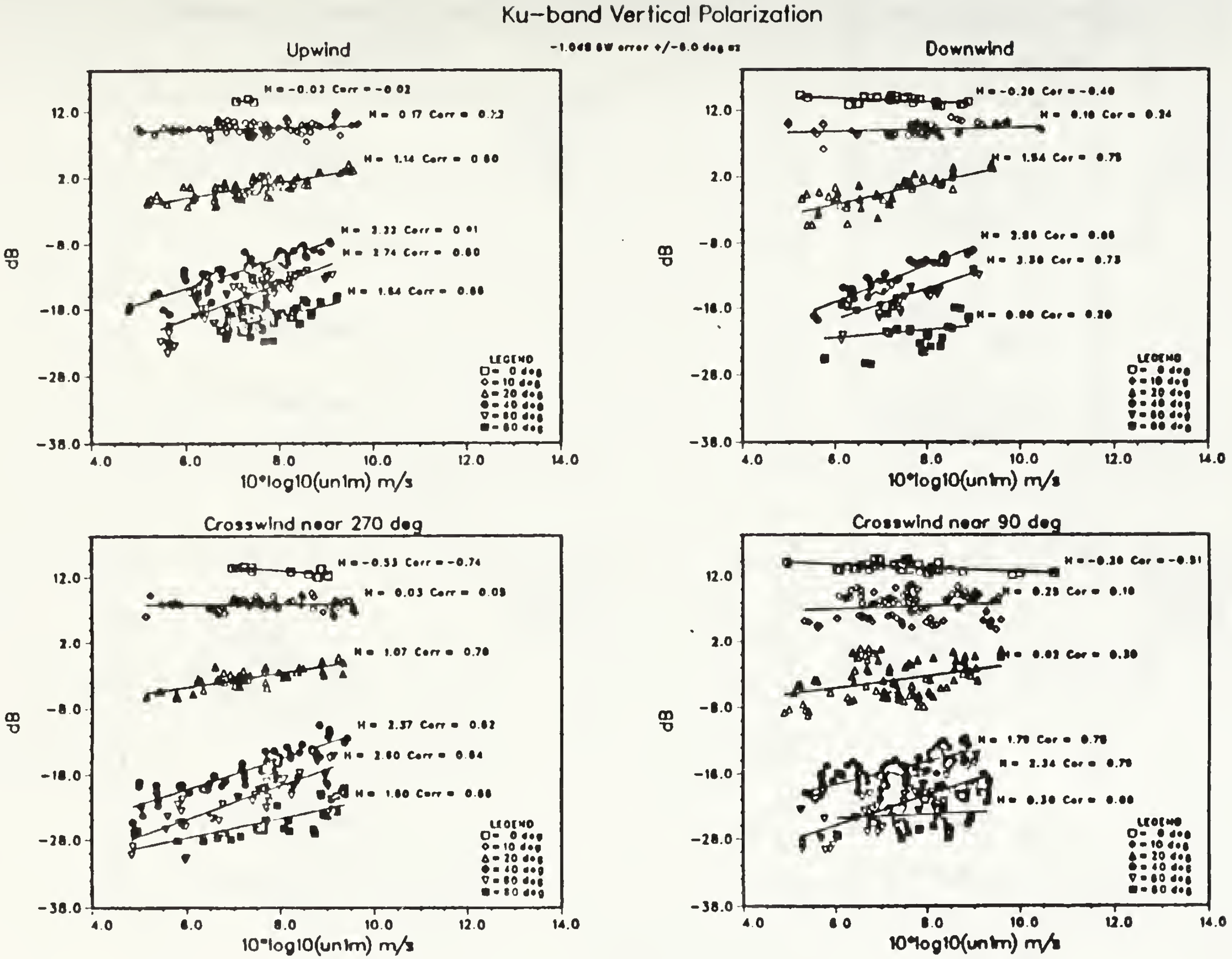

Figure 48. Ku-band NRCS (v-pol) Versus Neutral Wind Speed at 1m for Multiple Incidence Angles

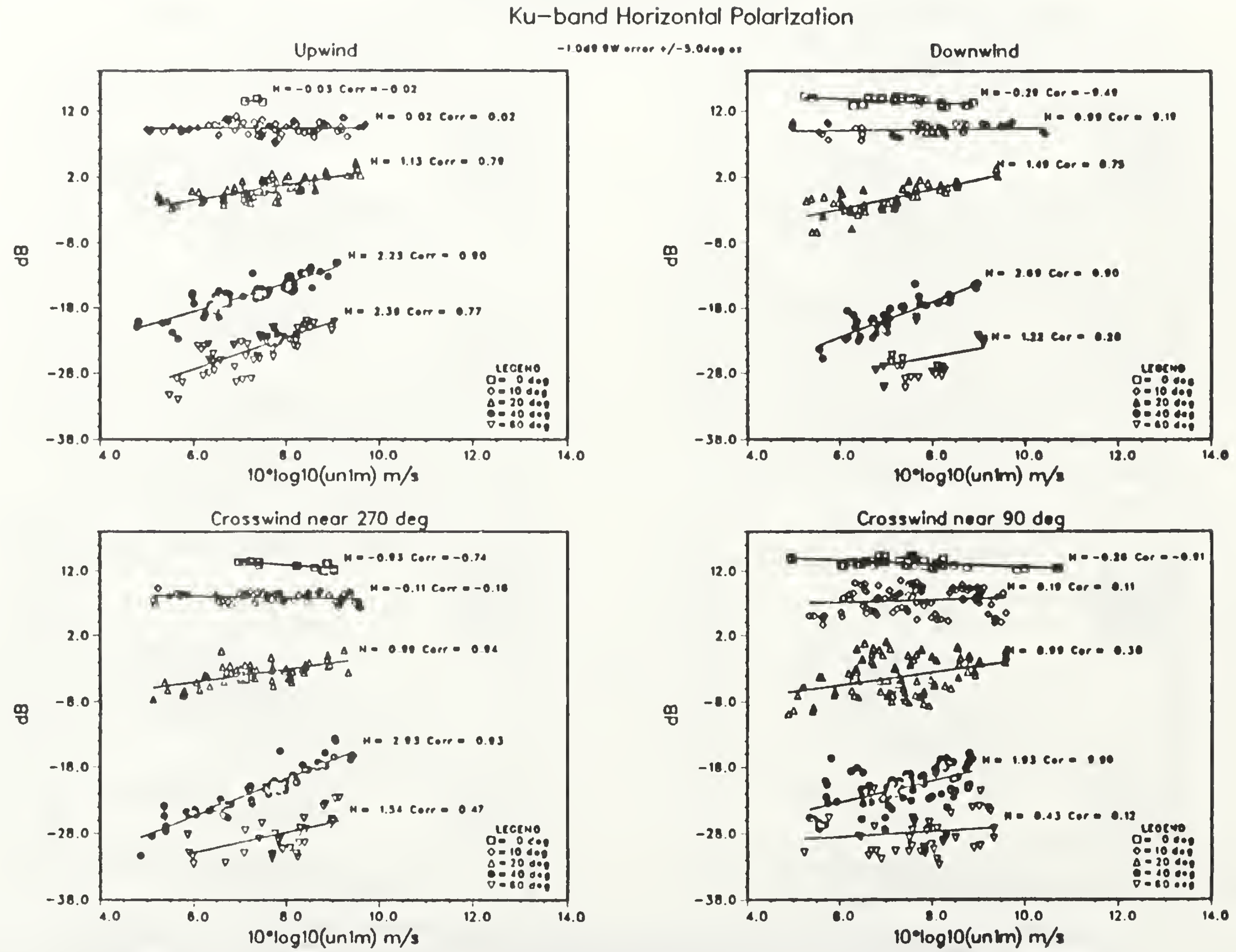

Figure 49. Ku-band NRCS (h-pol) Versus Neutral Wind Speed at 1m for Multiple Incidence Angles

Comparison of the slopes of the neutral wind speed lines with previous results show that the radar cross-sections from Lake Ontario display stronger dependence on the wind speed. A compilation of previous results for upwind v-pol data is reproduced here from Phillips (1988) in Table VI, where the Ku-band data are those listed under 13.9 and 14.6GHz. The slopes at 20° and 40° differ by about 0.3 to 0.7 and by about 1.0 to 2.0 at 60°. The slope coefficients (Figures 44 and 45) on the ustar curves at the lower three incidence angles (0°, 10° and 20°) are comparable to the neutral wind speed slopes, but are significantly lower at 40° and 60°, e.g., 1.6 v. 2.4 upwind, v-pol.

The correlations on friction velocity are poorer than the corresponding neutral wind speed values. In this analysis the neutral wind speeds are derived from the measured wind stress, but they have been smoothed by the ratio of the measured and neutral drag coefficient in the conversion process. That is, the neutral wind speed is defined by

$$U_N(11.5) = C_{DN}^{-\frac{1}{2}} u_* \qquad (144)$$

Here,

$$u_* = C_D^{\frac{1}{2}} U(11.5) \qquad (145)$$

TABLE VI. COMPARISON OF NRCS VERSUS WIND SPEED SLOPE COEFFICIENTS WITH PREVIOUS STUDIES

Partial table reproduced from Phillips (1988).

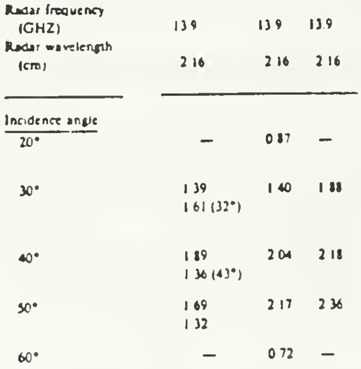

Radar frequency (GHZ)	13.9	13.9	13.9
Radar wavelength (cm)	2.16	2.16	2.16
Incidence angle			
20°	—	0.87	—
30°	1.39 1.61 (32°)	1.40	1.88
40°	1.89 1.36 (43°)	2.04	2.18
50°	1.69 1.32	2.17	2.36
60°	—	0.72	—

Summary of Upwind Slope Coefficients from Present Study

Incidence Angle	V-POL				H-POL			
	u_*	$u_N(19.5)$	$u_N(1)$	Scaled $u_N(19.5)$	u_*	$u_N(19.5)$	$u_N(1)$	Scaled $u_N(19.5)$
20°	.83	1.1	1.1	.98	.84	1.1	1.1	.97
40°	1.7	2.4	2.3	1.6	1.7	2.4	2.2	1.5
60°	1.6	2.7	2.7	1.3	1.3	2.3	2.4	.84
80°	.80	1.4	1.6	1.1	--	--	--	--

Summary of Upwind Correlation Coefficients from Present Study

Incidence Angle	V-POL				H-POL			
	u_*	$u_N(19.5)$	$u_N(1)$	Scaled $u_N(19.5)$	u_*	$u_N(19.5)$	$u_N(1)$	Scaled $u_N(19.5)$
20°	.76	0.85	.80	.77	.74	.82	.78	.74
40°	.79	.93	.91	.70	.78	.92	.90	.65
60°	.76	.85	.80	.55	.71	.82	.77	.42
80°	.70	.73	.66	.79	--	--	--	--

Summary of Upwind Exponent Standard Errors from Present Study

Incidence Angle	V-POL				H-POL			
	u_*	$u_N(19.5)$	$u_N(1)$	Scaled $u_N(19.5)$	u_*	$u_N(19.5)$	$u_N(1)$	Scaled $u_N(19.5)$
20°	.08	0.08	.09	.09	.08	.08	.10	.07
40°	.16	.11	.12	.19	.16	.12	.13	.10
60°	.17	.20	.25	.23	.16	.20	.24	.21
80°	.12	.20	.26	.13	--	--	--	--

Therefore, the neutral wind is obtained from

$$U_N(11.5) = \left(\frac{C_D}{C_{DN}}\right)^{\frac{1}{2}} U(11.5) \qquad (146)$$

This expression shows that the variability of the neutral wind is reduced, since the ratio of the measured and neutral drag coefficients is nearly equal to one except for very stable conditions for which the ratio decreases to about 0.5. Therefore, instead of being susceptible to variability in both the drag coefficient and the wind speed, the neutral wind variability is due mostly to changes in the wind speed, since stability is accounted for in the neutral drag coefficient.

If the friction velocity slope coefficients are accepted as valid, then the differences in slopes between the upper and lower incidence angles and the differences from the neutral wind values can be interpreted in terms of the sea state. At nadir and 10°, the cross-section values are due to scattering from a rough surface; i.e., basically the wind waves, not the Bragg-length capillary waves. However, as the incidence angle steps into the Bragg domain (say 20° to 60°), the capillary waves become the critical feature of the sea surface responsible for the observed returns. These waves of slow phase speed and large steepness are extremely responsive to changes in wind speed or stress and to the background state of the sea. One quantity which links all of the sea states is the drag coefficient, and the observed variations in the slopes of the wind stress/wind speed lines imply that this coefficient has a sea state dependence.

Recall the relationship between the wind stress, friction velocity and neutral wind speed,

$$\frac{\vec{\tau}}{\rho} = u_*^2 \cong C_D U_N^2 \tag{147}$$

If the neutral drag coefficient were only a function of wind speed, then according to this expression, the stress would be proportional to a power law dependence on U_N with an exponent greater than 2 and approaching 3. Similarly, if the NRCS is proportional to the wind stress then it should also have the same power law dependence on the neutral wind speed. The NRCS dependence on neutral wind is observed to be generally greater than two and approaching three at intermediate incidence angles which strongly suggests a stress dependence. However, the fact that both the friction velocity and the neutral wind speed slope coefficients are less than what is expected also suggests a different functional dependence for the drag coefficient; i.e., a dependence on sea state.

The possibility of a sea state dependent drag coefficient can be examined by comparing the lake NRCS versus wind speed slopes to those predicted by the model functions discussed earlier. The models were run at 40°, v-pol for windspeeds ranging from 1 to 15m/s. The cross-sections from each of the models and the lake observations are shown in Figure 50, where the line labelled "Lake normal" is the best fit line shown in Figure 46. The vertical error bar at $U_N(19.5)$ = 5.5m/s is the ±1 standard deviation of the absolute calibration error of the radar as determined from the ten degree data; i.e., the level of either of the lines could go up or down by about 1.9dB.

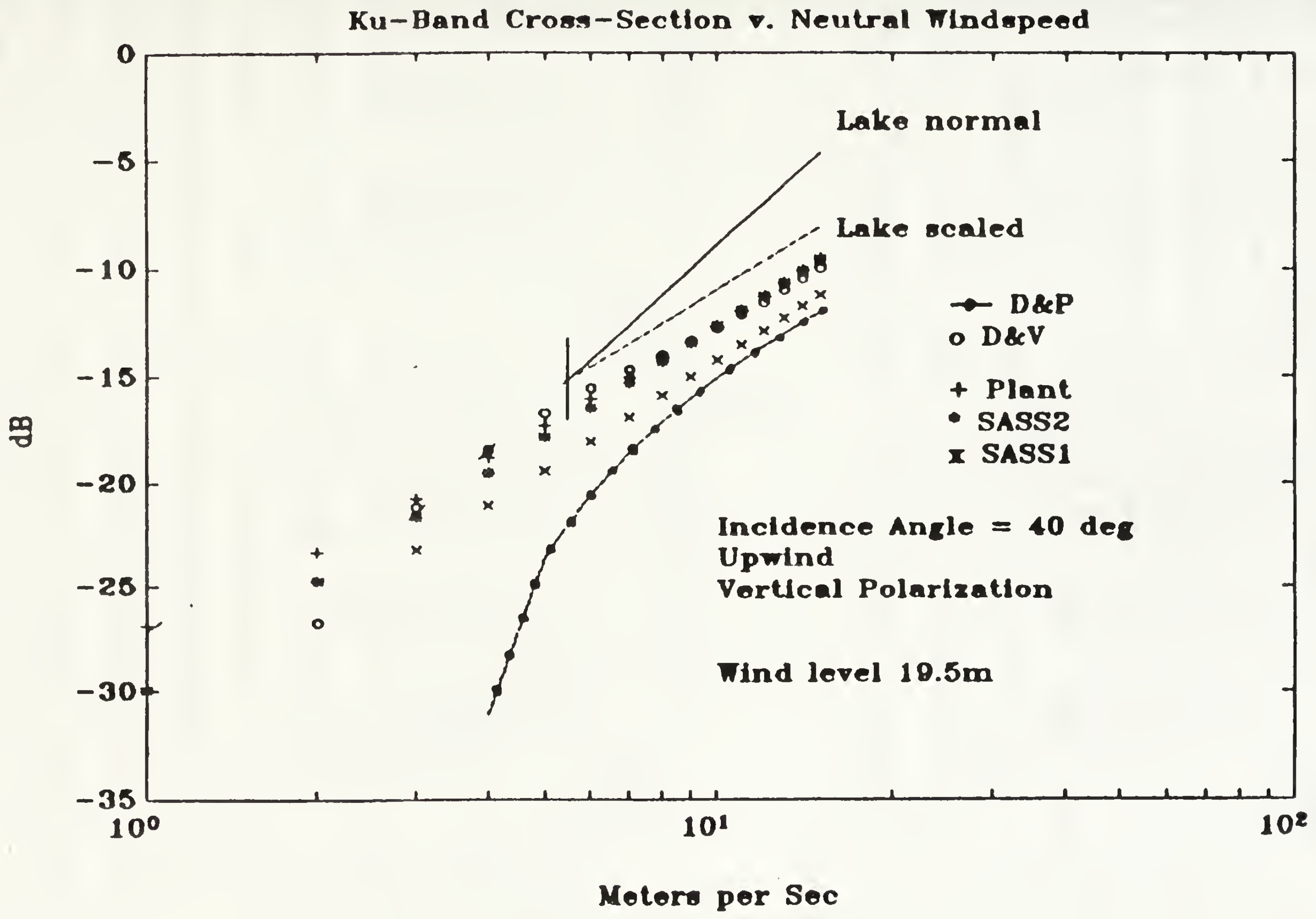

Figure 50. NRCS Versus Neutral Windspeed from Lake Data (as measured) Models, and Scaled Lake Data

The best fit line of the lake observations (Lake normal) is considerably steeper than the corresponding model function predictions. A possible explanation for this result is found by noting that all of the model functions displayed use the Large and Pond open ocean drag coefficient to convert measured wind speed to stress and/or neutral wind speed. However, in the lake the neutral drag coefficient has a greater dependence on wind speed than the Large and Pond results for the open ocean. This is due to the fact that the lake waves are often in an active growth stage and even the longest waves are quite steep by comparison to open ocean swell (recall Figure 12). Therefore, for a given wind stress (and hypothetically, also for a given NRCS) the neutral wind for open ocean conditions is higher than the corresponding lake value through the scaling

$$U_{N\,Ocean} = \left(\frac{C_{DN\,Lake}}{C_{DN\,Ocean}} \right)^{\frac{1}{2}} U_{N\,Lake} \qquad (148)$$

where the ratio of the Large and Pond (88) and Donelan (89) drag coefficients has been used as a first guess scaling factor. The line labelled "Lake scaled" illustrates the result of this scaling at 40° incidence and Figures 51 and 52 show the results for all of the incidence angles. The slope of the scaled line is now parallel to the open ocean results implying that the sea state difference between the lake and ocean has an effect and should be incorporated in the drag coefficient. This also implies that the wave influence on both the stress and NRCS is similar but not the same; i.e., for a given U_N, the NRCS and u_* both increase with increasing long wave slope. The scatter in the converted points in Figures 51 and 52 is a ramification of the fact that the Large and

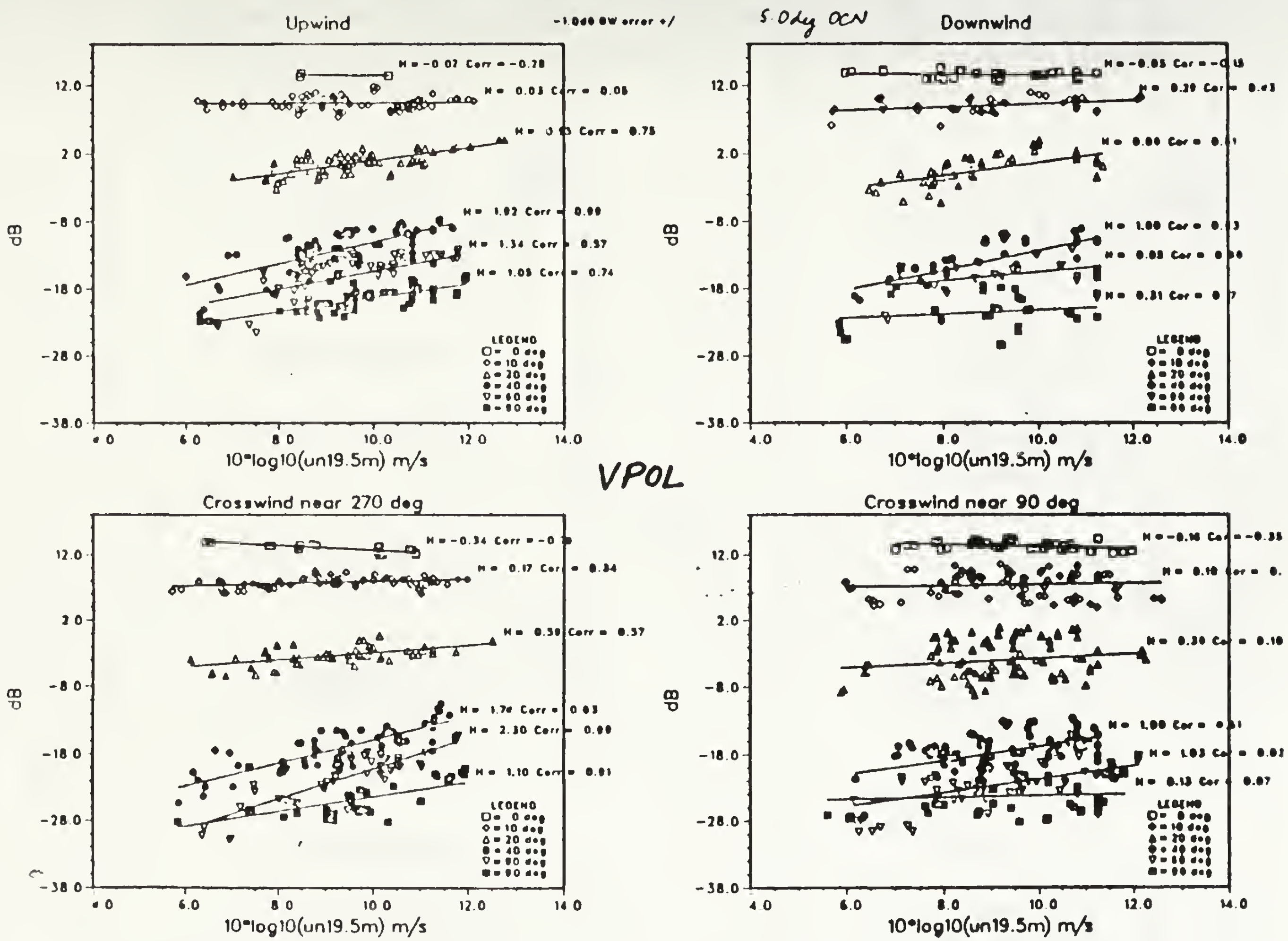

Figure 51. Scaled NRCS Versus Neutral Windspeed for Ku-band Vertical Polarized Data and Multiple Incidence Angles, Clockwise from Top Left: Upwind, Downwind, Cross-Wind near 90°, and Crosswind at 270°

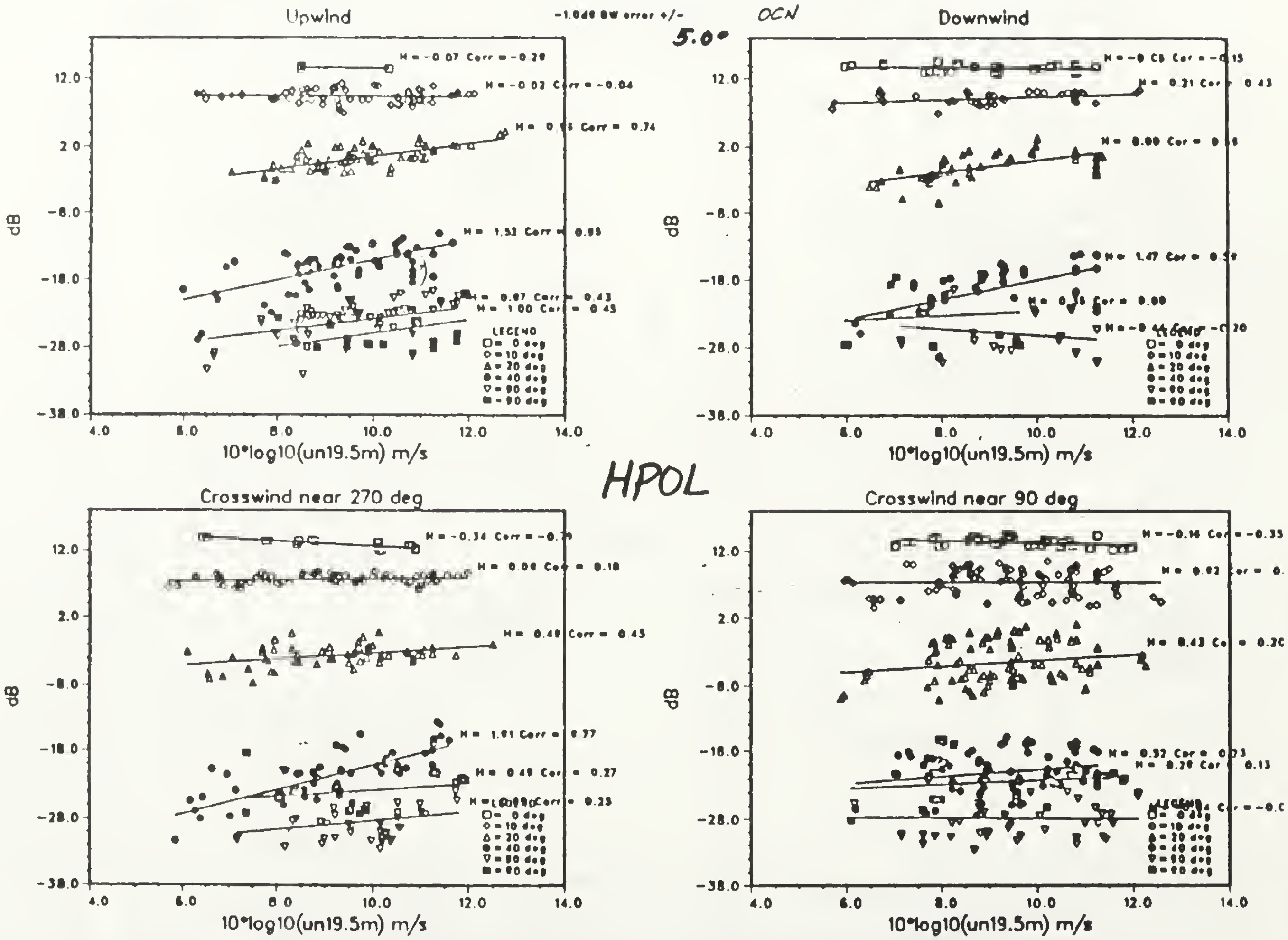

Figure 52. Scaled NRCS Versus Neutral Windspeed for Ku-band Horizontal Polarized Data and Multiple Incidence Angles, Clockwise from Top Left: Upwind, Downwind, Cross-Wind near 90°, and Crosswind at 270°

Pond and Donelan wind speed dependent drag coefficients explain only a part of the variance in the wind stress.

In summary, the radar cross-sections have been analyzed as a function of neutral wind speed and wind stress. The overall behavior of the cross-section vs. wind parameter curves are consistent with previous results which show the dependence to be negative at nadir, transitioning through zero slope at 10°, and becoming positively correlated above 10° incidence. The wind stress and neutral wind speed exponents are similar at lower incidence angles but the wind stress exponent is smaller than the wind speed exponent at the intermediate, Bragg-scatter incidence angles. This observation, and the steepness of the lake wind speed curve relative to the open ocean model function curves, suggests that the cross-section in the Bragg domain is affected by the spectral characteristics of the non-Bragg waves.

C. NRCS DEPENDENCE ON WIND DIRECTION

1. General Observations

The second most characteristic feature of the scatterometer signal is its cosine-like dependence on the relative angle between the radar antenna and the wind direction (recall Figure 2b). This behavior was first examined empirically with a series of aircraft flights in which circular flight tracks were used to generate the relative angles between the wind and radar (Jones, et al., 1977). Since that time, aircraft scatterometers with rotating or phased array antennas have been developed so that the airplane can fly a standard straight line "flight plan" thereby allowing more control over the type of ocean features to be examined (e.g., Fronts and Air-Sea Interaction Experiment, Li, et al., 1989).

In the WAVES87 experiment, the Ku-band scatterometer was mounted on an antenna rotator and extended away from the tower about 8m on a boom. The antenna rotator scanned about 300° in azimuth every ten minutes at set incidence angle settings as summarized in Table V (Chapter III). A full 360° rotation was desirable but impractical since the angles behind the radar would have intersected the tower and automatic operation of the radar would have required an additional level of sophistication to allow for a certain number electrical cable wraps before the antenna was reversed and the cabling unwound. Even with this angular gap of about 60°, the sinusoidal behavior of the cross-section is evident.

The observed "smoothed" cross-sections at each incidence angle and polarization were used to create three-dimensional surfaces of the cross-section as a function of wind stress and relative angle (Figures 53 and 54). The nadir surface is characteristically flat with azimuth; the cross-section scale used here is too large to reveal the small negative dependence on wind stress. At 10° incidence angle there are frequently large azimuthal modulations of 5 dB or more, which are not predicted by existing model functions. The cosine-like dependence becomes apparent for both polarizations at 20° and increasingly obvious at the higher incidence angles, especially for v-pol. The h-pol surfaces are rougher and the 60° and 80° data for this polarization are basically noise. The surfaces at 20°, 40° and 60° show the surfaces to have a positive slope with respect to the friction velocity.

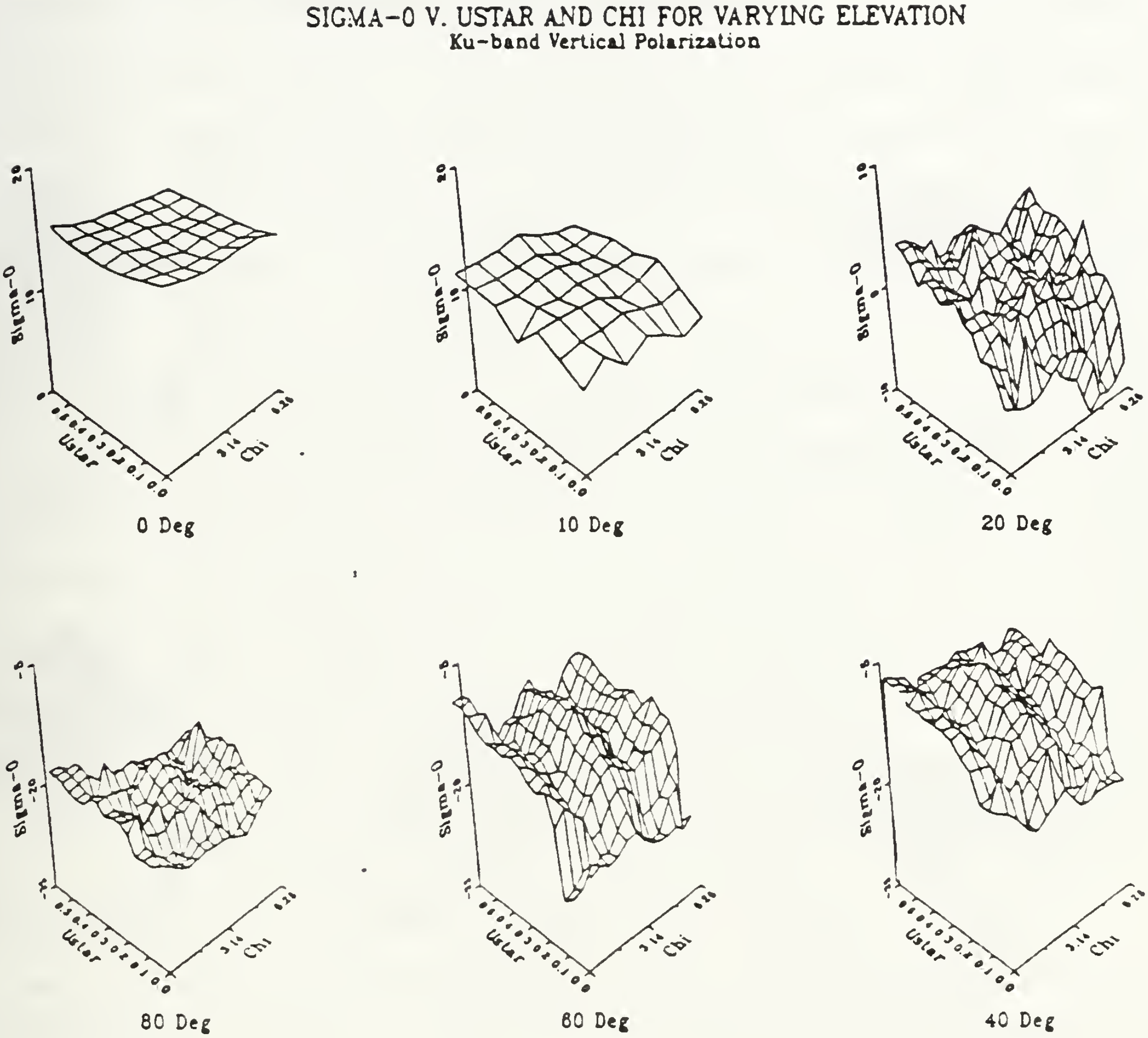

0 Deg

10 Deg

20 Deg

80 Deg

60 Deg

40 Deg

Figure 53. Three-dimensional Surfaces of Vertical-Polarized NRCS as a Function of Incidence Angles, Friction Velocity and Relative Angle, Chi, (Wind Minus Antenna Angle). Incidence Angle Increases Clockwise from Nadir at Top Left, the Relative Angle is Given in Radians with π Corresponding to the Downwind Look Direction

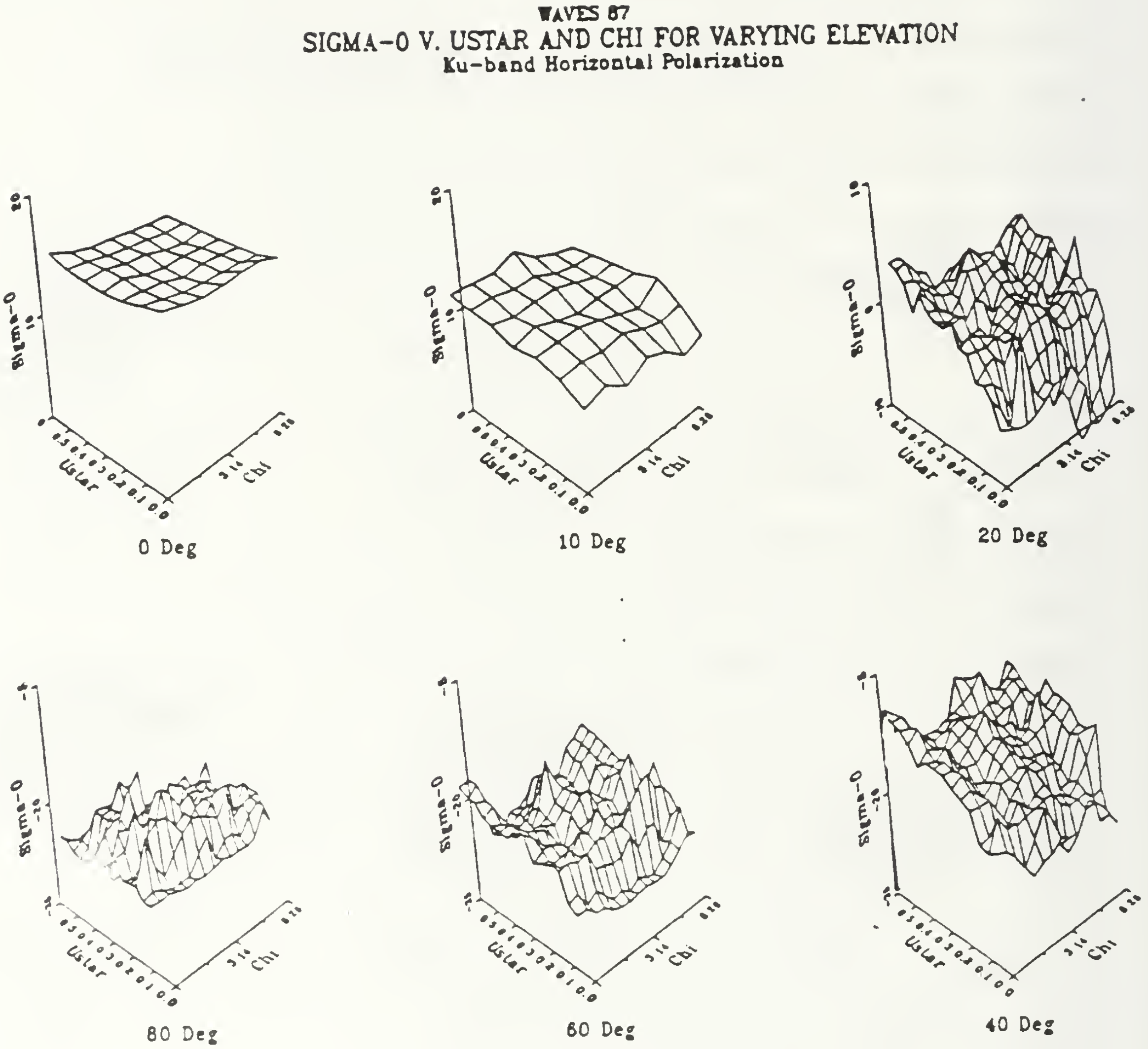

Figure 54. Three-dimensional Surfaces of Horizontal-Polarized NRCS as a Function of Incidence Angle, Friction Velocity and Relative Angle, Chi (Wind Minus Antenna Angle). Incidence Angle Increases Clockwise from Nadir at Top Left; the Relative Angle, Chi, is in Radians with π Corresponding to the Downwind Look Direction

After this holistic view of the wind and azimuth dependence, the smoothed cross-sections for each individual data run, incidence angle other than nadir and polarization were fit with a three term truncated Fourier series as described by equations (91). These observations of the azimuthal dependence of the scatterometer are unique as tower-based radar measurements; therefore, all of the available azimuthal plots at the various incidence angles for both polarizations are provided in Appendix B. Some examples of these fits are shown in Figure 55 (v-pol, 20°) in which it is seen that azimuthal variations at moderate wind speeds are apparent, but the variation is frequently asymmetric and the crosswind minima are not necessarily at 90° and 270°. The upwind/downwind asymmetry is more obvious for h-pol and increases with incidence angle (see Appendix B). Since the pure cosine fit cannot simultaneously fit both the upwind/downwind asymmetry and the position of the minima, the largest errors in minima placement occur for greater differences in the upwind/downwind cross-section values. Some of this asymmetry was hypothesized to be induced by the directionality of the wave field. As an attempt to quantify these phase shifts for comparison to wave spectrum quantities, a second order sine component was added to the three-term cosine series.

The fitted curves including the sine component improve the placement of the minima (cf., runs 80 to 92, Figures 55 and 56), but there are still problems with the overall fits due to data gaps and spikes and to relatively long sweep rate of the antenna; i.e., the field evolves in the twenty minute sampling period. The SASS1 model function team tested fits to

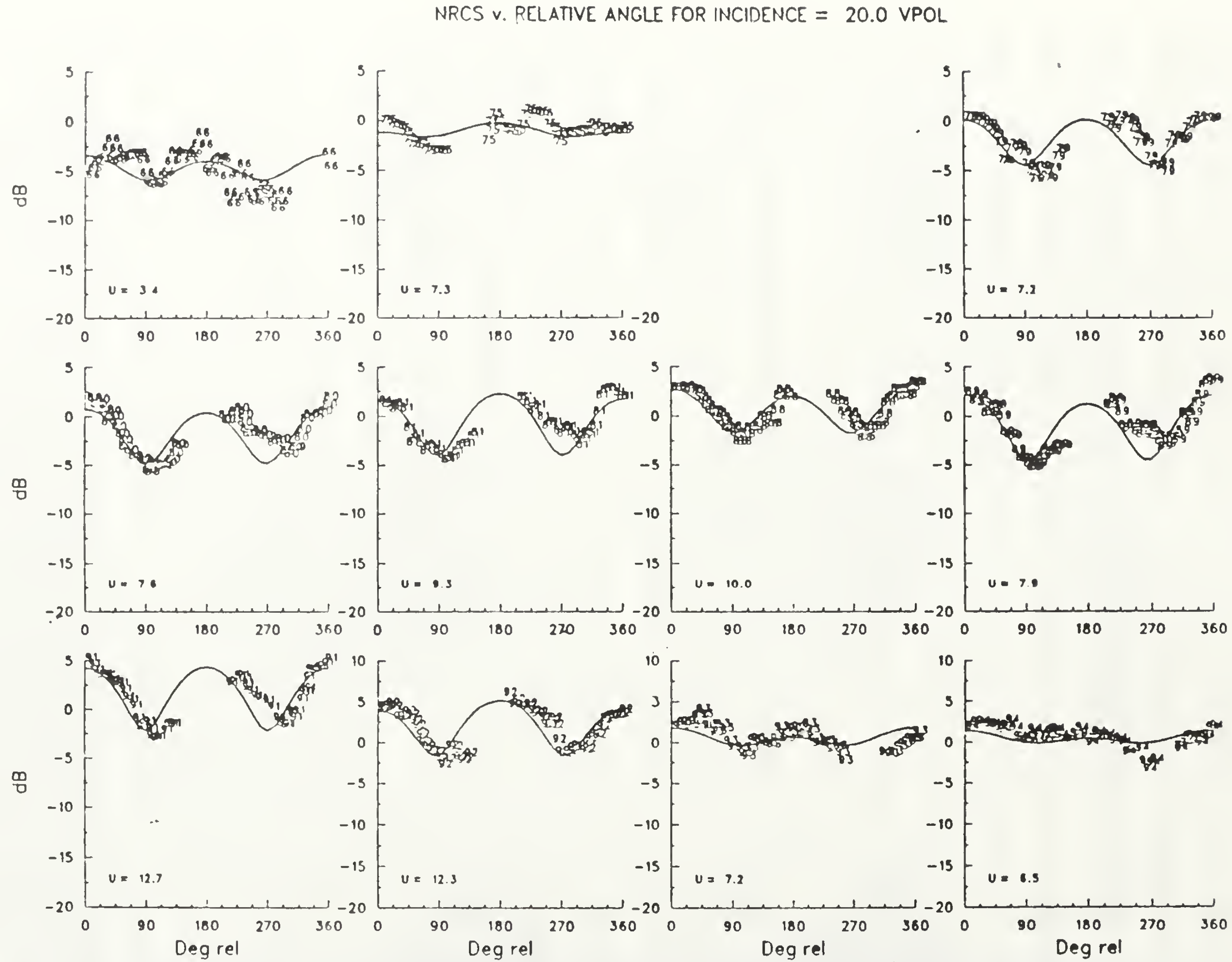

Figure 55. Samples of NRCS as a Function of Relative Wind Angle and Fitted Cosine Curves for 20°, v-pol. Windspeed is in Bottom Left Corner of Each Plot

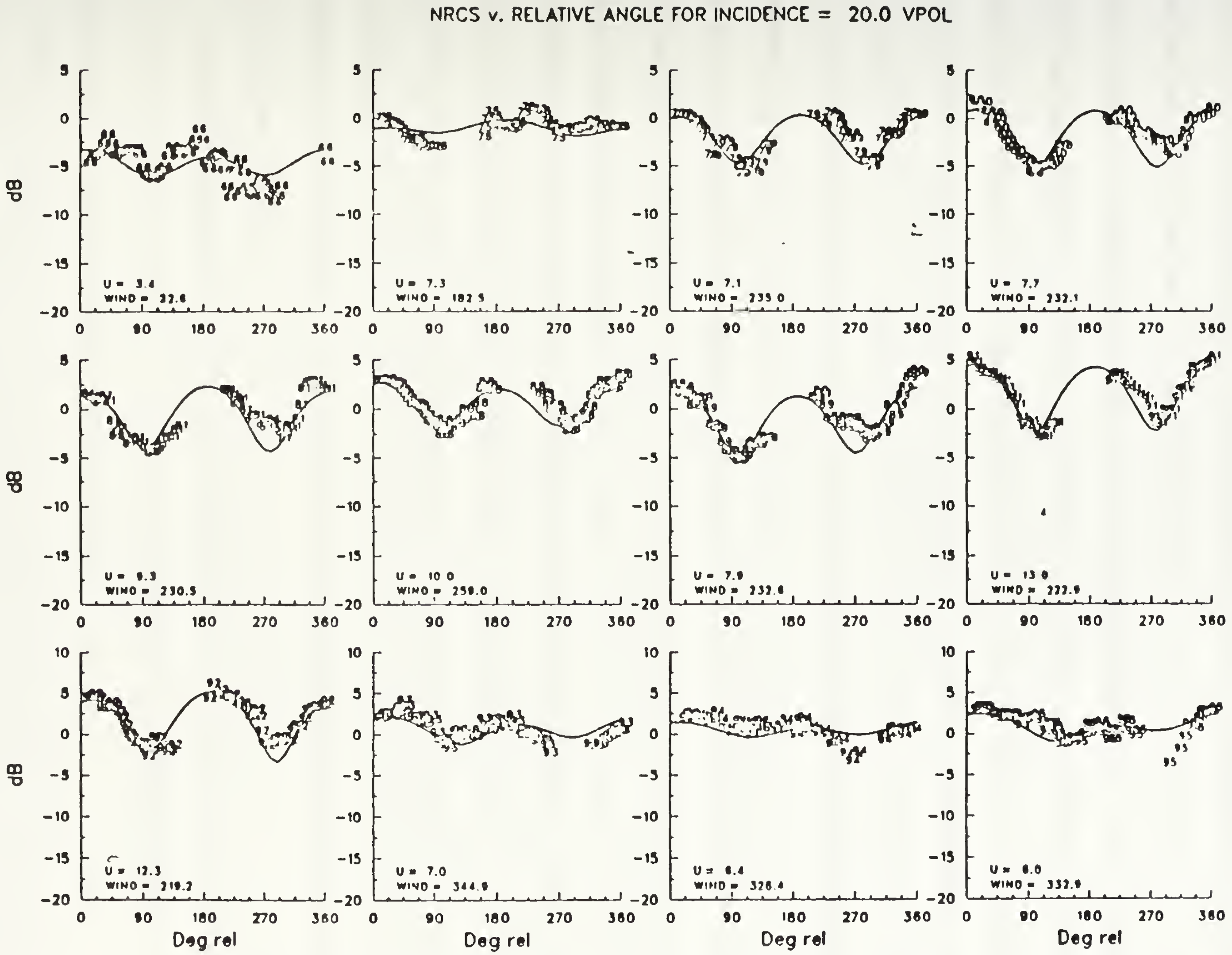

Figure 56. Samples of NRCS (v-pol) as a Function of Relative Wind Angle and Fitted Cosine Curves (Plus Sine) Curves

similar data by computing 36 terms in the series only to find that the first three explained most of the variance in their data (Schroeder et al., 1982). Recently in an examination of the azimuthal dependence observed with an aircraft scatterometer, Li et al. (1989) used an iterative method to locate the minima in which a truncated Fourier series of three sines and a cosine was used to estimate the position of the minima, followed by a polynomial fit to all points 45° on either side of the estimated minimum. Donelan and Pierson (1987) point out the fallacy of fitting the curves with a truncated series of any degree: inasmuch as the data points are not distributed evenly over 360° adding additional terms will not improve the fits in a general sense.

The azimuthal behavior shown in the WAVES87 data indicates the model functions which use the cosine series approach to predict the wind direction may be in error by ten degrees or more. The baseline configuration of all the models discussed previously results in predictions of symmetric dependence of the cross-section with relative wind angle; i.e., the minima are near 90° and 270° and separated by 180°. The physically based model functions contain coefficients which can be adjusted to examine wave effects such as wave slope and hydrodynamic modulation of the placement of the minima. Rather than perform this type of sensitivity test, it was decided to examine the behavior of the radar under different wave conditions as indicated by the directional wave spectra. These analyses will be discussed in the Section D.

2. Rain Effects on the NRCS

Entries in the experimental log indicate high rain rates during data runs 143 to 146. Prior to these runs, the wind had been blowing at moderate to high speeds from the long fetch direction for about two days. This relative constancy of speed and direction allowed the wave spectrum to become fully developed with a peak frequency of 0.16Hz and peak wavelength of about 60m. The direction of the primary wave was nearly in alignment with the wind, down the long axis of the lake.

Under these circumstances the 10° and 20° cross-sections (Figure 57) show a broad peak centered on the downwind direction (180°), indicative of a low amplitude swell propagating in the wind direction. The scenario suggested by the 40° data is that between runs 140 (wind speed of only 1.3m/s) and 143 (7.8m/s), a wind sea had begun to develop as evidenced by the near perfect sinusoidal shape of 143. The rain then started toward the end of 143 and continued through run 146 (12 hours). It appears that the rain drops augment the small, wind-generated capillary waves (of Bragg wavelength approximately 1cm) by creating new rain-generated capillary waves.[2] The resulting surface is then isotropic in wind direction (Stoker, 1977; LeMehaute, 1988) and the distribution and number of capillary waves is radically altered. As a result, the azimuthal dependence of the cross-section is obliterated (Bliven, et al., 1989) and the level of the cross-section is increased above that which is normal for the particular wind speed (cf., runs 134 and 144) (Moore et al., 1979) suggesting that there were additional Bragg-length scattering waves on the surface..

As the rain continues, it is possible for a thin rain induced mixed layer of relatively high eddy viscosity to form which damps the longer waves

---

[2] Path-loss of the Ku- and C-band signals through rain is negligible at the radar ranges used in this experiment (Battan, 1973); therefore, this interpretation of the rain effects in terms of the scattering surface is valid.

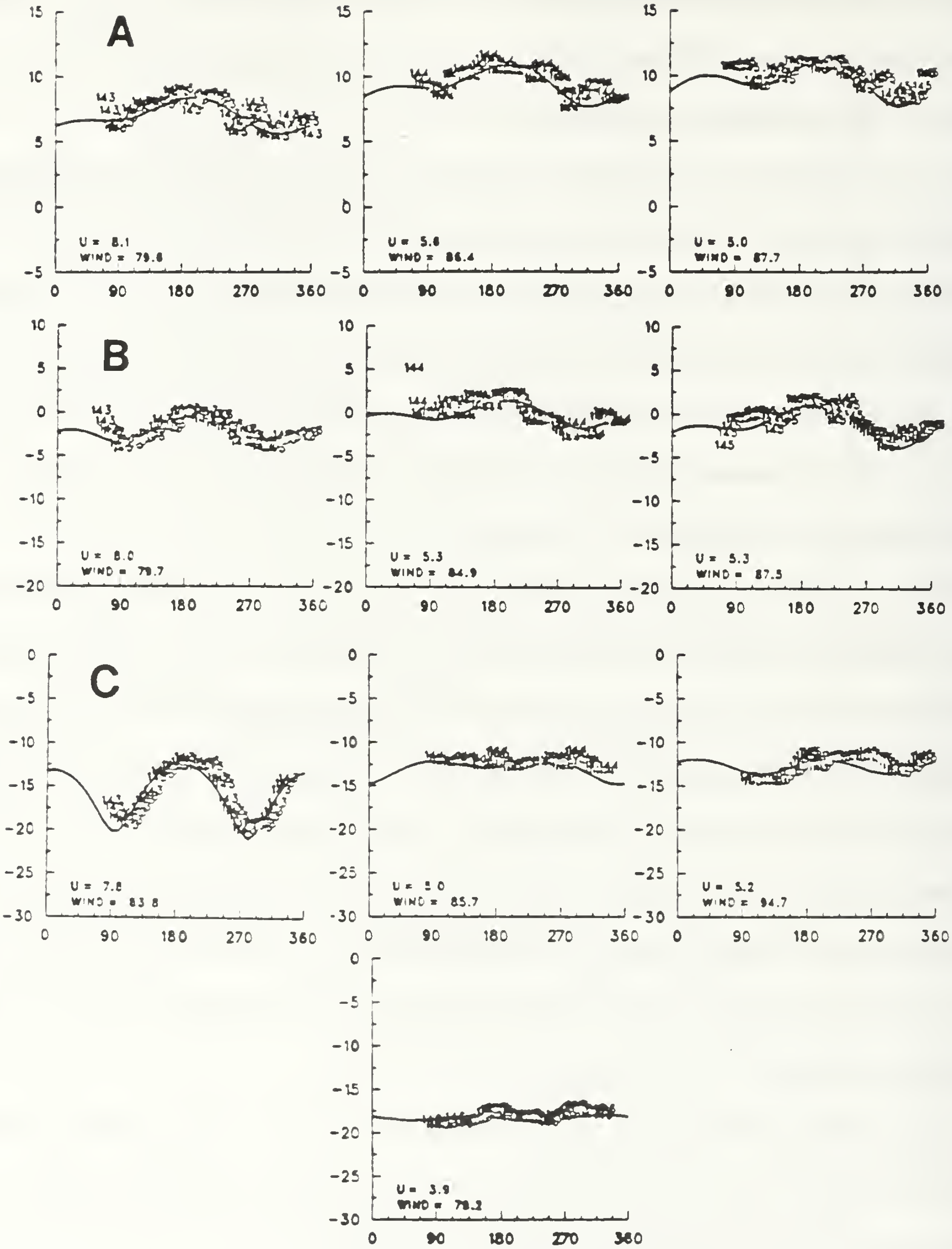

Figure 57. Azimuthal Dependence of the NRCS in the Presence of Rain: a) 10°, b) 20°, (Runs 143 to 145) and c) 40° v-pol for Runs 143 to 146. Note Attenuation of Azimuthal Modulation at 40° between Runs 143 and 144. Rain Started near the End of Run 143.

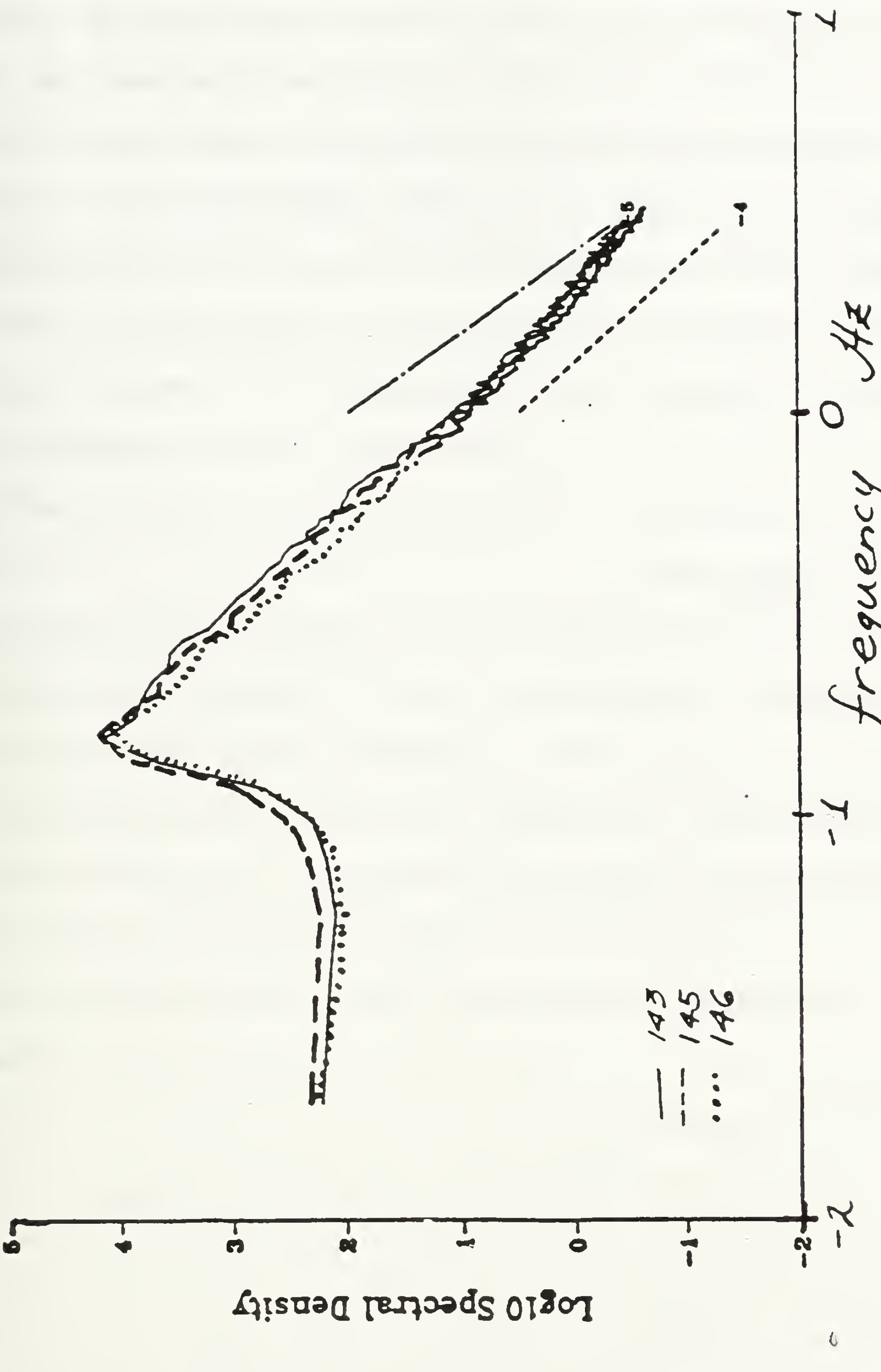

Figure 58. Wave Amplitude Spectra Showing Decrease of Spectral Density of Wavenumbers above the Spectral Peak from Runs 143 to 146.

present (Nystuen, 1989). The one-dimensional frequency spectra for runs 143 to 146 are overlaid in Figure 58, from which it is seen that the frequencies above the spectral peak decay as the rain continues. Therefore, runs 145 and 146 show no azimuthal dependence and the level of the curve falls as the longer waves are damped and the wind decreases. This scenario is appropriate at the C-band wavelength. In this case the rain damps the longer Bragg waves (3cm) but the rain drops are not large enough or distributed appropriately to create 3cm waves in their place. The corresponding C-band data for runs 144 to 146 show the cross-section to decrease steadily with the continuing rain and decreasing winds, rather than showing an initial increase as with the Ku-band NRCS.

This section has demonstrated that although the overall behavior of the cross-section as a function of relative wind angle is a cosine-like dependence, there appear to be circumstances under which the sinusoid becomes asymmetric or even isotropic. The observations do not support the predictions of existing model functions which show cross-section minima to be exactly at crosswind under all conditions. The polarization of the incident radiation is also a critical parameter: the v-pol data often showed an azimuthal dependence at 80° whereas the h-pol data were more scattered at 60° and mostly noise at 80°.

D. NRCS DEPENDENCE ON SPECTRAL WAVE PARAMETERS

The azimuthal behavior of the cross-sections shown in the previous section displayed significant asymmetry. In this data set, several related physical mechanisms could be working together to produce this asymmetry. In some instances, the wind speed changed in the twenty minute period over which the measurements were made so that the level of the NRCS was altered. Since the radar scanned back and forth instead of always starting from one side, the averaged cross-section at the start/finish azimuth bin consists of two NRCS measurements twenty minutes apart, whereas the averaged cross-section measurements near the center of each run consists of NRCS measurements taken within minutes of each other. This asynoptic measuring scheme usually results in an "odd" function of the NRCS with respect to the upwind or downwind maximum (see annotated Run 80, 40°, v-pol, Appendix B).

Alternatively, the azimuthal asymmetry may be due to different wave conditions; i.e., varying spectral forms from one run to another. To express this in terms of the two-scale model, the anisotropy of the cross-section with direction is due to changes in the large scale slope of the tilting surface and to the directional spread of the small scale waves about the wind direction. In this section, the azimuthal behavior of several data runs will be discussed within the framework of the spectral composition of the waves present as determined from frequency and directional spectra and descriptive parameters of the sea state. The observed effects are those due to long waves relative to the Bragg waves.

Three classes of wave spectra, having progressively more complex wave fields, are chosen for comparison to the azimuthal variations of the radar cross-sections: 1) a moderate wind speed (7.5m/s) wind wave sea (4m waves aligned with the wind, Runs 49 and 89); 2) a combined sea/swell in which the swell component opposes the sea (Runs 79 and 80); and 3) a moderate wind speed, "confused" sea of broad frequency and directional bandwidths (Run 75).

1. Class 1: Moderate Wind Speed and a Wind-driven Sea

This test case is presented as the "norm" which satisfies the basic assumptions of scatterometry upon which the model functions are based. That is, the wind and waves are aligned and the waves are locally generated wind waves. Two runs of similar wave conditions will be examined as a reliability measure.

The averaged environmental conditions during the 70 minutes of Run 49 (Figure 59) were 8.8m/s wind speed from 231°T. The significant wave height was about 25cm and the atmospheric stratification as inferred from the air-water temperature difference (+5.5°C) was stable. Under these conditions, the NRCS exhibited the azimuthal behavior relative to the wind direction shown in Figure 60a. The curve is flat at nadir, the 10° curve is different on either side of 180° due to a decrease in wind speed in the first five minutes of the 10° scan and sinusoidal curves are obvious at all other incidence angles. Even though the downwind maximum is in the tower gap and therefore not measured, it appears from the symmetry of the curves that the upwind/downwind difference is greater for h-pol than v-pol. This difference as well as the basic difference in NRCS magnitudes between h-pol and v-pol increases with increasing incidence angle (recall the reflection coefficient of horizontal polarized radiation has a stronger incidence angle dependence, (11a) and Figure 5).

A perspective diagram of the directional wave spectrum associated with this run (Figure 60b) shows a 4m wind wave sea propagating with the

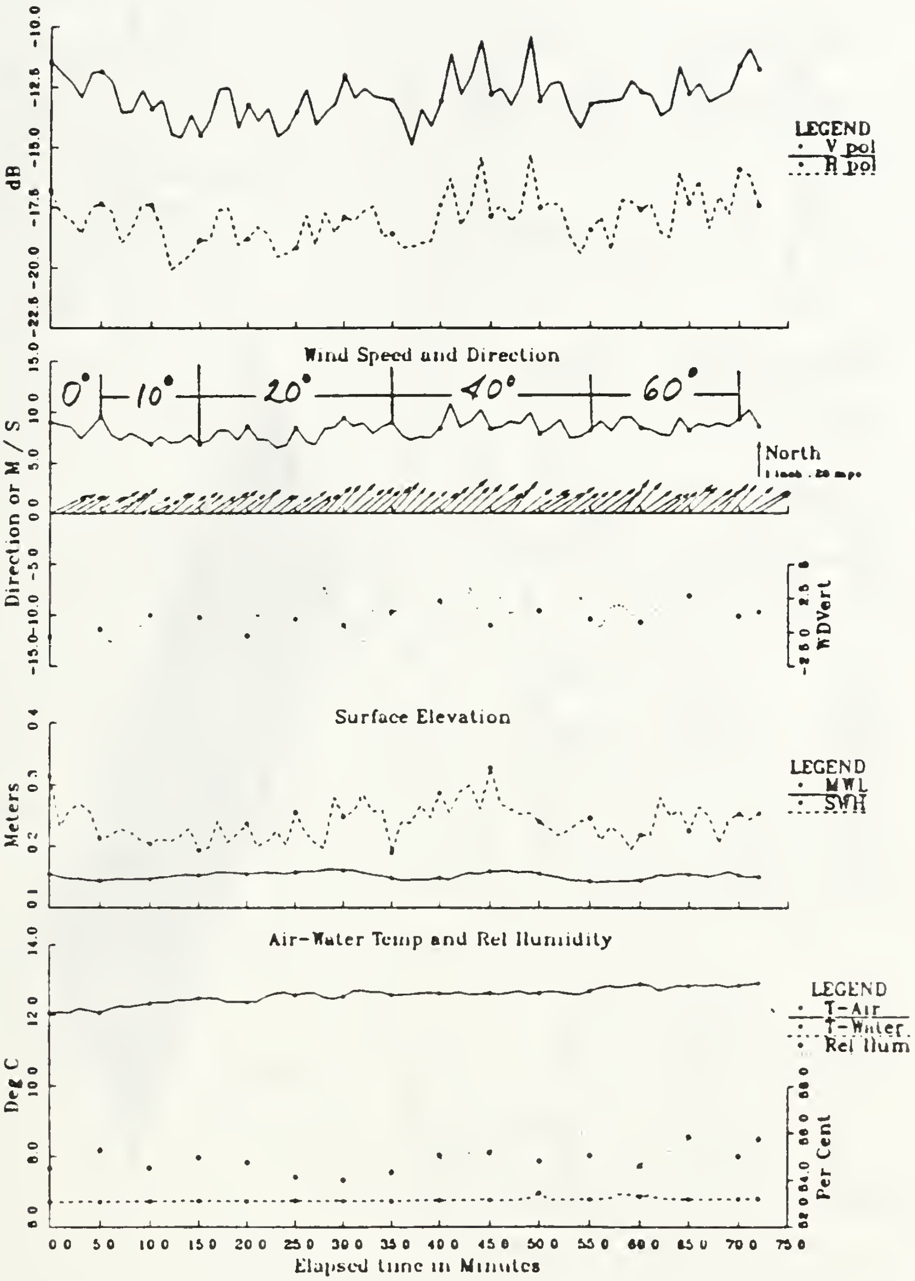

Figure 59. One-Minute Block-Averaged C-band NRCS and Environmental Data from Run 87049. Time Associated with Particular Incidence Angles of Ku-band Radar are Annotated on Wind Speed Plot

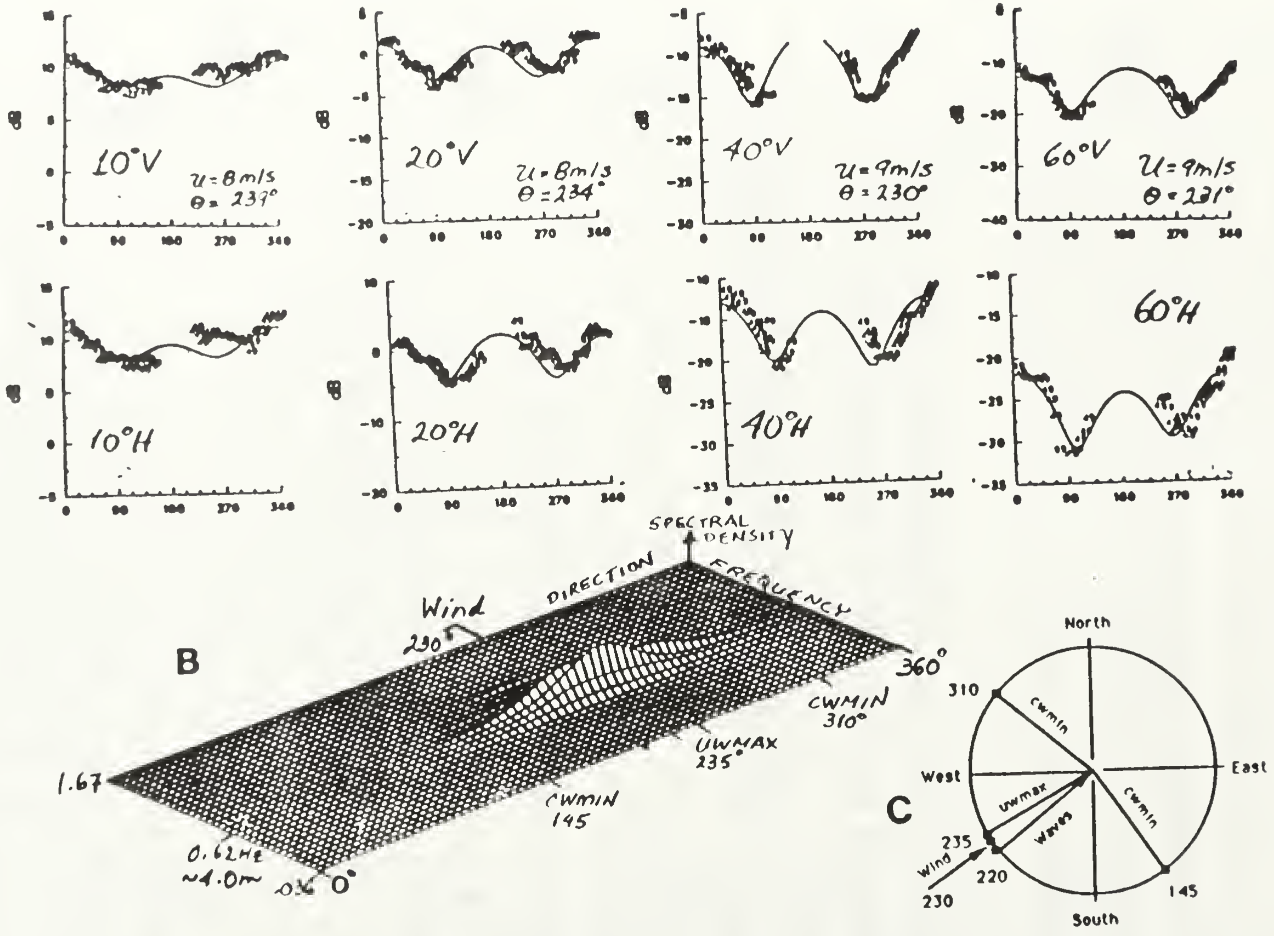

Figure 60. Run 49: a) NRCS Versus Relative Wind Angle for 10°, 20°, 40° 60° v-pol (Top Row) and h-pol (Bottom Row), b) Directional Spectrum, and c) Polar Plot of Relative Angles Among the Radar, Wind and Waves

wind at about 225°T. The one-dimensional frequency spectrum for Run 49 shows a bifurcated peak with two nearly equal frequency (.69Hz, .0.62Hz; 4m peak wavelength), equal energy wave components. The directional spectrum assigns directions of 220°T and 230°T to these waves; therefore, on the polar plot of the wind, wave and radar angles (Figure 60c), the direction of the peak wave is shown as a 10° arc rather than a single angle. The upwind maximum of the NRCS is within 5° of the wind/wave direction which is the best alignment one can expect in this experiment, since 5° is the minimum resolution of both the radar and directional spectra. The NRCS minima are separated by 160° and are 75° and 85° on either side of the maximum. The positions of the minima approximate the directional spread of the wind waves but the correlation cannot be made exact since 1) the directional spectrum can be altered by a change in the wave staff data processing parameters, and 2) the spectrum has no absolute minima.

The pure wind sea case allows the most legitimate comparison of the measurements with the model function predictions. All of the model functions were run for an average neutral wind speed of 8.8m/s and wind direction of 230°, corresponding to the conditions for Run 49, 40° v-pol. The NRCS values computed from the model functions are illustrated in Figure 61 from which it is seen that there is significant variation among the model functions with the SASS1, D&P and D&V models forming a set, separate from the SASS2 and Plant models. The D&P and D&V models were tuned to the same *in-situ* data set so it is not surprising that they produce similar values; the SASS2 was constrained by SEASAT data, SASS1 by other *in-situ* data and the Plant model was not tuned to any particular data set. The

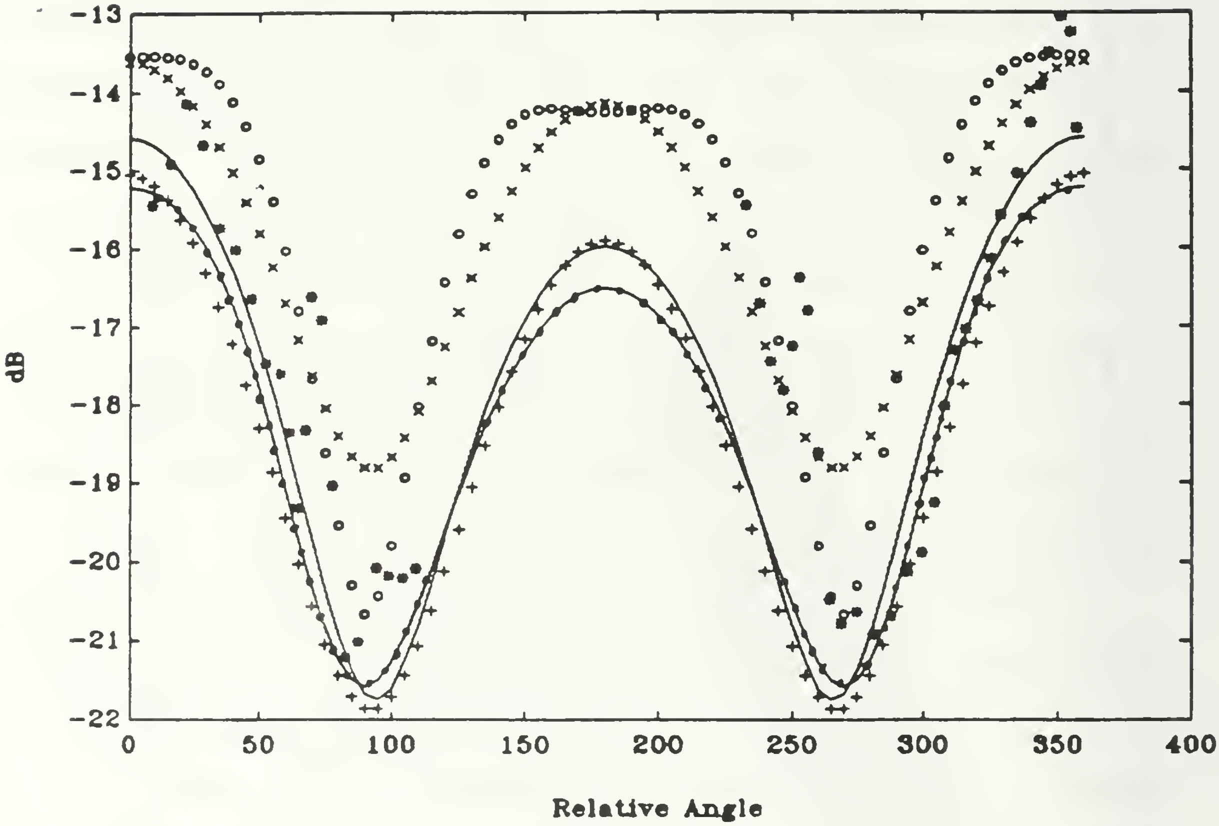

Figure 61. Azimuthal Modulations of Model Functions (o -- Plant, x -- SASS2, + -- D&P, -.- line SASS1, solid line D&V) and Measurements from Run 49 (*).

amount of upwind/crosswind modulation is least for SASS2 (5dB) and about 7dB for the other models; the upwind/downwind modulation varies from about 1 to 2dB (Plant, SASS2; D&P, D&V, SASS1). The overall shapes of the azimuthal modulation are all similar except for the Plant model which has broad, flat-topped maxima and sharper nulls at the crosswind minima.

The NRCS data points from Run 49 are superimposed on the model function predictions after subtracting a constant 5dB bias from the measurements to account for the lake/ocean wind speed scaling as discussed in the previous section. The sinusoidal pattern of the data points follows that of the model functions except the minima are located at relative wind angles of about 90° and 285°, instead of being located at 90°, 270° (SASS1, SASS2, Plant) or 95°, 265° (D&P, D&V). The cluster of three points of unusually high magnitudes near 110° are due to a data spike of unknown origin and do not change the location of the minimum at 90°. The distance between the relative wind angle minima in the measurements is 195° which corresponds to the angular separation of the minima in the wind wave directional spectrum. Therefore, there is a difference of 15° to 20° between the directional dependence of the model functions and the radar field measurements.

Run 89, which has a similar wind wave spectrum as Run 49, had an averaged wind speed of 7.5m/s from the short fetch direction, 230°T (Figure 62); however, the atmospheric stratification was unstable. The smoothed NRCS for all incidence angles and both polarizations are plotted against radar azimuth in degrees True North (Figures 63 and 64) from which it is seen that all of the incidence angles above nadir are azimuthally modulated in increasing amounts.

The maxima of the modulated curves fall in the vicinity of the upwind direction, with the 60° v-pol curve having the best conformance in shape with respect to the wind direction. The 40° v-pol curve is somewhat skewed and the 80° v-pol curve has a broad peak of relatively constant NRCS. As before, the difference between the h-pol and v-pol NRCS increases with incidence angle. The decrease in h-pol is dramatic enough that even at 7.5m/s the 60° h-pol values are frequently below the noise level of the radar. The polar plot of the radar wind and wave angles, and the perspective plot of the directional spectrum (Figure 65) confirm that in the case of a pure wind sea the NRCS is maximum in the upwind direction, perpendicular to the wind wave crests which carry the Bragg scatterers. The minima are not necessarily 180° apart nor 90° from the wind direction; rather, the angular distance between the minima approximates the angular spread of the wind wave directional spectrum.

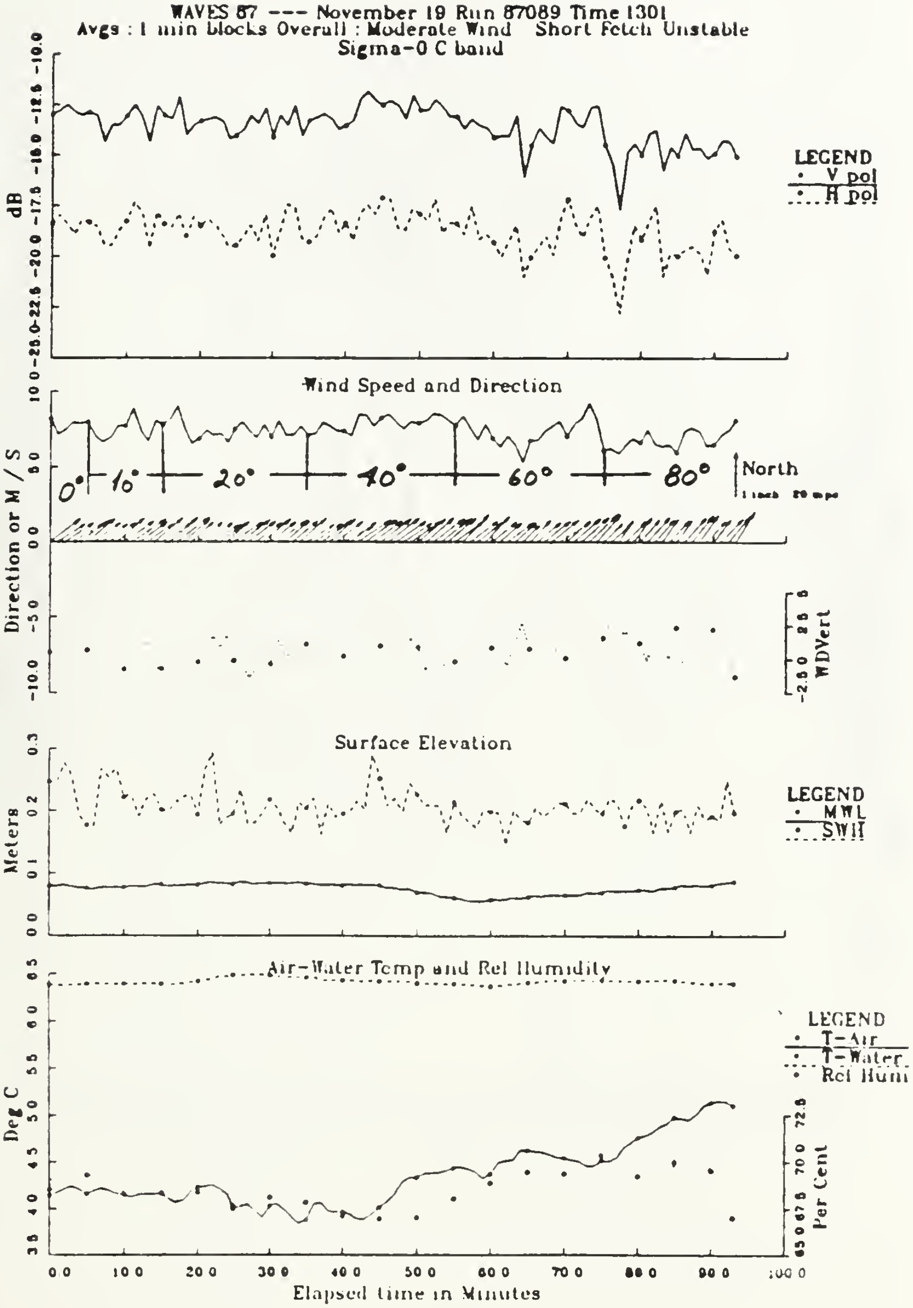

Figure 62. One-Minute Block Averaged C-band NRCS and Environmental Data From Run 89. Times Associated with Particular Incidence Angles of Ku-band Radar are Annotated on Wind Speed Plot

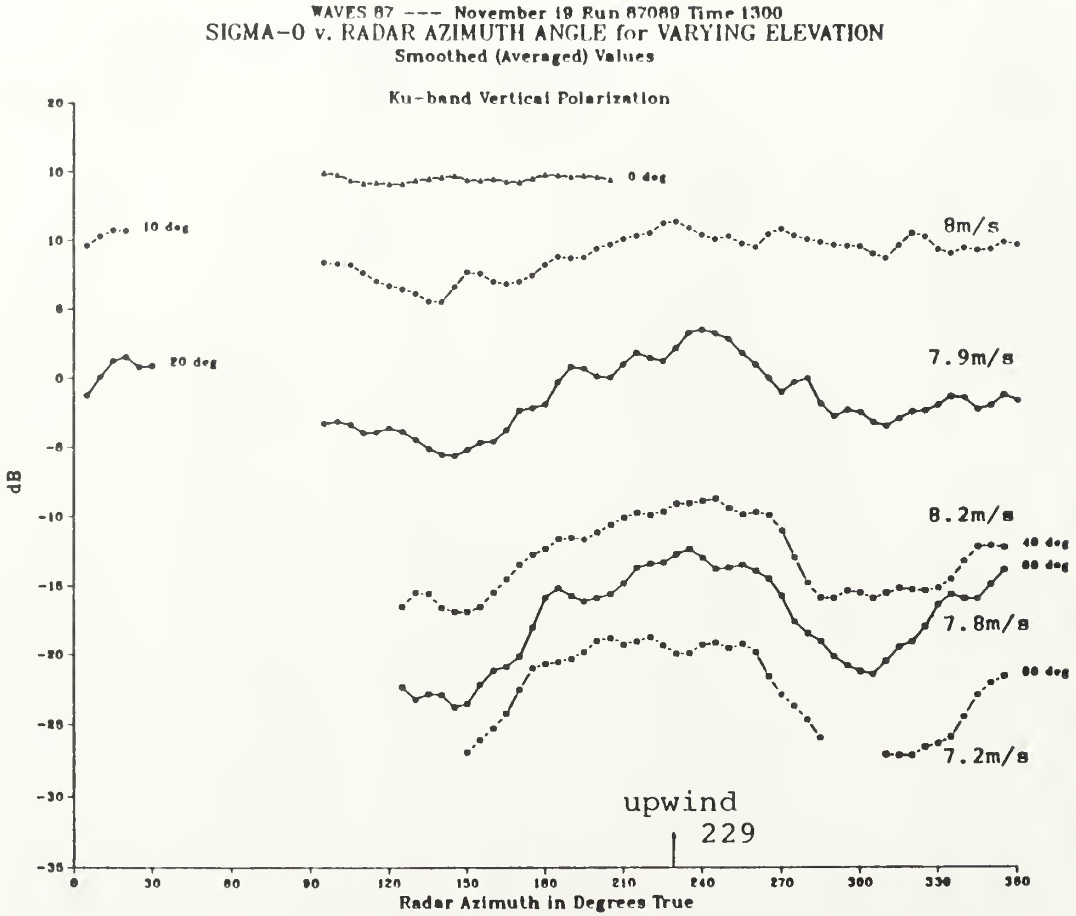

Figure 63. Run 89. NRCS (V-Pol) as a Function of Incidence Angle and Radar Azimuth Angle in Degrees True North. Average Wind Speed for each Incidence Angle is Marked at End of Each Curve

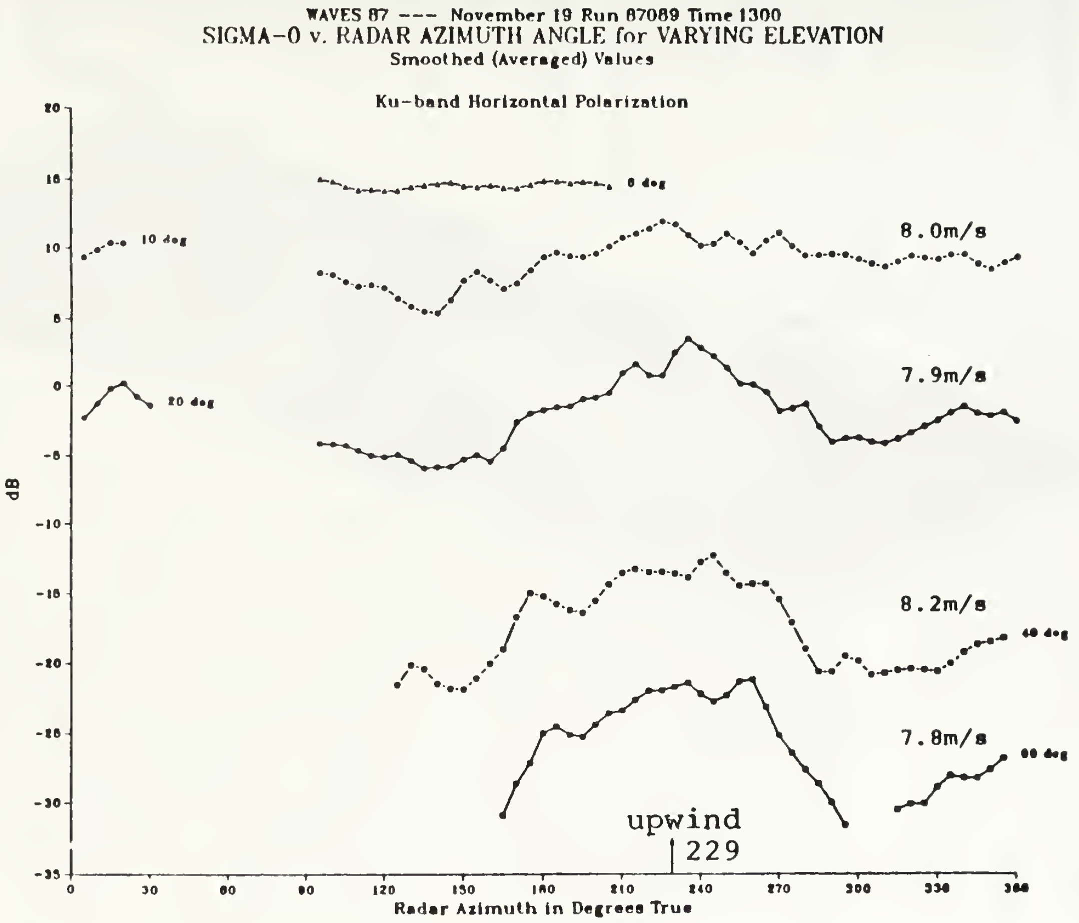

Figure 64. Run 89. NRCS (H-Pol) as a Function of Incidence Angle and Radar Azimuth Angle in Degrees True North

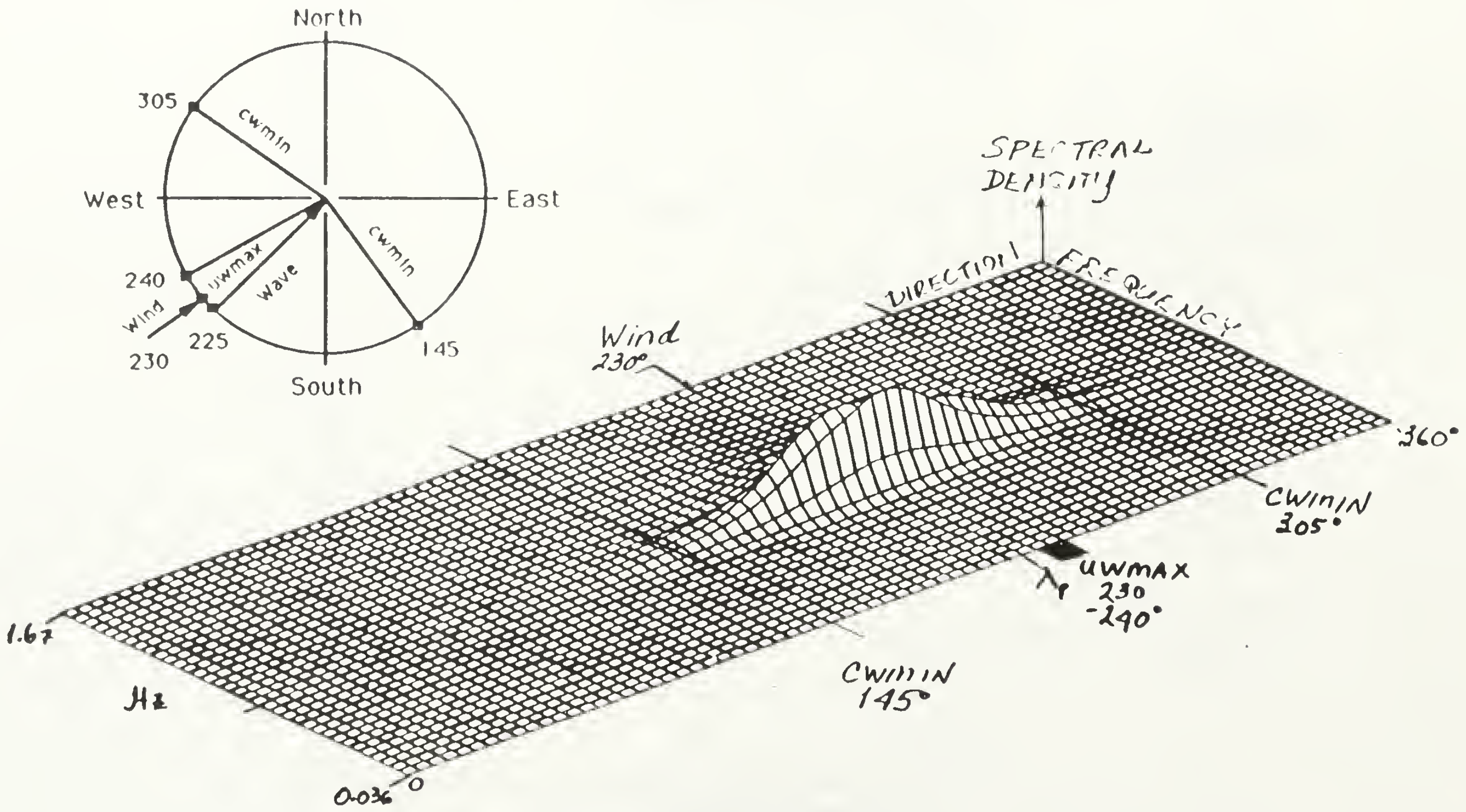

Figure 65. Run 89. Directional Spectrum and Polar Plot of Relative Geometry Among Radar, Wind and Wave Angles

2. Class 2: Moderate Wind Speed, Combined Sea and Swell

A bimodal spectrum in which a nonlocally generated long wave propagates through a local wind sea is a frequent possibility in the open ocean. Due to the fetch geometry of Lake Ontario, a small change in wind direction produces a similar bimodal spectrum in which the peak frequencies and directions of the component waves are quite distinct. In this test case, two data runs for which the wave field consisted of two primary wave components are examined.

The southern half of a semi-stationary, low pressure system was positioned over the lake for 19hrs on 17 and 18 November such that the wind velocity varied from about 7 to 10m/s and 190° to 170°T from the western to eastern end of the lake. The primary wave frequency and direction which developed were approximately $0.2s^{-1}$ and 60°T. The weather system progressed eastward on 18 November, and the wind direction and speed changed to about 230°T, 7.5m/s.

Three hours after the shift in wind direction, radar and environmental measurements were acquired, at which time the environmental conditions were as shown in Figure 66. The wind speed was somewhat erratic, varying between 5 and 9m/s, but the wind direction was uniformly from 230° to 240°T. The significant wave height was about 30cm and the mean water level indicated that a seiche may have been induced by the movement of the pressure system across the lake.

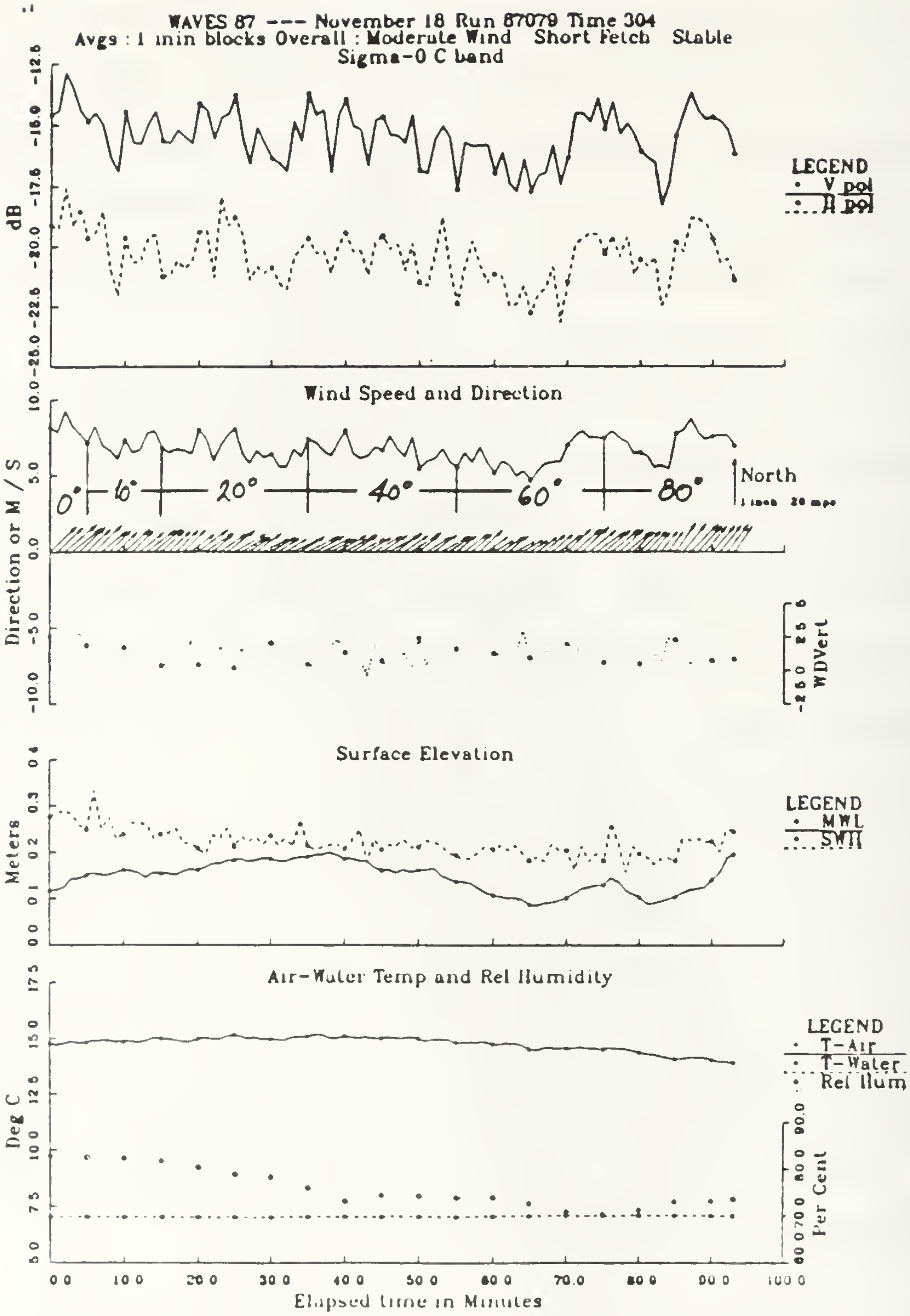

Figure 66. One-Minute Block-Averaged C-Band NRCS and Environmental Data from Run 79.

Analysis of the associated directional spectrum shows that a local wind sea developed in addition to the long wave in which the total power at the wind wave peak frequency is 76% of the power at the lower swell frequency. These two wave components propagated in nearly opposite directions: 66°T (44m long wave) and 221°T (3.2m short wave). The directional spread of the long wave is not well resolved by the maximum likelihood method for low spectral density (Donelan, pers. comm); therefore, only the peak direction will be used here.

The azimuthal modulations of the NRCS for both polarizations and all incidence angles except nadir (Figures 67 and 68) still exhibit sinusoidal dependence with wind direction even in the presence of the long wave. The magnitudes of the NRCS values appear nearly equal to the wind sea case (Run 89), after allowing for wind speed changes at each incidence angle (the average speed is marked on each incidence angle curve). However, the position of the NRCS maximum, located at 245°T, could be considered to be aligned with the either the wind or long wave as illustrated in Figure 69. The minima are not symmetric with any one of the wind, short wave or long wave directions, instead they are located at the midpoints between the long and short wave directions and are separated by 180°[3]. This effect may be due to the increased spreading of the wind wave directional spectrum that occurs

---

[3] A fourth directional choice, not examined here, is the direction of the stress vector. In the presence of waves and for differing atmospheric stratification, the wind and stress vectors are not necessarily aligned (Geernaert, 1988b).

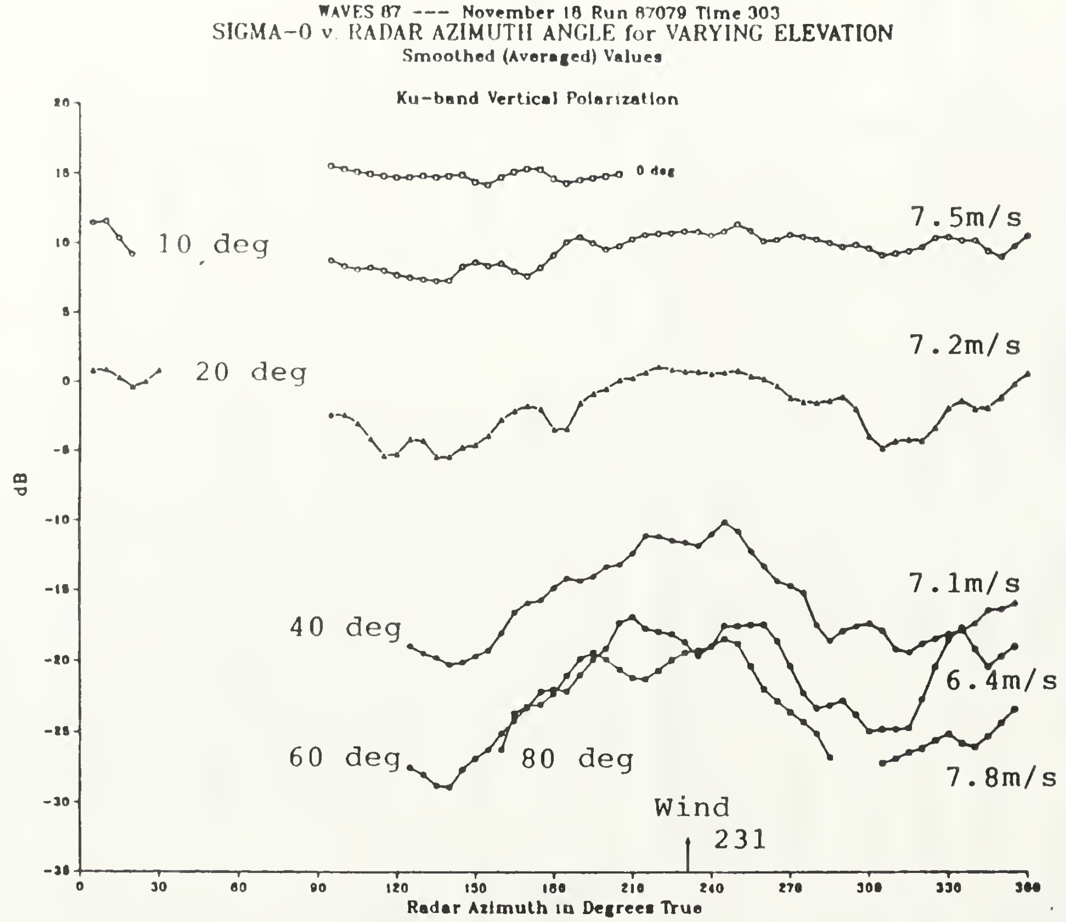

Figure 67. Run 79. NRCS (V-Pol) as a Function of Incidence Angle and Radar Azimuth Angle in Degrees True North. Average Wind Speed at each Incidence Angle is marked at end of Each Curve

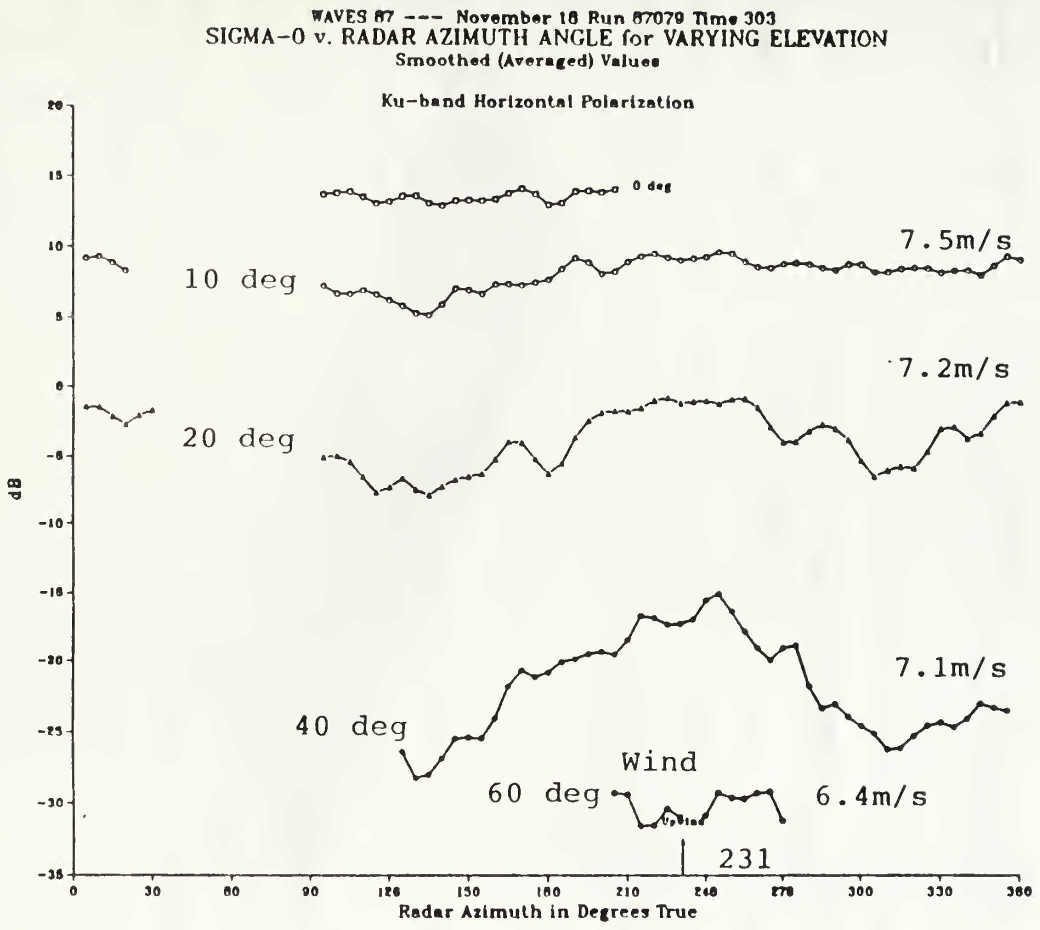

Figure 68. Run 79. NRCS (H-Pol) as a Function of Incidence Angle and Radar Azimuth Angle in Degrees True North

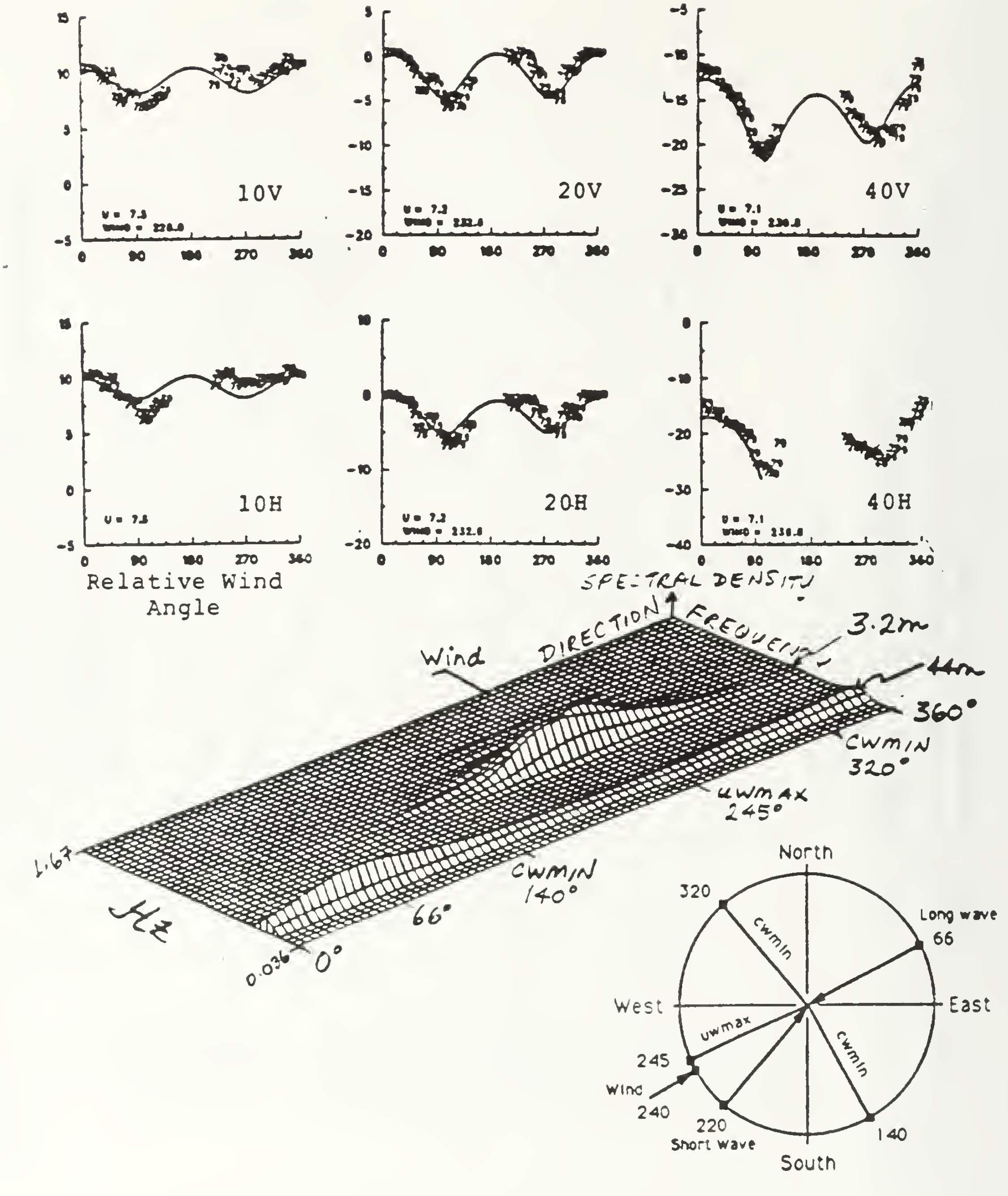

Figure 69. Azimuthal Modulation of Ku-band Radar in a Combined Wind/Swell Sea (Run 79) Top: NRCS v. Relative Wind Angle for 10°, 20°, 40° Incidence Angle (v-pol, h-pol); Midde: Perspective Plot of Directional Wave Spectrum; Bottom Right: Polar Plot of Tower, Radar, Wind and Wave Geometry

when a wind wave sea runs against an opposing current, in this case the orbital velocity of the longer wave component (Sugimori, et al., 1985).

The wind sea continued to grow during Run 79 and by the time Run 80 was completed, about three hours later, the total power at the wind wave frequency was twice that of the long wave, Figure 70. With the wind wave dominating the spectrum, the maximum of the NRCS is in the wind direction and the minima (polar plot, Figure 70) are again only 165° apart.

3. Class 3: Moderate Wind Speed, "Confused" Sea

When the low pressure system described above moved across the lake, the wind changed from a light, northerly wind, that had been prevailing, to a southerly direction, then from the southwest. Runs 79 and 80 described above were performed after the winds had settled into the final southwest direction. Between the initial northerly, and the final, southwesterly winds, the wave field was in a period of active readjustment to the changing winds.

The environmental conditions of Run 75 were steady winds of about 7.5m/s from the south for the first 55 minutes of the data run; at 55 minutes, the wind speed started to increase while the direction remained southerly; the atmospheric stratification was stable (Figure 71). The azimuthal modulations of the NRCS with respect to True North (Figures 72 and 73) for the various incidence angles differ quite markedly from the previous cases. At 10° and 20°, the modulation with wind direction is gone in both polarizations. The intermediate angles for the v-pol data (40° and 60°, Figure 72) show the peak-to-trough modulation to be smaller than the wind sea (only about 5dB) compared to 10dB) and overall, the curves are more noisy.[4] The maxima shift progressively toward the wind direction with increasing incidence angle while the cross-wind minimum stays near 270°. The h-pol curves at 40° and 60° display even less modulation (Figure 73).

The complexity of the wave/wind field is illustrated in Figure 74. The directional spectrum has three peaks spread out over 0.3Hz in frequency (0.27, 0.43, 0.58) and 211° in direction (56°, 101° and 136°). The polar diagram in Figure 74 shows the maxima and minimum positions for the 40° and 80° v-pol curves. No apparent symmetry of these positions with respect to any of the wave directions is obvious, but it is clear that away from the upwind direction the placement of NRCS minima is not a function of the wind alone.

---

[4] The near equal magnitudes of the 60° data with the 40° NRCS values is due to the lower wind speed during the 40° portion of the data run.

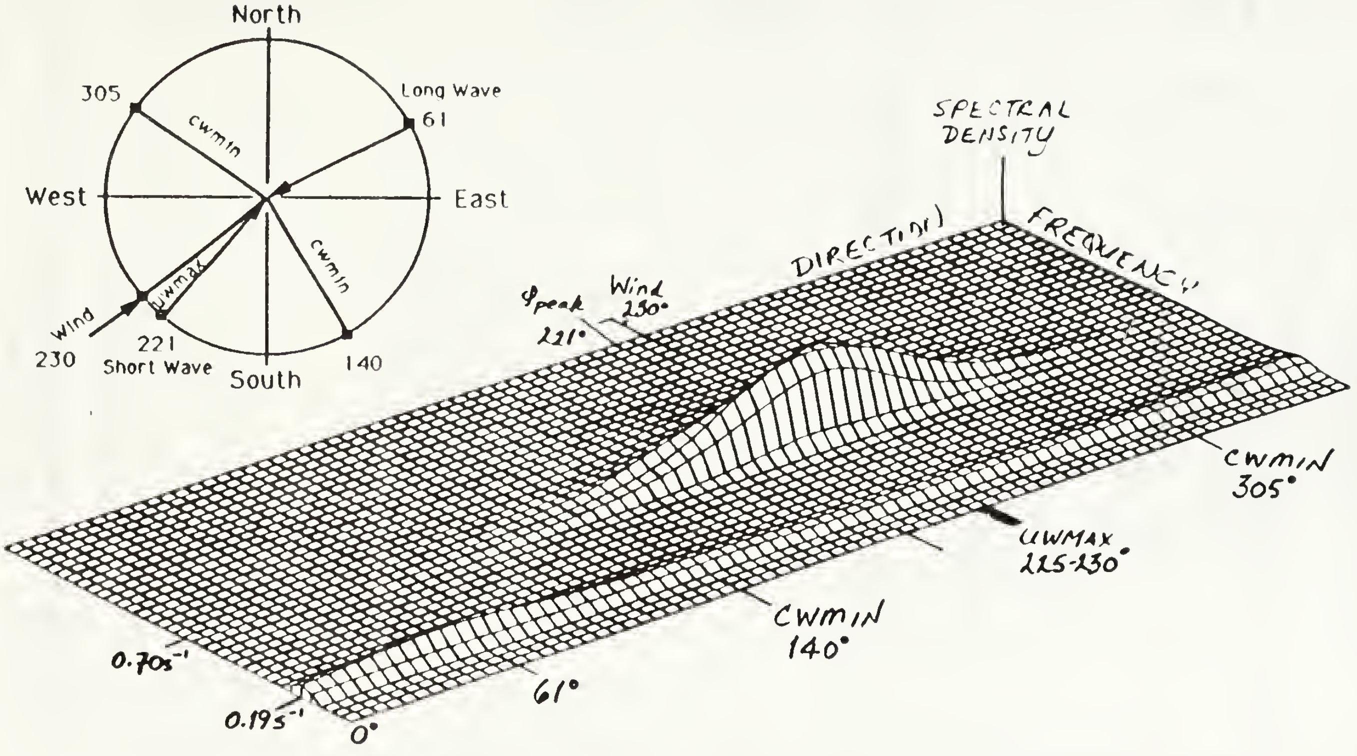

Figure 70. Run 80. Perspective Plot of Directional Spectrum and Polar Plot of Relative Geometry Among Radar, Wind and Wave Angles

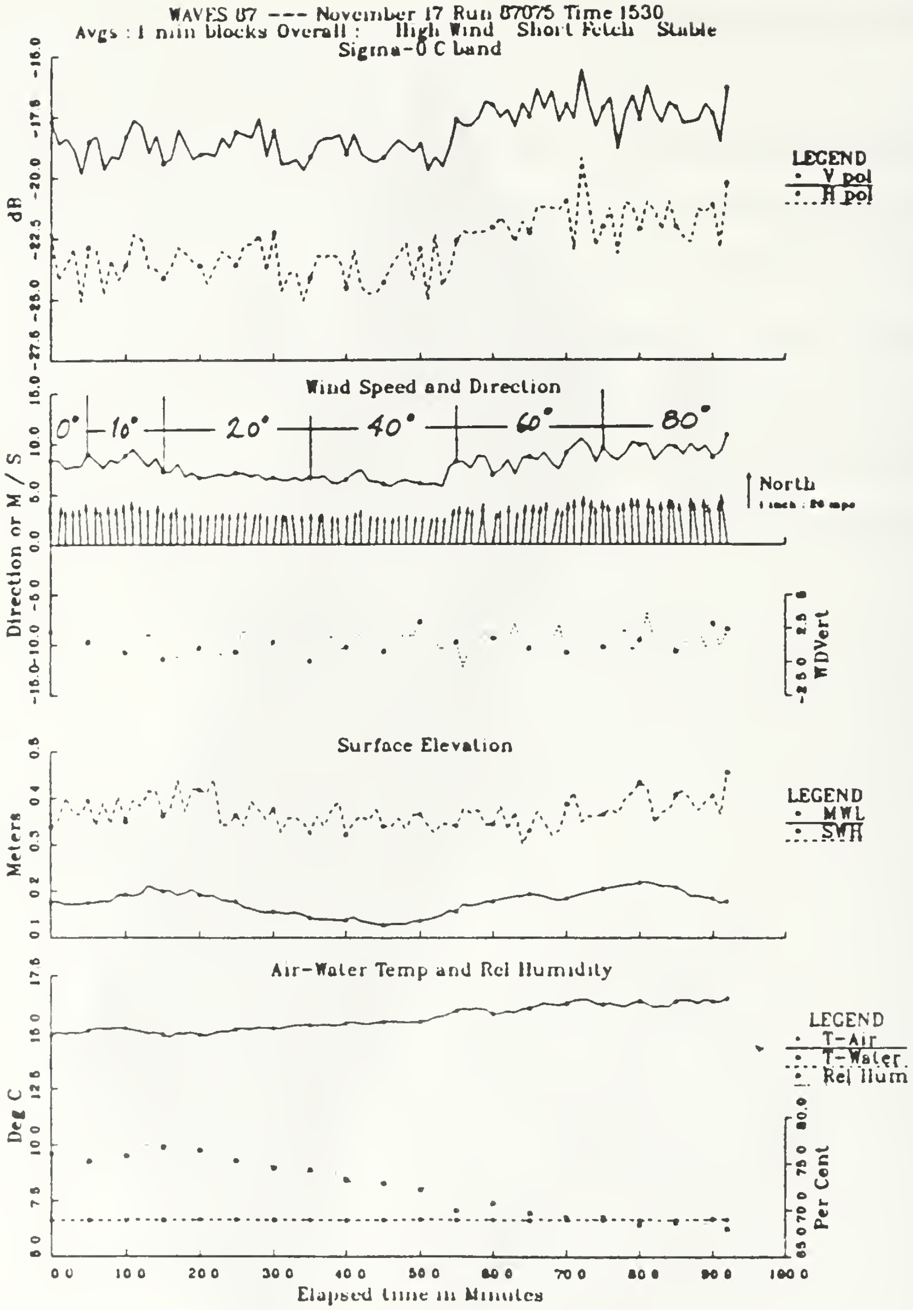

Figure 71. One-Minute Block-Averaged C-Band NRCS and Environmental Data for Run 75

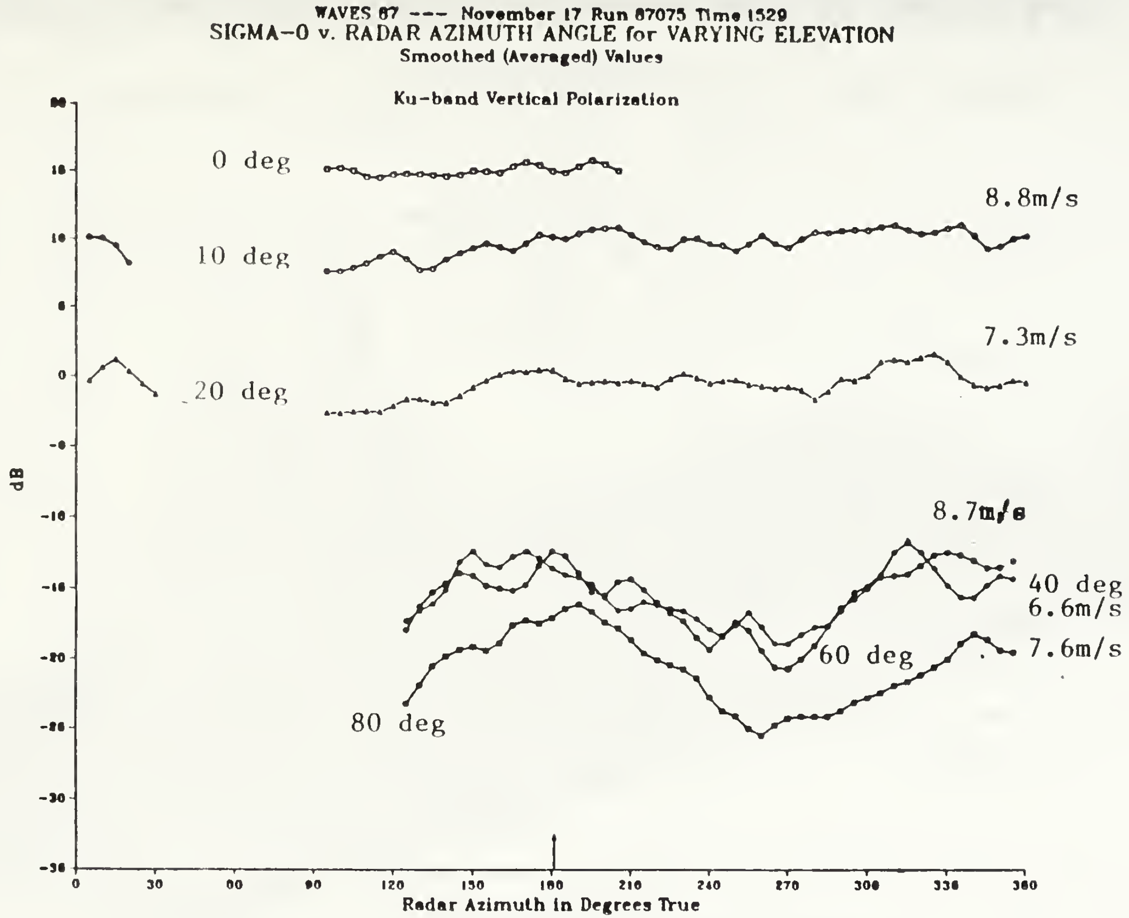

Figure 72. Run 75. NRCS (V-Pol) as a Function of Incidence Angle and Radar Azimuth Angle in Degree True North. Averaged Wind Speed for Each Incidence Angle is Marked at End of Each Curve

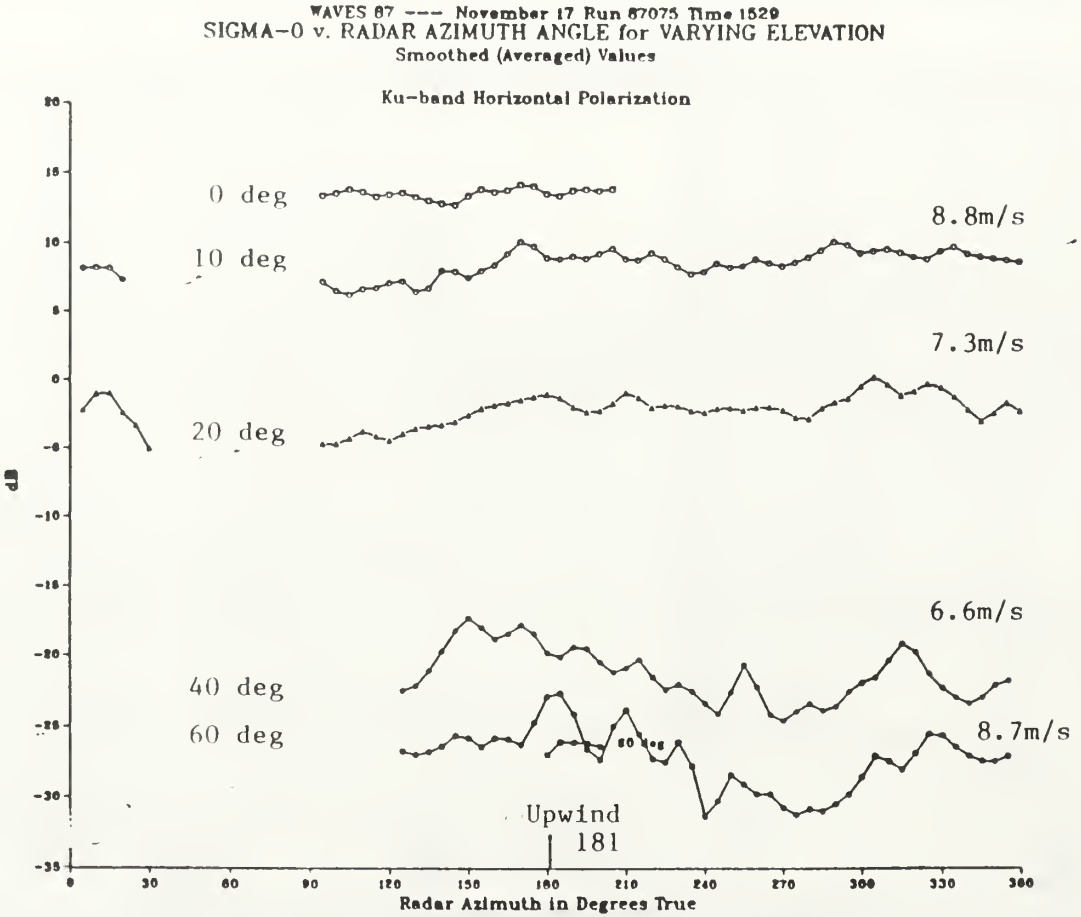

Figure 73. Run 75. NRCS (H-Pol) as a Function of Incidence Angle and Radar Azimuth Angle in Degree True North. Averaged Wind Speed for Each Incidence Angle is Marked at End of Each Curve

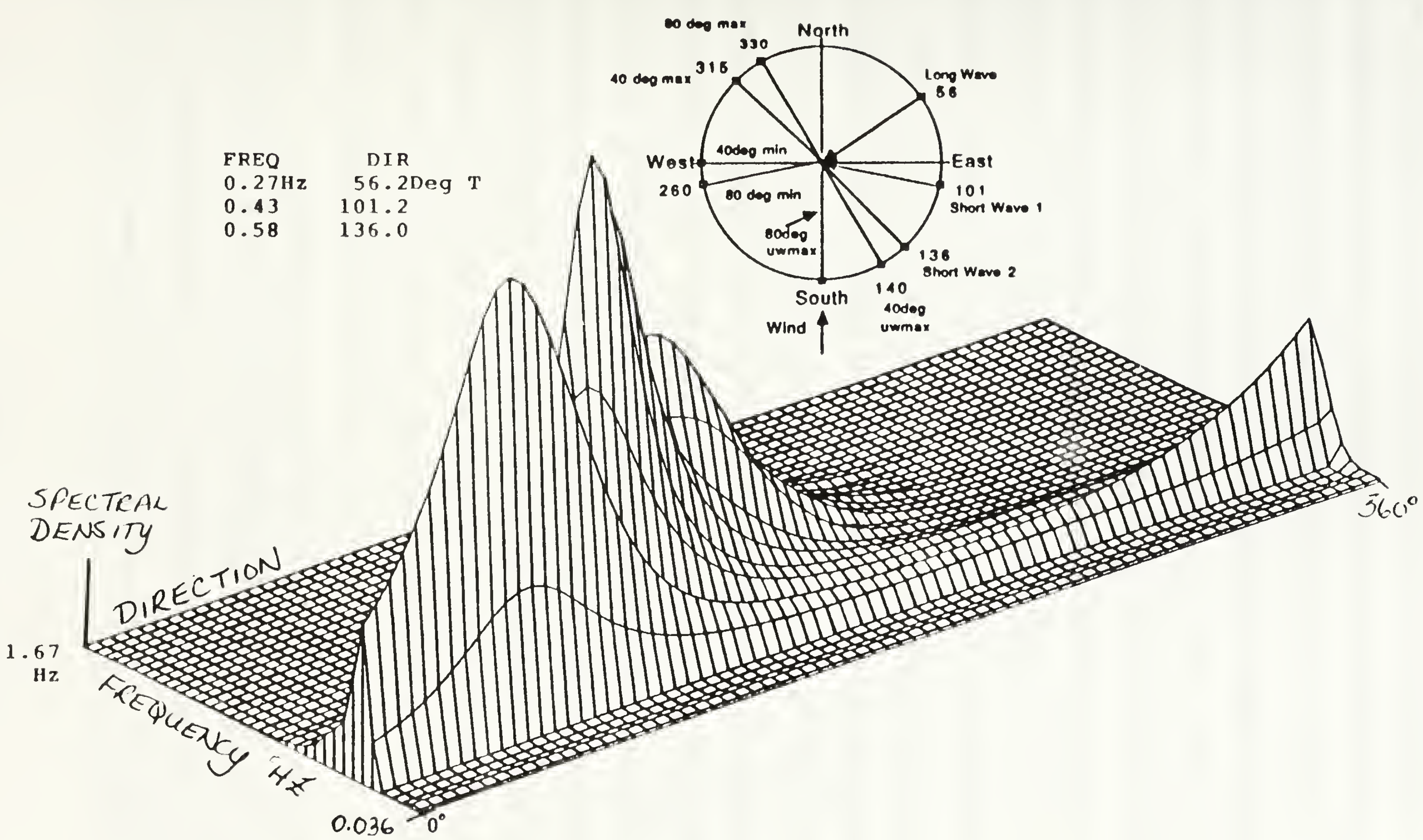

Figure 74. Run 75. Perspective Plot of Directional Spectrum and Polar Plot of Relative Geometry Among Radar, Wind and Wave Angles for 40° and 80°

4. Dependence of the NRCS on Descriptive Spectral Parameters

The azimuthal modulation at 10° and 20° was frequently observed to be 5 to 10dB which, for 10°, is significantly more than that predicted by the model functions. An initial visual examination of the data plots suggested a correlation between the amount of modulation and sea state, perhaps significant wave height. The modulation did not appear to be related directly to wind speed since both high and low wind speed cases were observed. A closer inspection of the data revealed that the modulation was greatest when the peak frequency of the wave amplitude spectrum increased to frequencies corresponding to wavelengths of 5m or less. This suggested a comparison of the modulation with wave steepness parameters, since shorter, steeper waves increase the mean-square slope of the surface, contributing to greater specular scattering at lower incidence angles.

Two spectral wave parameters which are indicators of wave steepness are the significant slope, § (eqn 141), and wave age, W (143). These quantities were objectively computed using the peak frequency from the wave amplitude spectrum. It will become clear in the ensuing discussion that misleading calculations of quantities based on the spectral peak can occur for doubly peaked spectra. The significant slope and wave age are "integral" representations of the wave field during the measurement period; therefore, a similar "integral" representation of the radar measurement is required for proper comparison of the NRCS to these wave parameters.

The coefficients of the cosine curves which approximate the NRCS azimuthal dependence (Section C) are used for comparison with the spectral wave parameters. In particular, the ratio of the A_2 to A_0 coefficients reflects the amount of cosine modulation, as normalized by the wind speed. Initial plots of the regression of the A_2/A_0 ratio with the wave parameters were scattered but much of the variance was associated with data runs which were taken when there was rain or low friction velocity values (< 0.12 - 0.17cm/s). The rainy days were immediately excluded from all incidence angles. The low friction velocity runs were at first eliminated only from the 40° data since the lower angles are less sensitive to wind speed. However, these low friction velocity values seemed always to be associated with outliers in the regression plots, so they were eventually eliminated from consideration at all angles[5].

The ratio of the A_2 to A_0 coefficients are plotted against significant slope in Figure 75 and coded as unstable, stable or neutral according to negative, positive, or zero Richardson number. An increase of the ratio with the significant slope is observed and the unstable and stable runs are clearly separated at the low and high ends of the curve. This is not interpreted as a stability effect, rather it seems to be a combined effect of stability and fetch. A plot of Richardson number with direction around the lake (not shown) indicates that all of the stable runs occur for (warm) winds from the west

---

[5] Based on the NRCS vs. friction velocity plots and these analyses, a lower limit of 0.12 - 0.17cm/s for friction velocity became a subjective editing criterion in order for the radar to behave "sensibly". This could indicate a threshold wind speed value for the radar as suggested by Donelan and Pierson (1987) however, there was no systematic dropoff of the NRCS values with wind speed observed here, only an increase in the scatter of the NRCS values when the low power returns extended beyond the dynamic range of the radar.

(short fetch), unstable runs occur mostly from the North (polar air and short fetch), neutral runs occur from the longer fetch directions (a marine layer).

A cluster of points (numbered and inside the dashed line, Figure 75) degrades the correlation of NRCS on the significant slope. These runs can be eliminated as follows: Runs 44, 52, 53 had low friction velocity values as explained in the footnote; Run 147 was at the end of a rain event and the remaining outliers all had low energy, bimodal wave spectra. For these cases, the spectral density of the lower frequency peaks was greater than, but nearly equal to that of the higher frequency peak; therefore, the lower frequency peak was chosen for the computation of the significant slope. However, the total variance of the spectrum was increased by the presence of the higher frequency waves so that in (141) the significant slope based on the peak of the spectrum appears "misplaced". The removal of these anomalous points improved the correlation from 0.62 to 0.91 (lines 1 and 2, Figure 76). This correlation indicates that the azimuthal modulation increases as the steepness of the dominant wave increases.

The significant slope is related to the wind in the sense that the total variance of the spectrum increases with the wind speed, and the wavelength corresponding to the peak frequency increases. However, the radar cross-section is only affected by the wave slope at second order: the wind speed or stress is still the primary factor in the variation of the NRCS. Therefore, the wave age is a more appropriate spectral parameter to compare to the NRCS.Utilizing the same editing criteria as described previously, A_2/A_0 at 20° h-pol was plotted against *inverse* wave age in order to yield a positive slope

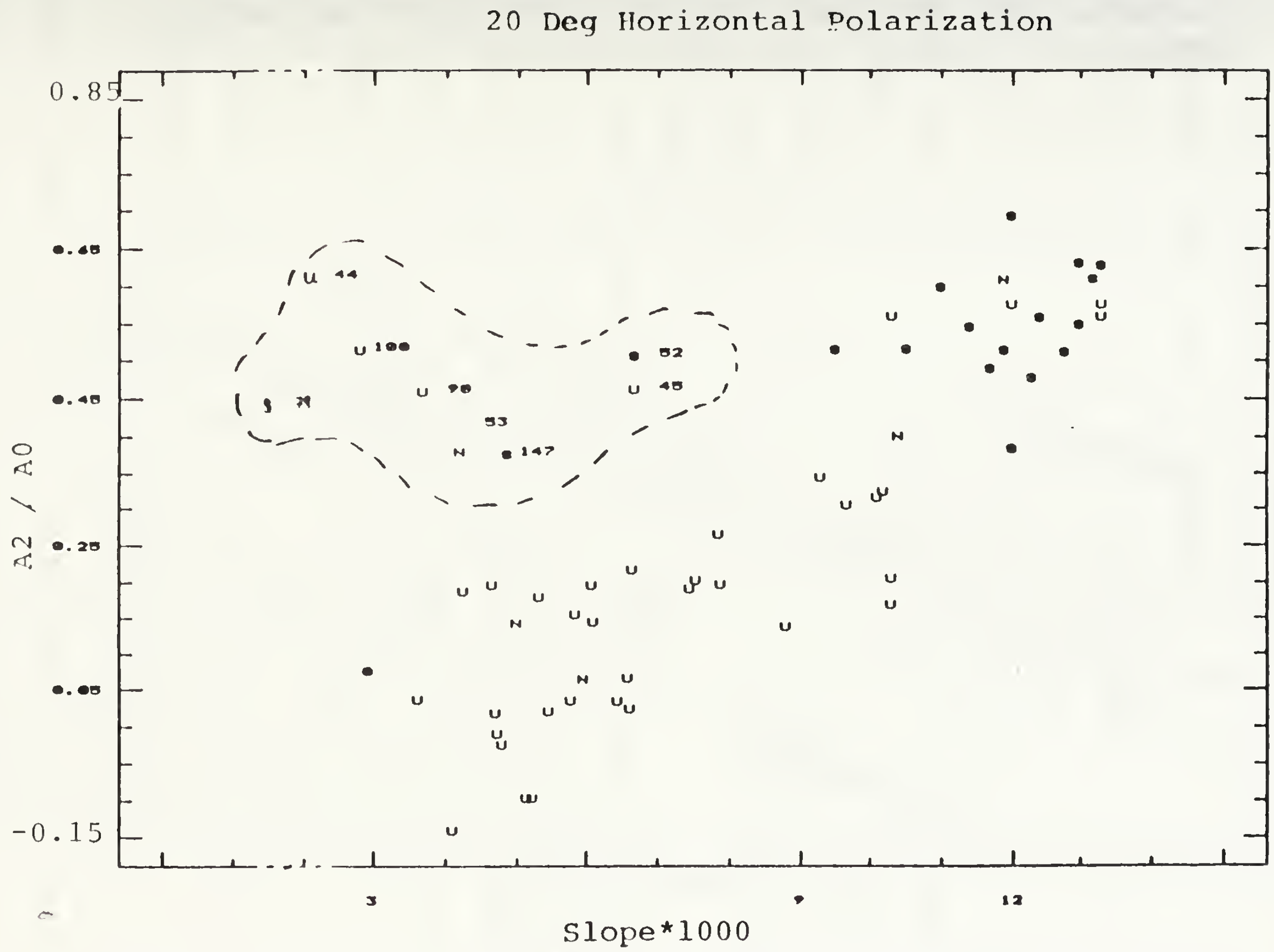

Figure 75. Ratio of A_2 and A_ϕ Coefficients from Cosine Fits to 20° Ku-Band NRCS (H--Pol) Against Significant Slope. Dashed Line Encircles Anomalous Points as Explained in Text. U: Unstable Atmospheric Stratification; N: Neutral; S: Stable

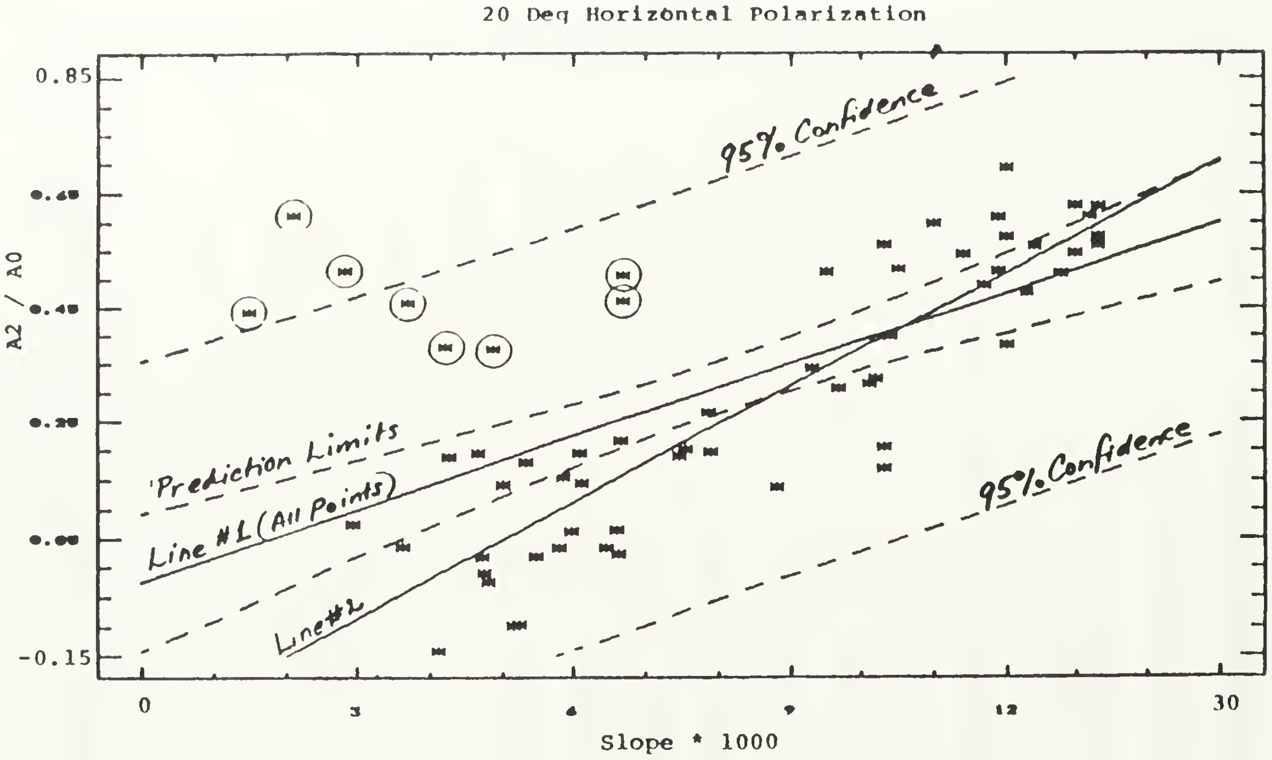

Figure 76. Ratio of A_2 and A_0 Coefficients from Cosine Fits to 20°, Ku-Band NRCS (H–Pol) Against Significant Slope. Circled Points were Eliminated from Regression (see text). Line 1: with Bad Points; Line 2: Points

on the regression line (Figure 77). The correlation of A_2/A_0 on inverse wave age is 0.91, after removal of the anomalous points listed above. Since the A_0 coefficient is highly correlated with wind speed, a multiple regression of A_2/A_0 on both wind speed and inverse wave age was performed to eliminate the possibility of any spurious correlations with wind speed. The partial correlation coefficient, adjusted for wind speed dependence, is 0.83.

The positive dependence of A_2/A_0 on inverse wave age is interpreted to mean that the azimuthal modulation at 20° increases for a growing sea composed of shorter, steeper waves. This result holds for 10° and 20°, both polarizations; at 40°, there is still a positive, albeit reduced correlation of A_2/A_0 on inverse wave age of 0.75 (Figure 78). For these higher incidence angles, the quasispecular return is reduced for increasing slopes, and the Bragg scattering term dominates (12).

The two-scale model by Plant (1986) expresses the NRCS in terms of the upwind and crosswind slopes. An adjustable parameter, ε, of the model represents the ratio of the crosswind to upwind slopes to be adjusted, where ε as set by Plant is 0.4. The Plant model was run to examine the effect of changing slopes on the azimuthal modulation at 20°, this parameter was varied from 0 to 1 (extreme range of 0 to 100% crosswind slope). The results, summarized in Table VII, show the expected inverse relationship between the azimuthal modulation and the crosswind slope. However, the modulation never disappears as was frequently observed in the lake Ontario NRCS data (recall Test Case 3 and see Appendix B). Since these "flat" curves occurred when the peak frequency of the wave spectrum was low, it was

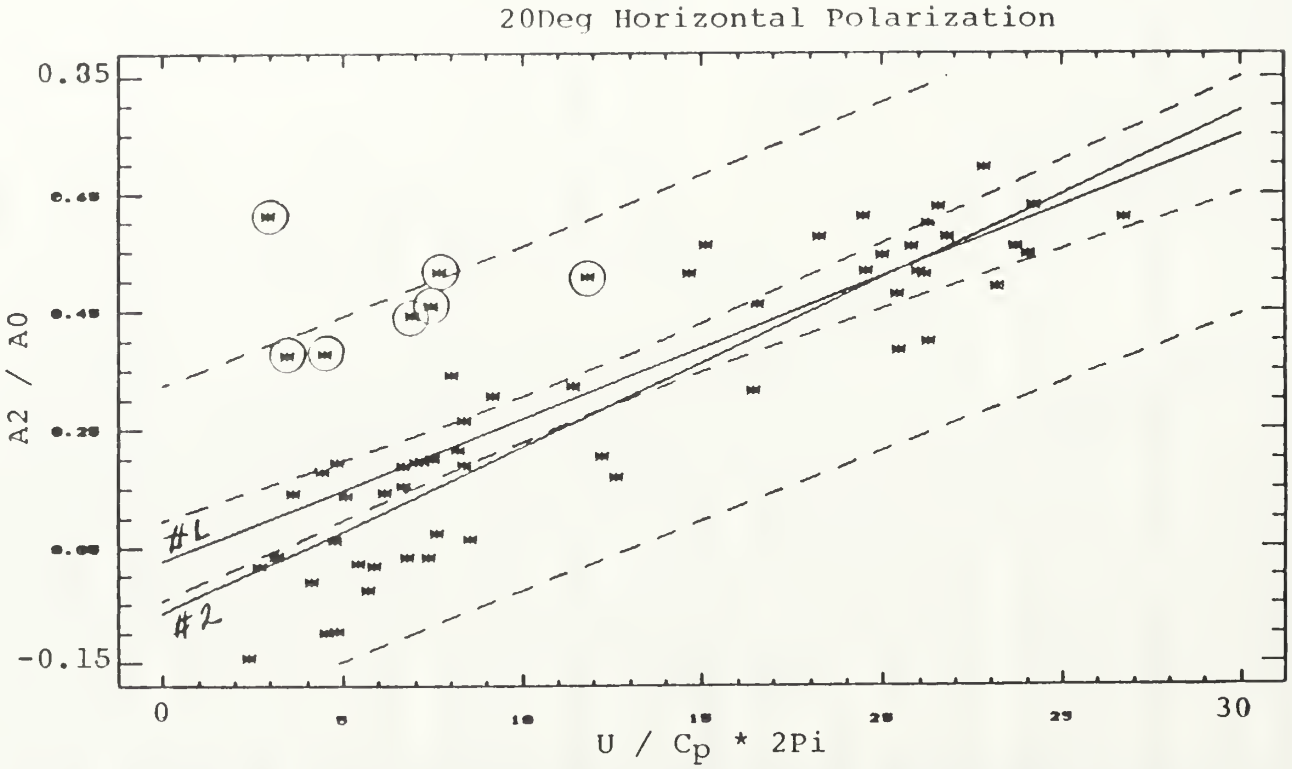

Figure 77. Ratio of A_2 and $A_\emptyset$ Coefficients of Cosine Fit to 20°, H-Pol, Ku-Band NRCS versus Inverse Wave Age. Circled Points Eliminated from regression as explained in Text. Line 1 with Points; Line 2: without Points

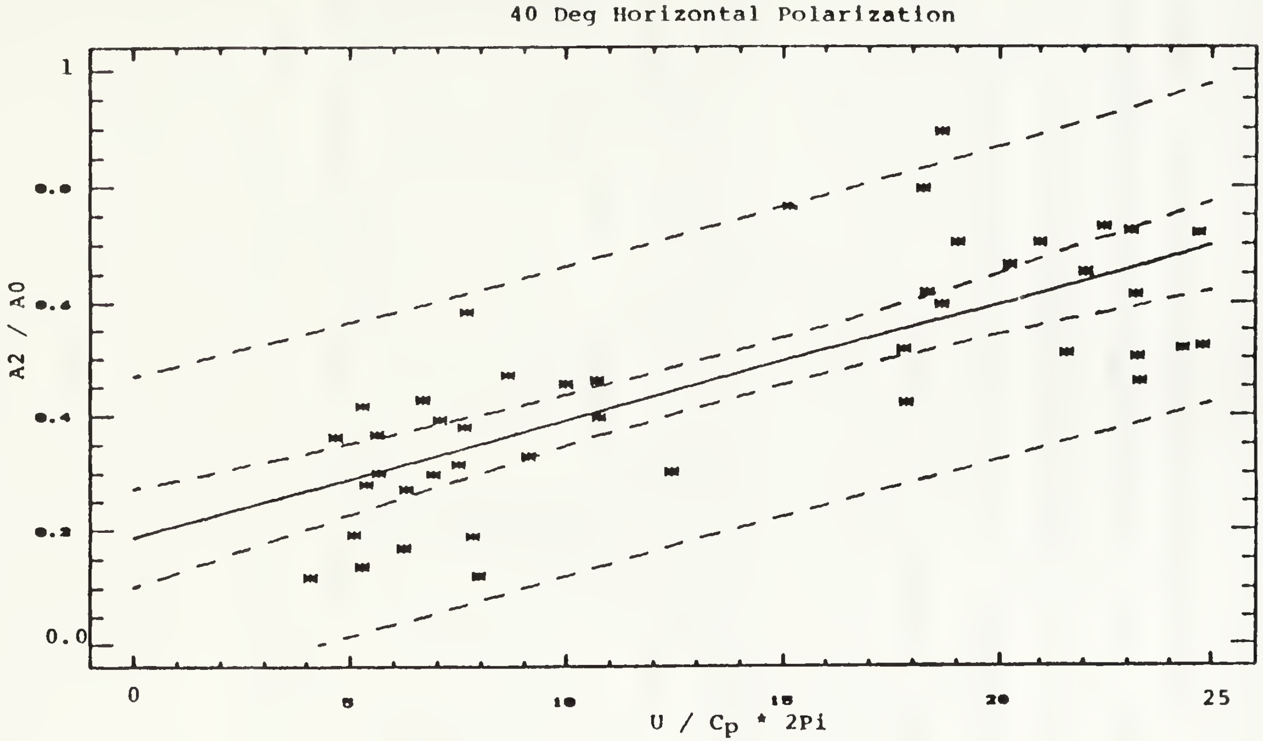

Figure 78. Ratio of A_χ and A_ϕ Coefficients of Cosine Fits to 40°, H-Pol, Ku-Band NRCS versus Inverse Wave Age.

hypothesized that the reduction in the modulation was due to a decrease in the total mean-square slope. The Plant model was run again with the mean square slope halved and ε equal to 0.4. The results show that the the upwind/downwind (UW/DW) difference increases while the crosswind minima maintain about the same value. Therefore, in this model the total slope determines the UW/DW values and the ratio of the upwind/crosswind slopes determines the amount of azimuthal modulation. The observed "flat" curves which prompted this sensitivity could not be reproduced with any realistic values of the slopes or crosswind/upwind ratio.

TABLE VII. PREDICTED EFFECTS OF SLOPE CHANGES ON NRCS FROM PLANT MODEL (20°, WIND SPEED 6M/S)

ε	UW/CW Difference		UW/DW Difference	
	vpol	hpol	vpol	hpol
0.0	12.5	13.4dB	0.5	0.5dB
0.2	10.8	11.2	0.5	0.6
0.4	9.4	9.4	0.6	0.7
0.6	8.1	7.8	0.7	0.8
1.0	Maximum no longer at upwind. Assumption of collinear wind and wave angles is violated.			

E. DEPENDENCE OF NRCS ON ATMOSPHERIC STRATIFICATION

The previous sections have shown the NRCS to be functionally dependent on wind speed, wind and wave directions and the state of wave development. If the atmospheric stability is now entered as an influencing variable, then the NRCS may be written as follows

$$\mathrm{NRCS} = \mathrm{NRCS}(u_i, \varphi, \gamma, z/L, s^2) \tag{149}$$

where u_i is either friction velocity or wind speed; φ, γ are the wind and wave directions; z/L is the stability parameter; and s^2 is the mean square slope.

In the effort to define an operational algorithm for the NRCS, the wind speed, wind direction and stability dependencies are accounted for in the SASS1 and SASS2 algorithms, which parameterize the NRCS as a power law of neutral wind and a Fourier series in relative wind direction. Studies subsequent to SEASAT (Keller et al., 1985; 1989) revealed that the NRCS was also related to atmospheric stratification and long wave slope (recall Figure 2), although a unique relationship of NRCS on friction velocity, wave slope and stability could not be established for all stability conditions. The conclusion of Keller et al.(1985) was that the surface layer theory used to estimate the friction velocity did not properly account for stability, or that the NRCS was not determined by the stress in any simple fashion.

The problem lies in the assumption of independence of the variables contributing to the NRCS measurement. The Lake Ontario data provide an extreme example of how tangled the web can become when the interdependence of the physical parameters is considered. It was noted earlier in the discussion of the NRCS azimuthal variations that the stability varied systematically with direction around the lake: the most unstable data were from the North-Northwest (cold polar air), near-neutral, from the North-Northeast (marine winds), and most stable from the South-Southwest. Inasmuch as the fetch gradient of the lake has a similar directionality, stability and fetch, hence stability and sea state, are highly correlated in this study. This correlation was displayed in Figure 75, in which all but one of the stable values of the ratio of A_2 to A_0 corresponded to higher values of significant wave slope or inverse wave age.

The comparison of the NRCS values with any particular geophysical parameter then requires that all other influencing variables be held constant. This filtering of the data quickly reduces many thousands of points to a few dozen. Therefore, to keep as many of the Ku-band radar NRCS values as possible in this examination of stability effects, and to eliminate the influence on the NRCS from the primary factors of wind speed and direction, the data were normalized using the fitted sinusoidal curves which approximate the dependence of NRCS on relative wind angle as shown in Section C. The difference of the measured NRCS (in linear units) and the fitted value at a particular azimuth was computed at each data point to account for the wind speed dependence of each curve. All of the residuals were then normalized to the "upwind" value, for a particular run, by adding to it the sum of the three cosine coefficients (eqn(91) with $\chi = 0$); i.e., all points were translated to the same relative angle position.

The normalized "upwind" points were stratified by ranges of a particular wind parameter and plotted against air-sea temperature difference, bulk Richardson number and z/L as determined from the bulk Richardson number and Donelan's ratio of z/L to Richardson number. The residuals for 20° incidence (v-pol) stratified on measured wind speed at 11.5m, $U_N(19.5)$, $U_N(1)$, and friction velocity are shown in Figures 79 to 82, in which the measured wind speed range is from 6.5 to 7.5m/s and the other wind parameters were scaled to correspond with this wind speed range. The NRCS values show a steady decline amounting to about 5dB in 25°C. The obvious decrease of the cross-section with increasing stability is not removed by any of the wind speed parameters.

A similar decrease of the NRCS is observed in the 40° v-pol data for the same measured wind speed range of 6.5 to 7.5m/s (Figure 83). However, stratification of the NRCS residuals on the corresponding friction velocity (which is independent of stability) or neutral wind (which has been corrected for stability) removes most of the dependence of the NRCS on stability (Figures 84 to 86). Comparison of the plots based on the three stability-independent wind speed parameters used, shows the neutral wind at 1m appears to be more effective than the friction velocity at removing the stability dependence.

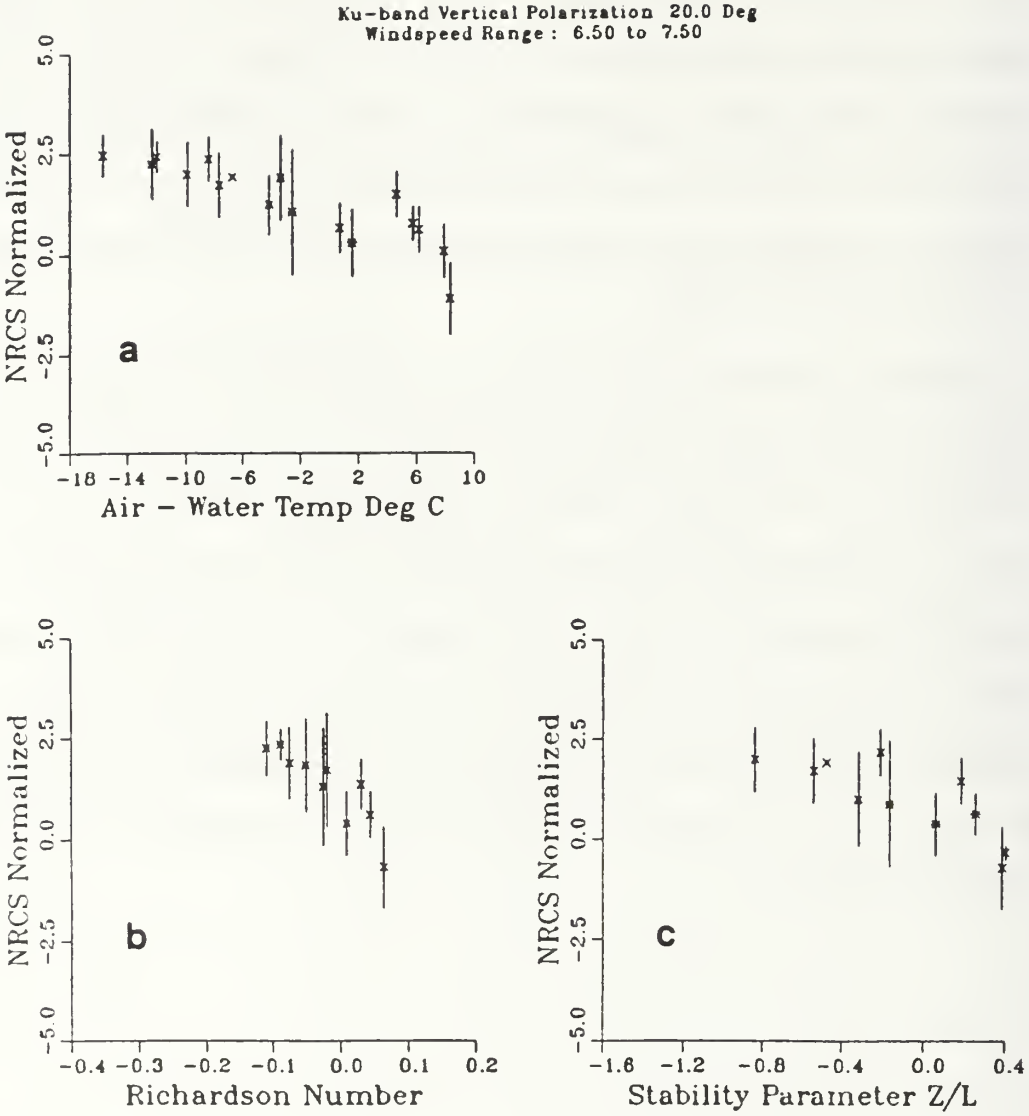

Figure 79. Normalized 20°, V-Pol Ku-Band NRCS for Measured Wind Speed of 6.5 to 7.5m/s as a Function of a) Air-Water Temperature Difference, b) Bulk Richardson Number, and c) Stability Parameter.

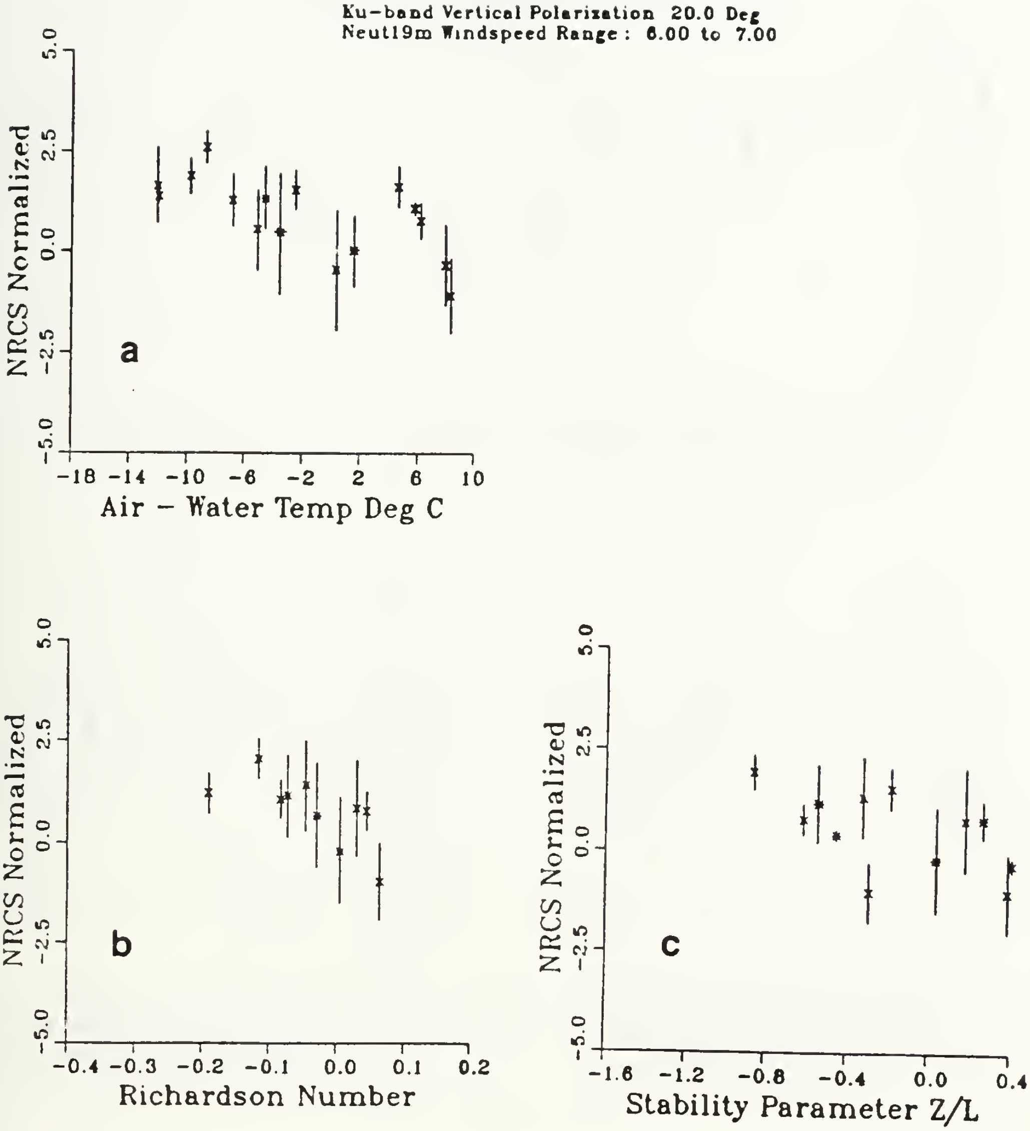

Figure 80. Normalized 20°, V-Pol, Ku-Band NRCS for $7.0<U_N(19.5)<8.0$m/s as a Function of a) Air-Water Temperature Difference, b) Bulk Richardson Number and c) Stability Parameter

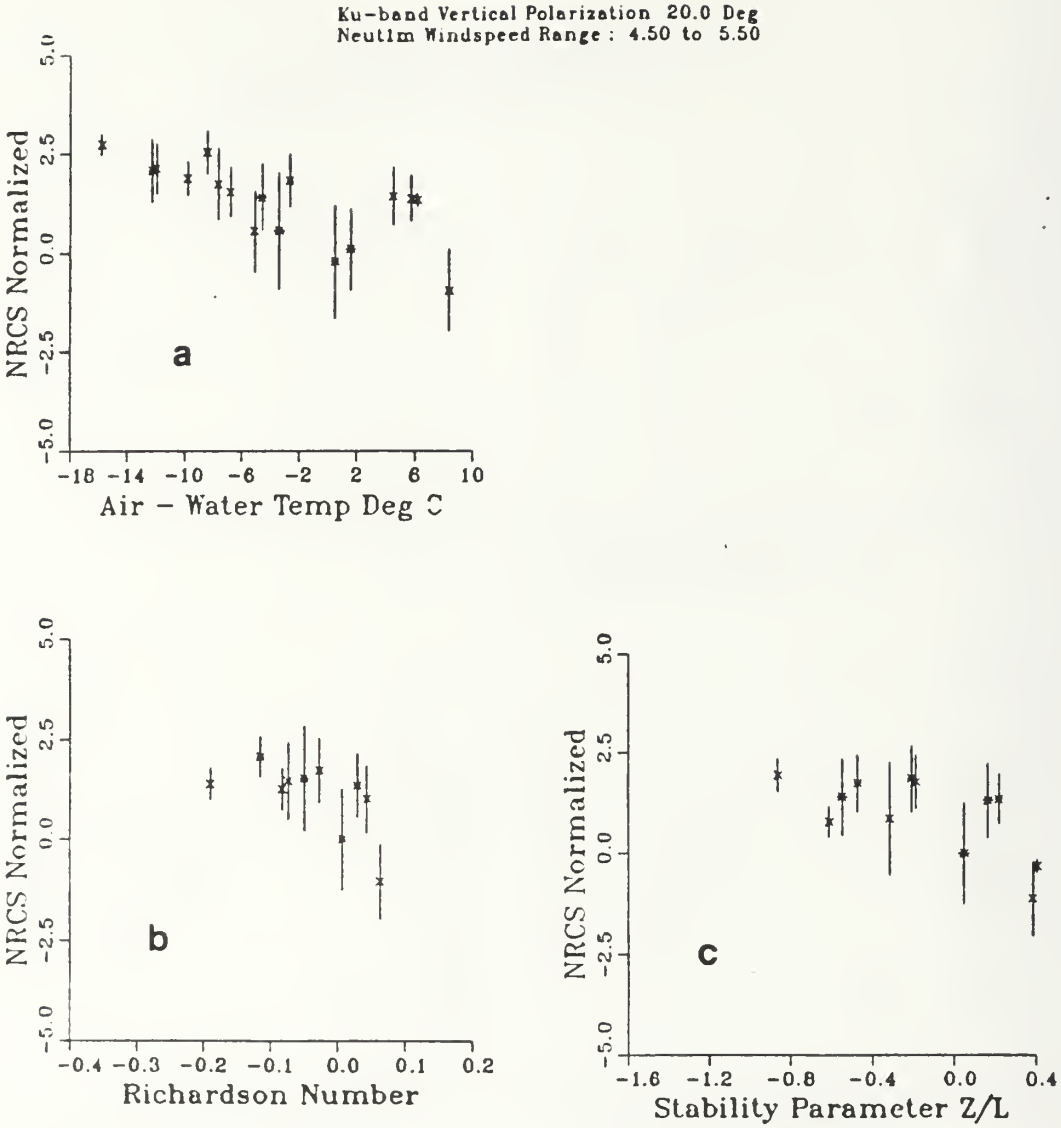

Figure 81. Normalized 20°, V-Pol NRCS for $4.5 < U_N(1) < 5.5$ m/s as a Function of a) Air-Water Temperature Difference, b) Bulk Richardson Number and c) Stability Parameter

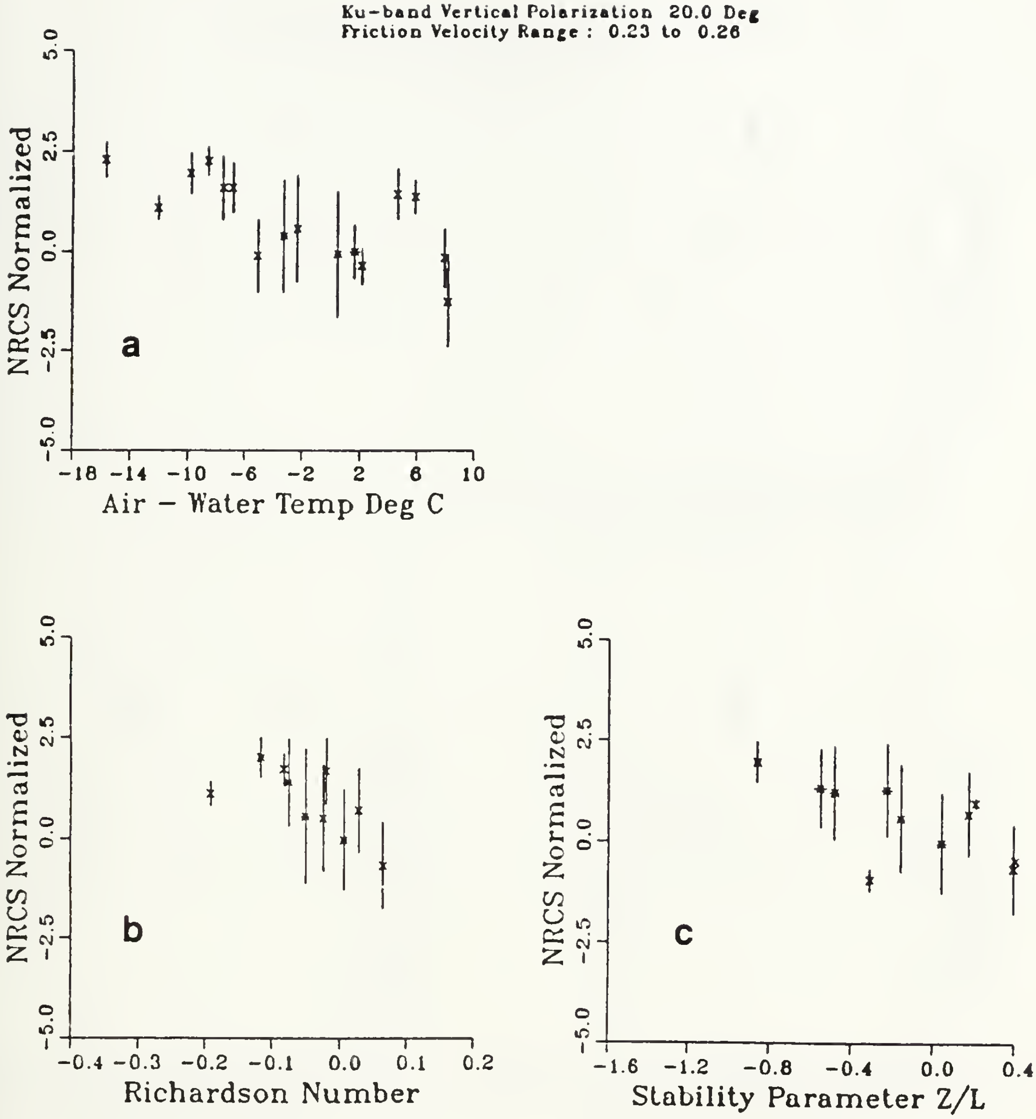

Figure 82. Normalized 20°, V-Pol NRCS for $0.23<u_*< 0.26$m/s as a Function of a) Air-Water Temperature Difference, b) Bulk Richardson Number and c) Stability Parameter

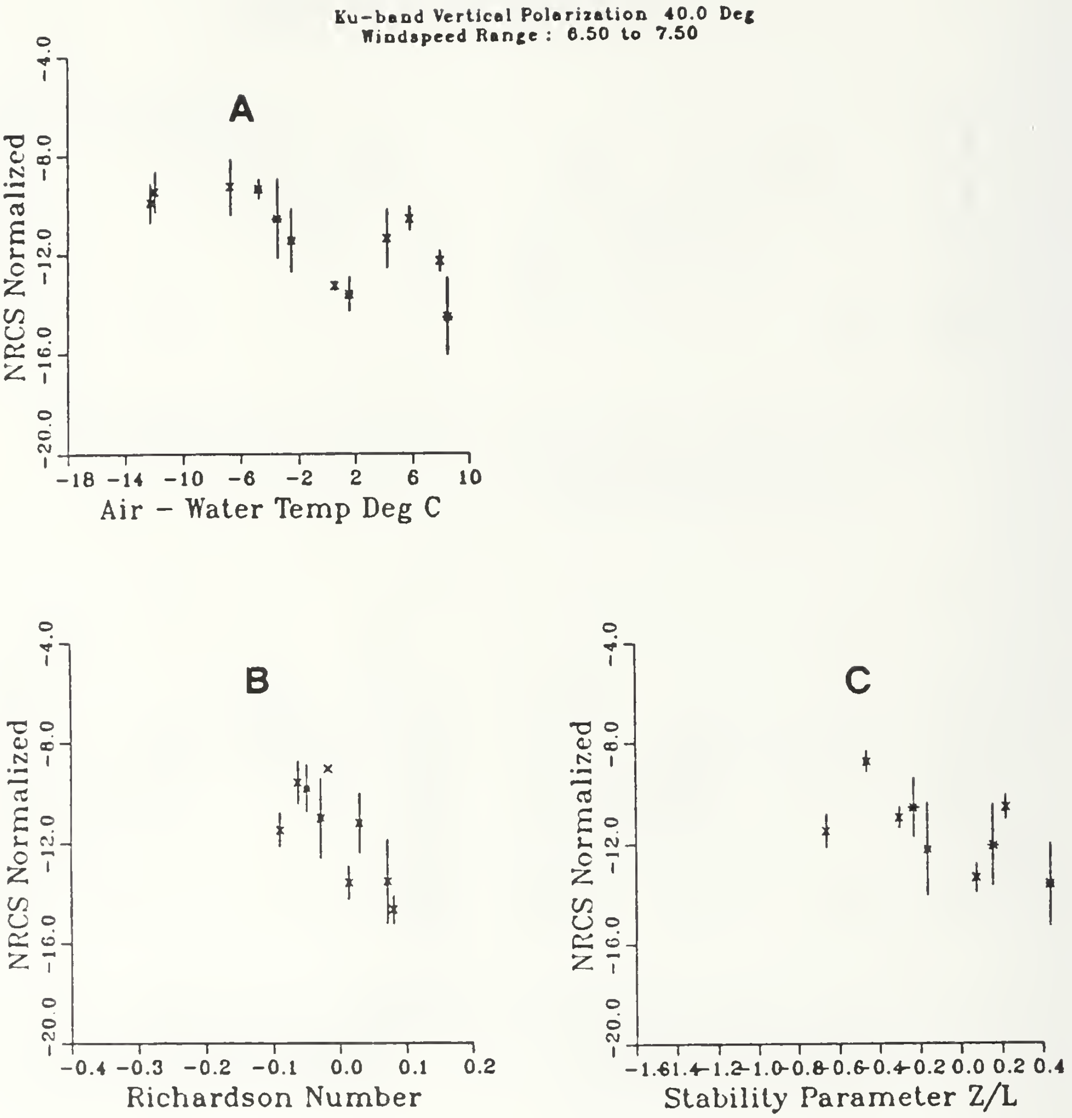

Figure 83. Normalized 40°, V-Pol Ku-Band NRCS for Measured Wind Speed of 6.5 to 7.5m/s as a Function of a) Air-Water Temperature Difference, b) Bulk Richardson Number, and c) Stability Parameter.

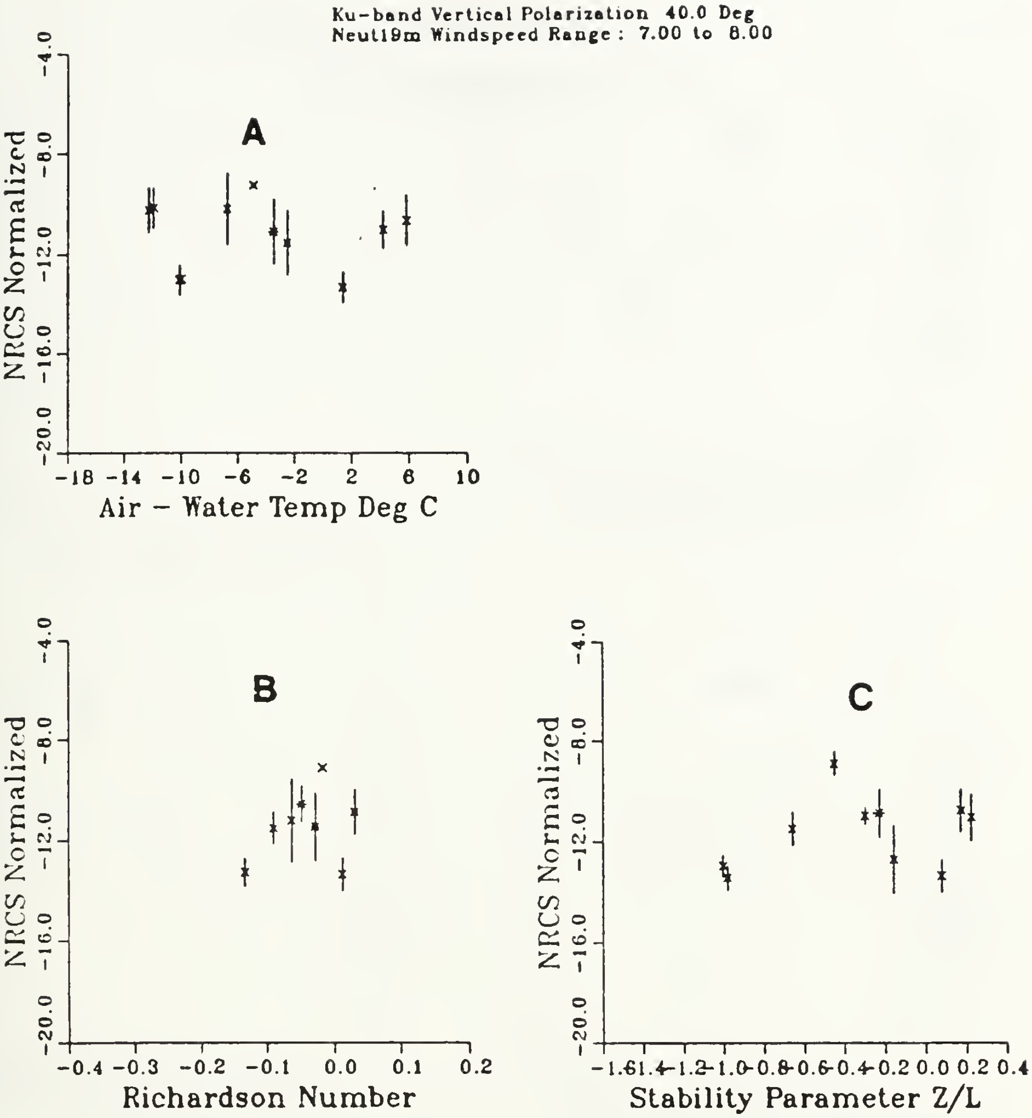

Figure 84. Normalized 40°, V-Pol, Ku-Band NRCS for $7.0<U_N(19.5)<8.0$m/s as a Function of a) Air-Water Temperature Difference, b) Bulk Richardson Number and c) Stability Parameter

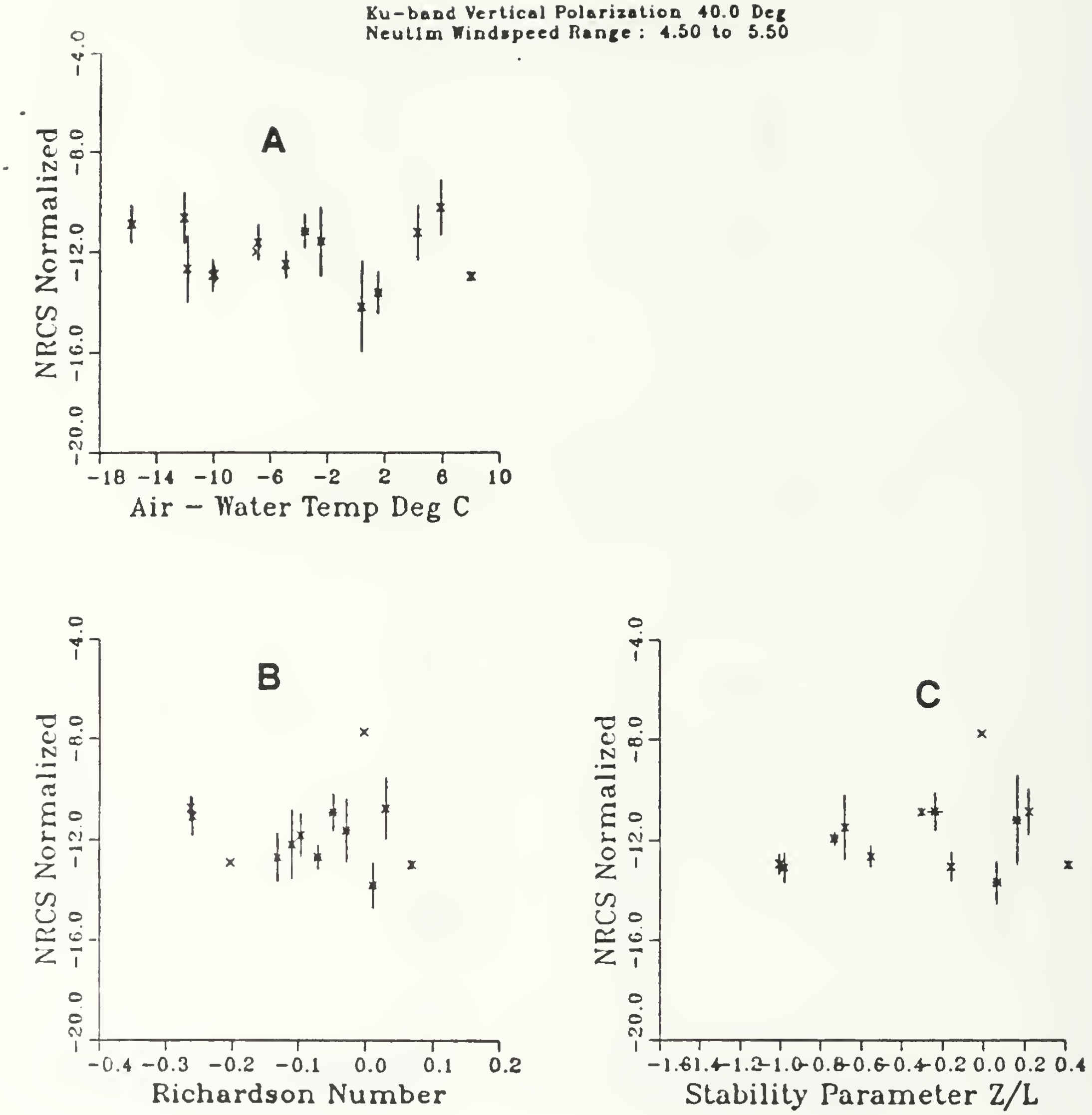

Figure 85. Normalized 40°, V-Pol NRCS for $4.5<U_N(1)< 5.5$ m/s as a Function of a) Air-Water Temperature Difference, b) Bulk Richardson Number and c) Stability Parameter

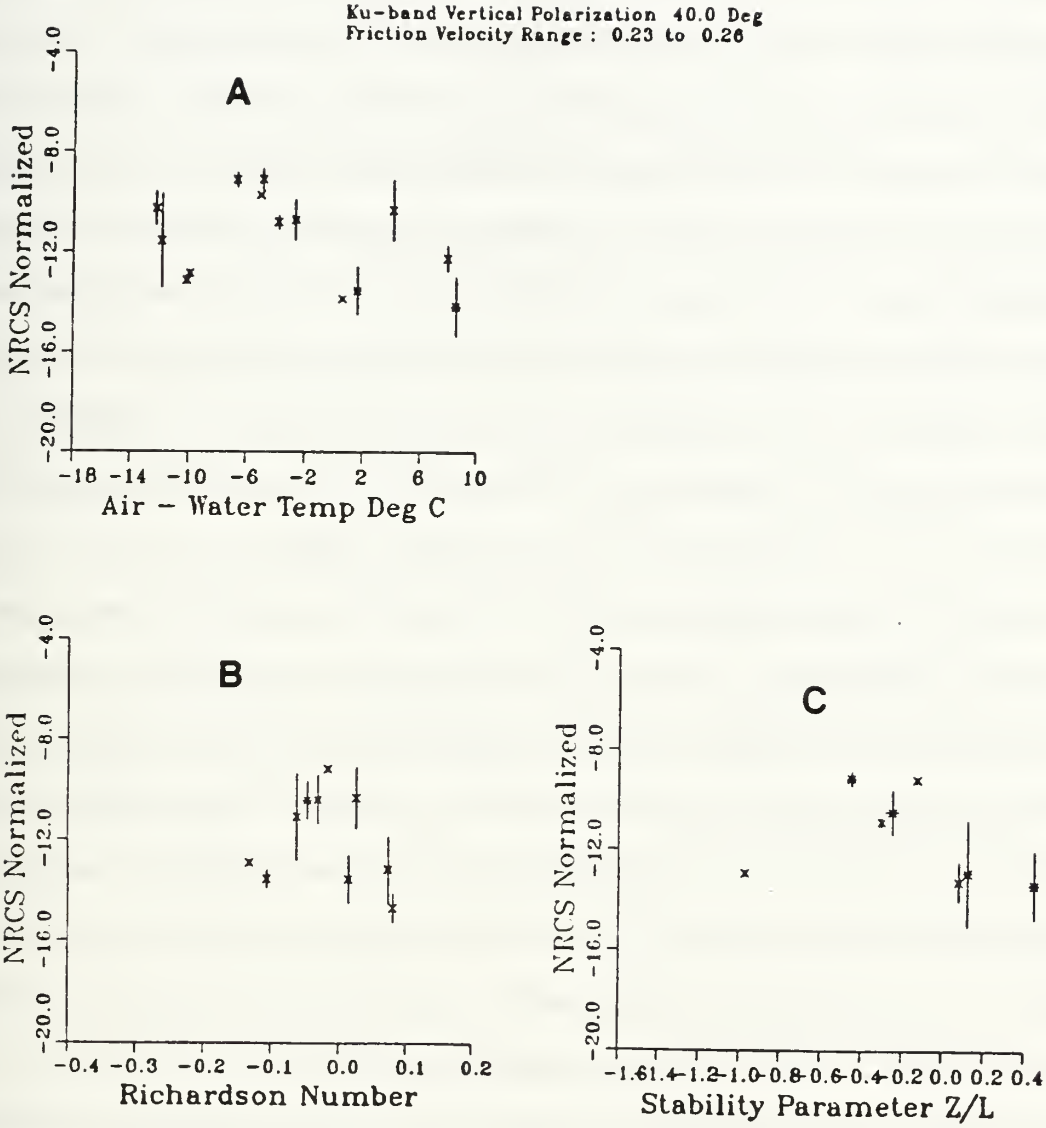

Figure 86. Normalized 40°, V-Pol NRCS for $0.23 < u_* < 0.26$m/s as a Function of a) Air-Water Temperature Difference, b) Bulk Richardson Number and c) Stability Parameter

The simple functional expression for the NRCS stated at the beginning of this section (149) can be used in the interpretation of these observations. Given that the NRCS decreases with increasing stability for a particular measured wind speed mandates that a stability independent wind parameter must be used in any parameterization of NRCS on wind speed. This would account for the wind parameters and stability in (149). However, the observations at 20° which show the stability dependence to remain, even after stratification of the data with a stability independent wind speed parameter, implies that the accounting for stability is not complete. Since the azimuthal asymmetry in the NRCS at 20° is highly correlated with long wave slope and the stability is similarly correlated with slope (Figure 75), it is suggested here that the "stability dependence" observed at 20° is actually a guise for a stability/slope dependence (Janssen and Komen, 1985).

At 40°, where Bragg-resonance dominates and the slope is not as important, the friction velocity or neutral wind speed fully accounts for atmospheric stratification. The observation that the neutral wind speed at 1m seems to remove the dependence most completely, negates Keller et al.'s (1985) suggestion that the stability correction to the friction velocity for neutral wind speed (equation 81) is inadequate since the same correction was applied here. Instead the results affirm their second conclusion, which was that the NRCS is not a function of wind stress alone.

These findings have bearing on the surface layer theories incorporated in the model functions. Evidently, the choice of a neutral wind parameterization at 19.5m was appropriate for the statistical models (SASS1 and SASS2) in spite of being physically unsatisfying. Assuming a logarithmic wind speed profile enables the neutral wind speed at a higher (measurable) level to be lowered to a near-surface level; in this analysis the neutral wind at 1m was used with some success. This supports the contention by Donelan and Pierson (1987) that the wind speed nearer the surface is the controlling parameter, however, it does not support their assumption that the neutral profile can be extended to within 1cm of the surface. Since the neutral wind speed in this study was computed from a direct measure of the wind stress and the stability parameter, and by virtue of the observed slope effect, Plant's model which incorporates friction velocity and long wave slope could be exercised to examine the combined friction velocity/stability/slope effects. However, in its current form, neutral conditions are assumed so that incorporation of a stability correction to the friction velocity is required before the effect of stability can be evaluated.

Finally, the Durden and Vesecky (1986) model does include a stability correction to the neutral wind speed. Based on the observations here that the neutral wind is effective at removing the dependence of the NRCS on stability implies that the model NRCS predictions should similarly have no dependence on air-sea temperature difference, at a constant neutral wind speed. To test this, the D&V model was run for air-sea temperature differences from -20°C to 9°C for 40° incidence, v-pol, and $U_N(19.5) = 7$m/s. The NRCS predictions show a 2.8dB decrease from -14.1dB at -20°C to -16.9dB at +10°C; i.e., there is still a residual stability dependence predicted by this model. As stated previously, the expressions used for the drag coefficient and z_o in this model are inconsistent. Correcting the numerical coefficients in the

z_0 expression may eliminate altogether the small dependence of the NRCS on stability predicted by this model.

F. NRCS DEPENDENCE ON WATER TEMPERATURE

The Donelan and Pierson model function specifies the waves in the Bragg domain to be the result of a balance between wind input and viscous dissipation. Since viscosity is inversely proportional to water temperature, the NRCS predictions from their model are water temperature dependent. The differences are small, e.g., only 1dB between the NRCS values for water temperatures of 0°C and 30°C and wind speed of 7m/s. In the WAVES87 experiment, the water temperature variation was only about 4°C; therefore, the predicted effect of water temperature on the NRCS could not be verified. Examination of the WAVES86 data, which spanned 10°C, also showed no discernible dependence of NRCS on water temperature.

G. SUMMARY

In this chapter the dependence of the NRCS on the individual and combined effects of wind speed, wind direction, wave direction and spectral parameters, atmospheric stratification and water temperature were discussed. Where indicated, model function experiments were performed to provide additional insight into the observations.

The NRCS was shown to have a greater dependence on neutral wind speed than that of the model predictions based on open ocean NRCS data. It was found that more favorable comparisons between the NRCS versus wind speed curves were obtained after re-scaling the data to account for the steeper waves, hence larger drag coefficient of the lake. The wind direction and friction velocity dependence was examined in three-dimensions to confirm the characteristic sinusoidal modulation of the NRCS and the positive slope of the surface with increasing friction velocity. Individual curves of the wind speed as a function of the relative angle were examined within the context of wave effects. Placement of the minima of these curves appeared to be related to the angular spread of the wind waves, taken here to be indicative of the spreading of the Bragg waves. Increased upwind/crosswind modulation of the cross-sections at lower incidence angles was determined to be a function of significant wave slope. It was suggested that the effect of atmospheric stratification at 20° was not completely accounted for by simply using a stability independent wind speed parameter since there was a correlation of stability and slope in this experiment. However, it was found at 40°, where Bragg resonance dominates, and scatterometers are designed to operate, the selection of friction velocity or neutral wind speed removed the stratification dependence with the neutral wind speed at 1m providing the best normalization. A parametric check of the effect of water temperature on the NRCS could not be performed due to the limited range of water temperatures encountered during the experimental period.

VI. SUMMARY AND CONCLUSIONS

A. SYNOPSIS OF THE STUDY AND MAJOR RESULTS

Microwave radar scatterometers transmit radiation of centimetric wavelength to the sea surface and receive the averaged power reflected from the sea surface by ocean waves of approximately one-half the electromagnetic wavelength. The number and distribution of ocean waves of the appropriate centimeter wavelength are primarily due to the speed and direction of the wind. Therefore, it is possible to relate the intensity of the power received by a radar scatterometer to the wind velocity at the sea surface in the form of a "transfer function," commonly referred to as a "model function."

A satellite scatterometer was flown on a oceanographic satellite, SEASAT, in 1978, to demonstrate the concept of measuring global oceanic winds from space. The data from this mission, processed according to a model function known as SASS1, were analyzed to produce detailed maps of the synoptic oceanic wind field with resolution previously unimaginable. Unfortunately, systematic errors in the SASS1 algorithm were discovered in subsequent analyses and additional empirical studies implicated effects on the measured radar returns due to geophysical variables other than the wind. The documentation of the SASS1 weaknesses, the appearance of new model functions in the literature, and the suggestions of additional environmental effects on the model function provided the motivation for the present study.

The development of a scatterometer model function requires consideration of electromagnetic, ocean wave and air-sea surface layer theories. Concepts from each of these areas pertinent to scatterometry were discussed to provide the background for the description of existing model functions. Based on these model functions, environmental parameters were identified which may influence the fundamental measurement of the scatterometer, the Normalized Radar Cross-Section (NRCS).

The Water-Air Vertical Exchanges 1987 experiment (WAVES'87), designed in part to evaluate the effects of environmental parameters on the NRCS, was performed from a research tower located in Lake Ontario, on which two radar scatterometers operating at Ku- and C-band (14.0 and 5.0GHz) were installed for six weeks in the autumn of 1987. A novel aspect of the radar portion of this experiment was that the Ku-band radar was installed on a rotating, incidence angle adjustable, antenna platform. Therefore, both the azimuth and incidence angle variations in the received power were examined within the context of environmental effects. The noteworthy aspects of the *in-situ* measurements were the simultaneous acquisition of wind stress from a bivane anemometer and high resolution directional wave spectra. The attributes of the scatterometers and the supporting meteorological/limnological instrumentation were described, as well as the data processing required to reduce the uncalibrated voltage measurements to a set of collocated radar cross-section and geophysical variables. Using this collocated data set, the dependence of the NRCS on each of the individual effects of wind speed, wind direction, wave spectra and spectral parameters, and atmospheric stability was examined. The limited (4°) range of water temperature encountered during this experiment prevented a similar parametric analysis of the effect of water temperature on the NRCS.

The NRCS measured by the multiple incidence angle, Ku-Band scatterometer in Lake Ontario exhibits the characteristic *incidence angle behavior as a function of wind speed at 19.5m* measured in previous studies: i.e., a negative dependence on wind speed at nadir, transitioning through almost no wind speed dependence at 10° and a positive dependence at 40° (2.4, ±0.11, upwind, vpol) to 60° (2.7, ±0.20, upwind v-pol). The *slopes of the NRCS curves as a function of neutral wind speed* are steeper than the corresponding curves obtained from existing model functions, which are based on open ocean conditions (cf., 2.4 and 1.7, 40° v-pol, upwind). Scaling the lake data to simulate open ocean conditions by using the ratio of a lake drag coefficient to an ocean drag coefficient reduces the slopes of the NRCS versus neutral wind speed curves and makes them parallel to those predicted by the model functions (cf., 1.6 and 1.7, 40°, v-pol). The successful adjustment of the curves using this lake/ocean drag coefficient scaling indicates the drag coefficient should include a sea state dependence. If the drag coefficient is considered to be a function of wind speed alone, then the nearly cubic dependence of the NRCS on neutral wind also implies the NRCS is proportional to the wind stress.

However, the *correlation coefficients for the regressions of NRCS against neutral wind speeds at 19.5m and 1m and friction velocity* were higher for the neutral wind speed than for the friction velocity (cf., 0.91 and 0.79, 40°, upwind, v-pol). This statistic alone is insufficient to declare the neutral wind speed to be a better predictor of NRCS. Although the neutral wind speeds, at levels higher and lower than the anemometer height, were deduced from the friction velocity in this experiment, they were smoothed by the ratio of the measured and neutral drag coefficients in the conversion process. Therefore, the neutral wind speeds have less inherent variability and the correlations are improved.

The two primary characteristics of the NRCS, that is, the *azimuthal modulation of the NRCS as a function of both relative wind angle and friction velocity* were viewed in three dimensions for the six incidence angle settings of the Ku-band radar. The sinusoidal modulation becomes evident at 20° and more obvious at 40°. The 60° and 80° surfaces at v-pol continue to display the sinusoidal modulation whereas the sinusoidal appearance of the 60° h-pol NRCS surface is much less apparent, and not at all apparent at 80° where the NRCS measurement is generally at the noise level of the radar.

The minima in the *azimuthal modulation of the NRCS as a function of relative wind angle* are often shifted by as much as 45° such that the minima do not always occur at 90° and 270° cross-wind angles. The addition of a second order sine term to the standard three term cosine fit of the azimuthal modulation often places the minima better. It cannot be said that the fits with the additional sine term improve the fits in a general sense since the NRCS values were not distributed evenly over 360°. The effect of rain on the NRCS azimuthal modulation is to increase initially, then decrease, the level of the Ku-band NRCS, and to flatten out the azimuthal variability in the NRCS; i.e., the NRCS is isotropic in the presence of rain. The C-band NRCS does not appear to be similarly affected by the rain, indicative of the greater influence of rain on 1cm Bragg waves compared with 3cm Bragg waves. Further comparisons of rain effects on the Ku- and C-band NRCS values will be performed with additional test cases identified in the WAVES'87 data.

The *azimuthal modulation as a function of relative wave angles* indicate that the shape of the azimuthal dependence conforms best to the sinusoidal model when the wave state is dominated by wind waves in the direction of the wind. However, the angular spread between the NRCS minima is generally rather less than 180°; therefore, the minima in the NRCS do not occur at 90° angles to the wind. In the case of a long swell component opposing the wind sea, the minima become symmetric to the relative angles between the primary wave components and the separation of the minima widens to 180°. The azimuthal modulation disappeared altogether in the case of a "confused" sea consisting of multiple peaks and broad directionality.

The *azimuthal modulation as a function of wave spectrum parameters* is highly correlated with significant slope and inverse wave age at 20° (correlation coefficient of approximately 0.90) and moderately correlated with these same parameters at 40° (0.75). Therefore, increased azimuthal modulation at 20° is associated with a steeper wave field, which increases the specular contribution to the NRCS at this angle. At higher incidence angles, Bragg-resonance with the capillary waves is the dominant scattering mechanism.

The *dependence of the NRCS on atmospheric stability* shows the NRCS to decrease by about 5dB between air-sea temperature differences of about -16° to +10°C. This means that the NRCS in an unstable environment indicates a wind speed at least 2m/s higher than for a stable environment, if a square-law dependence between the NRCS and wind speed is assumed. Since the design error for the scatterometer wind speed is 2m/s, improper accounting for this effect alone will prohibit the design criterion from being met. It was not possible to remove the stability dependence at 20° for stratification of the NRCS on any wind speed parameter or friction velocity. The conclusion is that the assumption of independence among the variables influencing the NRCS was violated in this experiment since the stability and fetch (hence wave state) are correlated. Therefore, at 20° the failure of a wind speed parameter to remove the stability dependence is an indication of an additional correlation between stability and wave slope. At 40°, where the NRCS is more dependent on wind speed than mean-square slope, stratifying the data on either the friction velocity or neutral wind speed removes the stability dependence. Therefore, model function parameterization of the NRCS in terms of the friction velocity or neutral wind speed accounts for the observed decrease in NRCS with atmospheric stability.

In light of the interdependence of the factors influencing the NRCS, a diagnostic model for the NRCS must either use a physical approach to model the evolution of the sea surface through the wavenumber spectrum, or be derived from an enormous statistical data base which represents all possible environmental conditions. Quantification of the relative importance of a particular environmental parameter can only be established as a function of scale and application; i.e., increased resolution and accuracy requirements of a satellite sensor demand physical understanding and measurements at correspondingly finer scales.

In this study, existing model functions of both types (physical and statistical) have been examined to elucidate how and why certain environmental parameters are included in the models. The attributes and basic predictive characteristics of each of the models (SASS1, SASS2, Durden and Vesecky, Plant, and Donelan and Pierson) were described. All of the model functions, with the exception of SASS1, are prototypes which have not been evaluated for operational use. Therefore, this analysis focussed on the validity of the basic assumptions regarding environmental parameters within the models, rather than establishing the skill of the different models. Further, the electromagnetic scattering model *per se* was not critically analyzed; however, the greater importance of the significant slope at lower incidence angles as compared to the intermediate incidence angles does suggest a composite surface approach.

The empirical results described above indicate that two of the major aspects of the model functions which need to be reconsidered are the methods by which the wind waves are spread about the wind direction and the assumption of fully developed wind seas of one primary wave direction. Since the minima in the azimuthal modulation of the NRCS appear to approximate the angular spread of the wave spectrum rather than the actual crosswind directions, the manner in which the wave spectrum models spread the Bragg waves about the wind direction is important. The D&V and D&P models do allow for this effect by factorizing the wavenumber spectrum into a product of wavenumber amplitude and directional dependence terms. However, the adjustable parameters in these models are still tuned to produce minima near the cross-wind directions. In the model function by Plant, the directionality of the NRCS is obtained by expanding the cosine dependence of the wave growth expression and by the mean-square slopes of the longer waves. This model also produces cross-wind minima at 90° and 270° and rather flat-topped, broad maxima. None of the models described currently consider additional wave components such as long waves propagating at an angle to the wind. Both of these wave effects shift by 15° to 20° the positions of the NRCS minima away from a simple ±90° relationship with the wind; therefore, forcing the minima to be at 90° and 270° through the use of a three-term cosine fit will not produce an accurate representation of the directionality of the scatterometer measurements.

The azimuthal modulation was also shown to be correlated with the significant slope of the wave spectrum. In the physical models of Plant (1986) and Durden and Vesecky (1985), the Cox and Munk (1954) mean-square slope expressions are used; however, there have been recent studies of the short wave slope which suggest different parameterizations. The Donelan and Pierson (1987) model integrates the long-wave portion of their wavenumber spectrum to obtain mean-square slopes, but they could not reconcile their numerical values with those of the Cox and Munk values. Therefore, a re-evaluation of the mean-square slopes used in the model functions is warranted.

The third area of the models which needs updating is in the basic surface layer theory that connects the measured wind speed to the surface. The apparent effect of atmospheric stability at intermediate Bragg angles is properly accounted for if a stability independent wind speed parameter; i.e., either friction velocity or neutral wind at a level near the surface, is used in the parameterization of the NRCS on wind speed. If the friction velocity is measured at any substantial distance above the surface, model functions which then parameterize the NRCS in terms of a neutral wind speed at a lower level, need air-sea temperature differences to compute the stability correction. Except for the D&V model, the models presently assume averaged neutral conditions over the sea, therefore, the air-sea temperature is not required. In either case of neutral wind speed or friction velocity, improvement of the model functions will depend on improved measurements of the friction velocity at sea, either for direct comparisons to the NRCS or for the establishment of an open ocean drag coefficient which is normalized for wind speed, stability and sea state.

B. CLOSURE

This study began by establishing the perimeter of the scatterometry model function problem. Contained within this perimeter were the scientific issues facing model function developers, the special *operational* requirements of the Navy for surface winds and the programmatic status of scatterometry in the US and abroad.

This study has shown that radar scatterometers are an especially sensitive means by which to study the air-sea interface. The magnitudes of the Bragg-resonant NRCS measurements from radar scatterometers respond nearly instantaneously to changes in the near-surface winds, but the azimuthal modulation of the (Ku-band) NRCS appears to be a strong function of the angular spread and slopes of the dominant waves on the sea surface, rather than a simple sinusoidal dependence on the wind direction. In this analysis, the neutral wind speed at 1m, obtained from the measured friction velocity and corrected for atmospheric stability, was a better predictor of NRCS magnitude and was a better normalization quantity for removing the observed stability dependence of the NRCS. Taken together, these observations state that the radar scatterometer can measure surface winds to the accuracy desired by the Navy, if the interdependence of the influencing variables is properly taken into account. That is, by modeling the NRCS in terms of 1) a neutral wind speed near the surface determined from a neutral drag coefficient formulated in terms of sea state, friction velocity and stability, 2) updated mean-square slopes and spreading functions of the wind waves and 3) the background wave field which includes wave components traveling obliquely to the wind vector.

The launch of the European Space Agency satellite in the near future will carry a combination of instruments designed to study wind and waves and thus, will provide a means by which to validate the above conclusions and examine model function improvements.

APPENDIX A. DEFINITION OF THE NORMALIZED RADAR CROSS SECTION

When microwave radiation strikes the sea surface it is scattered in many directions. Some part of this scattered radiation is eventually received by the radar. The mathematical relationship which describes that portion of the transmitted power received at the radar after having been reflected from a surface scatterer is called the *radar equation*. The definition of the radar cross-section arises in the derivation of the radar equation and can be thought of as the equivalent surface area of a target as observed at microwave frequencies (Long, 1989). The Normalized Radar Cross-Section (NRCS) is the radar cross-section divided by the target area.

Suppose that the surface consists of a dominant scatterer, then the geometry and quantities related to the scattering problem are as in Figure A1. Following Ulaby, et al., (Chapter 7, v. 2, 1982), the final received power at the radar may be thought of as the result of a sequence of events starting with a radar transmission of power, P_T, in the direction of the scatterer. The radar antenna pattern is nonisotropic so that the transmitted power must be multiplied by the antenna gain, G_T, in a particular direction. Also, the transmitted power is spread over a sphere surrounding the antenna of radius, R_T, equal to the distance between the antenna and the scatterer.

Therefore, at the scatterer,

Power per Unit Area Incident = Power Transmitted * Spreading Loss
on Scatterer toward Scatterer

$$S_s = \frac{P_T G_T}{4\pi R^2} \tag{A1}$$

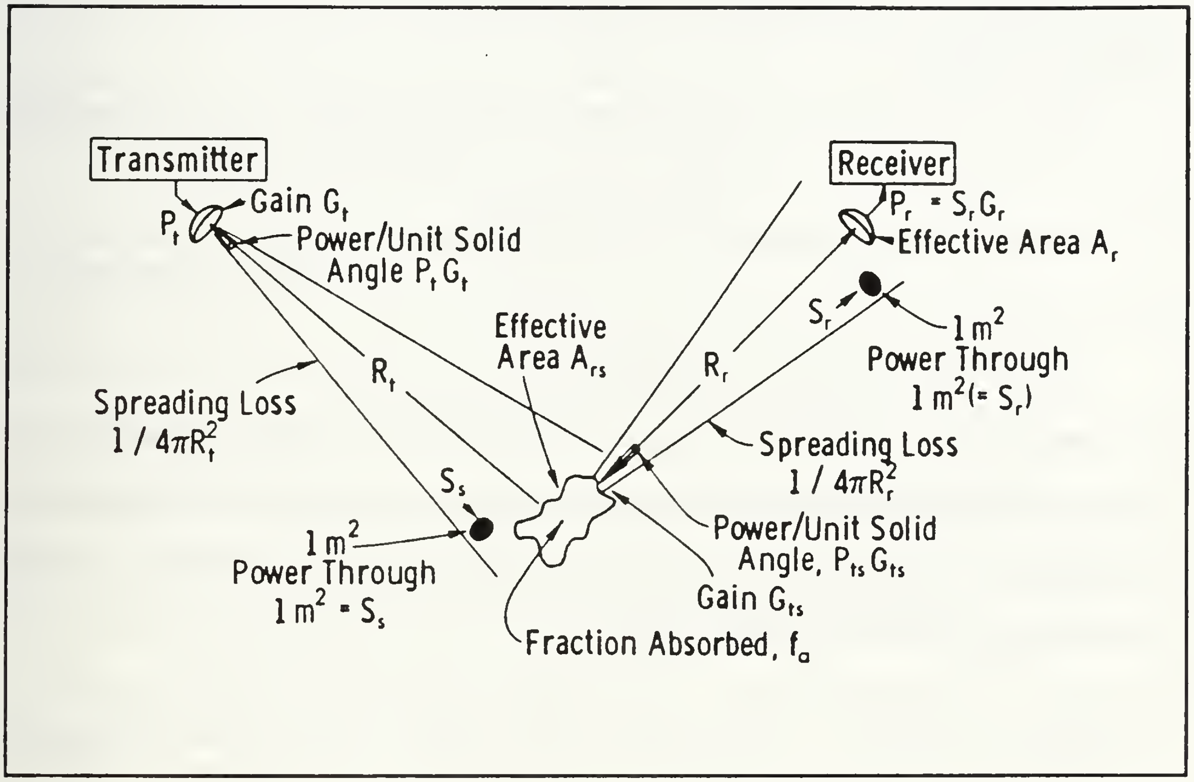

Transmitter
Gain G_t
P_t
Power/Unit Solid Angle $P_t G_t$
Spreading Loss $1 / 4\pi R_t^2$
R_t
Effective Area A_{rs}
S_s
$1\ m^2$
Power Through $1\ m^2 = S_s$
Fraction Absorbed, f_a
Receiver
$P_r = S_r G_r$
Effective Area A_r
S_r
$1\ m^2$
Power Through $1\ m^2 (= S_r)$
R_r
Spreading Loss $1 / 4\pi R_r^2$
Power/Unit Solid Angle, $P_{ts} G_{ts}$
Gain G_{ts}

Figure A1. Geometry of and quantities involved in the radar equation (from Ulaby, et al., 1981).

If the scatterer is considered to be a receiving antenna, then it removes power from the effective area of the incidence beam which it intercepts. The effective area is that area of the incident beam from which all power would be removed if one assumed that the power going through all the rest of the beam continued uninterrupted. The total power intercepted at the scatterer is then

Power Intercepted by Scatterer = Incident Power per Unit Area * Effective Area of the Scatterer

$$P_{RS} = S_S A_{RS} \tag{A2}$$

The actual value of A_{RS} depends upon the effectiveness of the scatterer as a receiving antenna.

The power received by the scatterer is not all reflected: some is absorbed, f_A , the remainder $1 - f_A$, is reflected in various directions. That is,

Power Reflected by Scatter = Power Intercepted by Scatterer * Fraction of Power not absorbed

$$P_{TS} = P_{RS}(1 - f_A) \tag{A3}$$

Inasmuch as the scatterer receives radiation as an antenna, it also radiates as one. Therefore, the power leaving the surface, P_{TS}, must be multiplied by the gain of the receiver, G_T. Again, the power spreads out along a spherical wavefront and is thus reduced. Then

Power per Unit Area at Receiver = Power radiated by Scatterer * Gain toward receiver * Spreading Loss

$$S_R = \frac{P_{TS} G_{TS}}{4 \pi R_R^2} \tag{A4}$$

Finally, the total power at the receiver is

Total Power at the Receiver = Power per Unit Area at Receiver *EffectiveArea of Receiver

$$P_R = S_R A_R \tag{A5}$$

Substituting for S_R from the previous four equations gives

$$P_R = \left(\frac{P_T G_T A_R}{(4\pi)^2 R_T^2 R_R^2} \right) \left[A_R (1 - f_A) G_{TS} \right] \tag{A6}$$

The quantity in square brackets describes the radiating characteristics of the surface scatterer. Individually, the variables are difficult to measure and they are not particularly relevant if the measurement of interest is the magnitude of the received power. Taken together, the variables define the radar *scattering cross-section,*

$$\sigma = A_{RS}(1 - f_A) G_{TS} \tag{A7}$$

The cross-section is a function of the incident and reflected wave directions, the *shape* of the surface scatterer and the scatterer's dielectric properties.

In the case of a monostatic radar in which a single antenna is used for transmitting and receiving, the following equalities hold: $R_T = R_R = R$, $G_T = G_R = G$, $A_T = A_R = A$. Further, the effective area of the antenna is related to the gain of the antenna by $A=\lambda^2 G/4\pi$. The radar equation appropriate to scattering from a single point target using monostatic radar may then be written as

$$P_R = \frac{P_T G \lambda^2 \sigma}{(4\pi)^3 R^4} \tag{A8}$$

However, the sea surface does not represent a single point target, rather the scatterers are distributed over some area A on the surface.

In this case, it is typical to think of the average received power rather than the power at a particular instant, and the scattering cross-section *per unit area,* σ^o, such that

$$P_R = \frac{\lambda^2}{(4\pi)^3} \int_{Area} \frac{P_T G^2}{R^4} \sigma^o dA \qquad \text{(A9)}$$

This is the area extensive form of the radar equation used for remote sensing radars. There are restrictions on the application of this form of the equation which guarantee that no one scatterer dominates:

(1) In a differential area, ΔA, in which P, G, and R are nearly constant, there must be enough scattering centers for a reasonable average to be computed and allow substitution of $\sigma^\circ \Delta A$ for σ_i, and

(2) In the total illuminated area there must exist many more scatterers to allow replacement of the differential form with an integral.

In a real system, to solve for σ° from (A8) then requires inversion of the integral. Since the antenna gain, cross-section and range are not constant over the target area, Bracalente, et al., (1980) approximated σ° by including correction factors in the SASS algorithm to allow the equation for σ° to be written as

$$\sigma^o = \frac{64\pi^3 P_R R^4}{P_T \lambda^2 L_S G_o \left(\frac{G}{G_o}\right)^2 A} \qquad \text{(A10)}$$

where L_S is an electronics loss term, G is the peak antenna gain, G/G_o is the gain loss ratio (both as functions of the antenna look direction) and A is the illuminated area on the earth. Values from this approximating equation over a parametric range of conditions were compared with the exact equation to show that the error in σ° due to the use of (A10) was less than 0.1dB.

A particular σ° can be evaluated from (A10) given measured values of P_R, P_T, calculated values of R and A, and laboratory determined values of L_S, G and G_o. Noise contamination is eliminated by sampling the noise-only power and subtracting it from the received power (signal) measurement. The problem is then how to relate the measured NRCS to the physical characteristics of the scattering surface.

APPENDIX B

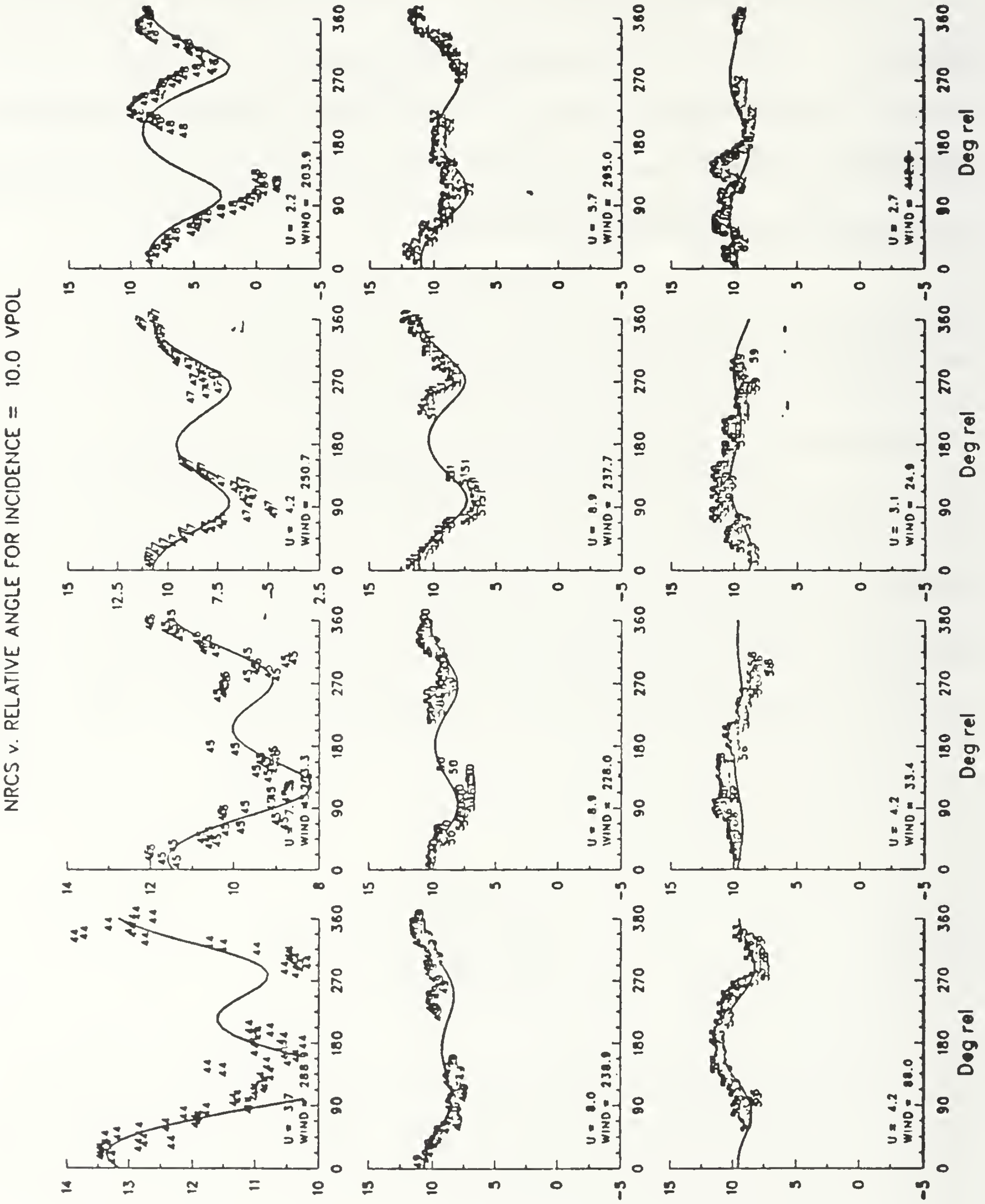

NRCS v. RELATIVE ANGLE FOR INCIDENCE = 10.0 VPOL

NRCS v. RELATIVE ANGLE FOR INCIDENCE = 10.0 VPOL

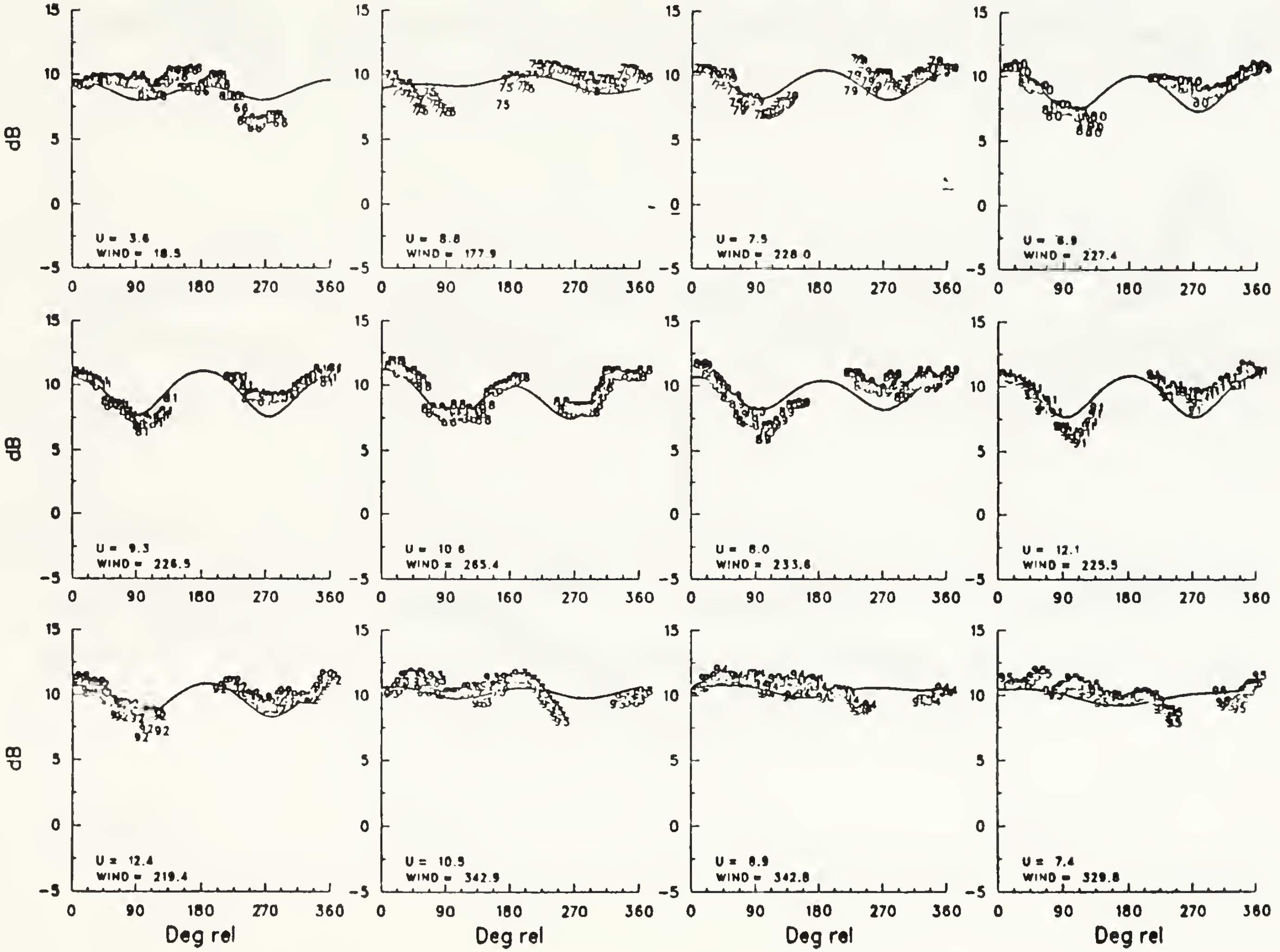

NRCS v. RELATIVE ANGLE FOR INCIDENCE = 10.0 VPOL

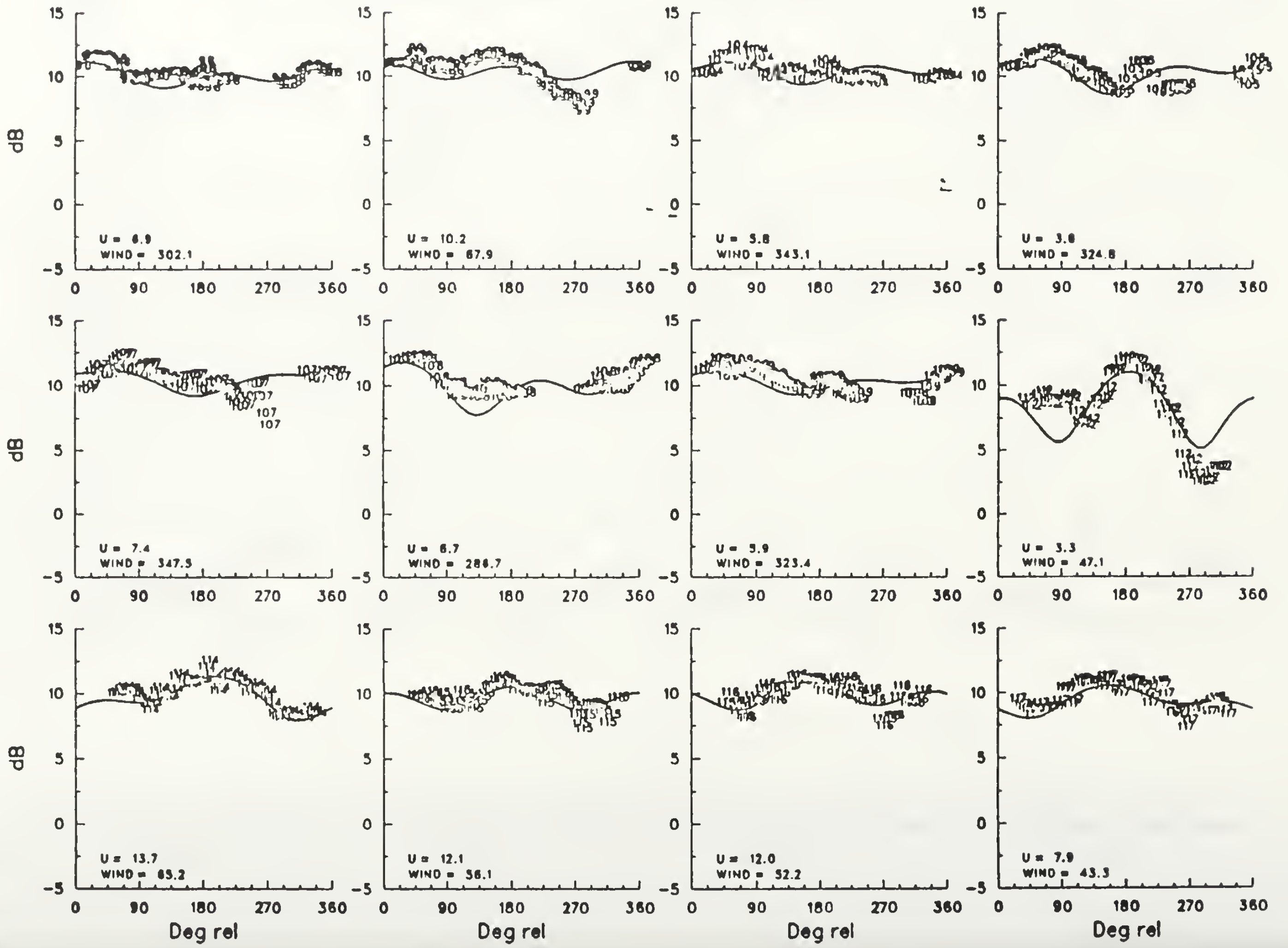

NRCS v. RELATIVE ANGLE FOR INCIDENCE = 10.0 VPOL

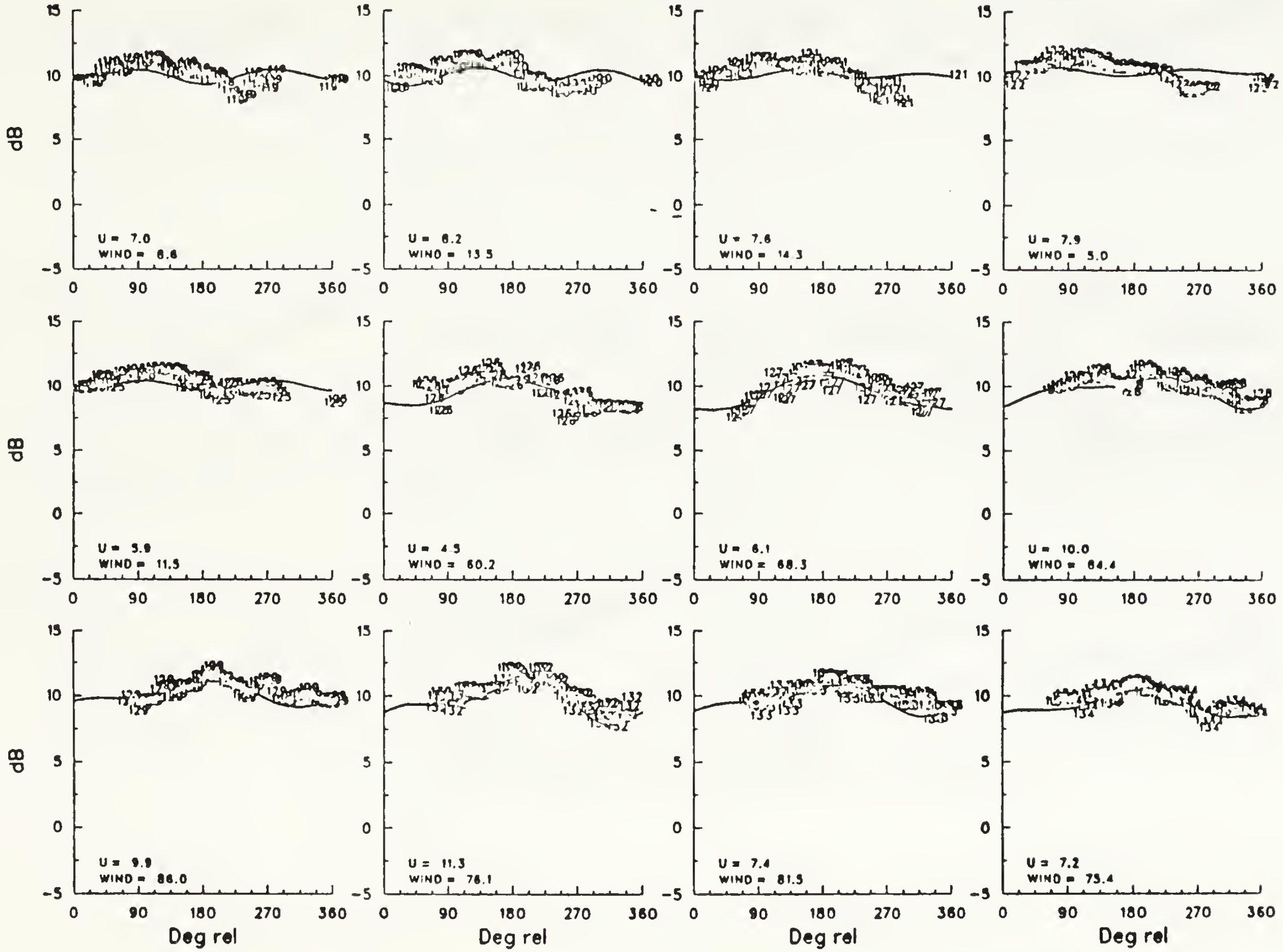

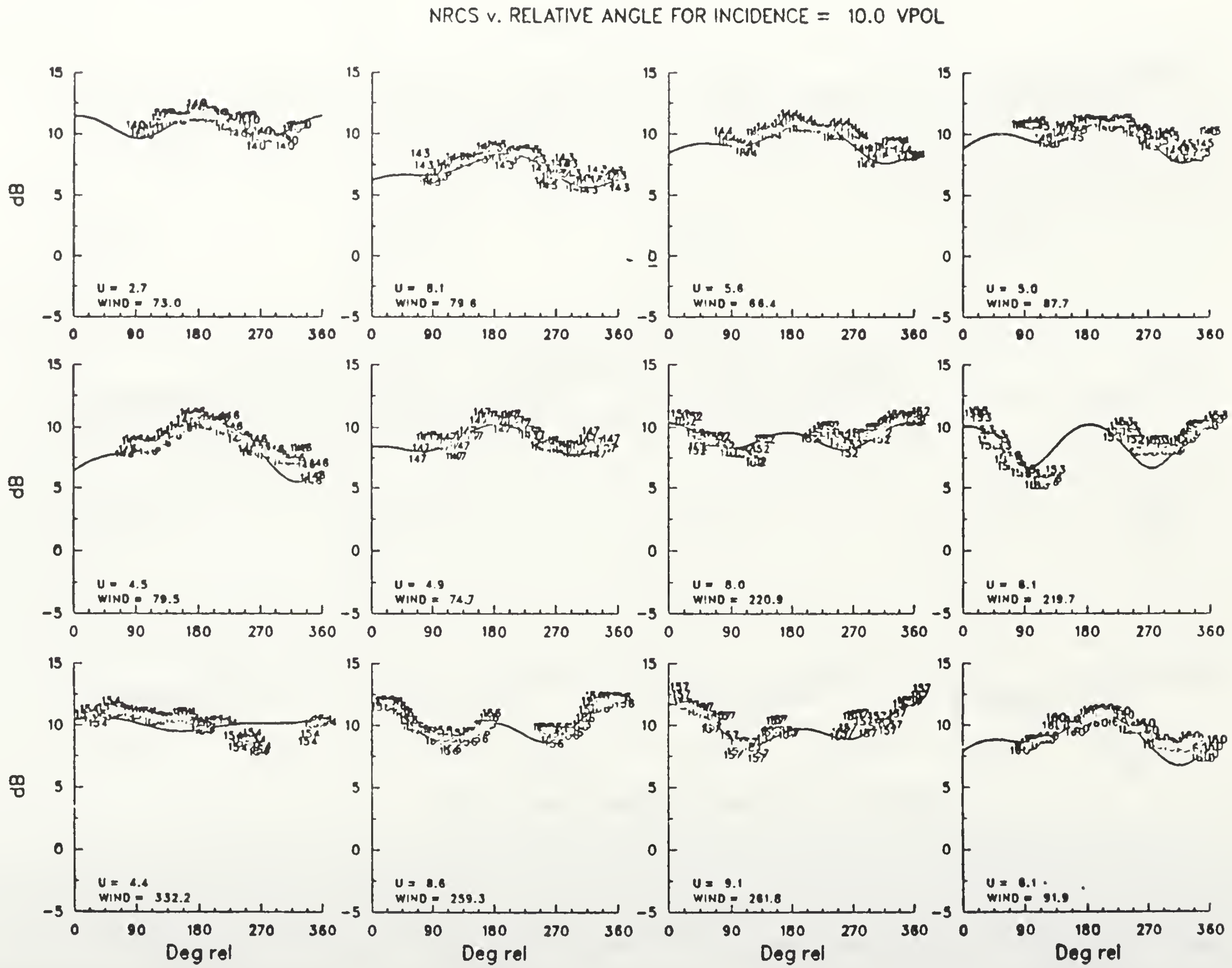NRCS v. RELATIVE ANGLE FOR INCIDENCE = 10.0 VPOL
dB
Deg rel
U = 2.7
WIND = 73.0
U = 8.1
WIND = 79.6
U = 5.6
WIND = 66.4
U = 5.0
WIND = 87.7
U = 4.5
WIND = 79.5
U = 4.9
WIND = 74.7
U = 8.0
WIND = 220.9
U = 8.1
WIND = 219.7
U = 4.4
WIND = 332.2
U = 8.6
WIND = 259.3
U = 9.1
WIND = 261.8
U = 8.1
WIND = 91.9
15
10
5
0
-5
0
90
180
270
360

NRCS v. RELATIVE ANGLE FOR INCIDENCE = 10.0 VPOL

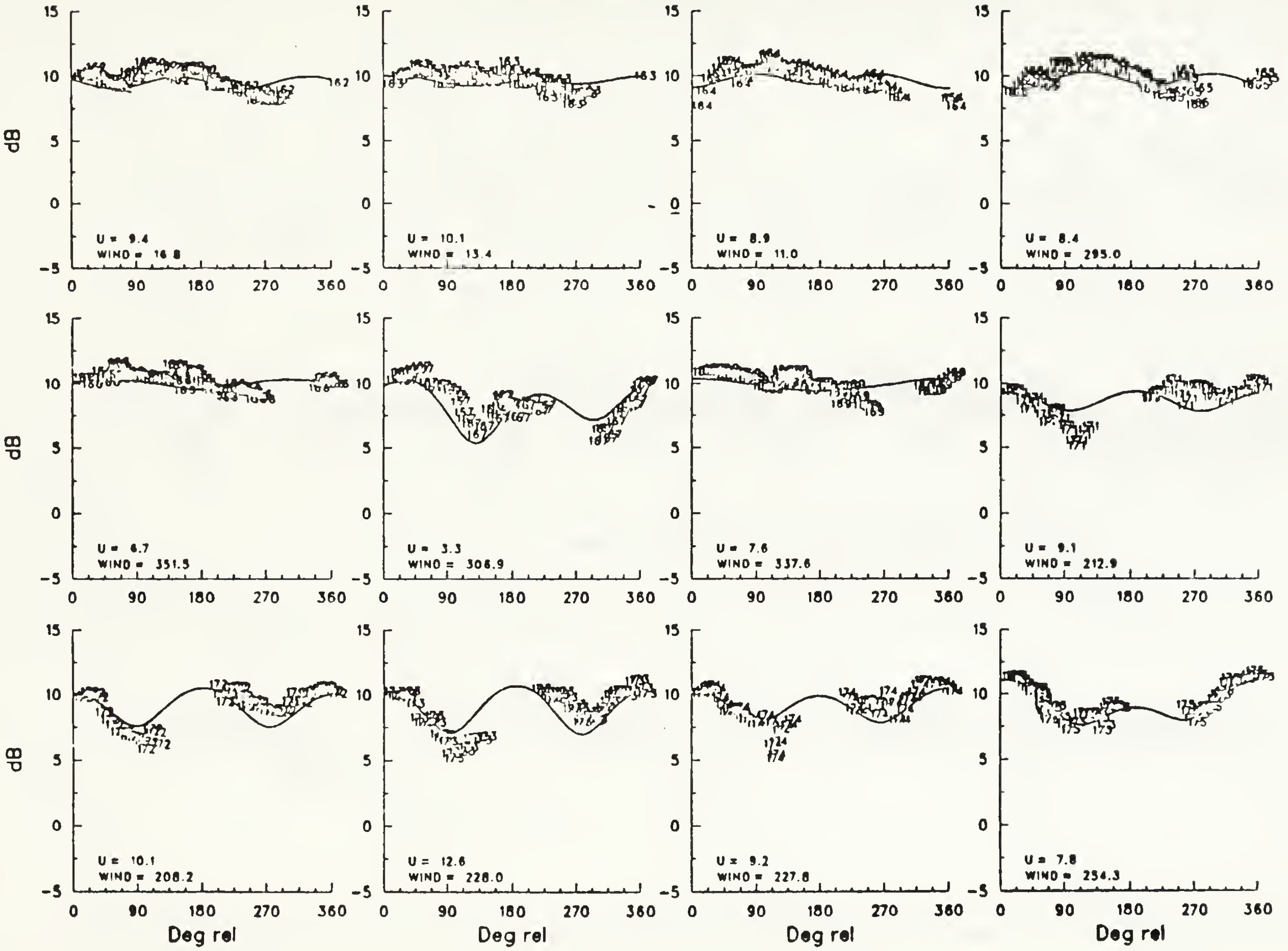

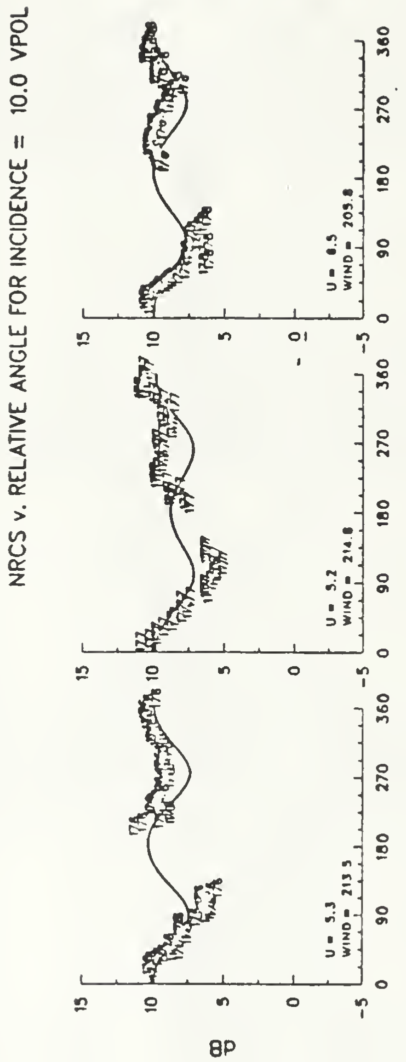

NRCS v. RELATIVE ANGLE FOR INCIDENCE = 20.0 VPOL

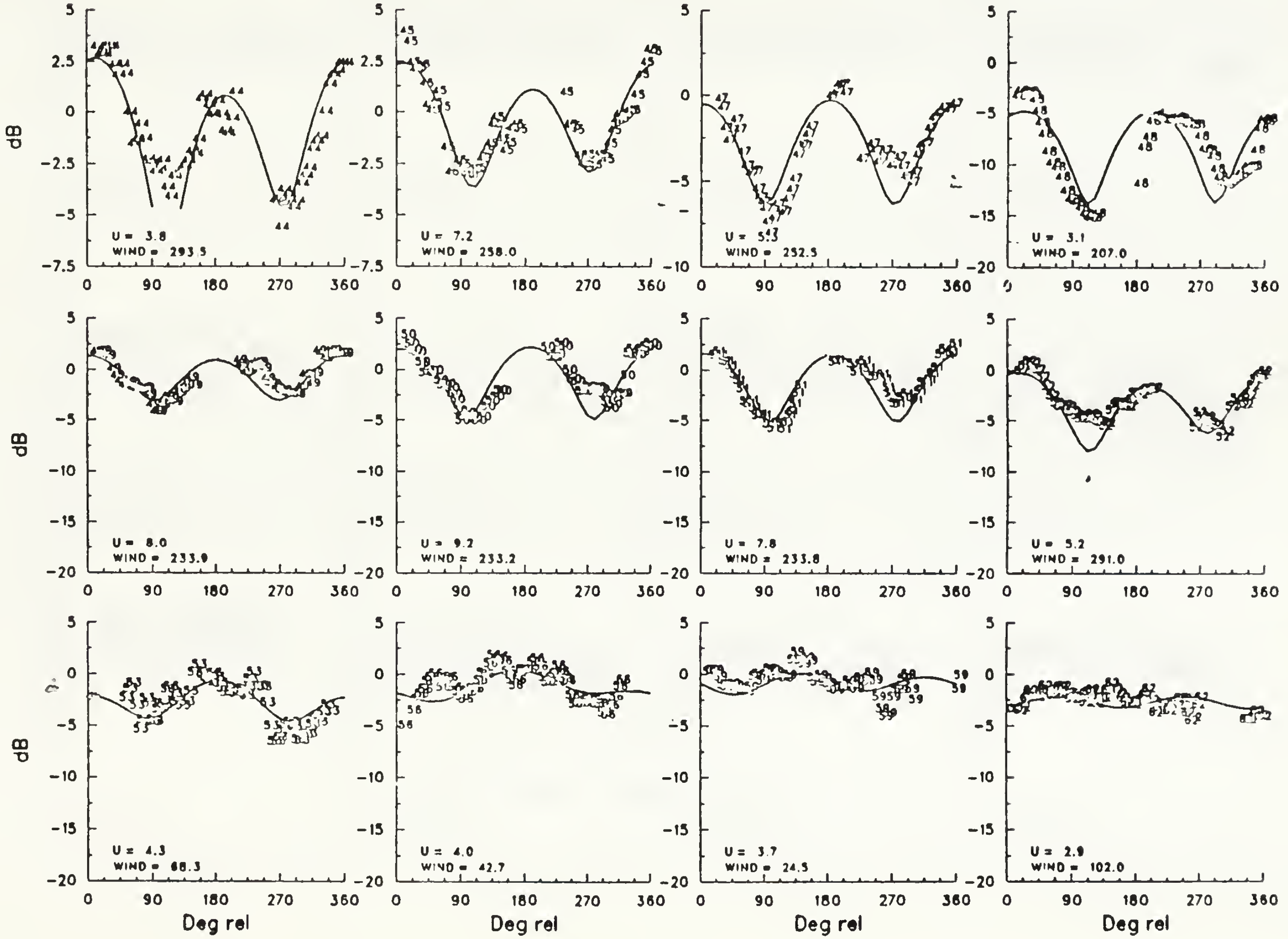

NRCS v. RELATIVE ANGLE FOR INCIDENCE = 20.0 VPOL

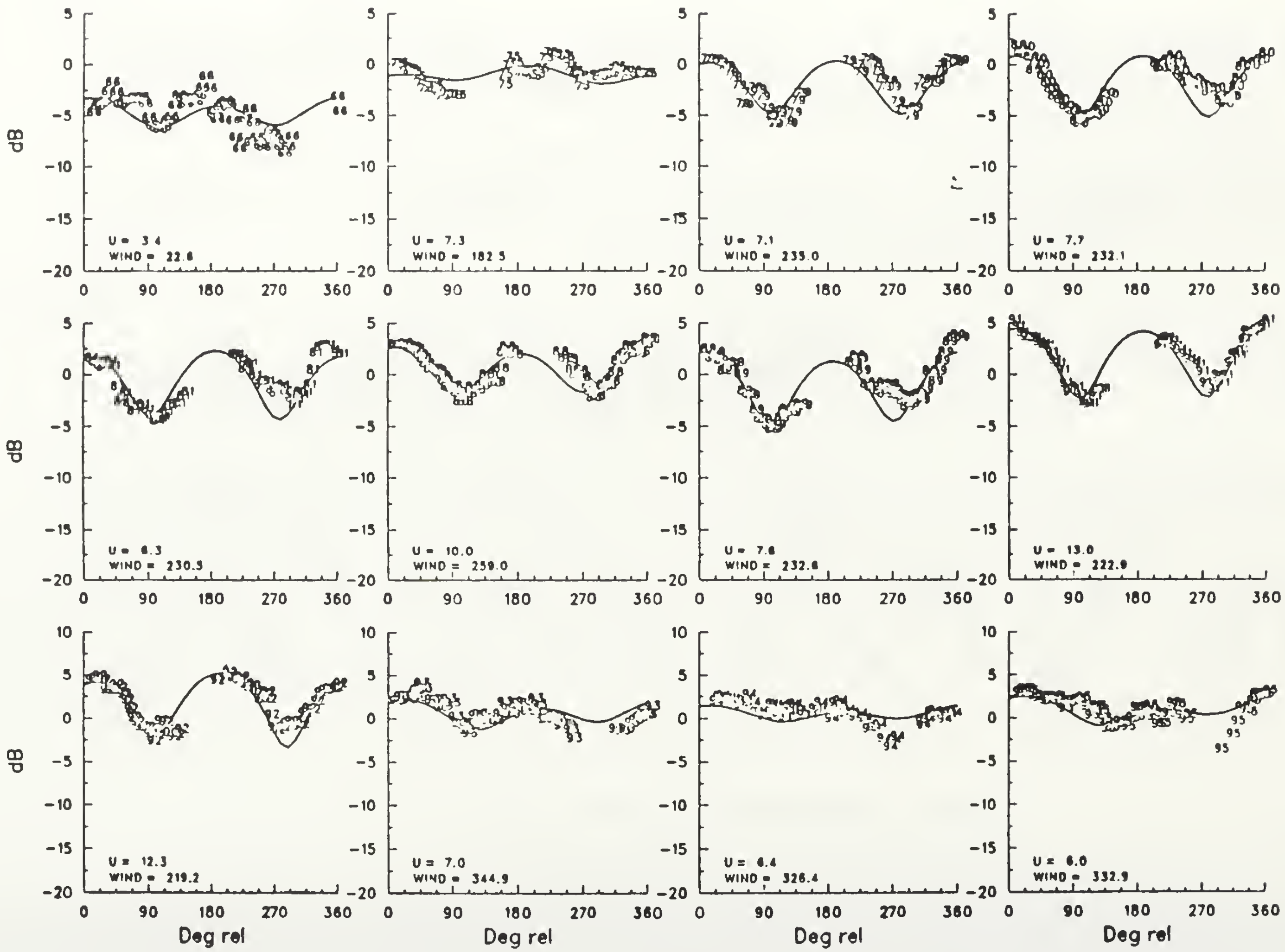

NRCS v. RELATIVE ANGLE FOR INCIDENCE = 20.0 VPOL

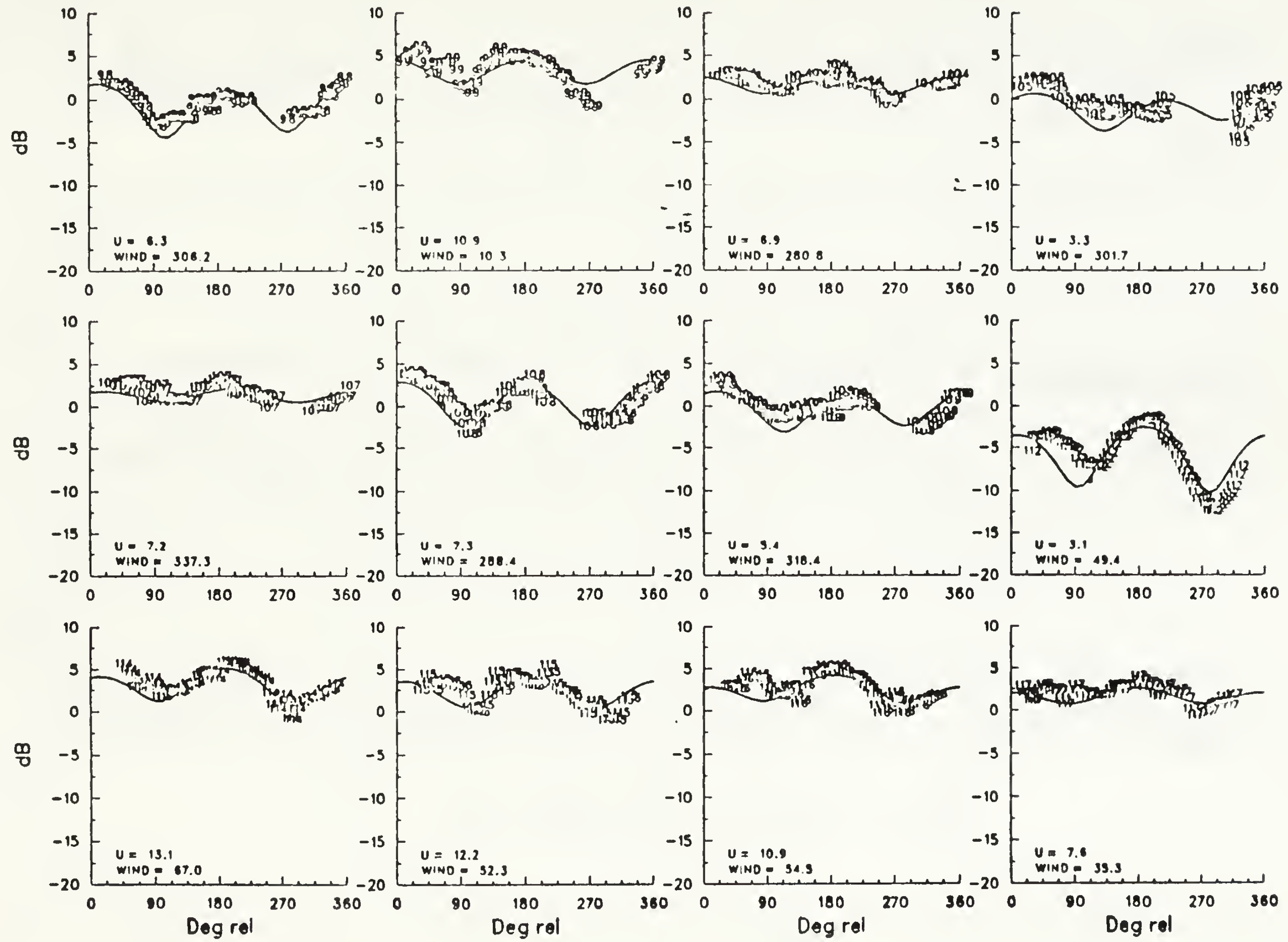

NRCS v. RELATIVE ANGLE FOR INCIDENCE = 20.0 VPOL

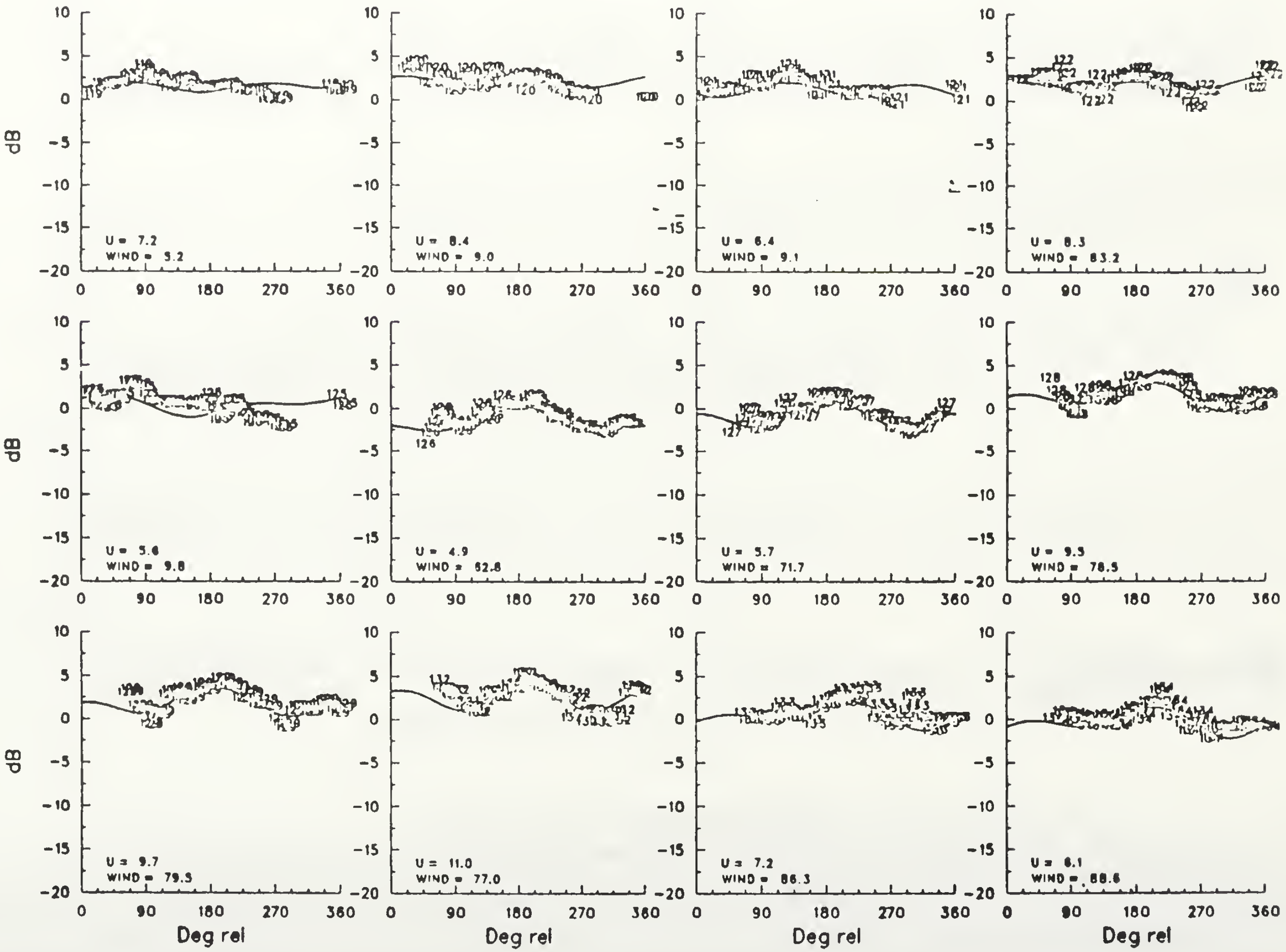

NRCS v. RELATIVE ANGLE FOR INCIDENCE = 20.0 VPOL

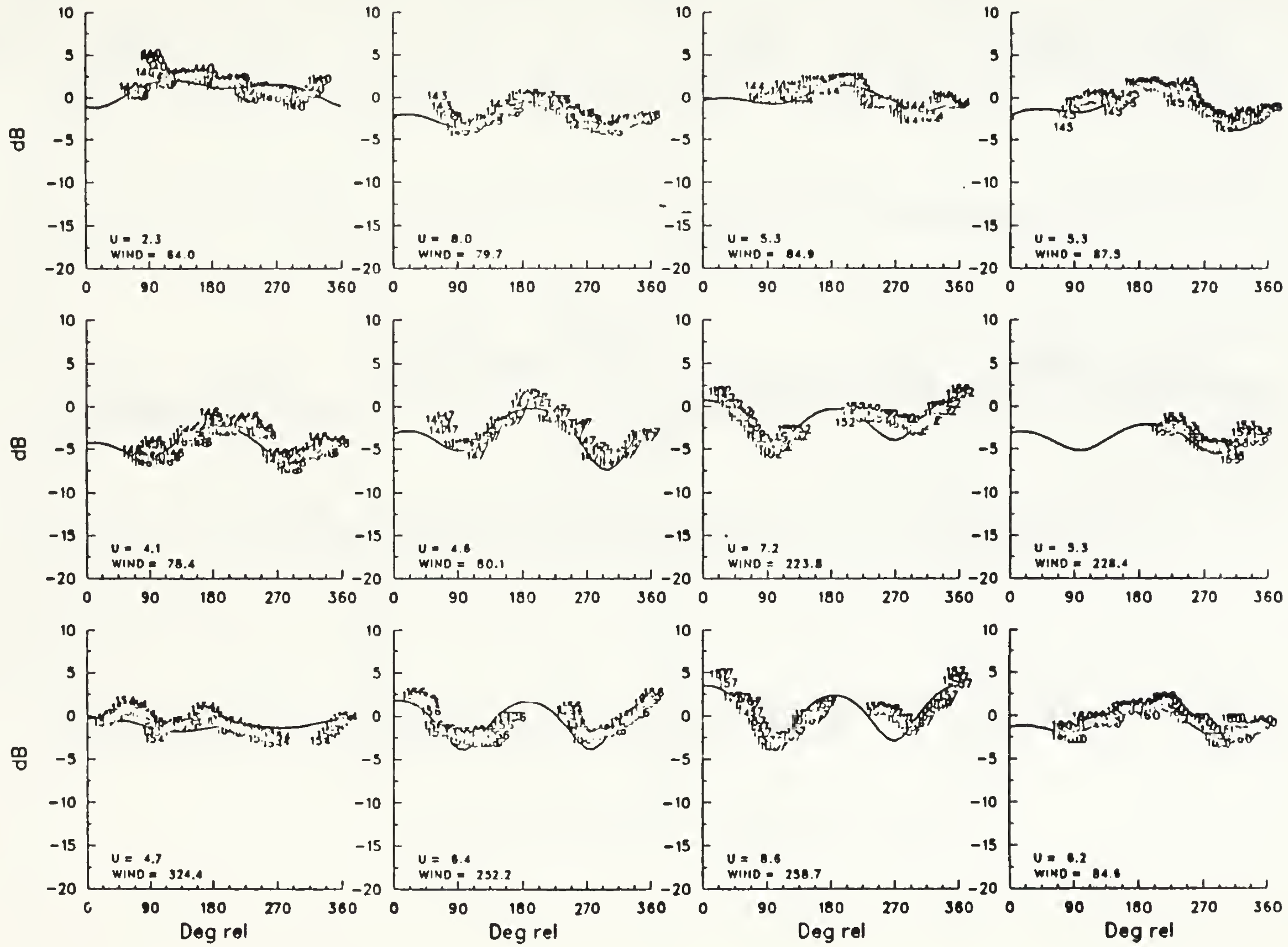

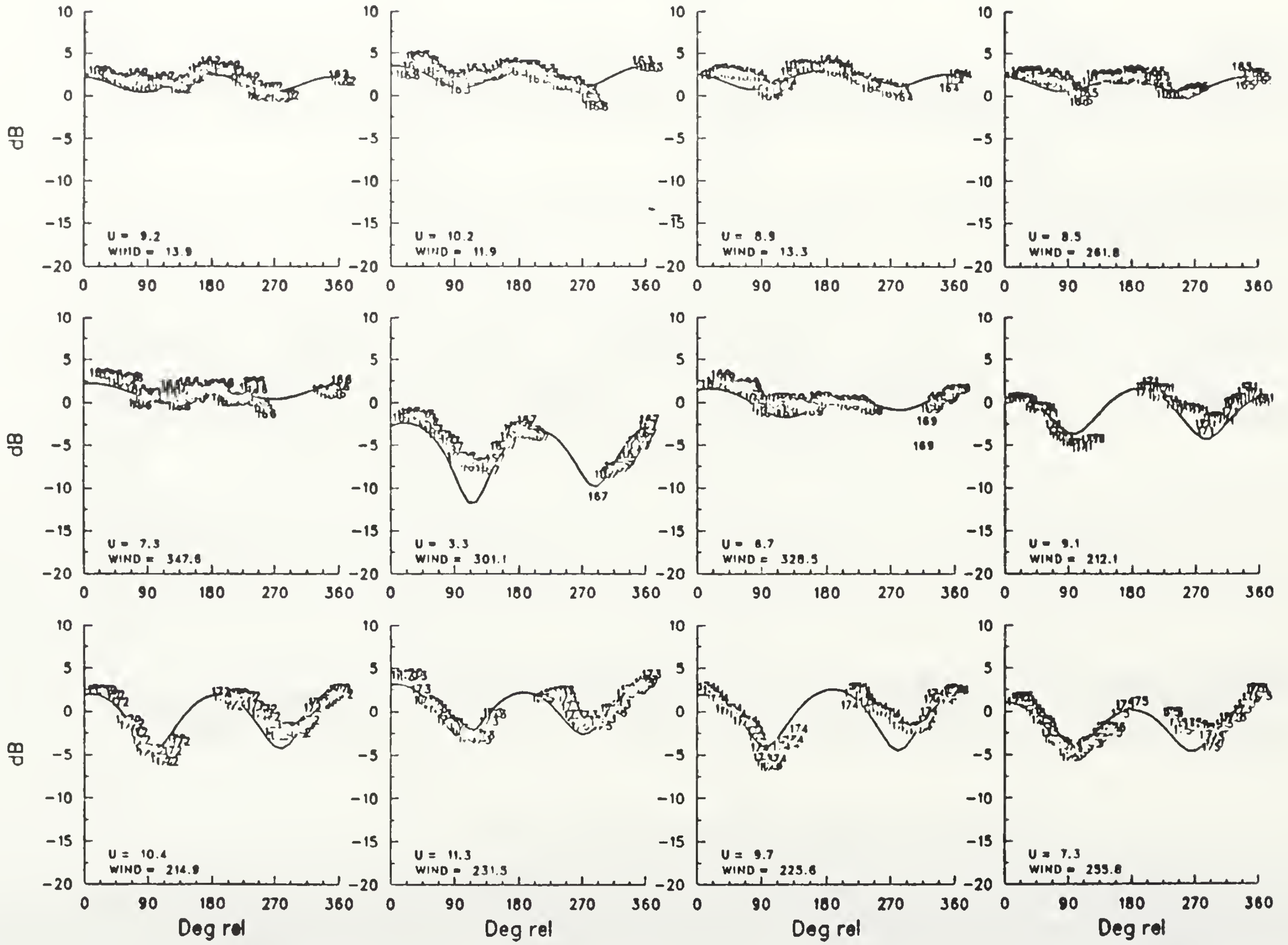
NRCS v. RELATIVE ANGLE FOR INCIDENCE = 20.0 VPOL

NRCS v. RELATIVE ANGLE FOR INCIDENCE = 20.0 VPOL

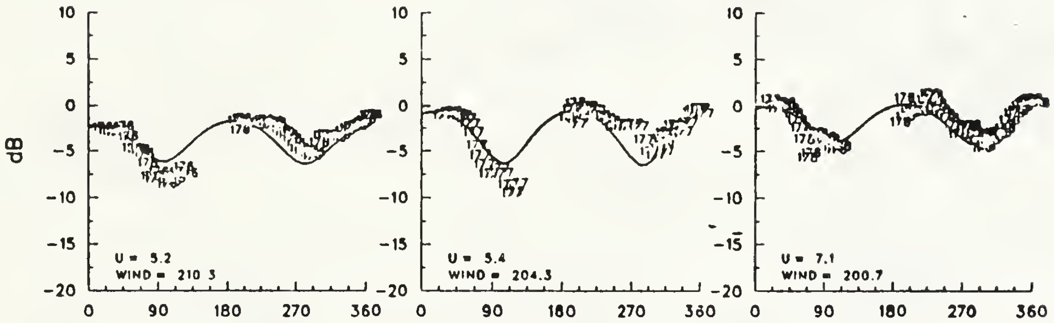

NRCS v. RELATIVE ANGLE FOR INCIDENCE = 40.0 VPOL

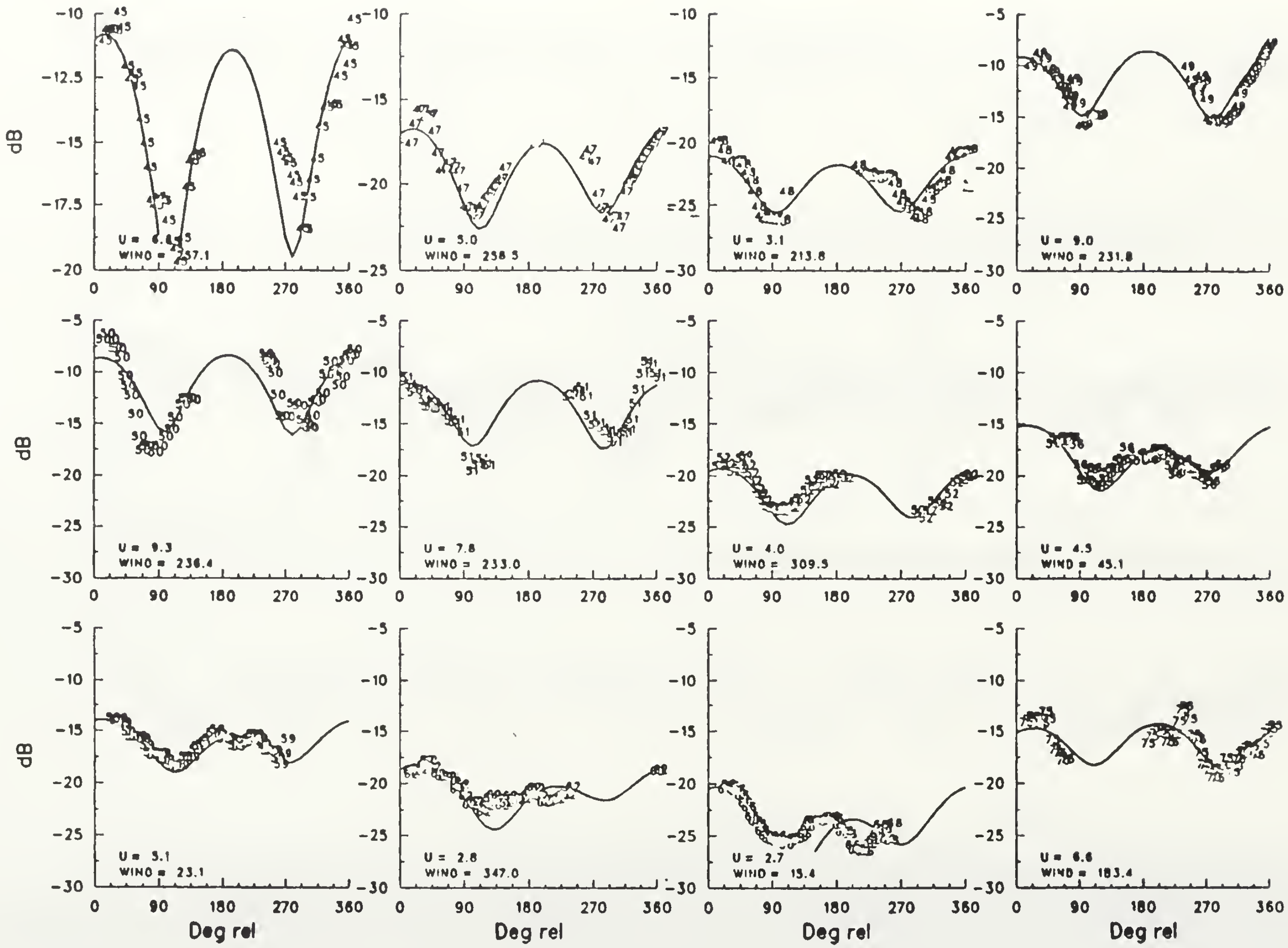

NRCS v. RELATIVE ANGLE FOR INCIDENCE = 40.0 VPOL

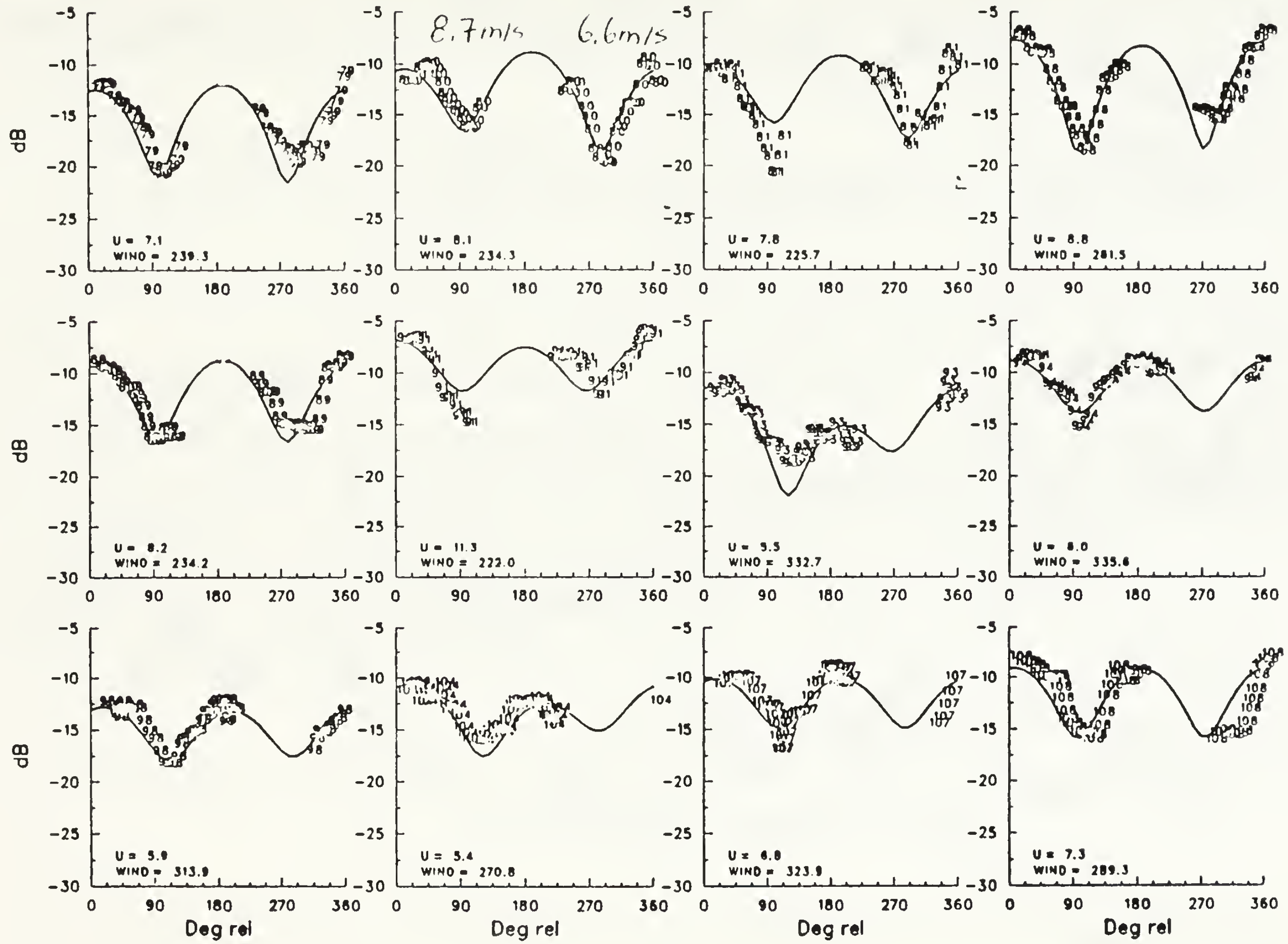

NRCS v. RELATIVE ANGLE FOR INCIDENCE = 40.0 VPOL

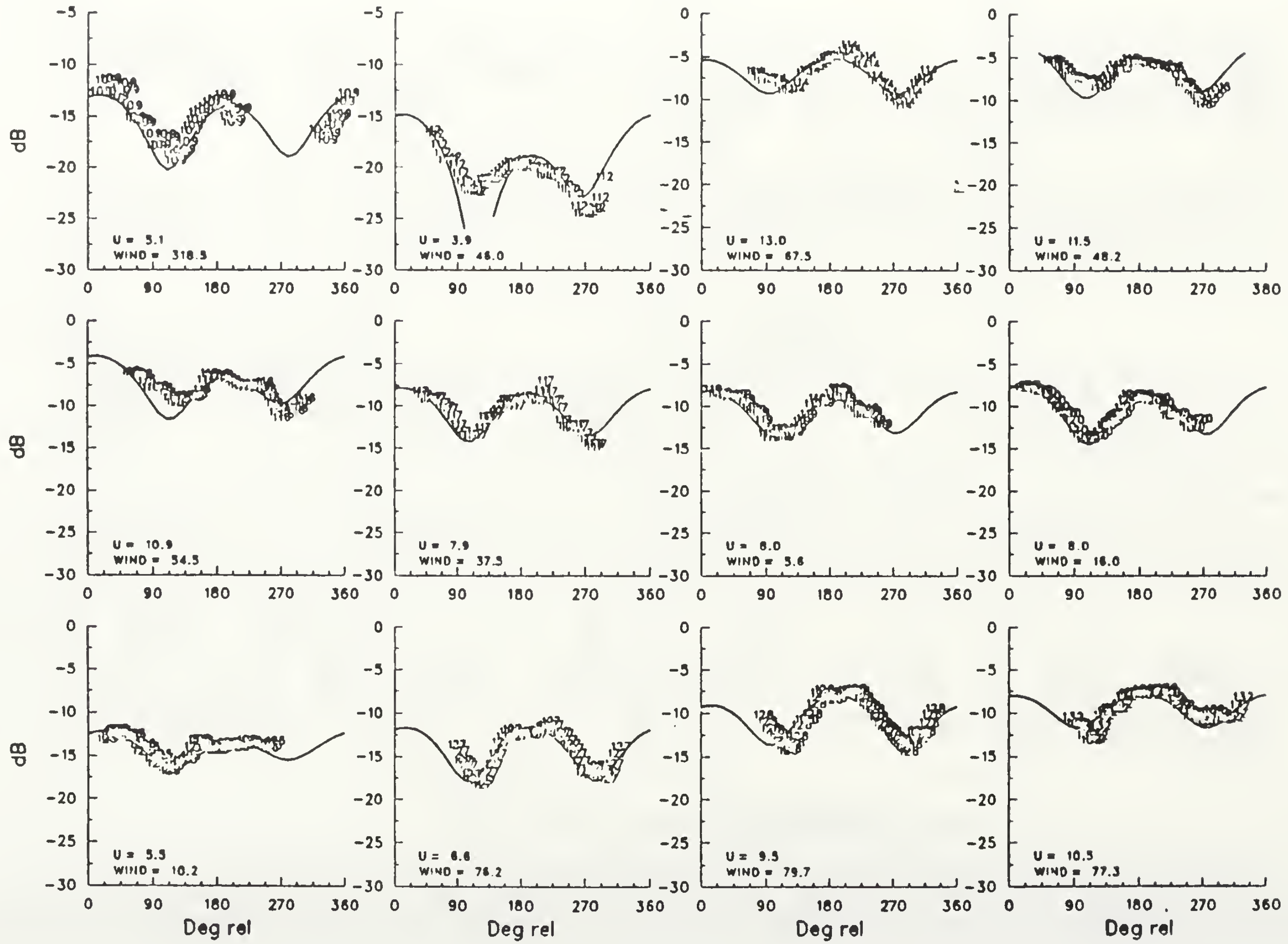

NRCS v. RELATIVE ANGLE FOR INCIDENCE = 40.0 VPOL

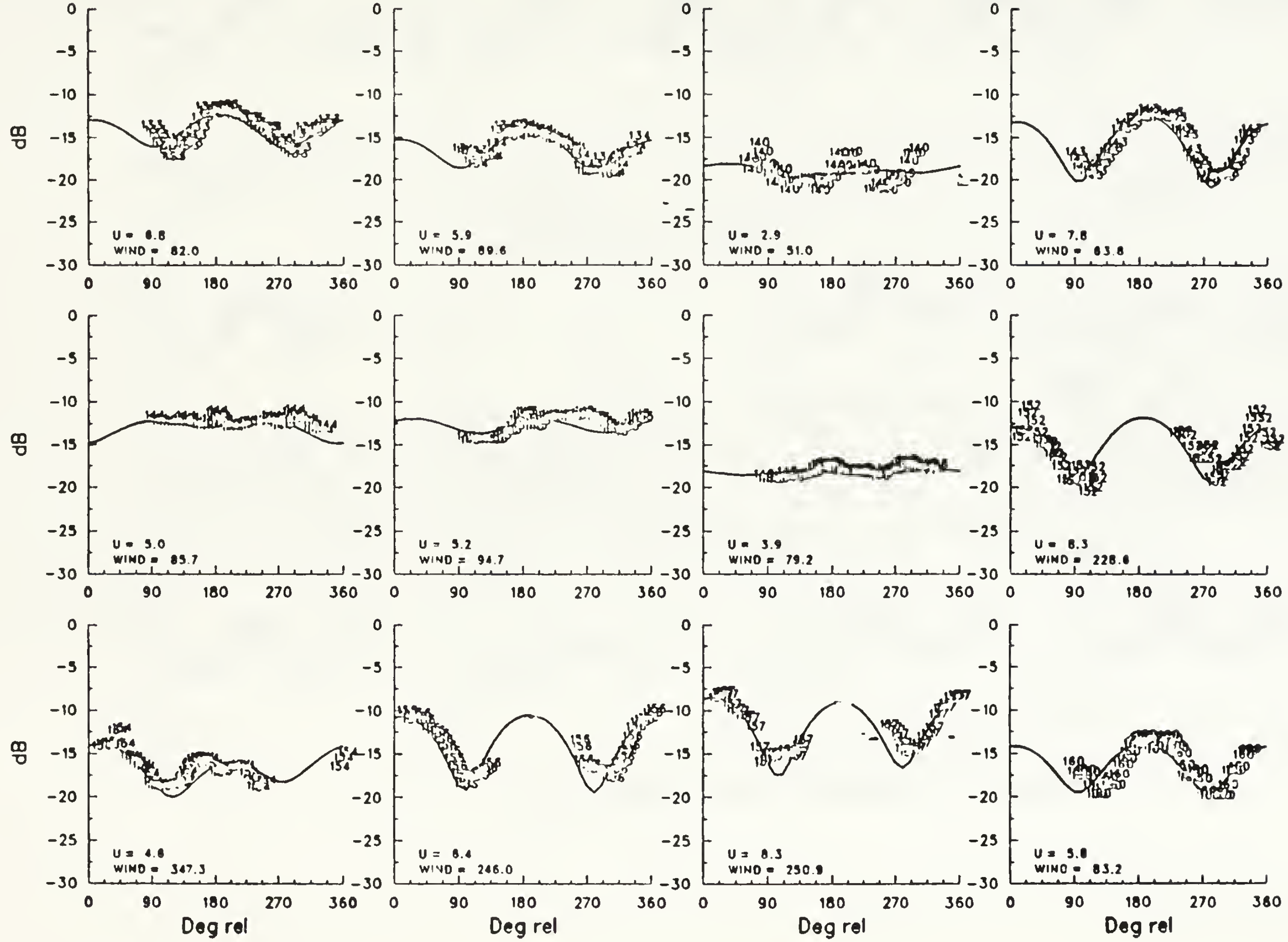

NRCS v. RELATIVE ANGLE FOR INCIDENCE = 40.0 VPOL

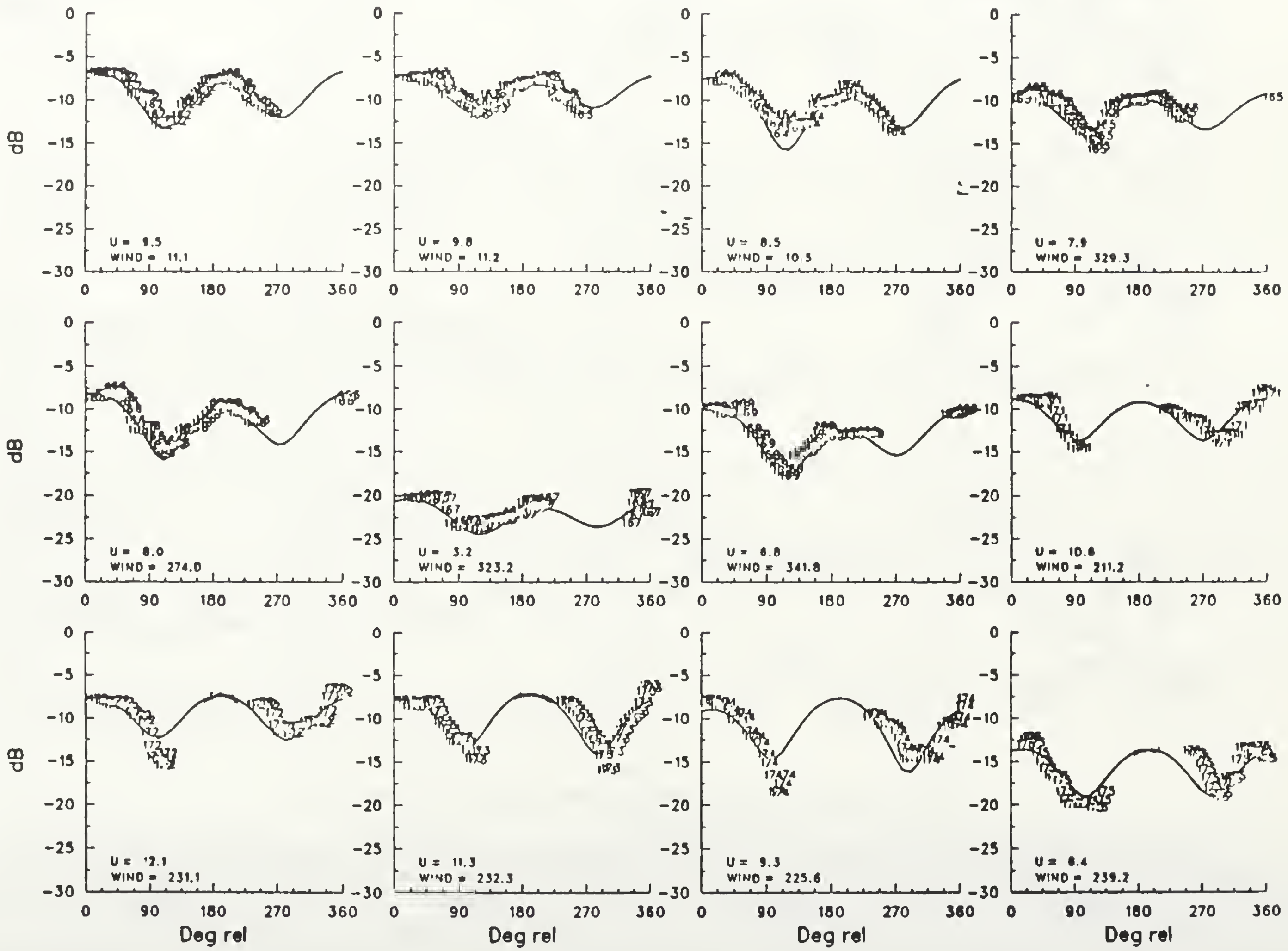

NRCS v. RELATIVE ANGLE FOR INCIDENCE = 40.0 VPOL

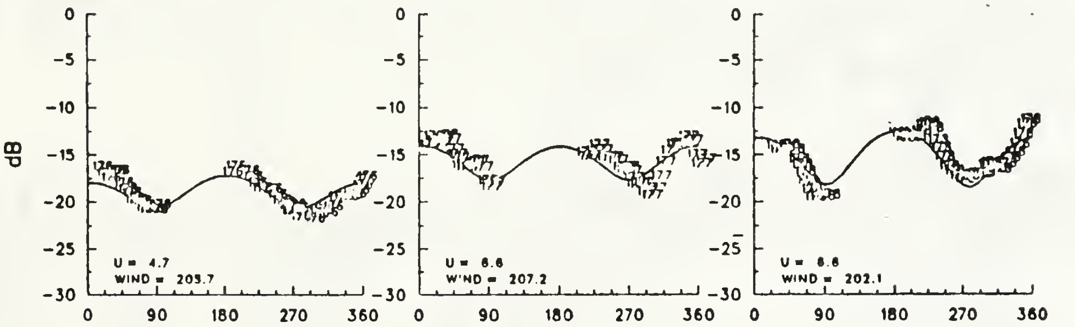

NRCS v. RELATIVE ANGLE FOR INCIDENCE = 60.0 VPOL

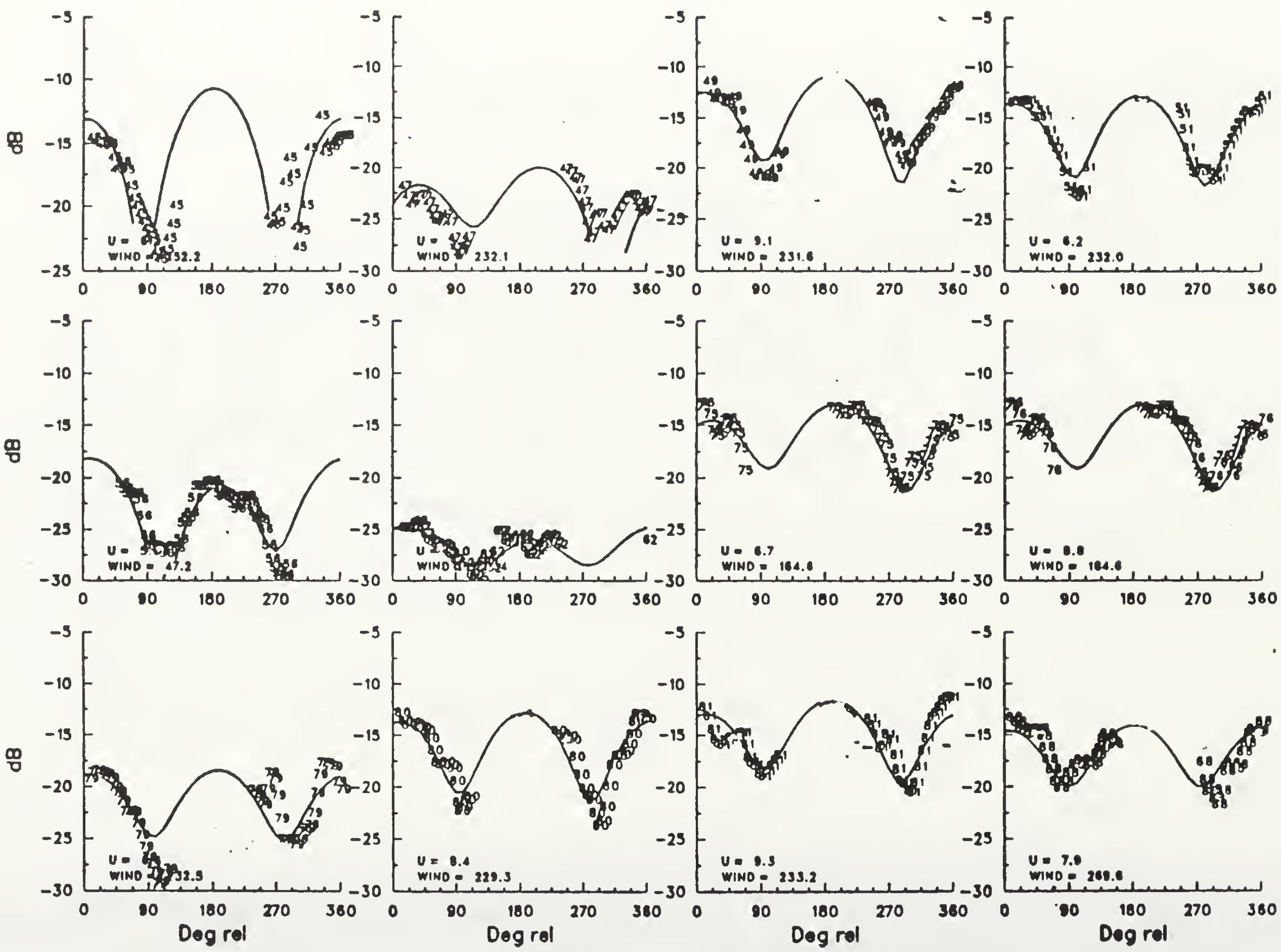

NRCS v. RELATIVE ANGLE FOR INCIDENCE = 60.0 VPOL

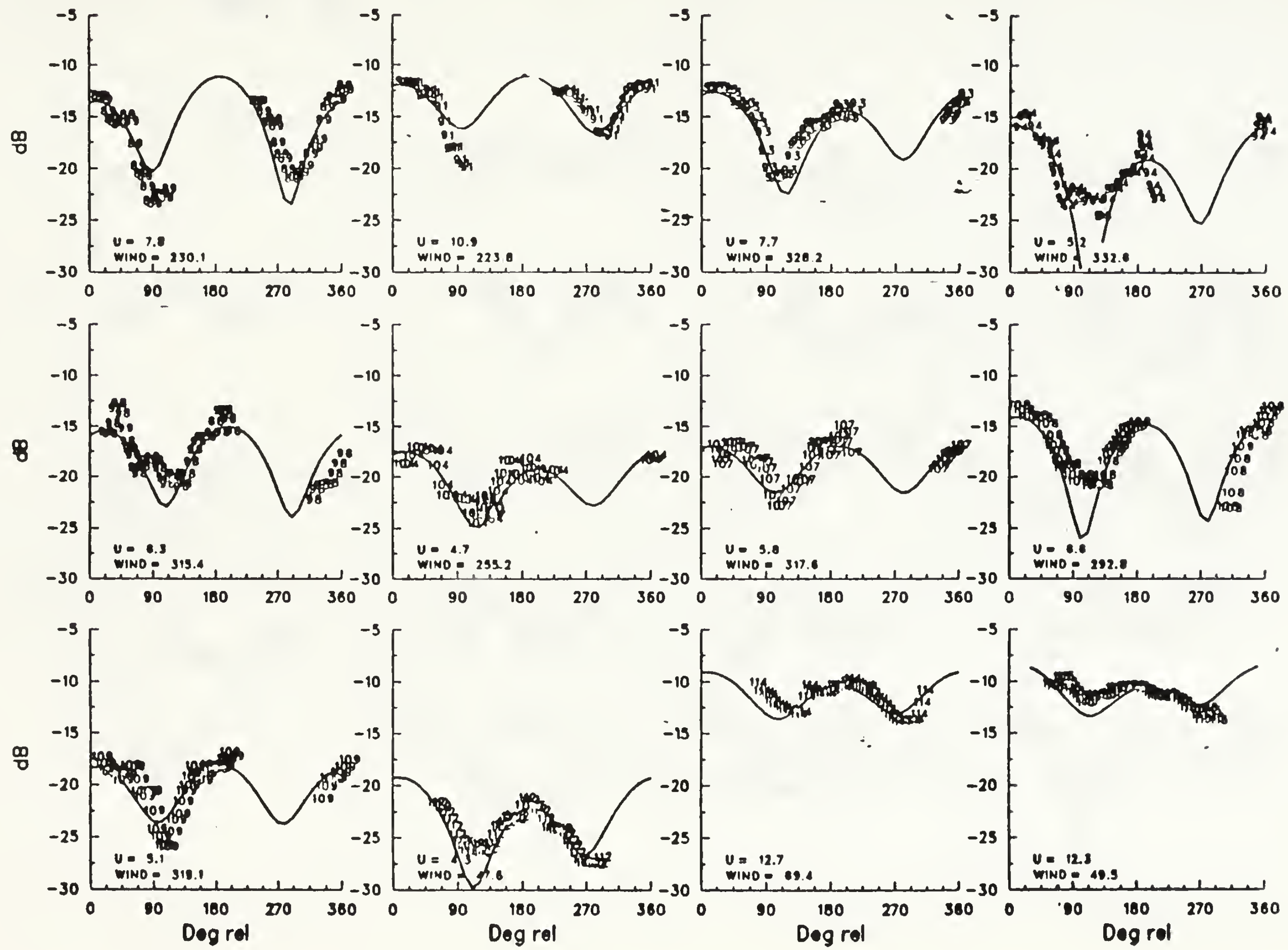

NRCS v. RELATIVE ANGLE FOR INCIDENCE = 60.0 VPOL

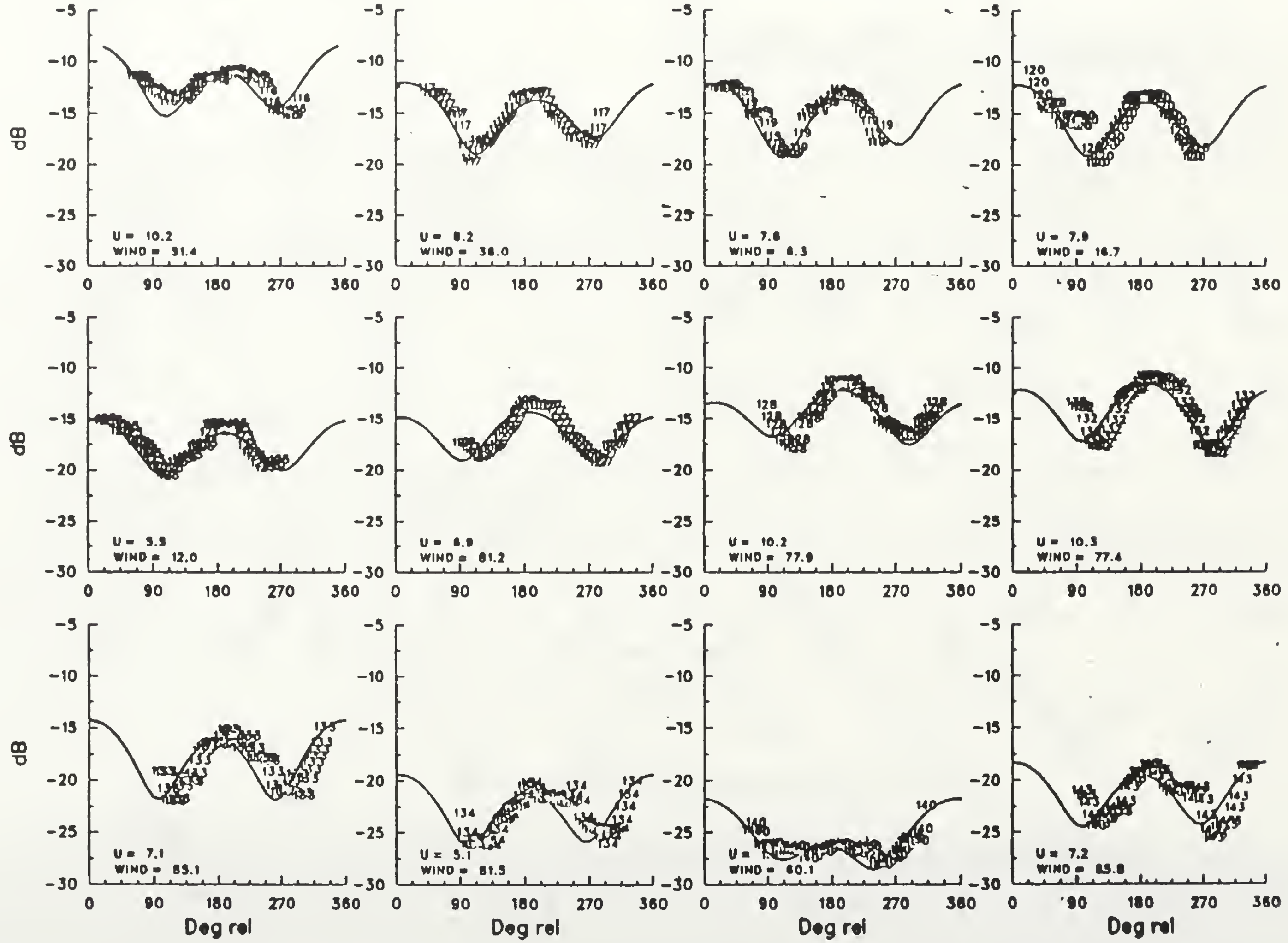

NRCS v. RELATIVE ANGLE FOR INCIDENCE = 60.0 VPOL

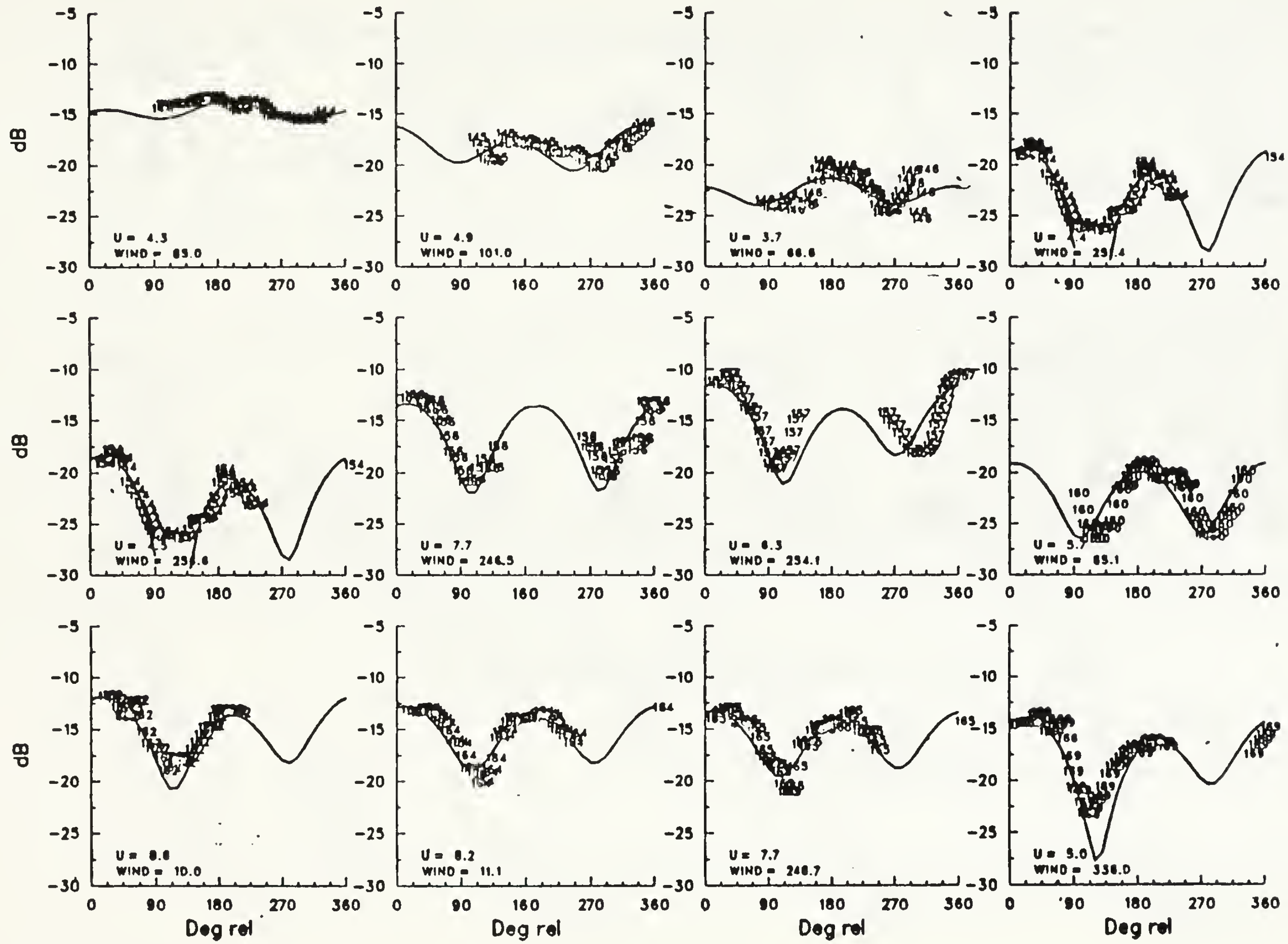

NRCS v. RELATIVE ANGLE FOR INCIDENCE = 60.0 VPOL

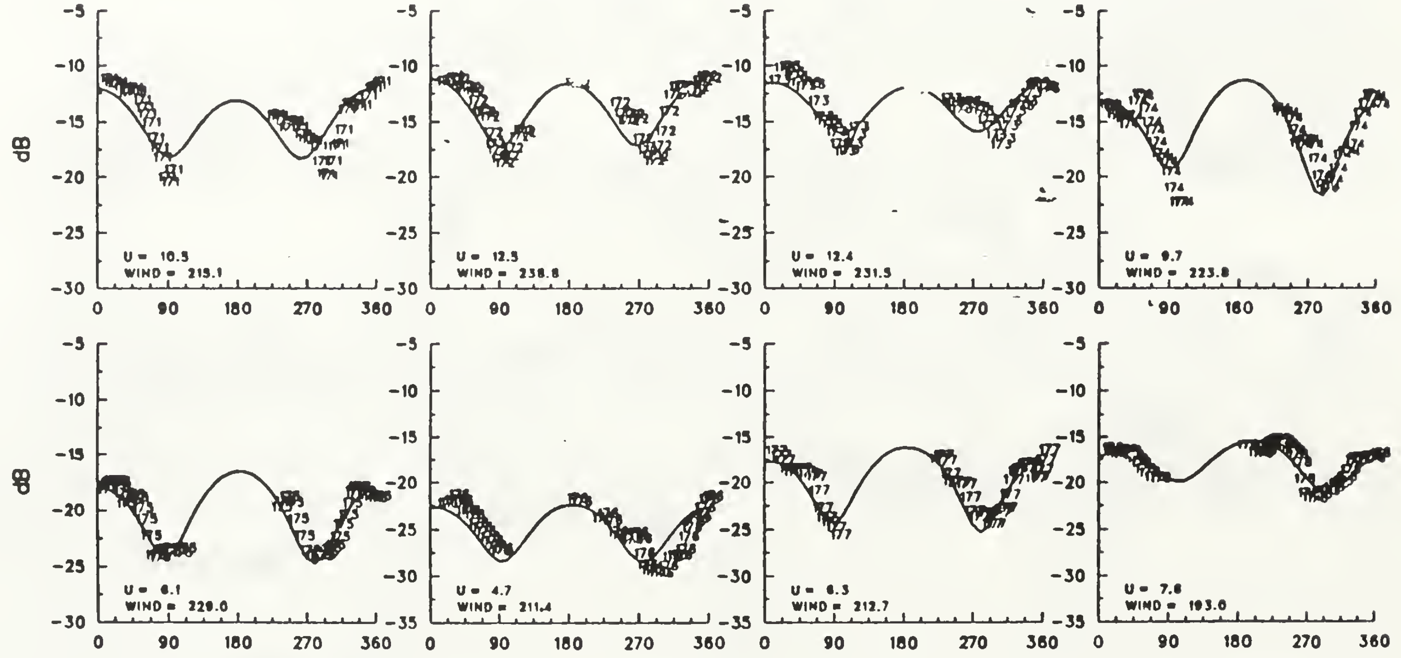

NRCS v. RELATIVE ANGLE FOR INCIDENCE = 80.0 VPOL

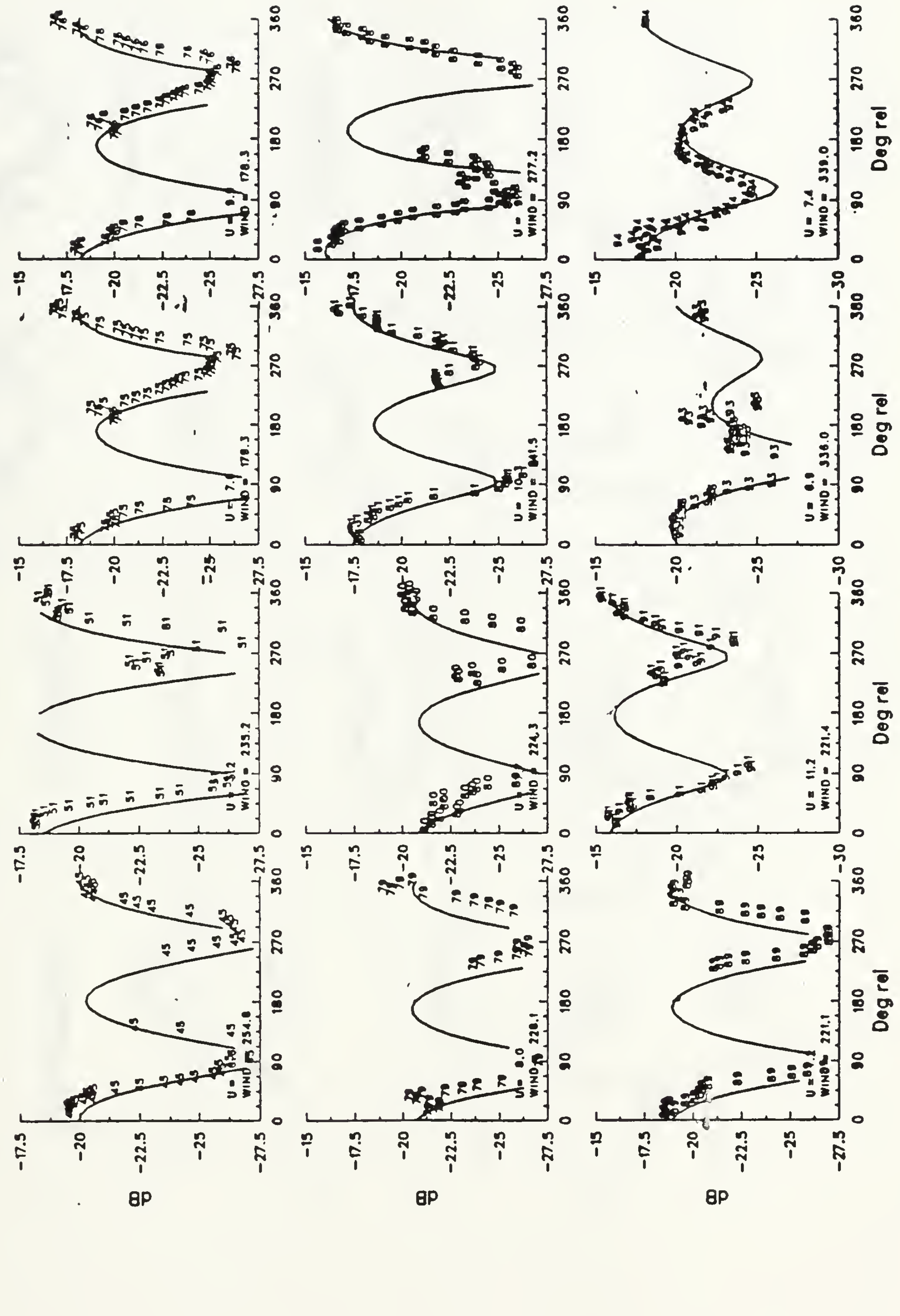

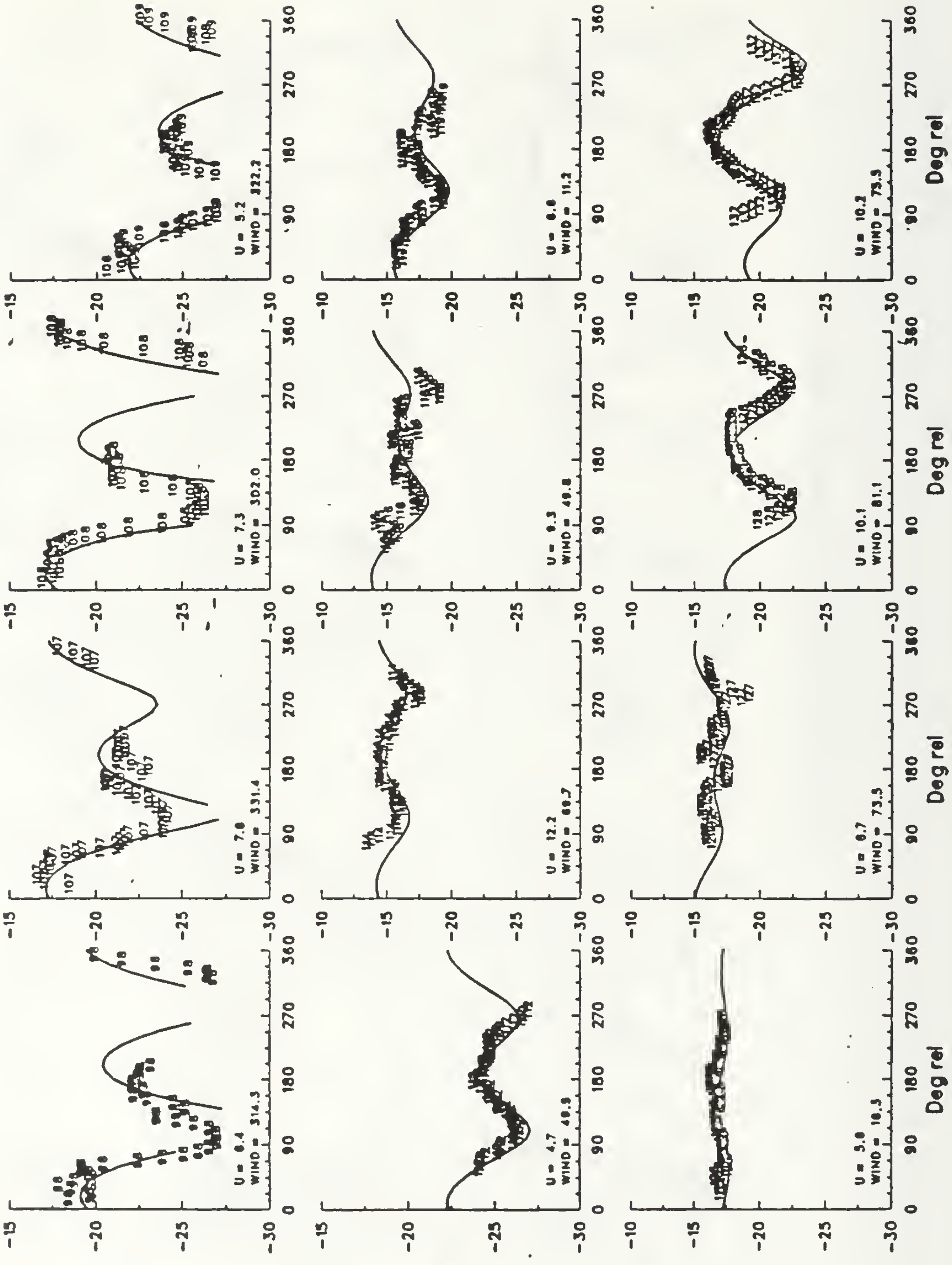

NRCS v. RELATIVE ANGLE FOR INCIDENCE = 80.0 VPOL

NRCS v. RELATIVE ANGLE FOR INCIDENCE = 80.0 VPOL

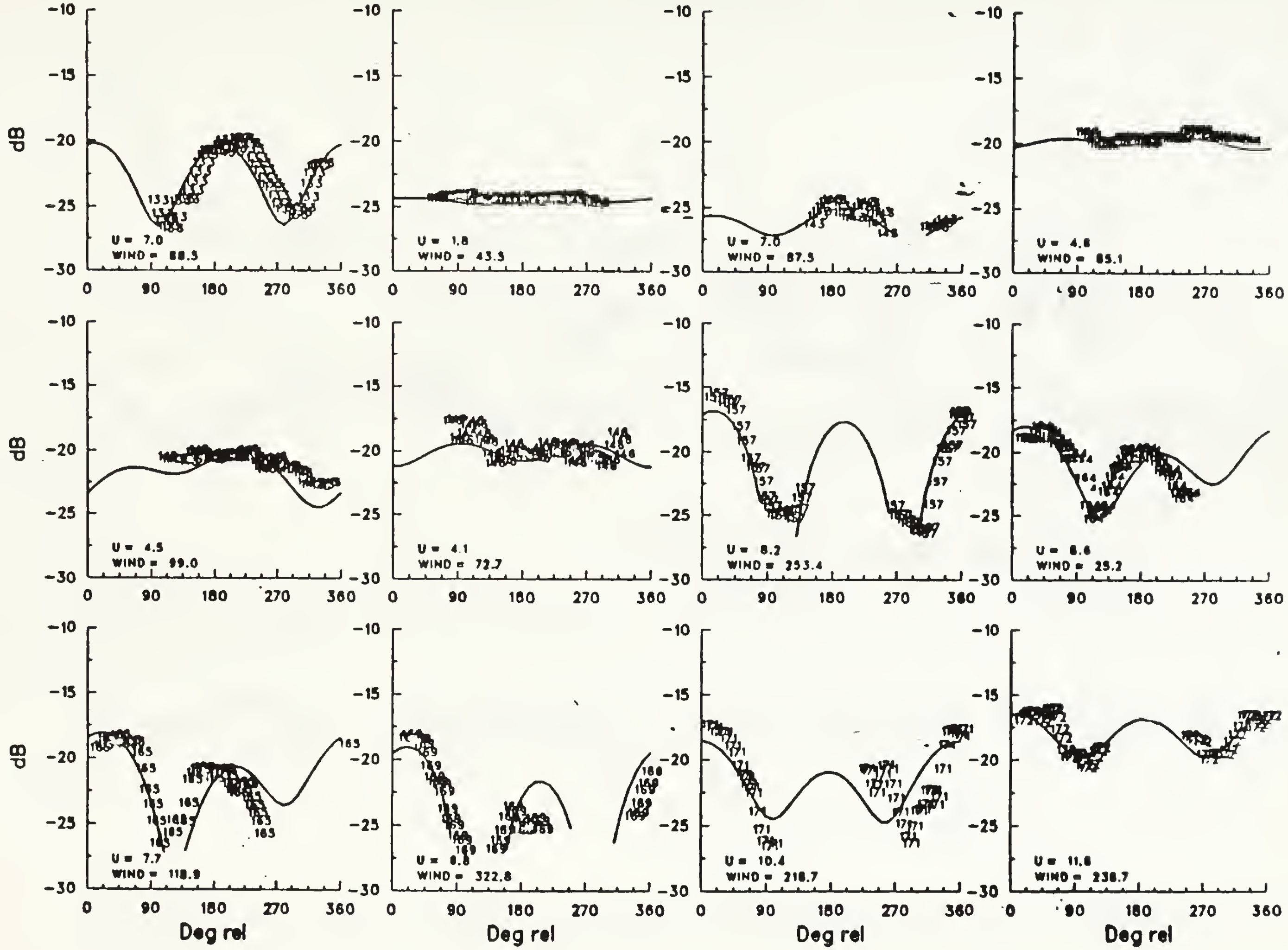

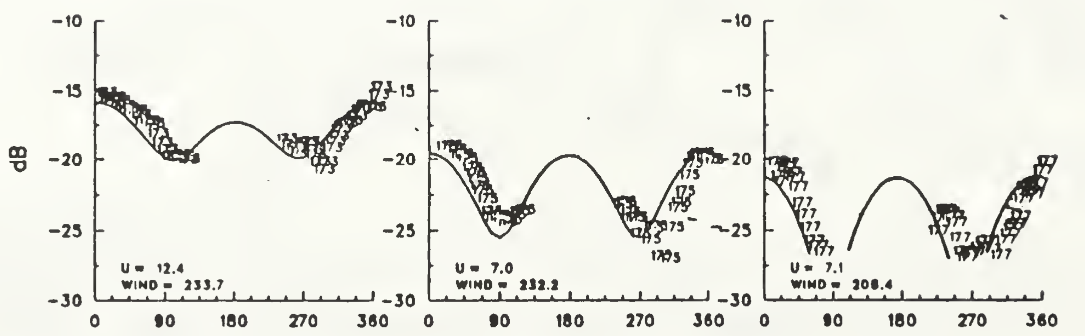

NRCS v. RELATIVE ANGLE FOR INCIDENCE = 80.0 VPOL

NRCS v. RELATIVE ANGLE FOR INCIDENCE = 10.0 HPOL

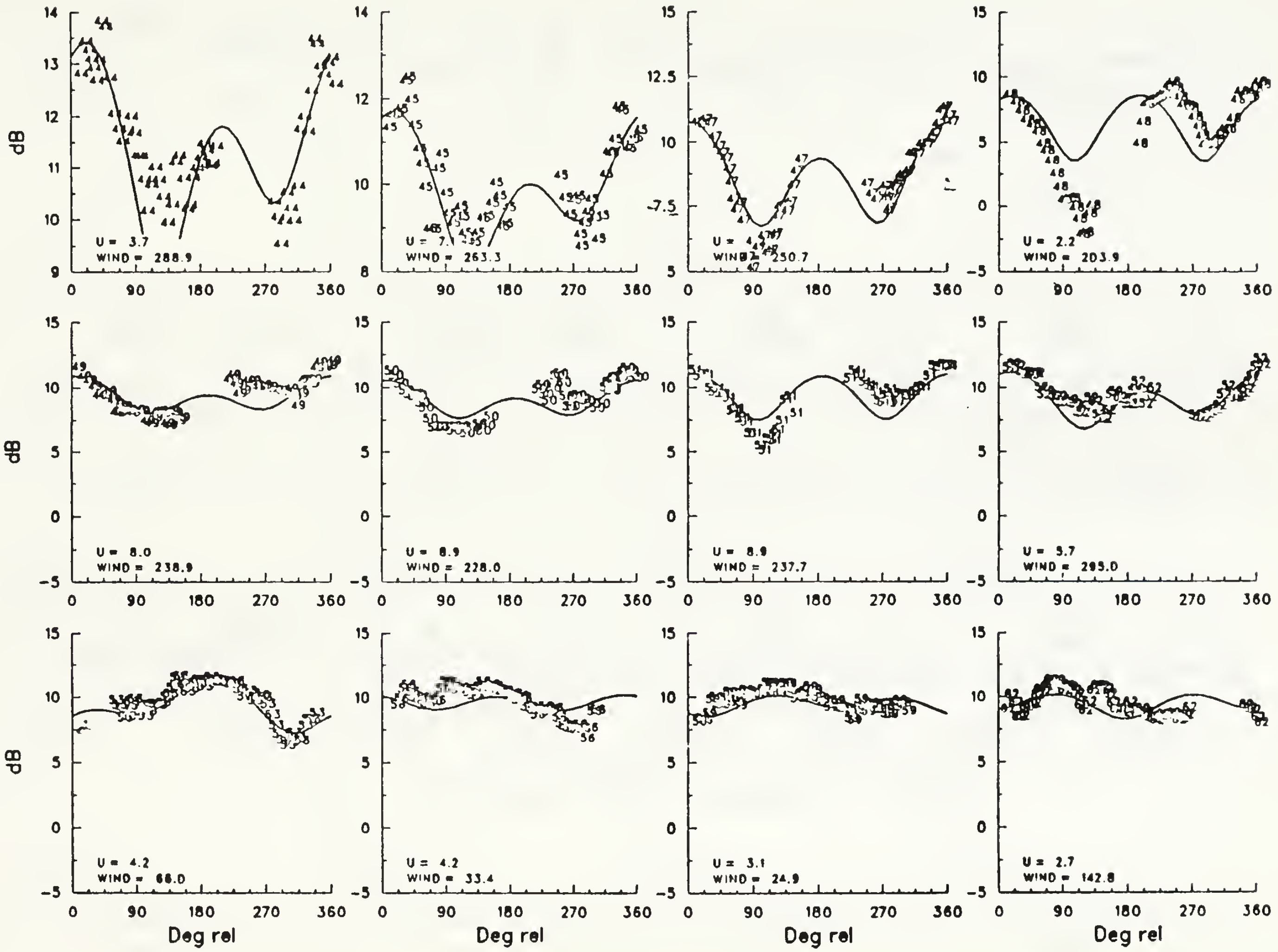

NRCS v. RELATIVE ANGLE FOR INCIDENCE = 10.0 HPOL

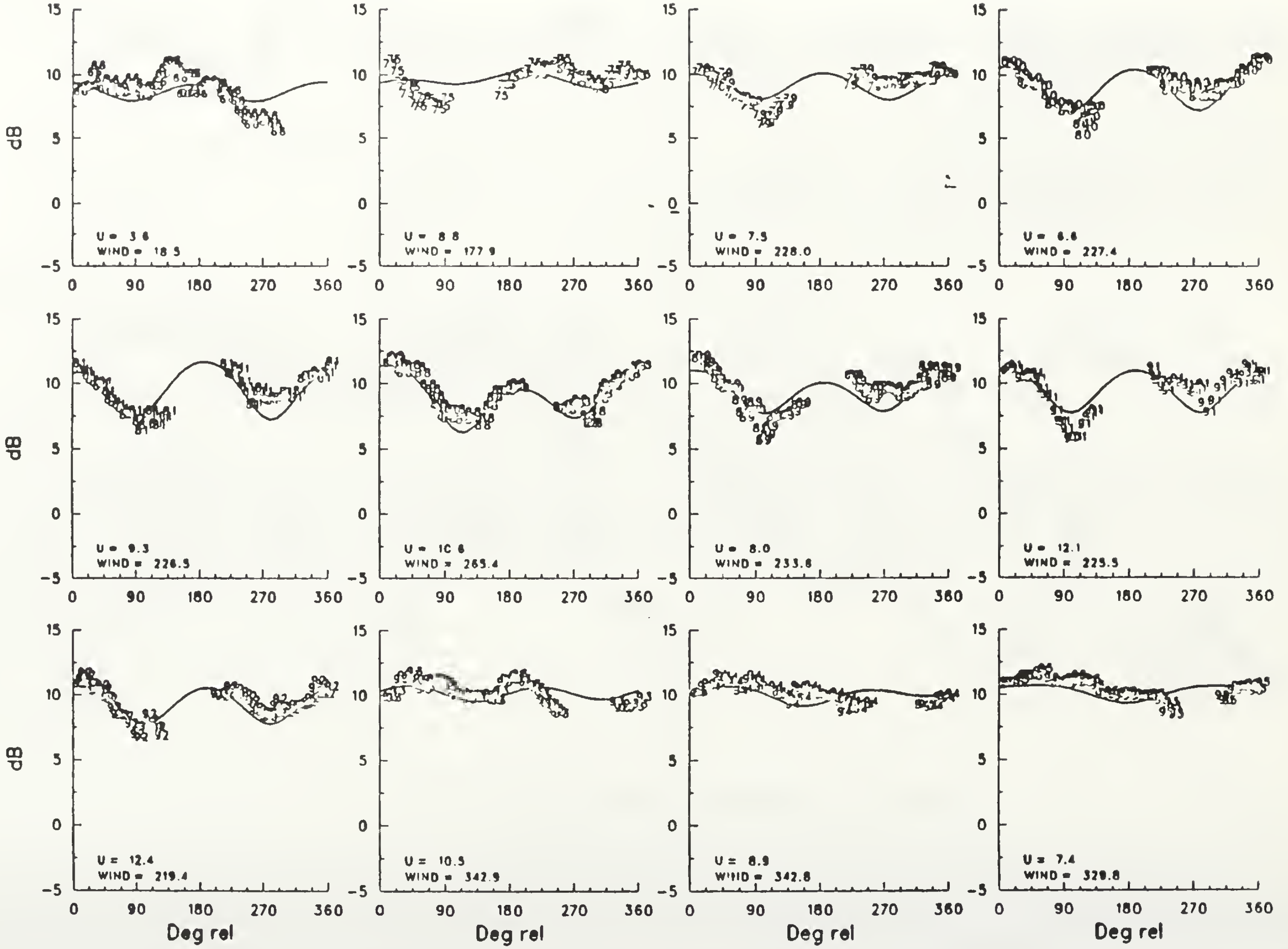

NRCS v. RELATIVE ANGLE FOR INCIDENCE = 10.0 HPOL

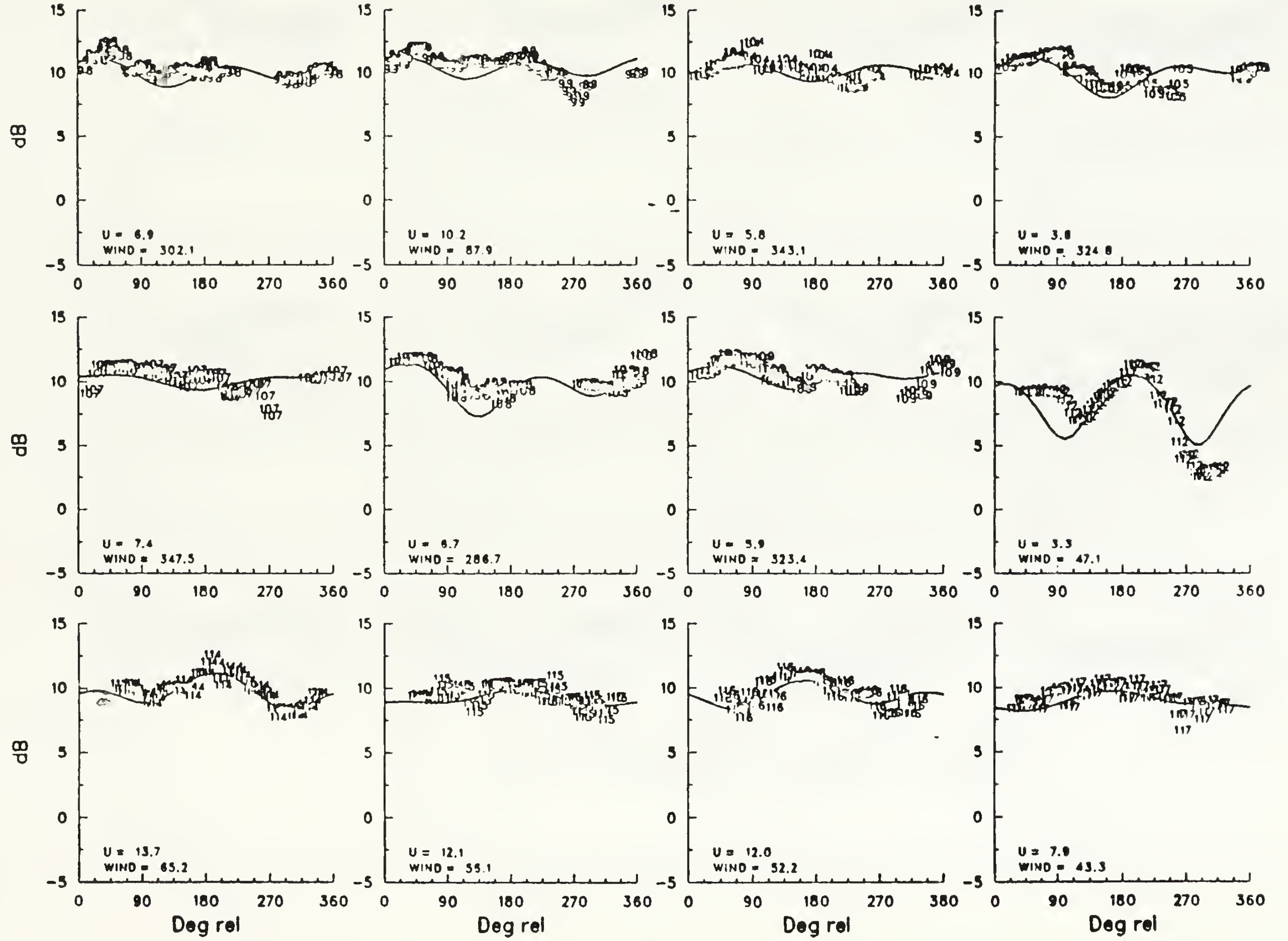

NRCS v. RELATIVE ANGLE FOR INCIDENCE = 10.0 HPOL

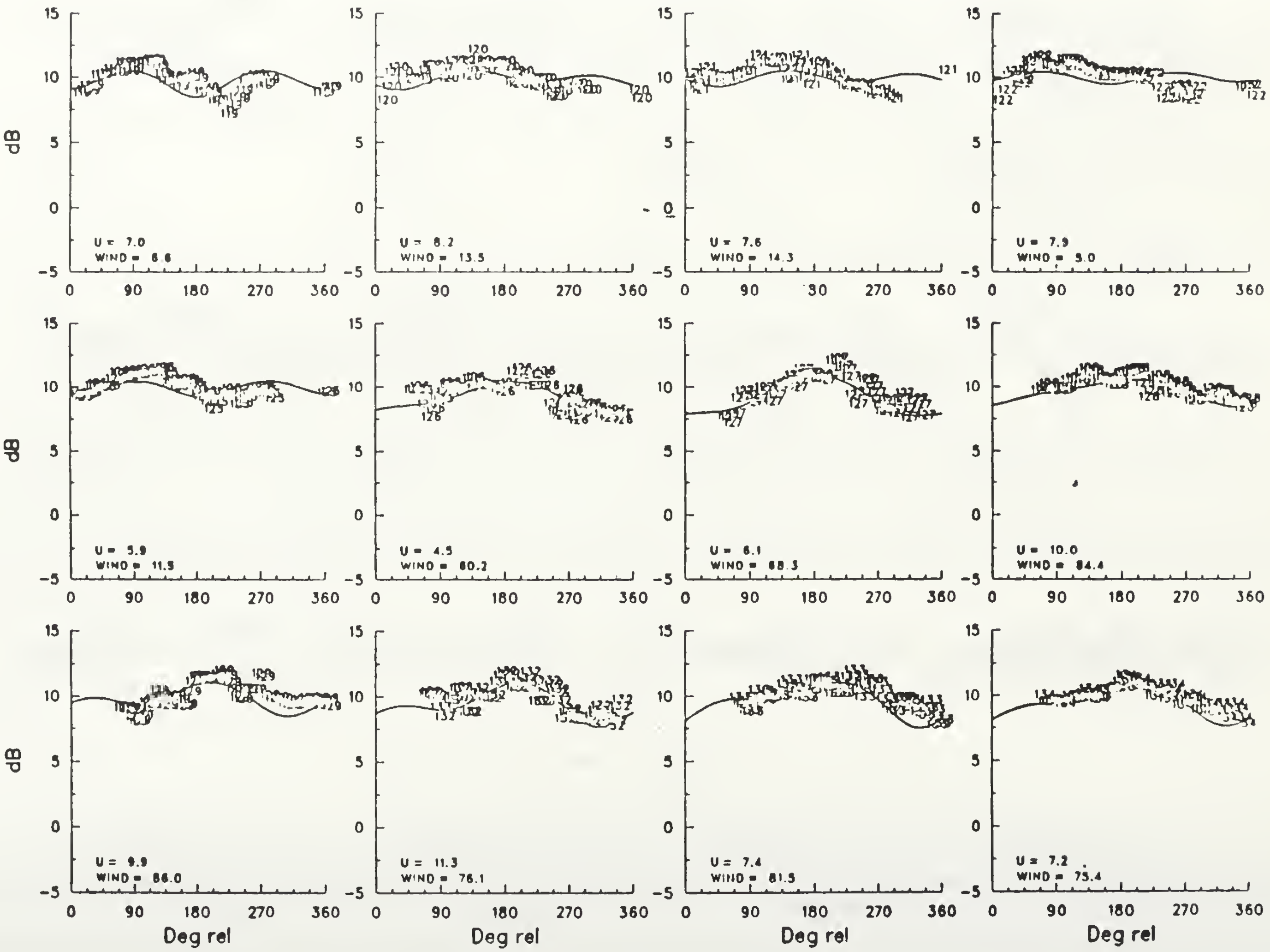

NRCS v. RELATIVE ANGLE FOR INCIDENCE = 10.0 HPOL

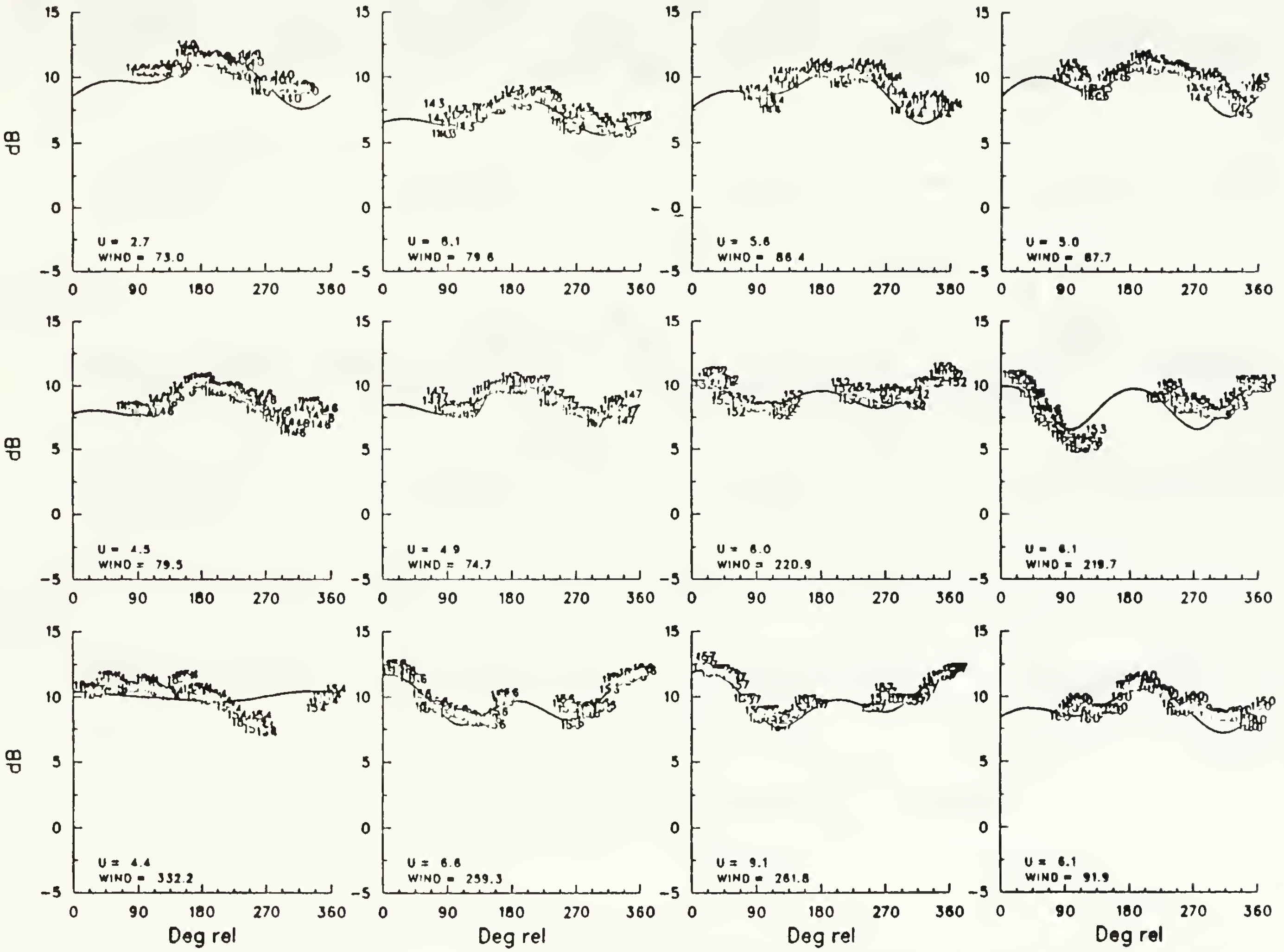

NRCS v. RELATIVE ANGLE FOR INCIDENCE = 10.0 HPOL

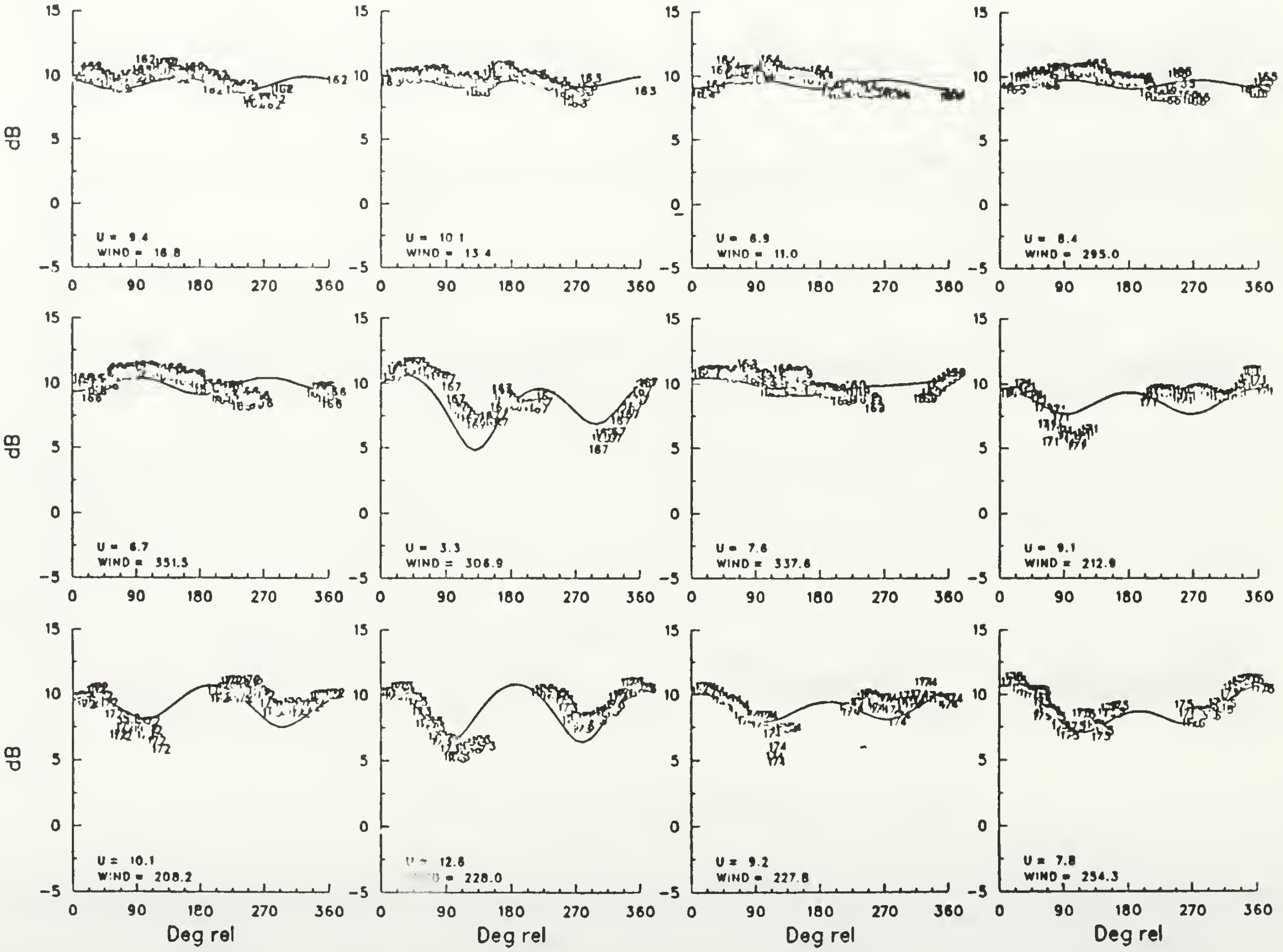

NRCS v. RELATIVE ANGLE FOR INCIDENCE = 10.0 HPOL

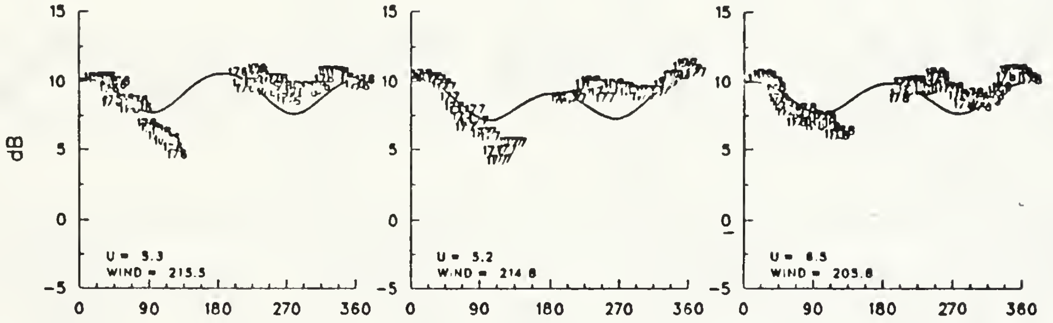

NRCS v. RELATIVE ANGLE FOR INCIDENCE = 20.0 HPOL

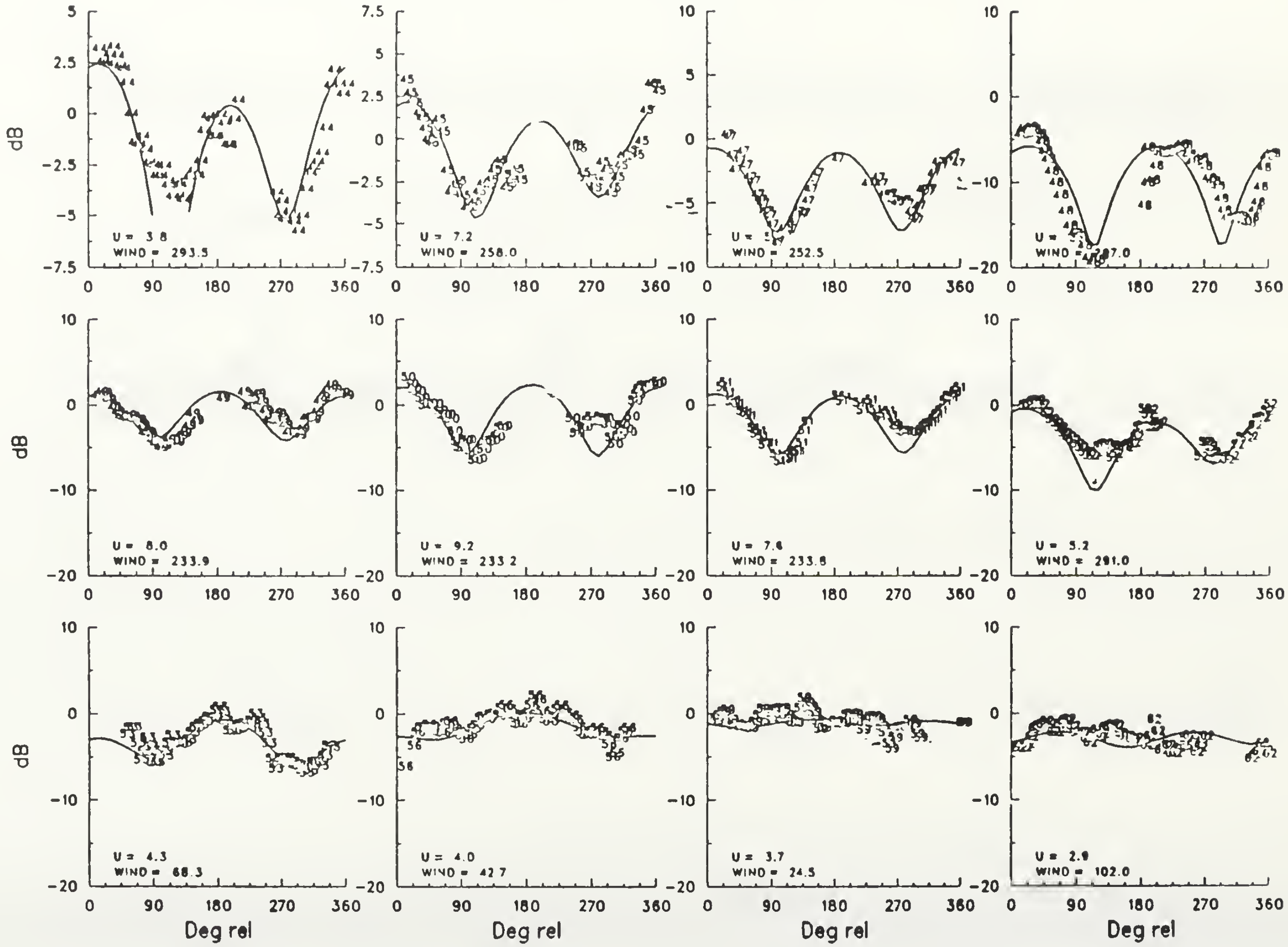

NRCS v. RELATIVE ANGLE FOR INCIDENCE = 20.0 HPOL

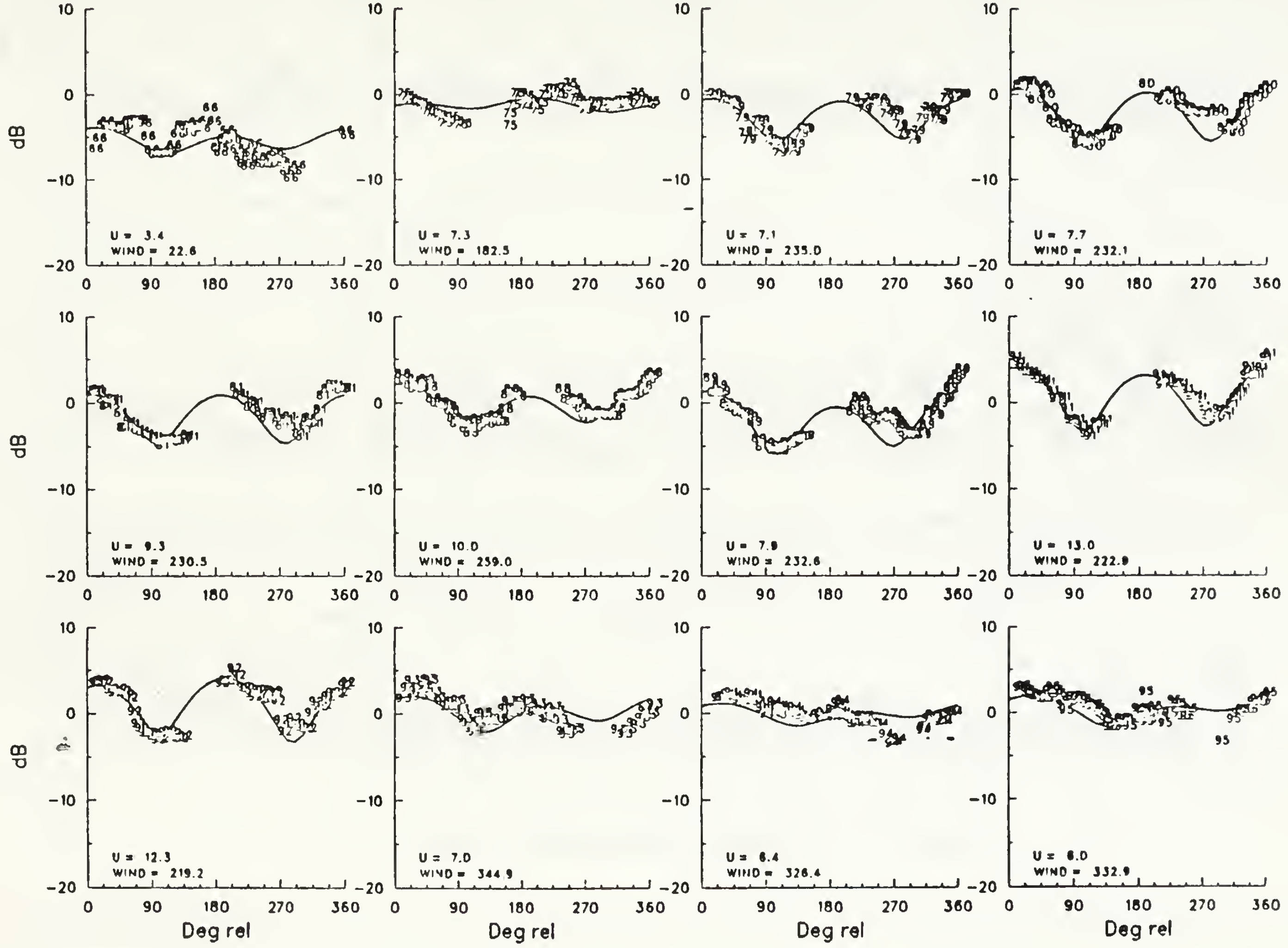

NRCS v. RELATIVE ANGLE FOR INCIDENCE = 20.0 HPOL

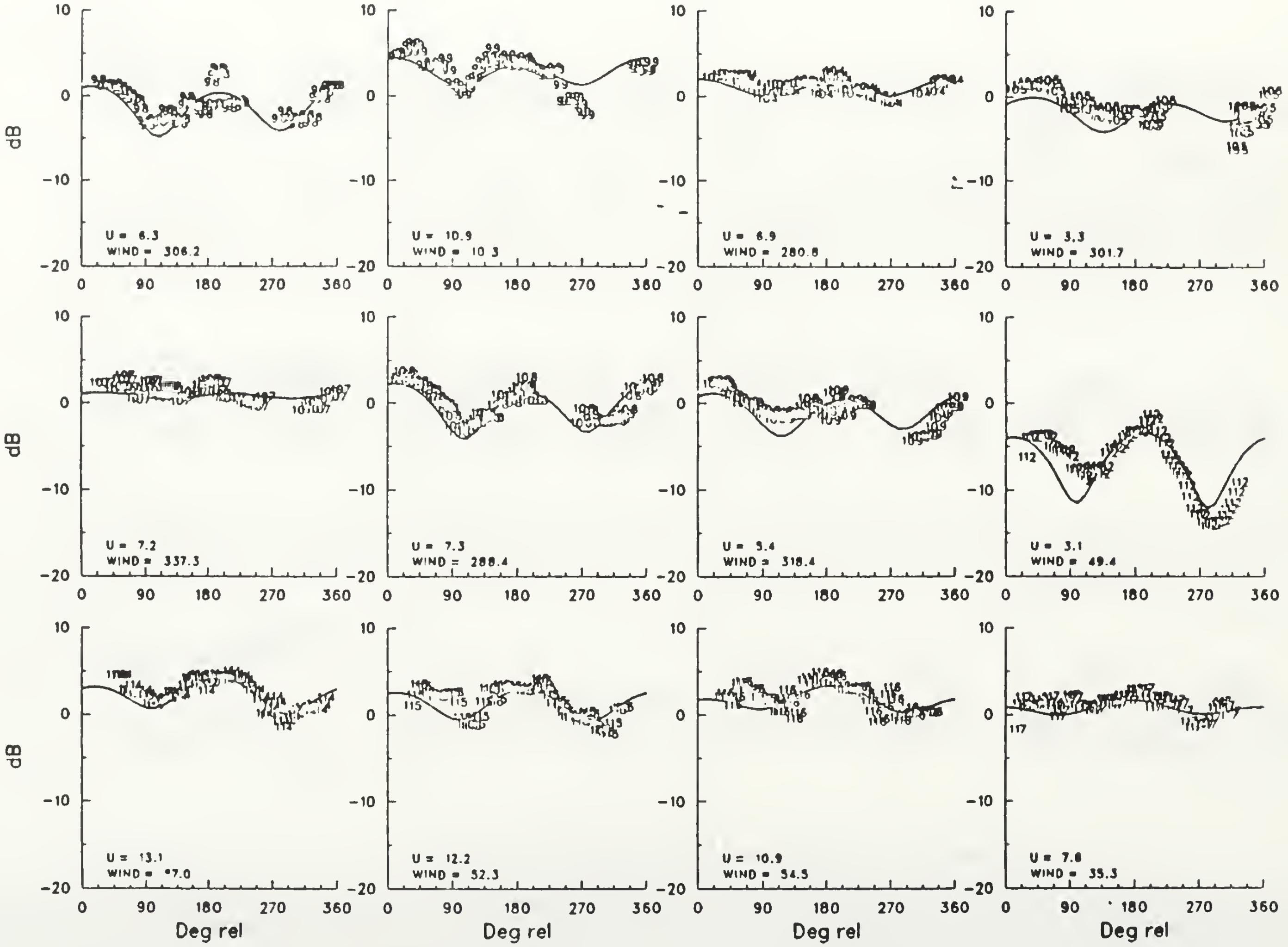

NRCS v. RELATIVE ANGLE FOR INCIDENCE = 20.0 HPOL

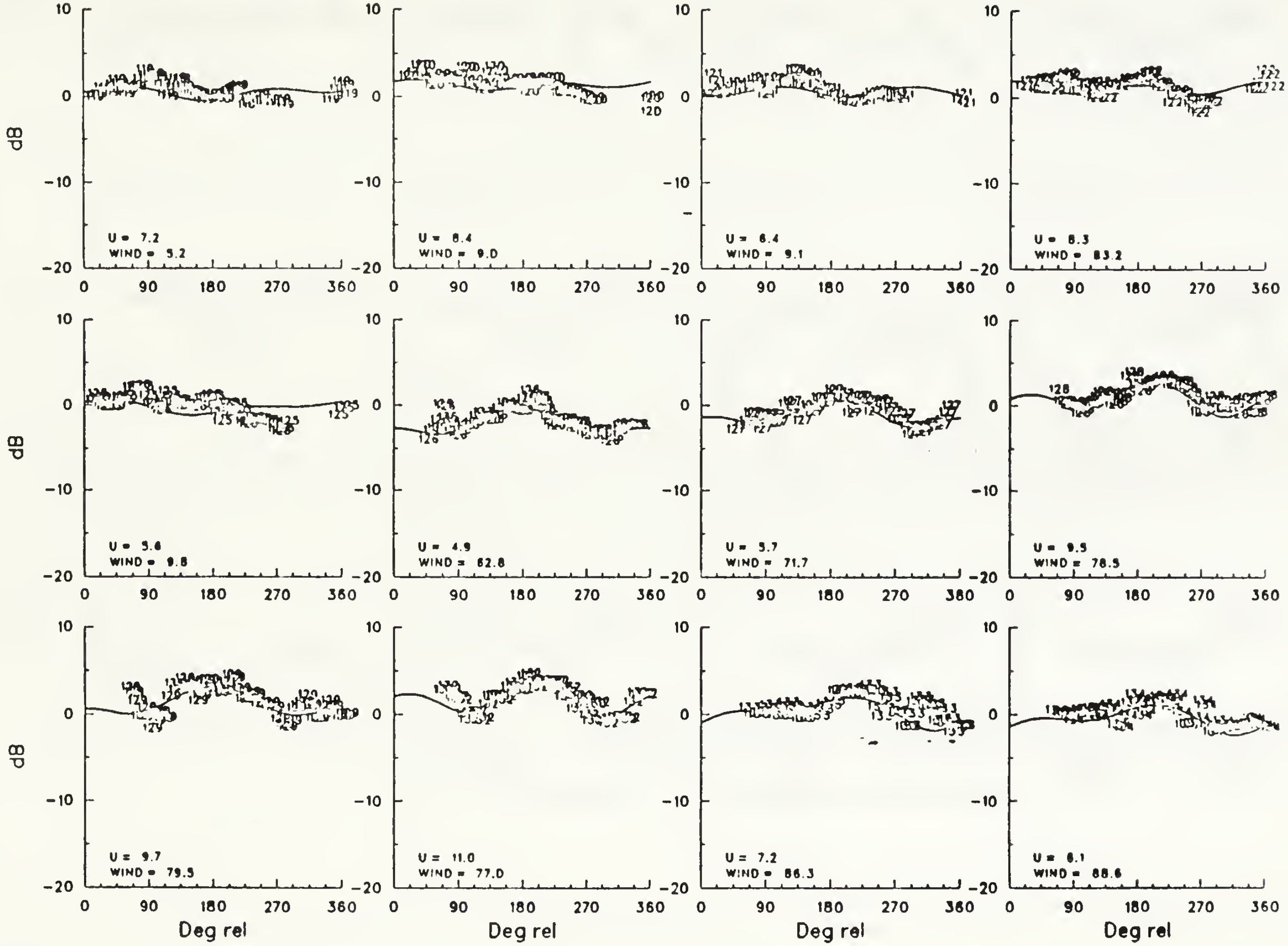

NRCS v. RELATIVE ANGLE FOR INCIDENCE = 20.0 HPOL

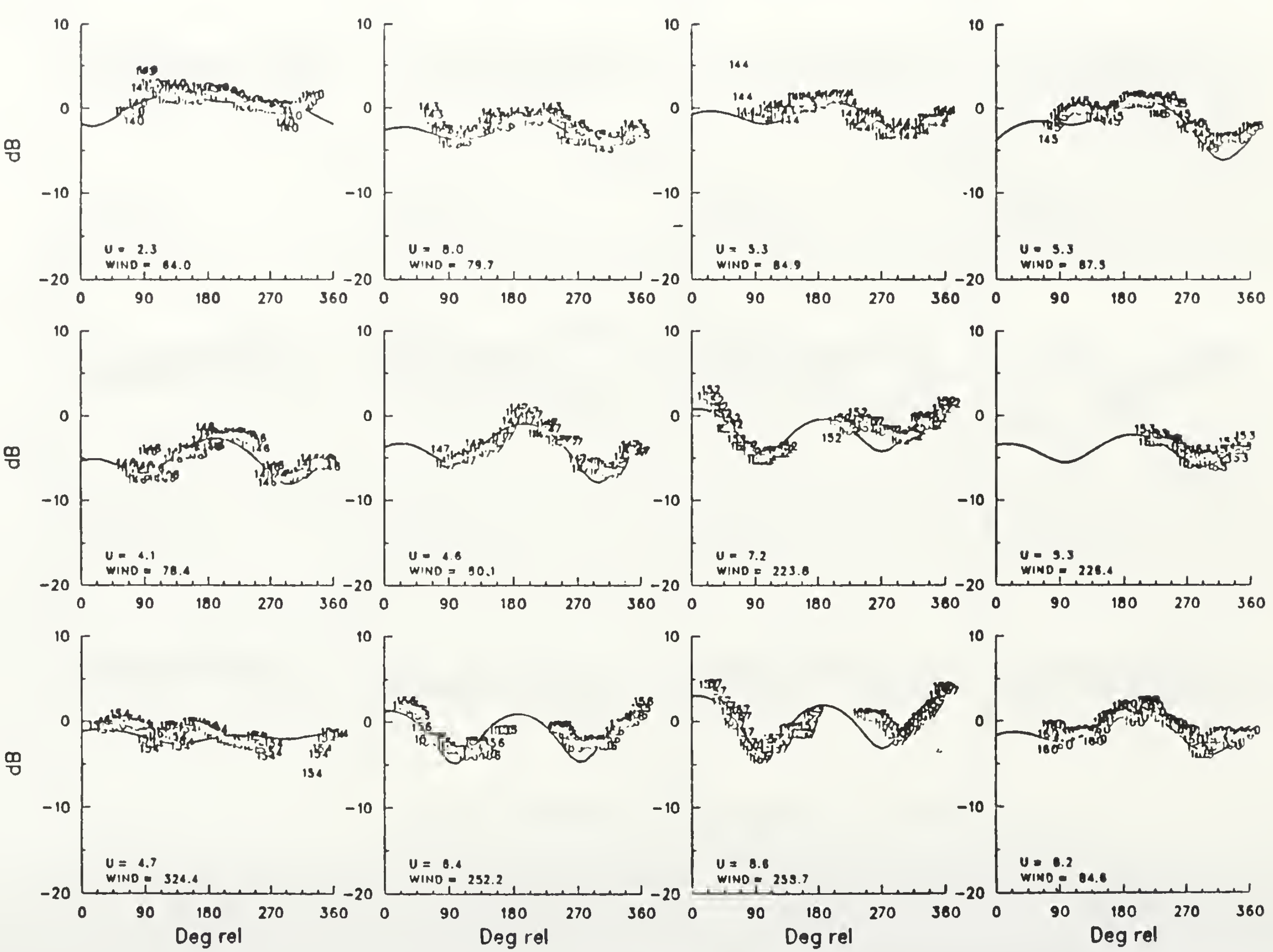

NRCS v. RELATIVE ANGLE FOR INCIDENCE = 20.0 HPOL

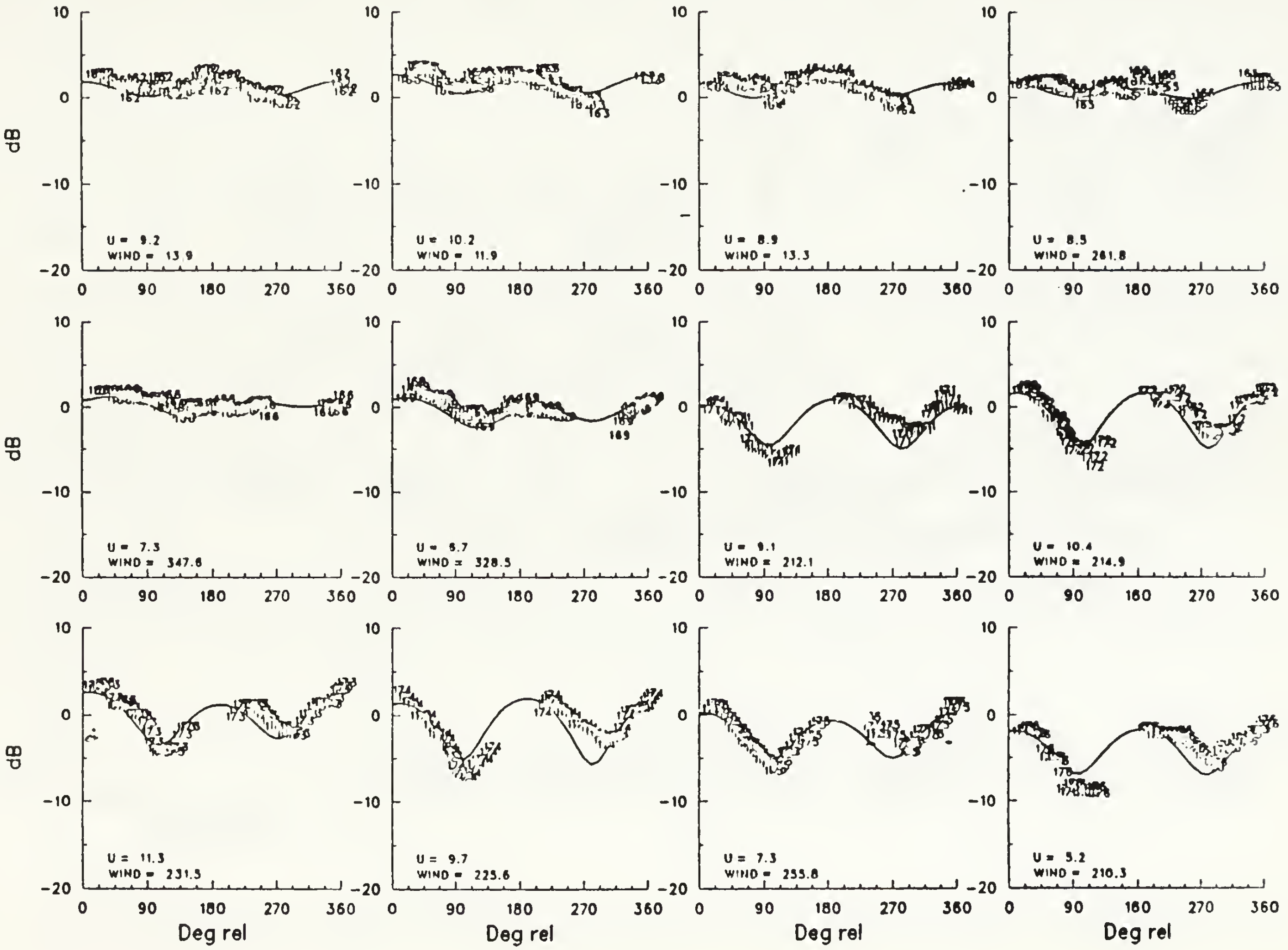

NRCS v. RELATIVE ANGLE FOR INCIDENCE = 20.0 HPOL

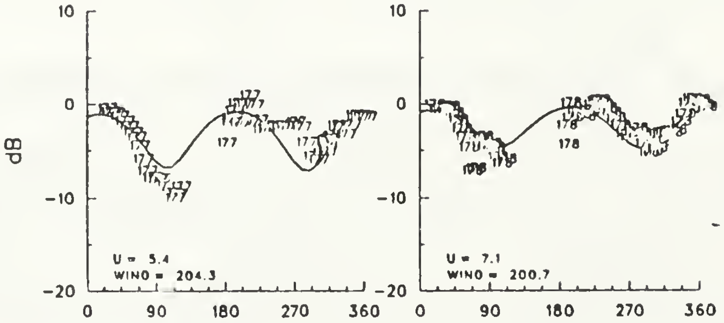

NRCS v. RELATIVE ANGLE FOR INCIDENCE = 40.0 HPOL

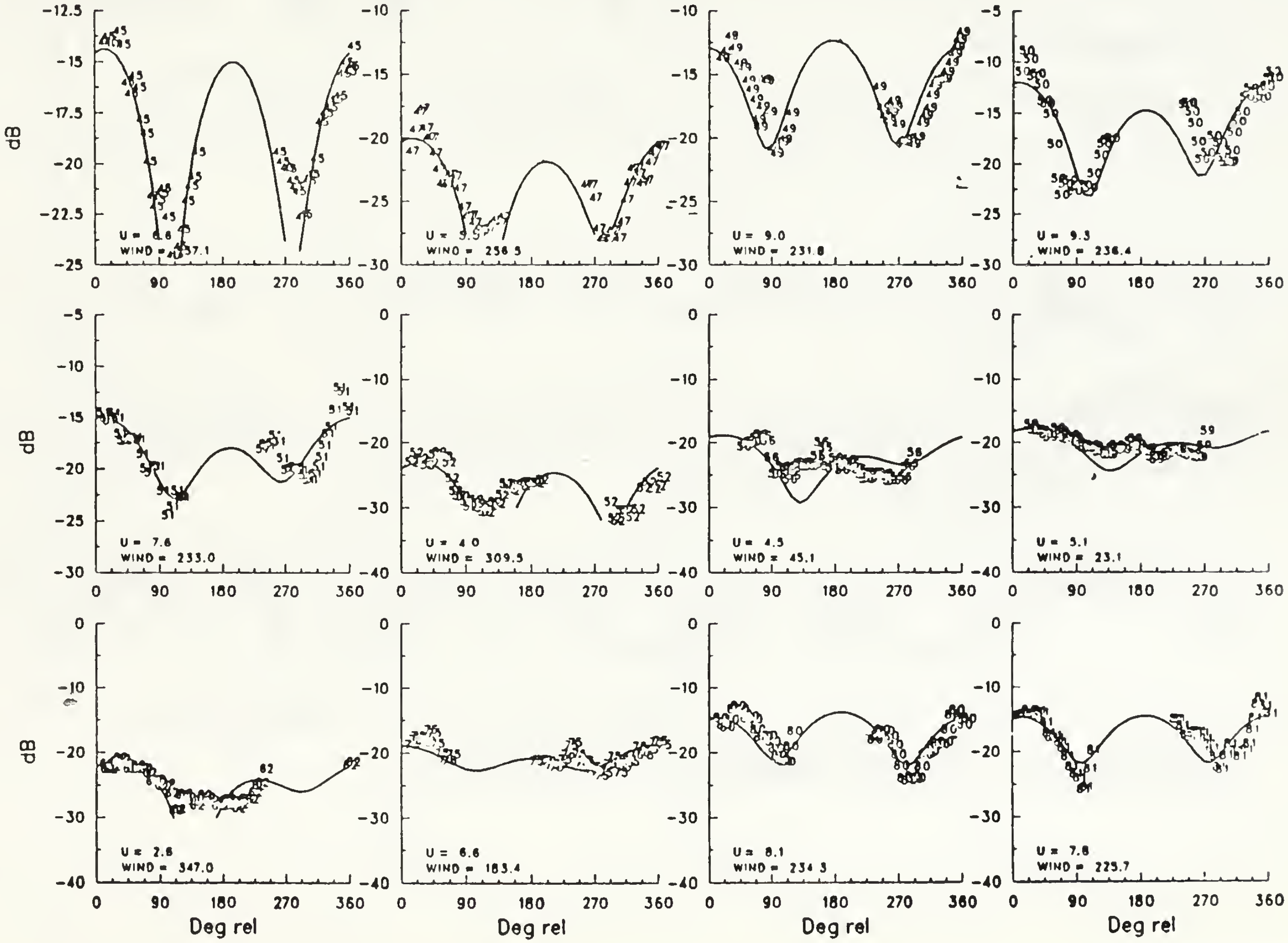

NRCS v. RELATIVE ANGLE FOR INCIDENCE = 40.0 HPOL

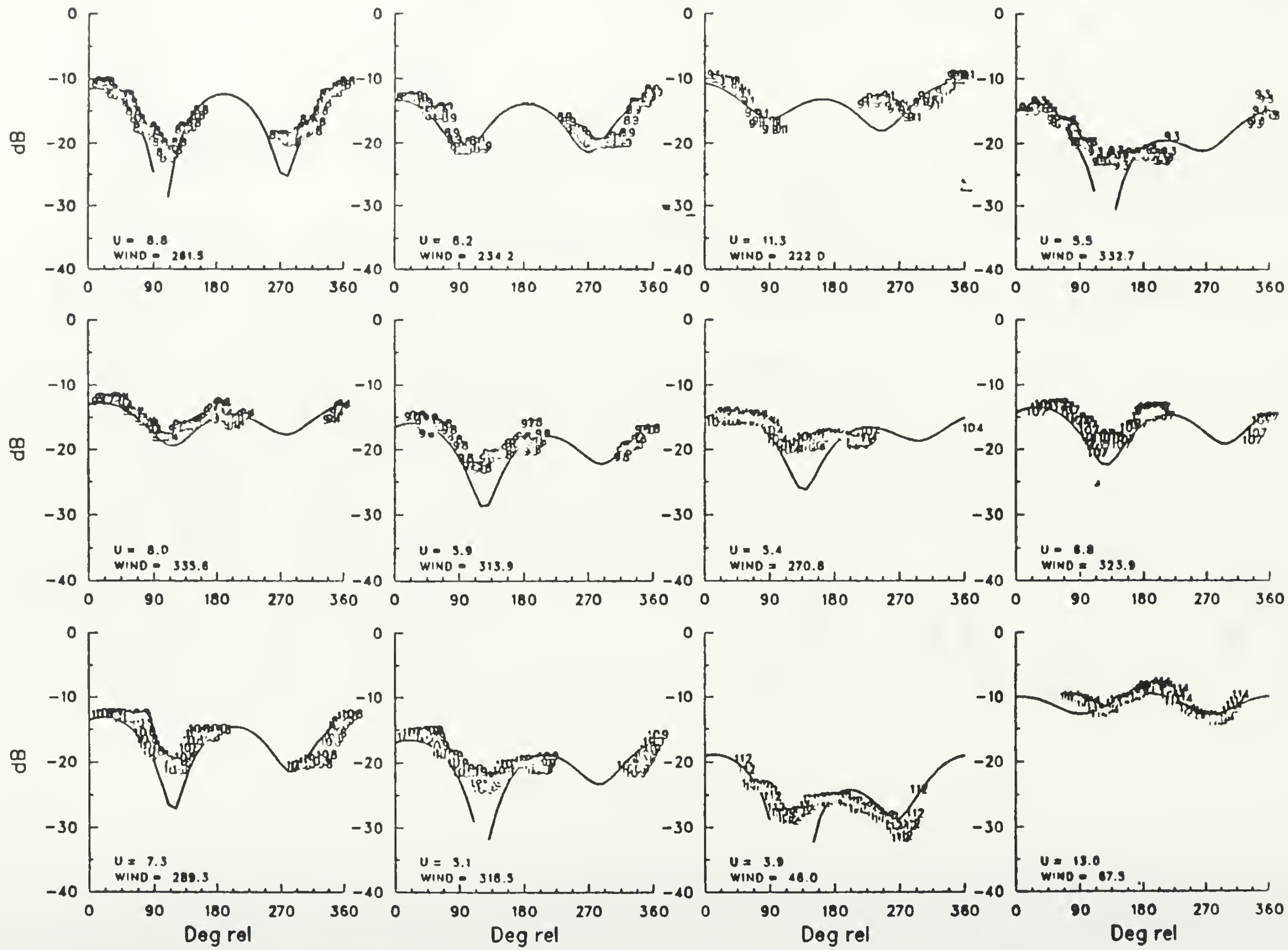

NRCS v. RELATIVE ANGLE FOR INCIDENCE = 40.0 HPOL

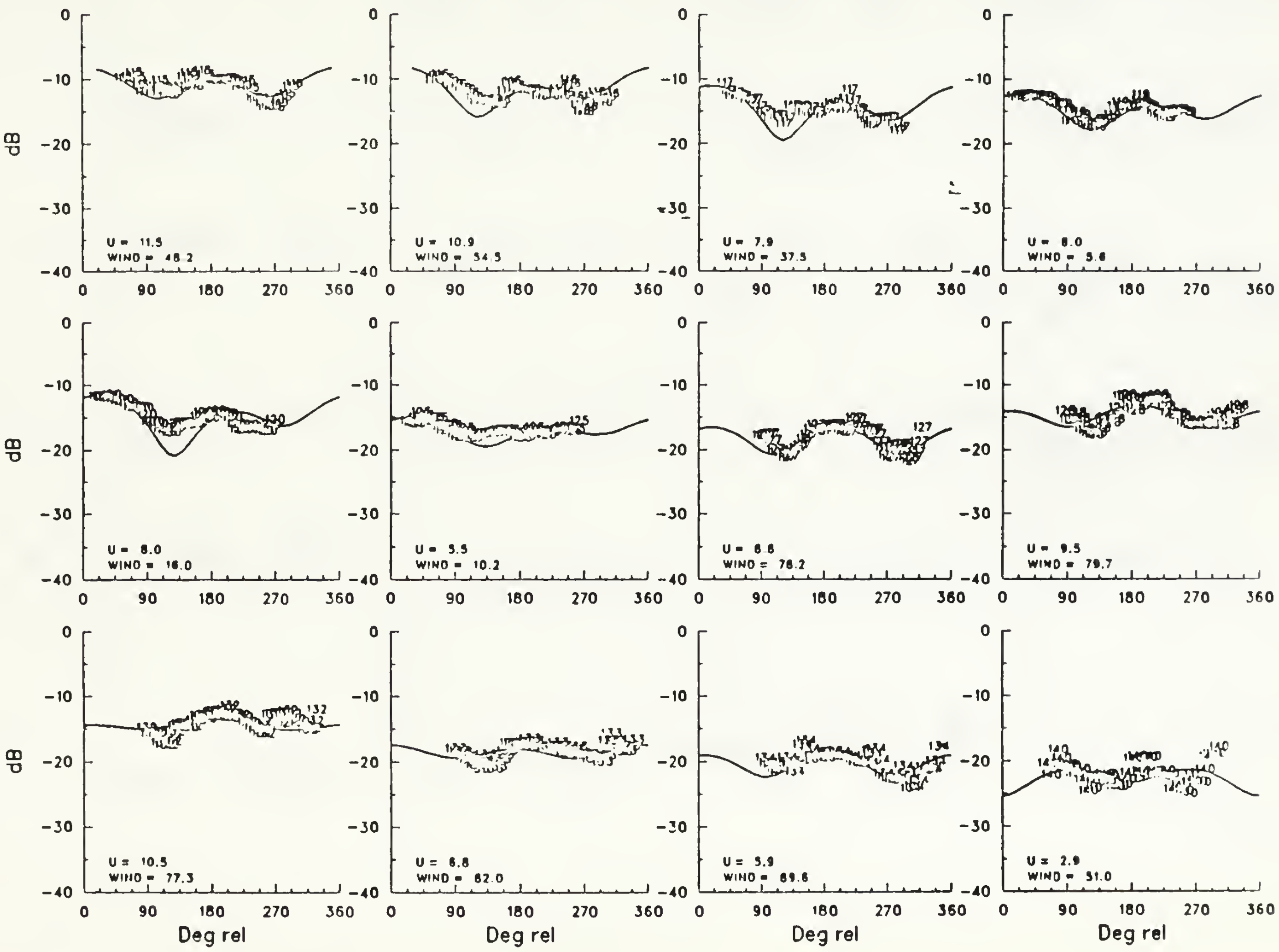

NRCS v. RELATIVE ANGLE FOR INCIDENCE = 40.0 HPOL

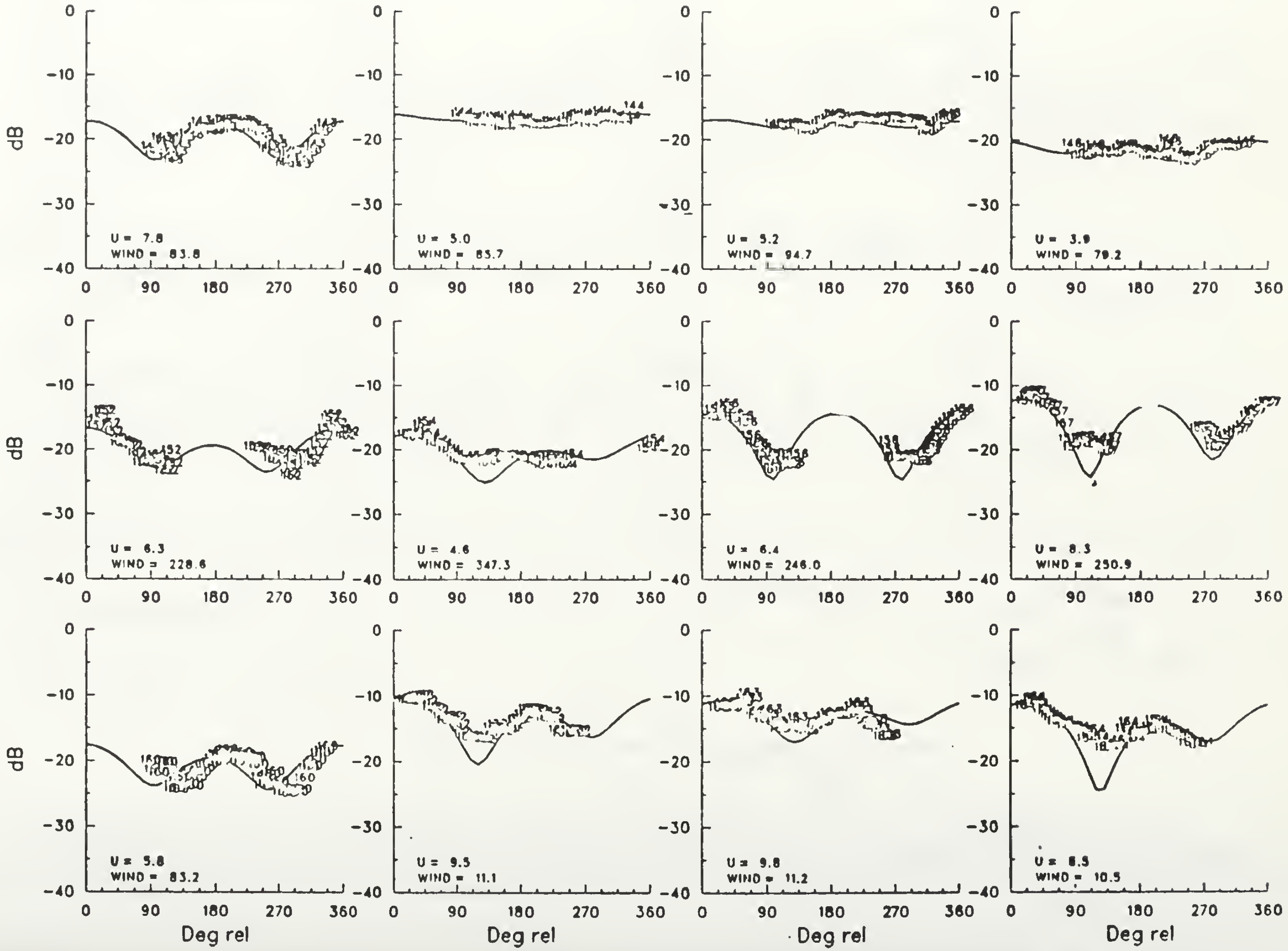

NRCS v. RELATIVE ANGLE FOR INCIDENCE = 40.0 HPOL

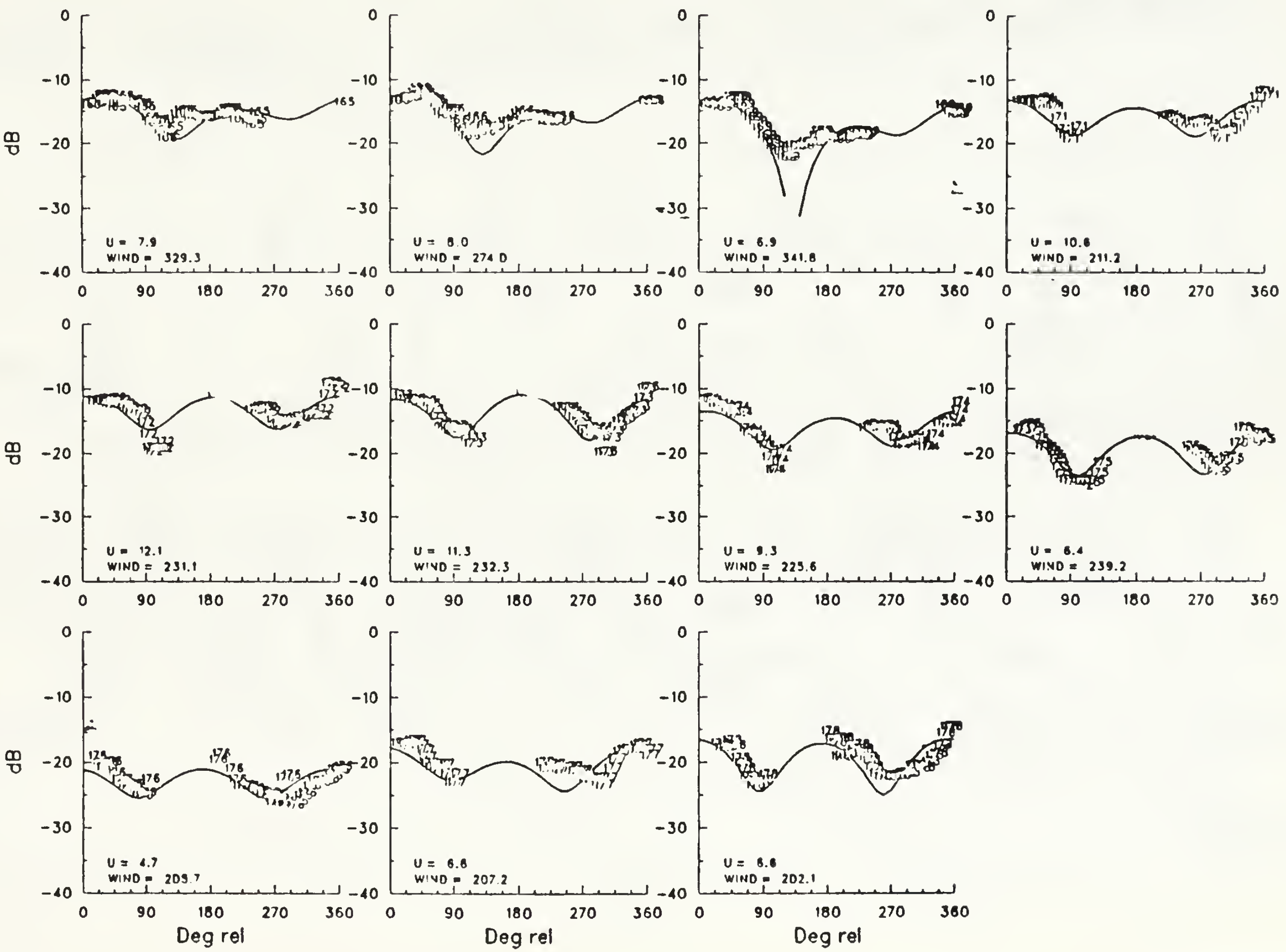

NRCS v. RELATIVE ANGLE FOR INCIDENCE = 60.0 HPOL

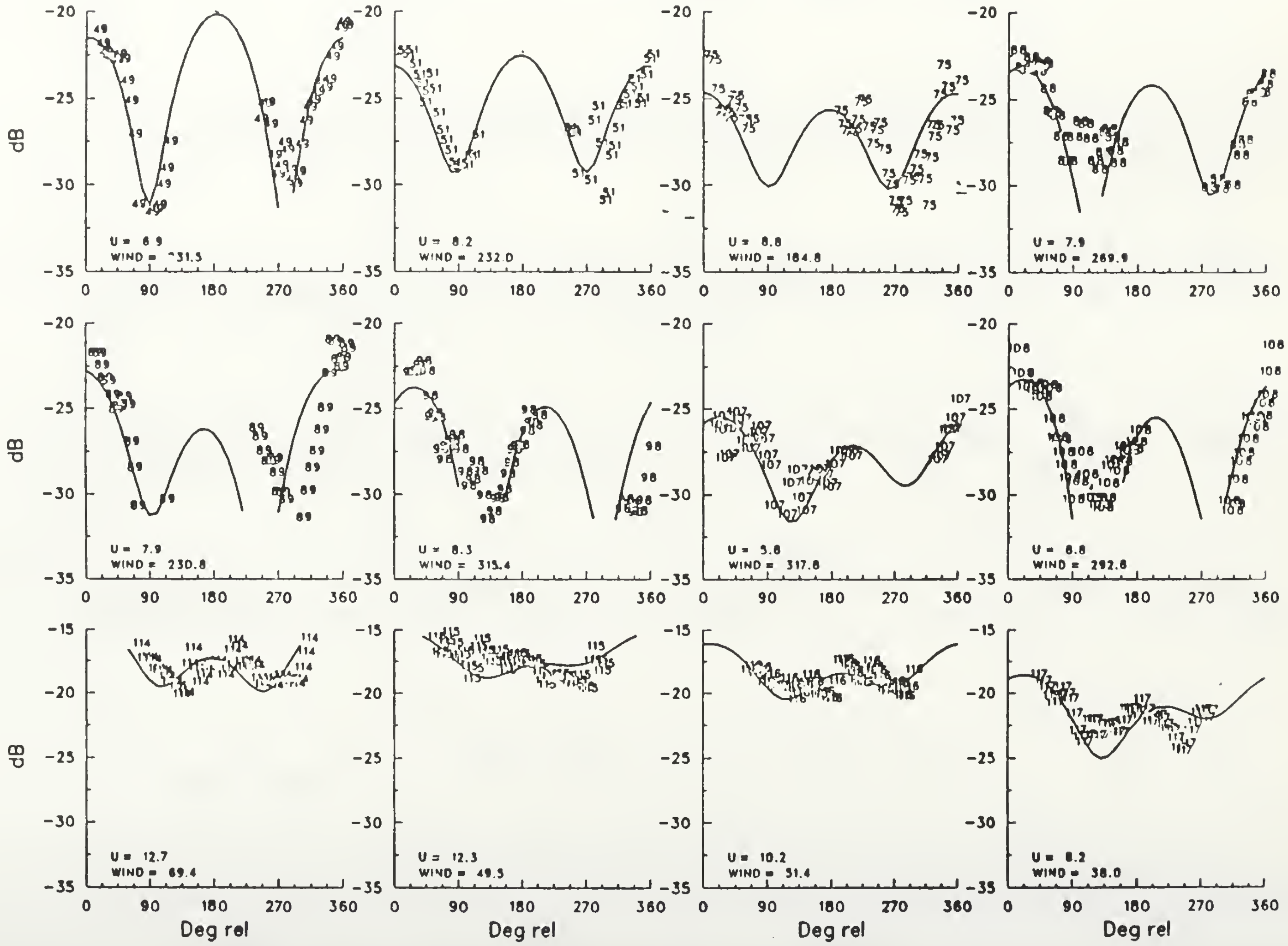

NRCS v. RELATIVE ANGLE FOR INCIDENCE = 60.0 HPOL

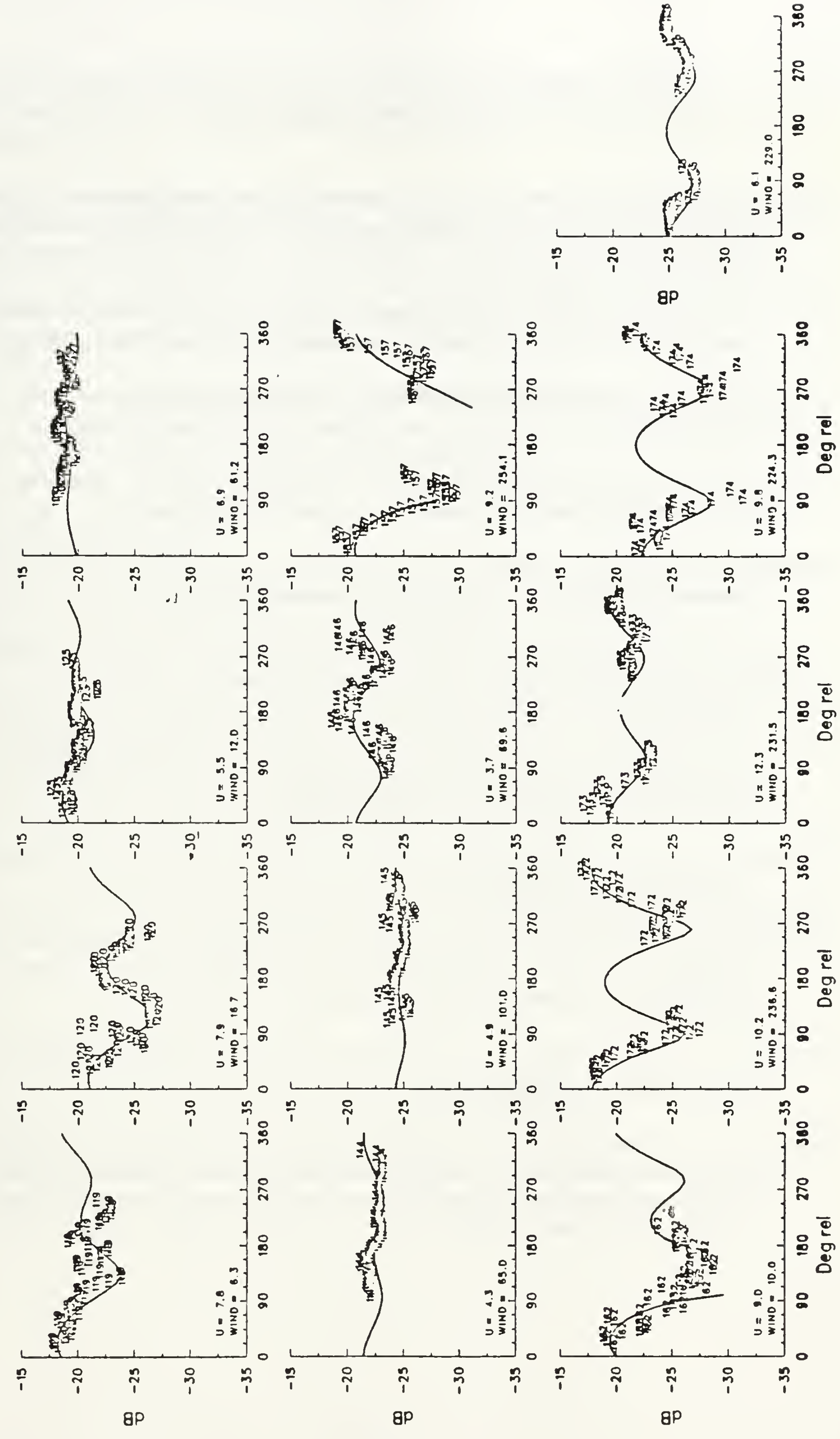

LIST OF REFERENCES

Atakturk, S. S., and Katsaros, K. B., "Intrinsic Frequency Spectra of Short Gravity-Capillary Waves Obtained from Temporal Measurements of Wave Height on a Lake," *J. Geophys. Res.*, v. 92, pp. 5131-5141, 1987.

Arya, S. P., *Introduction to Micrometeorology* , v. 42 of International Geophysics Series, Academic Press, Inc., San Diego, Calif., 307 pp., 1988.

Bahar, E., "Scattering Cross-Sections for Composite Rough Surfaces: Full Wave Analysis," *Radio Science* , v. 16, , pp. 331-341, 1981a.

Bahar, E., "Scattering Cross-Sections for Composite Rough Surfaces: Full Wave Analysis," *Radio Science* , pp. 1327-1335, 1981b.

Barrick, D. E., "Rough Surface Scattering Based on the Specular Point Theory," *IEEE Trans.* , v. AP-16, pp. 449-454, 1968.

Banner, M. L., and Phillips, O. M., "On the Incipient Breaking of Small Scale Waves," *J. Fluid Mech.*, v. 65, pp. 647-656, 1974.

Bass, F. G., Fuks, I. M., Kalmykov, A. E., Ostrovsky, I. E., and Rosenberg, A. D., "Very-high Frequency Radiowave Scattering by a Disturbed Sea Surface," *IEEE Trans.* , v. AP-16, pp. 554-568, 1968.

Battan, L. J., *Radar Observations of the Atmosphere,* Univ. of Chicago Press, Chicago, pp. 71-73, 1973.

Beckmann, P. and Spizzichino, A., *The Scattering of Electromagnetic Waves from Rough Surfaces* , MacMillan Co., New York, 503 pp., 1963. (Reprinted by Artech House, Inc., 1987).

Bendat, J. S., and Piersol, A. G., *Random Data* , Second Edition, John Wiley and Sons, Inc., 566 pp., 1986.

Bliven, L., Giovanangeli, J. P., and Norcross, G., "Scatterometer Directional Response during Rain," preprints from the 12th Canadian Symposium on Remote Sensing, IGARSS'89, 10 - 14 July, Vancouver, Canada, pp. 1887-1890, 1989.

Boggs, D. H., *Seasat Geophysical Data Record (GDR) Users Handbook: Scatterometer*, Jet Propulsion Laboratory Document 129, Pasadena, CA, August, 1982.

Bracalente, E. M., Boggs, D. H., Grantham, W. L., "The SASS Scattering Coefficient Algorithm," *IEEE J. Oceanic Eng.*, v. OE-5, pp. 145-154, 1980.

Brown, D. N. and McCandless, S. W., "Technical Reference Guide for Naval Oceanography from Space," Report prepared for Chief, Naval Oceanography Command, December, 1988.

Brown, G. S., "Backscattering from a Gaussian-Distributed Perfectly Conducting Rough Surface," *IEEE Trans. Ant. Prop.* , V. AP-26, pp. 472-482, 1978. (Corrected in AP-28, pp. 943-946, 1980).

Brown, R. A., "On the Scatterometer as an Anemometer," *J. Geophys. Res.*, v. 88, pp. 1663-1673, 1983.

Businger, J. A., "Flux Profile Relationships in the Atmospheric Surface Layer," *J. Atmos. Sci.*, v. 28, pp. 181-189, 1971.

Businger, J. A., "Turbulent Transfer in the Atmospheric Surface Layer," in *Workshop on Micrometeorology*, D. Haugen (ed.), Amer. Met. Soc., Boston, pp. 67-100, 1973.

Byers, B. J., "Variation of the Drag Coefficient with Wind and Wave State," M.S. Thesis, Naval Postgraduate School, 110 pp., 1985.

Cardone, V. J., "Specification of the Wind Distribution in the Marine Boundary Layer for Wave Forecasting," Geophysical Sciences Laboratory TR-69-1, New York Univ., 131 pp., 1969.

Charnock, H., "Wind Stress on a Water Surface," *Quart. J. Royal Met. Soc.*, v. 81, pp. 639-640, 1955.

Chaudrey, A. H., and Moore, R. K., "Tower-based Backscatter Measurements of the Sea," *IEEE J. Ocean. Eng.*, v. OE-9, pp. 309-316, 1984.

Chen, M. F., and Fung, A. K., "A Numerical Study of the Regions of Validity of the Kirchoff and Small-Perturbation Rough Surface Scattering Models," *Radio Science*, v. 23, pp. 163-170, 1988.

Cox, C. S,, and Munk, W., "Measurements of the Roughness of the Sea Surface from Photographs of the Sun's Glitter," *J. Opt. Soc. Am.*, v. 44, pp. 838-850, 1954.

Cox, C. S., "Measurements of Slopes of High-Frequency Wind Waves," *J. Mar. Res.*, v. 16, pp. 199-225, 1958.

Daley, J. C., "Wind Dependence of the Radar Sea Return," *J. Geophys. Res.*, v. 78, pp. 7823-7833, 1973.

Daley, G., Plant, W. J., Schuler, D.L., and Miller, A. C., "N-ROSS Scatterometer Issue Paper," NRL Letter 7910-256, 1984.

Der, C., "A Summary Data Package on the CCIW Capacitive Wave Staff Sensors," Canada Centre for Inland Waters, Engineering Services Division Internal Report, Burlington, Ontario, Canada, 17 May, 1976.

Donelan, M. A., Birch, N. K., and Beesley, D. C., "Generalized Profiles of Wind Speed, Temperature and Humidity", *Proc. 17th Conf. Great Lakes Res.*, Internat. Assoc. Great Lakes Res., pp. 369-388, 1974.

Donelan, M.A., "The Dependence of the Aerodynamic Drag Coefficient on Wave Parameters," in the *First International Conf. on Met. and Air-Sea Interaction of the Coastal Zone*, Amer. Met. Soc., Boston, pp. 381-387, 1982.

Donelan, M. A., Hamilton, J. and Hui, W. H., "Directional Spectra of Wind-Generated Waves," *Phil. Trans. R. Soc. Lond.* , v. A-315, pp. 509-562, 1985.

Donelan, M. A., and Pierson, W. J., Jr., "Radar Scattering and Equilibrium Ranges in Wind-Generated Waves with Application to Scatterometry", *J. Geophys. Res.*, v. 92, pp. 4971-5029, 1987.

Donelan, M. A., "Air-Sea Interaction", in *The Sea*, v. 9, LeMehaute, B., and Hanes, D. (eds.), Interscience-Wiley, New York, in press, 1989.

Donelan, M. A., and Hui, W. H., "Mechanics of Ocean Surface Waves," in *Surface Waves and Fluxes: Current Theory and Remote Sensing*, Geernaert, G. L., and Plant, W. J. (eds.), Kluwer Press, Dordricht, The Netherlands, in press, 1990.

Durden, S. L., and Vesecky, J. F., "A Physical Radar Cross-Section Model for a Wind-Driven Sea with Swell," *IEEE J. Ocean. Eng.*, v. OE-10, pp. 445-451, 1985.

Durden, S. L, *Microwave Scattering from the Ocean Surface,* Ph.D Dissertation, Stanford Univ. Scientific Rep. No. D901-1986-1, 177 pp., June, 1986.

Fairall, C. W., Edson, J. B., Larsen, S. E., and Mestayer, P. G., "A Comparison of Inertial-Dissipation and Eddy Covariance Surface Flux Measurements during the HEXMAX experiment," preprints from the seventh Conf. on Ocean-Atmosphere Interaction, 1 - 5 Feb 1988, Anaheim, CA, Amer. Met. Soc., Boston, MA, pp. 4-9, 1988.

Fung, A. K. and Chan, H.,"Backscattering of Waves by Composite Rough Surfaces," *IEEE Trans.*, v. AP-17, pp. 590-597, 1969.

Fung, A. K., and Lee, K. K., "A Semi-empirical Sea-spectrum Model for Scattering Coefficient Estimation," *IEEE J. Ocean Eng.*, v. OE-7, pp. 166-176, 1982.

Garrett, J. R., "Review of Drag Coefficient over Oceans and Continents," *Mon. Wea. Rev.*, v. 105, pp. 915-929, 1977.

Garrett, J. R., "The Stably Stratified Internal Boundary Layer for Steady and Duirnally Varying Offshore Flow," *Bound. Layer Met.*, v. 38, pp. 369-394, 1987.

Geernaert, G. L., Katsaros, K. B., and Richter, K., "Variation of the Drag Coefficient and its Dependence on Sea State," *J. Geophys. Res.*. v. 91, pp. 7667-7679, 1986.

Geernaert, G. L., Davidson, K. L., Larsen, S. E., and Mikkelsen, T., "Measurements of the Wind Stress during the Tower Ocean Wave and Radar Dependence Experiment," *J. Geophys. Res.*, v. 93, pp. 13913-13923, 1988a.

Geernaert, G. L., "Measurements of the Angle between the Wind Vector and Wind Stress Vector in the Surface Layer over the North Sea," *J. Geophys. Res.* , v. 93, pp. 8215-8220, 1988b.

Geernaert, G. L., "Bulk Parameterizations for the Wind Stress and Heat Flux", in *Surface Waves and Fluxes: Current Theory and Remote Sensing,* Geernaert, G.L. and Plant, W.J. (eds.), Kluwer Press, Dordricht, The Netherlands, in press, 1990.

Goldstein, H., "The Frequency Dependence of Radar Echoes from the Surface of the Sea," *Phys. Rev.*, v. 69, p. 695, 1946.

Graham, D. M., "Getting Along without NROSS," *Sea Techn.* , Feb., 1987.

Great Lakes Climatological Atlas, Canadian Government Publication Centre, Montreal, Canada, 1986.

Gucinski, H., "Bubble Coalescence in Sea- and Freshwater: Requisites for an Explanation," in *Oceanic Whitecaps and Their Role in Air-Sea Exchange Processes* , Monahan, E.C. and MacNiocaill, G. (eds.), D. Reidel Pub. Co., p. 270, 1986.

Guinard, N. W., Ransone, J. T., and Daley, J. C., "Variations of the NRCS of the Sea with Increasing Roughness," *J. Geophys. Res.* , v. 76, pp. 1525-1538, 1971.

Guissard, A., Baufays, C., and Sobieski, P., "Sea Surface Description Requirements fro Electromagnetic Scattering Calculations," v. 91, pp. 2477-2492, 1986.

Hasselmann, K., "On the Nonlinear Energy Transfer in a Gravity Wave Spectrum," *J. Fluid Mech.,* v. 12, pp. 481-500, 1962.

Hasselmann, K., and others, "Measurements of Wind Wave Growth and Swell Decay during the North Sea Wave Project (JONSWAP)," *Deutsche Hydrogr. Z.* , Suppl. A, no. 12, 1973.

Holliday, D., St-Cyr, C., and Woods, N. E., "A Radar Ocean Imaging Model for Small to Moderate Incidence Angles," *Int. J. Remote Sensing,* v. 7, pp. 1809-1834, 1986.

Holton, J. R., *An Introduction to Dynamic Meteorology,* International Geophysics Series v. 23, Academic Press, New York, 391 pp., 1979.

Honhart, D. C., "Requirements for Space-Sensed Oceanographic Data," in *Proc. of SPIE,* v. 481, pp. 142-148, 1984.

Hsaio, and Shemdin, "Measurements of Wind Velocity and Pressure with a Wave Follower during MARSEN," *J. Geophys. Res.*, v. 88, pp. 9841- 9849, 1983.

Hsu, S. A., "The Relationship between the Monin-Obukhov Stability Parameter and the Bulk Richardson Number of the Sea," *J. Geophys. Res.*, v. 94, pp. 8053-8055, 1989a.

Hsu, S. A., "A Verification of an Analytic Formula for Estimating the Height of the Stable Internal Boundary Layer," *Bound. Layer Met.*, v. 48, pp. 197-201, 1989b.

Huebner, G. L., "The Marine Environment," in (Ed.) *Manual of Remote Sensing*, 1975.

Hughes, B. A., and Gower, J. M., "SAR Imagery and Surface Truth Comparisons of Internal Waves in Georgia Strait, British Columbia, Canada," *J. Geophys. Res.*, v. 88, pp. 1809-1824, 1983.

Huhnerfuss, H. W., Alpers, W., Cross, A., Garrett, W. D., Keller, W. C., Lange, P. A., Plant, W. J., and Schulde, F., "The Modification of X and L Band Radar Signals by Monomolecular Sea Slicks," *J. Geophys. Res.*, v. 88, pp. 9817-9822, 1983.

Hwang, P. A., and Shemdin, O. H., "The dependence of Sea Surface Slope on Atmospheric Stability and Swell Conditions," *J. Geophys. Res.*, v. 93, pp. 13903-13912, 1988.

Janssen, P. A. E. M., and Komen G. J., "Atmospheric Stability Effects on the Growth of Surface Gravity Waves," in *The Ocean Surface: Wave Breaking, Turbulent Mixing and Radio Probing*, Toba, Y., and Mitsuyasu, H. (eds.), D. Reidel Pub. Co., pp. 99-104, 1985.

Janssen, P. A. E. M., Lionell, P., Reistad, M., and Hollingsworth, A., "Hindcasts and Data Assimilation Studies with the WAM Model during the SEASAT Period," *J. Geophys. Res.*, v. 94, pp. 973-993, 1989.

Jones, W. L., Schroeder, L. C., and Mitchell, J. L., "Aircraft Measurements of the Microwave Scattering Signature of the Ocean," *IEEE J. Oceanic Eng.*, v. OE-2, pp. 52-61, 1977.

Jones, W. L., Schroeder, L. C., Boggs, D. H., Bracalente, E. M., Brown, R. A., Dome, G. J., Pierson, W. J., and Wentz, F. J., "The Seasat-A Satellite Scatterometer: The Geophysical Evaluation of Remotely Sensed Winds over the Ocean," *J. Geophys. Res.*, v. 87, pp. 3297-3317, 1982.

Kahma, K. K., and Donelan, M. A., "A Laboratory Study of the Minimum Wind Speed for Wind Wave Generation," *J. Fluid Mech.*, v. 192, pp. 339-364, 1988.

Keller, M. R. and Plant, W. J., "X-band Scatterometer Measurements at Low Winds in a Wavetank," Preprint Volume Third Conference on Satellite Meteorology and Oceanography, pp. J41-J43, American Meteorological Society, Jan 31-Feb 5, Anaheim, CA, 1988.

Keller, W. C., and Gotwals, B., "Two-Dimensional Optical Measurement of Wave Slope," *Applied Optics* , v. 22, pp. 3476-3478, 1983.

Keller, W. C., Wismann, V. and Alpers, W.,"Tower-Based Measurements of the Ocean C-Band Radar Backscattering Cross-Section," *J. Geophys. Res.* , v.94, pp. 924-930, 1989.

Keller, W. C., Plant, W. J., and Weissman, D. E., "The Dependence of X-Band Microwave Sea Return on Atmospheric Stability and Sea State," *J. Geophys. Res.*, v. 90, pp. 1019-1029, 1985.

Keller, W. C., and Wright, J. W., "Microwave Scattering and the Straining of Wind-Generated Waves," *Radio Science*, v. 10, pp. 139-147, 1977.

Kinsman, B., *Wind Waves* , Prentice-Hall Inc., Englewood Cliffs, N.J., 1965. (Reprinted by Dover Publications, Inc. Mineola, NY, 1984).

Kitaigorodskii, S. A., "Applications of the Theory of Similarity to the Analysis of Wind-Generated Wave Motion as a Stochastic Process," *Izv. Akad. Nauk. USSR Geophys. Ser. 1*, pp. 105-117, 1962.

Kitaigorodskii, S. A., "On the Theory of the Equilibrium Range in the Spectrum of Wind-Generated Gravity Waves," *J. Phys. Oceanogr.*, v. 13, pp. 816-827, 1983.

Kitaigorodskii, S. A., and Donelan, M. A., "Wind-Wave Effects on Gas Transfer," in *Gas Transfer at the Air-Water Surface*, D. Reidel Pub. Co., pp. 147-170, 1984.

Kitaigorodskii, S. A., "A General Explanation of the Quasi-Universal Form of the Spectra of Wind Generated Gravity Waves at Different Stages of their Development," *Johns Hopkins APL Technical Digest*, v. 8, pp. 11-14, 1987.

Klaptsov, V. M., "Dependence of the Drag, Heat Exchange and Evaporation Coefficients on Meteorological Parameters," *Izvestiya, Atmos. and Ocean. Phys.*, v. 19, p. 61-63, 1983.

Kondo, J., "Air-Sea Bulk Transfer Coefficients in Diabatic Conditions," *Bound. Layer Met.*, pp. 91-112, 1975.

Lamb H., *Hydrodynamics*, sixth ed., Cambridge Univ. Press, 738 pp., 1932 (reprinted by Dover Publications, New York, 1945).

Large, W. G., and Pond S., "Open Ocean Momentum Flux Measurements in Moderate to Strong Winds,", *J. Phys. Ocean.*, v. 11, pp. 324-336, 1981.

Lawner, R. T., and Moore, R. K., "Short Gravity and Capillary Wave Spectra from Tower-Based Radar," *IEEE J. Ocean Eng.*, v. OE-9, pp. 314-324, 1984.

LeBlond, P. H., and Mysak, L. A., *Waves in the Ocean* , Elsevier Scientific Publishing Co., 602 pp., 1978.

LeMehaute, B., "Gravity-Capillary Rings Generated by Water Drops," *J. Fluid Mech.*, v. 197, pp. 415-427, 1988.

Leykin, I. A., and Rozenberg, A. D., "Sea Tower Measurements of Wind-Wave Spectra in the Caspian Sea", *J. Phys. Ocean.*, v. 14, pp. 168-176, 1984.

Li, F., Large, W., Shaw, W., Walsh, E. J., and Davidson, K.,"Ocean Radar Backscatter Relationship with Near-Surface Winds: A Case Study during FASINEX," *J. Phys. Oceanogr.*, v. 19, pp. 342-353, 1989.

Lleonart, C. T., and Blackmann, D. R., "Spectral Characteristics of Wind Generated Waves," *J. Fluid Mech.*, v. 97, pp. 455-479, 1980.

Long, D. G., *Model Based Estimation Theory of Wind Fields from Wind Scatterometer Measurements*, Ph.D Dissertation, Univ. of Southern California, Jan., 1989.

Lumley, J. L., and Panofsky, H. A., *Structure of Atmospheric Turbulence*, Interscience-Wiley, 239 pp., 1964.

Masuko, H., Okamoto, K., Shimada, M., and Niwa, S., "Measurement of Microwave Backscattering Signatures of the Ocean Surface using X and Ka band Airborne Scatterometers," *J. Geophys. Res.*, v. 91, pp. 13065-13083, 1986.

Matthews, C. D., "NROSS, A Valuable Ocean Resource in Jeopardy," *Sea Techn.*, p. 73, Feb, 1987.

Miles, J. W., "On the Generation of Surface Waves by Shear Flow," *J. Fluid Mech.*, v. 3, pp. 185-204, 1957.

Miles, J. W., "On the Generation of Surface Waves by Shear Flow, Parts 2 and 3," *J. Fluid Mech.*, v. 6, pp. 568-598, 1959.

Monin, A. S., and Obukhov, A. M., "Basic Laws of Turbulence in the Ground Layer of the Atmosphere," *Akad. Nauk. USSR Geofiz. Inst. Tr.*, v. 151, pp. 163-187, 1954.

Monin, A. S., and Yaglom, A. M., *Statistical Fluid Dynamics* , v. I and II, English translation, J. L. Lumley (ed.), MIT Press, 639 pp., 720 pp., 1965, 1967.

Moore, R. K., and Pierson, W. J., "Measuring Sea State and Estimating Surface Winds from a Polar Orbiting Satellite," paper presented at Proceedings of International Symposium on Electromagnetic Sensing of Earth from Satellites, Miami Beach, Florida, 1966.

Moore, R. K., and Fung, A. K., "Radar Determination of Winds at Sea," *Proc. IEEE*, v. 67, pp. 1504-1521, 1979.

Moore, R. K., Yu, Y.S., Fung, A. K., Kaneko, D., Dome, G. J., and Werp, R. E., "Preliminary Study of Rain Effects on Radar Scattering from Water Surfaces," *IEEE J. Ocean. Eng.*, v. OE-4, pp. 31-32, 1979.

Mulhearn, P. J., "On the Formation of a Stably Stratified Boundary Layer by Advection of Warm Air over a Cooler Sea," *Bound. Layer Met.*, v. 21, pp. 247-254, 1981.

Nystuen, J. , "A Note on the Attenuation of Surface Gravity Waves by Rainfall," Naval Postgraduate School, manuscript submitted, 1989.

Panofsky, H. A., and Dutton, J. A., *Atmospheric Turbulence*, John Wiley and Sons, New York, 397 pp., 1984.

Paulson, C. A., "The Mathematical Representation of Windspeed and Temperature Profiles in the Unstable Atmosphere," *J. Appl. Met.*, v. 9, pp. 857-861, 1970.

Phillips, O. M. ,"On the Generation of Waves by Turbulent Wind," *J. Fluid Mech.*, v. 4 pp. 426-434, 1957.

Phillips, O. M. ,"The Equilibrium Range in the Spectrum of Wind-Generated Waves," *J. Fluid Mech.*, v. 4, pp. 426-434, 1958.

Phillips, O. M., "On the Dynamics of Unsteady Gravity Waves of Finite Amplitude, 1. The Elementary Interactions," *J. Fluid Mech.*, v. 9, pp. 193-217, 1960.

Phillips, O. M., *The Dynamics of the Upper Ocean,* Cambridge University Press, Cambridge, 2nd ed., 336 pp., 1977.

Phillips, O. M., "Spectral and Statistical Properties of the Equilibrium Range in Wind-Generated Gravity Waves," *J. Fluid Mech.*, v. 156, pp. 505-531, 1985.

Phillips, O. M., "Ocean-Wave Prediction: Where Are We?", *Johns Hopkins APL Technical Digest*, v. 8, pp. 7-10, 1987.

Phillips, O. M., "Radar Returns from the Sea Surface: Bragg Scattering and Breaking Waves," *J. Phys. Oceanogr.*, v. 18, pp. 1065-1074, 1988.

Pierson, W. J., Jr., Neumann, G., and James, R., *Observing and Forecasting Ocean Waves,"* U.S. Navy Hydrographic Office, Pub. no. 603, 1955.

Pierson, W. J., Jr., and Moskowitz, L., "A Proposed Spectral Form for Fully Developed Wind Seas Based on the Similarity Theory of S. Kitaigorodskii," *J. Geophys. Res.*, v. 69, pp. 5281-5290, 1964.

Pierson, W. J., Jr., and Stacey, R. A., "The Elevation, Slope and Curvature Spectra of the Wind Roughened Sea," NASA *Contract. Rep.*, Rep. CR-2247, 1973.

Pierson, W. J., Jr., "The Measurement of the Synoptic Scale Wind over the Ocean," *J. Geophys. Res.*, v. 88, pp. 1682 - 1708, 1983.

Plant, W. J., and Wright, J. W., "Growth and Equilibrium of Short Gravity Waves in a Wind Wave Tank," *J. Fluid Mech.* , v. 82, pp. 767-793, 1977.

Plant, W. J., "A Relationship between Wind Stress and Wave Slope," *J. Geophys. Res.*, v. 87, pp. 1961-1967, 1982.

Plant, W. J., "A Two-Scale Model of Short Wind-Generated Waves and Scatterometry," *J. Geophys. Res.*, v. 91, pp. 10735-10749, 1986.

Plant, W. J., and Keller, W. C., "Evidence of Bragg Scattering in Microwave Doppler Spectra of Sea Return," manuscript submitted, 1989.

Plant, W. J., "Bragg Scattering of Electromagnetic Waves from the Air-Sea Interface", in *Surface Waves and Fluxes: Current Theory and Remote Sensing,* Geernaert, G.L. and Plant, W. J. (eds.), Kluwer Press, Dordricht, The Netherlands, in press, 1990.

Pounder, E., "SEASAT Final Report Volume 1: Program Summary", Jet Propulsion Laboratory Publication 80-38, Pasadena, Calif., 1980.

Rao, K. S., Wyngaard, J. C., and Cote, O. R., "The Structure of the Two-Dimensional Internal Boundary Layer over a Sudden Change in Surface Roughness," *J. Atmos. Sci.*, v. 31, pp. 738-746, 1974.

Reece, A. M., Jr., "Modulation of Short Waves by Long Waves," *Bound. Layer Met.*, v. 13, pp. 203 - 214, 1978.

Rice, S. O.,"Reflection of Electromagnetic Waves from Slightly Rough Surfaces," *Comm. Pure Appl. Math.*, v. 4, pp. 351-378, 1951.

Saxton, J. A., and Lane, J. A., "Electrical Properties of Seawater," *Wireless Eng.*, v. 291, pp. 269-275, 1952.

Schroeder, L. C., Boggs, D. H., Dome, G., Halberstam, I., Jones, W. L., Pierson, W. J., and Wentz, F. J., "The Relationship between Wind Vector and Normalized Radar Cross-Section Used to Derive SEASAT-A Scatterometer Winds," *J. Geophys. Res.*, v. 87, pp. 3318-3336, 1982.

Shemdin, O. H., Tran, H. M., and Wu, S. C., "Directional Measurement of Short Ocean Waves with Stereophotography," *J. Geophys. Res.* , v. 93, pp. 13891-13901, 1988.

Silver, S. (ed.), *Microwave Antenna Theory and Design,* MIT Radiation Laboratory, v. 12, McGraw-Hill, New York, 1949.

Smith, S. D., "Coefficients for Sea Surface Wind Stress, Heat Flux, and Wind Profiles as a Function of Wind Speed and Temperature", *J. Geophys. Res.*, v. 93, pp. 15467-15472, 1988.

Snyder, R. L., Dobson, F. W., Elliott, J. A., and Long, R. B., "Array Measurements of Atmospheric Pressure Fluctuations above Surface Gravity Waves," *J. Fluid Mech.*, v. 102, pp. 1-59, 1981.

Stewart, R. H., *Methods of Satellite Oceanography* , University of California Press, San Diego, CA, 360 pp., 1985.

Stoker, J. J., *Water Waves*, Interscience-Wiley, New York, 567 pp., 1957.

Sugimori, Y., Akagi, K., and Ogihara, M., "Effect of Wave-Current Interction on the Determination of the Volume Scattering Function of Microwaves at the Sea Surface," in *The Ocean Surface: Wave Breaking, Turbulent Mixing and Radio Probing*, Toba, Y., and Mitsuyasu, H. (eds.), D. Reidel Pub. Co., pp. 335-344, 1985.

Tang, S., and Shemdin, O. H., "Measurement of High Frequency Waves using a Wave Follower," *J. Geophys. Res.* , v. 88, pp. 9832-9840, 1983.

Tennekes, H., "The Logarithmic Wind Profile," *J. Atmos. Sci.* , v. 30, p. 234, 1973.

Tsanis, I., and Donelan, M. A.,"The WAVES Programme on the CCIW Research Tower," *National Water Research Institute (NWRI) Report No. 87-65*, Research and Applications Branch, Canada Centre for Inland Waters, 1987.

Tsanis, I., and Donelan, M. A., "Wave Directional Spectra in Mixed Seas," presented at 2nd International Workshop of Wave Hindcasting and Forecasting, Downsview, Ontario, Canada, 25 - 28 April, Environment Canada, pp. 387-396, 1989.

Ulaby, F. T., Moore, R. K., and Fung, A. K., *Microwave Remote Sensing: Active and Passive*, Addison-Wesley Publishing Co., vols. I to III, 1981, 1982.

Valenzuela, G. R., "Scattering of Electromagnetic Waves from a Slightly Rough Surface," *Radio Science* , v. 3, pp. 1057-1066, 1968.

Valenzuela, G. R., "Theories for the Interaction of Electromagnetic and Oceanic Waves- A Review," *Bound. Layer Met.*, v. 13, pp. 61-85, 1978.

Valenzuela, G.R., Plant, W. J., Schuler, D. L., Chen, D. T., and Keller, W.C., "Microwave Probing of Shallow Water Bottom Topography in the Nantucket Shoals," *J. Geophys. Res.*, v. 90, pp. 4931-4942, 1985.

Verma, V., Vesecky, J. F., Napolitano, D., Durden, S. L, and Colton, M.C., "Radar Scattering from a Wind-Driven Sea: A Model Comparison," paper presented at IGARSS'89, 12th Canadian Symposium on Remote Sensing, Vancouver, British Columbia, Canada, 14 July, 1989.

Wentz, F. J., and Mattox, L. A., "New Algorithms for Microwave Measurements of Ocean Winds: Applications to SEASAT and the Special Sensor Microwave Imager," *J. Geophys. Res.*, v. 91, pp. 2289-2307, 1986.

Wentz, F. J., Peteherych, S., and Thomas, L. A., "A Model Function for Ocean Radar Cross-Sections at 14.6 Ghz," *J. Geophys. Res.*, v. 89, pp. 3689-3704, 1984.

Woiceshyn, P. M., Wurtele, M. G., Boggs, D. H., McGoldrick, L.F., and Peteherych, S., "The Necessity for a New Parameterization of an Empirical Model for Wind/Ocean Scatterometry," *J. Geophys. Res.* , v. 91, pp. 2273-2288, 1986.

Wright, J. W., "A New Model for Sea Clutter," *IEEE Trans.* , v. AP-16, pp. 217-223, 1968.

Wright, J. W., "Backscattering from Capillary Waves with Application to Sea Clutter," *IEEE Trans.*, v. AP-14, pp. 749-754, 1966.

Wu, J., "Wind Induced Drift Currents," *J. Fluid Mech.*, v. 68, pp. 49-70, 1975.

Wu, C.S., and Thornton, E. B., "Wave Numbers of Linear Progressive Waves", *J. Waterway, Port, Coastal and Ocean Eng.*, v. 112, pp. 536-540, 1986.

INITIAL DISTRIBUTION LIST

1. Defense Technical Information Center 2
Cameron Station
Alexandria, VA 22304-6145

2. Library, Code 0142 2
Naval Postgraduate School
Monterey, CA 93943-5002

3. Library 1
Naval Oceanographic and Atmospheric Research Laboratory
Atmospheric Directorate
Monterey, CA 93943

4. Naval Postgraduate School
Department of Oceanography
Monterey, CA 93943

Prof. Edward B. Thornton 2
Prof. Roland W. Garwood 1
Prof. Jeffrey A. Nystuen 1

5. Naval Postgraduate School
Department of Meteorology
Monterey, CA 93943-5002

Prof. Kenneth L. Davidson 1
Prof. Carlyle H. Wash 1
Prof. William Shaw 1

6. Naval Postgraduate School
Department of Mathematics
Monterey, CA 93943-5002

Prof. Gordon E. Latta 1

7. Naval Postgraduate School
Department of Electrical and Computer Engineering
Monterey, CA 93943-5002

Prof. Rama Janaswamy 1

8. Naval Oceanographic and Atmospheric Research Laboratory
Atmospheric Directorate
Monterey, CA 93943

Dr. John B. Hovermale	1
Dr. Edward B. Barker	1
Dr. Ted Tsui	1
Dr. Andreas K. Goroch	1
Dr. Marie C. Colton	5

9. Naval Oceanographic and Atmospheric Research Laboratory
Head, Remote Sensing Branch
Stennis Space Center, MS 39529-5004

Mr. Albert E. Pressman	1

10. Naval Research Laboratory
Space Sensing Branch
Code 8310
4555 Overlook Ave. SW
Washington, DC 20375-5000

Dr. Vince Noble	1
Mr. William Keller	1
Ms. Mary Keller	1

11. Naval Research Laboratory
Code 1003.8
4555 Overlook Ave. SW
Washington, DC 20375-5000

Dr. Gerald L. Geernaert	1

12. Office of Naval Research
Director, Applied Oceanography and Acoustics
Code 124
800 N. Quincy St.
Arlington, VA 22217

Dr. Melbourne Briscoe	1

13. Office of Naval Research
Code 1121RS
800 N. Quincy St.
Arlington, VA 22217

Dr. Frank Herr	1

14. Canada Centre for Inland Waters
National Water Institute
Research Applications Branch
PO Box 5050
Burlington, Ontario
Canada L7R 4A6

Dr. Mark Donelan	2

15. Woods Hole Oceanographic Institution
Department of Ocean Engineering
Woods Hole, MA 02543

Dr. William Plant	1
Dr. Hans Graber	1

16. Jet Propulsion Laboratory
4800 Oak Grove
Pasadena, CA 91109

Dr. Fuk Li	1
Dr. David Long	1
Mr. Peter Woiceshyn	1
Dr. Steven Durden	1

17. Scripps Institute of Oceanography
Center for Coastal Studies
Mail Stop A-009
La Jolla, CA 92903

Dr. Michael Freilich	1

18. Scripps Institute of Oceanography
Center for Climate Research
Mail Stop A-030
La Jolla, CA 92903

Dr. Jerome Smith	1

19. University of Washington
Department of Atmospheric Sciences
Seattle, WA 98195

Prof. Kristina B. Katsaros 1

20. City University of New York
Institute of Marine and Atmospheric Sciences at City College
New York, NY 10031

Prof. Willard J. Pierson 1

21. University of New Hampshire
Ocean Processes Analysis Laboratory
SERB
Durham, NH 03824-3525

Prof. Christopher N. K. Mooers 1

22. Hofstra University
Department of Engineering
Hampstead, NY 11550

Prof. David E. Weissman 1

23. Stanford University
Center for Radar Astronomy
232 Durand
Stanford, CA 94035

Mr. Vikra Verma 1

24. National Aeronautics and Space Administration
NASA Headquarters
Code EED
Washington, DC 20546

Dr. W. Linwood Jones 1

25. Remote Sensing Systems
1101 College Ave.
Suite 220
Santa Rosa, CA 95404

Dr. Frank Wentz 1

26. Commanding Officer 1
Fleet Numerical Oceanography Center
Monterey, CA 93943

27. Commanding Officer 1
Naval Oceanographic Office
Stennis Space Center, MS 39522-5001

28. Oceanographer of the Navy 1
Code OP-096
Naval Observatory
34th and Massachusetts Ave. NW
Washington, DC 20390

29. User Systems, Inc. 1
4608 Willet Dr.
Annandale, VA 22003

Dr. Samuel W. McCandless

616-585

NAVAL POSTGRADUATE SCHOOL
MONTEREY, CALIFORNIA 93943-8002

Thesis
C6455 Colton
c.1 Dependence of radar
backscatter on the
energetics of the air-sea
interface.

Thesis
C6455 Colton
c.1 Dependence of radar
backscatter on the
energetics of the air-sea
interface.

AMERICAN BINDERY
TOPEKA KANSAS

thesC6455
Dependence of radar backscatter on the e
3 2768 000 87742 7
DUDLEY KNOX LIBRARY